

Using induced pluripotent stem cells for modeling POLG mitochondrial disease



Sepideh Mostafavi

Thesis for the degree of Philosophiae Doctor (PhD)
University of Bergen, Norway
2022

UNIVERSITY OF BERGEN



Using induced pluripotent stem cells for modeling POLG mitochondrial disease

Sepideh Mostafavi



Thesis for the degree of Philosophiae Doctor (PhD)
at the University of Bergen

Date of defense: 03.02.2022

© Copyright Sepideh Mostafavi

The material in this publication is covered by the provisions of the Copyright Act.

Year: 2022

Title: Using induced pluripotent stem cells for modeling POLG mitochondrial disease

Name: Sepideh Mostafavi

Print: Skipnes Kommunikasjon / University of Bergen

" فرصت کوتاه بود و سفر جانکاه بود

اما یگانه بود و هیچ کم نداشت

به جان منت پذیرم و حق گزارم "

ا. شاملو

*"The opportunity was short and the journey was grievous,
nevertheless, it was unique and had all.*

I receive with all my soul and give high praise! "

A.Shamlou

Table of Contents

| | |
|---|-----------|
| <i>Scientific Environment</i> | 1 |
| <i>Acknowledgements</i> | 3 |
| <i>Abstract</i> | 7 |
| <i>List of publications</i> | 11 |
| <i>List of Abbreviation</i> | 13 |
| 1. Introduction | 15 |
| 1.1. Mitochondria | 15 |
| 1.1.1. Mitochondrial structure..... | 15 |
| 1.1.2. Mitochondrial bioenergetics | 16 |
| 1.1.3. Reactive Oxygen Species (ROS)..... | 18 |
| 1.1.4. Mitochondrial DNA (mtDNA)..... | 19 |
| 1.1.4.1. DNA Polymerase Gamma (POLG)..... | 19 |
| 1.1.4.2. Regulation of mtDNA levels in different tissues..... | 20 |
| 1.2. Mitochondrial disease / POLG-related disease | 20 |
| 1.2.1. The W748S and A467T animal models..... | 21 |
| 1.3. Stem cells | 22 |
| 1.3.1. Mitochondrial changes during development and differentiation..... | 24 |
| 1.4. Cardiogenesis | 26 |
| 1.4.1. Signaling pathways involved in cardiogenesis | 27 |
| 1.4.2. Generating cardiomyocytes in vitro from stem cells..... | 28 |
| 1.5. Generation of neural stem cells (NSC) | 29 |
| 1.5.1. Signaling pathways involved in NSCs generation | 31 |
| 1.5.2. Generating NSCs in vitro from stem cells | 32 |
| 2. Aims | 33 |
| 3. Methods | 35 |
| 3.1. Biological samples | 35 |
| 3.1.1. Generating human induced pluripotent stem cell lines (iPSC)..... | 35 |
| 3.1.2. Human embryonic stem cell lines (ESC)..... | 36 |
| 3.1.3. Human pluripotent stem cell (PSC) culture | 36 |
| 3.1.4. Tissue studies | 37 |
| 3.2. Human pluripotent stem cells differentiation and characterization | 37 |
| 3.2.1. Human pluripotent stem cell differentiation | 37 |
| 3.2.1.1. Neural induction and generation of NSCs | 37 |
| 3.2.1.2. Generating dopaminergic neurons (DA)..... | 38 |
| 3.2.1.3. Cardiomyocyte differentiation | 38 |
| 3.2.1.4. Hepatocyte differentiation | 39 |
| 3.2.2. Characterization of PSCs and differentiated cells | 39 |
| 3.2.2.1. Gene expression analysis via real-time PCR..... | 40 |
| 3.2.2.2. Immunocytochemistry and immunofluorescence (ICC/IF) | 41 |
| 3.2.2.3. Microelectrode array measurement (MEA) | 41 |
| 3.2.2.4. Quantification of cell composition in cardiac culture..... | 42 |
| 3.2.2.4.1. Quality assurance for polychromatic flow cytometry | 43 |
| 3.3. Assessment of mitochondrial biogenesis and mitochondrial function | 43 |
| 3.3.1. Mitochondrial DNA (mtDNA) assessment..... | 43 |

| | |
|--|-----------|
| 3.3.1.1. Mitochondrial DNA quantification and deletion assessment using polymerase chain reaction (PCR) | 44 |
| 3.3.1.2. Assessment of mtDNA level per mitochondrion..... | 44 |
| 3.3.2. Assessment of metabolic state and mitochondrial function | 45 |
| 3.3.2.1. Comparing metabolic state of PSC- derived cardiomyocyte with their undifferentiated origin using Seahorse XF-96 analyzer | 45 |
| 3.3.2.2. Measurement of mitochondrial membrane potential (MMP) | 46 |
| 3.3.2.3. Assessment of POLG mutation effect on cellular redox state | 47 |
| 3.3.2.3.1. Assessment of electron transport chain (ETC) level in cells and tissues | 47 |
| 3.3.2.3.2. Measurement of ROS level and cellular senescence..... | 48 |
| 3.3.2.3.3. Comparison of NAD ⁺ metabolism between patient and control cell lines | 48 |
| 3.3.2.3.4. Assessment of ATP level | 49 |
| 3.3.3. Assessment of mitochondrial ultrastructure | 49 |
| 3.4. RNA sequencing | 50 |
| 3.5. Statistical analysis..... | 51 |
| 4. Results and Discussion..... | 53 |
| 4.1. Paper I; “Disease-specific phenotypes in iPSC-derived neural stem cells with <i>POLG</i> mutations” | 53 |
| 4.1.1. Mutant fibroblasts and iPSCs partially manifest the mitochondrial abnormalities | 54 |
| 4.1.2. Neuronal differentiated cells; NSCs and DA neurons, manifest greater mitochondrial function impairment compared with iPSCs and parental fibroblasts | 56 |
| 4.1.3. Changes in cellular redox status occur only in mutant NSCs..... | 57 |
| 4.1.4. UCP2/SirT1- regulated cellular senescence and BNIP3 pathway-mediated mitophagy are involved in the pathogenesis of mutant NSCs | 58 |
| 4.2. Paper II; “A method for differentiating human induced pluripotent stem cells toward functional cardiomyocytes in 96-well microplates”..... | 60 |
| 4.2.1. Optimizing cardiomyocyte differentiation in 96 well format..... | 60 |
| 4.2.2. Monitoring cardiomyocyte differentiation process..... | 61 |
| 4.2.3. Assessment of cell composition in the culture and yield of differentiation..... | 62 |
| 4.2.4. Electrophysiological validation of PSC-derived cardiomyocyte..... | 63 |
| 4.2.5. Investigation of inter-well heterogeneity..... | 63 |
| 4.3. Paper III; “Distinct mitochondrial remodeling during mesoderm differentiation in a human-based stem cell model” | 65 |
| 4.3.1. Investigation of mitochondrial changes during cardiomyocyte differentiation | 66 |
| 4.3.2. Mitochondrial content falls progressively during mesoderm differentiation..... | 67 |
| 4.3.3. Despite lower mitochondrial mass, differentiated cells at S5 contain mature mitochondria that can generate more energy through TCA rather than glycolysis | 69 |
| 4.3.4. Cristae remodeling during cardiomyocytes differentiation | 70 |
| 5. Concluding remarks and future perspectives | 73 |
| 6. References | 77 |
| 7. Appendix Figures..... | 95 |

Scientific Environment

The work presented in this thesis was carried out at the department of Clinical Medicine institute, K1, University of Bergen. The study was performed under supervision of Professors Laurence A. Bindoff as the main supervisor and Christian A. Vedeler as co-supervisor at the Center for Mitochondrial Medicine & Neurogenetics, Department of Clinical Medicine, and Neuro-SysMed, Center of excellence for Experimental therapy in Neurology.

Acknowledgements

Writing a PhD is a privilege and quite a journey but rewarding. None of this would have been possible without the sacrifices and supports of the wonderful people whom I would like to acknowledge.

I wish to start by thanking two important people in my life, whom I am standing on their shoulders; my parents. Even through our video calls, I can always feel the warmth of their heart, the confidence they have in me, and their endless unconditional love and generosity. I truly have no idea where I would have been without your financial and emotional support. Thank you, Mom! Thank you Dad!

I am extremely grateful to my main supervisor Prof. Laurence A. Bindoff for the opportunity to join his research group before starting my PhD in 2014. He accepted me as a volunteer when no one supported me and helped me to get the PhD position. I consider myself so lucky to be introduced to the complicated field of neurodegenerative disorders by him, one of the experts in the field. He taught me how to evaluate evidence, to criticize them, and to see them from different angles. Nevertheless, he was not just my scientific mentor, he was the person who shed light on my weaknesses and helped me to overcome some of them and grow. Without him, I would have never known how tough I could be. Dear Laurence, being your student was an honor.

I also want to thank my co-supervisor Prof. Christian A. Vedeler for all his support and encouragement. When I was about to give up, your positive feedbacks helped me to stand on my feet again and continue. Thank you for all the confidence you had in me and for the time that you generously spent on our helpful discussions.

The world is a better place with people who want to develop and lead others. What makes it even better are people who strive to grow and help others grow. I truly believe that one of those people is Dr. Novin Balafkan. Although he was not my official mentor, he stood by my side and guided me as a co-supervisor, helped me as a friend, and listened to me as a brother. I was always amazed by his enthusiasm for science, his ambition, and his passion for learning more and finding answers to unknowns. I will never forget our scientific conversations, which he always colored with his great sense

of humor. Dear Novin, without you this project would never have started nor ended. I sincerely owe you a great gratitude.

Another wonderful person who I believe is a teacher by nature is Dr. Gonzalo Nido. He always accepted me with my naïve endless questions. His contribution to analyzing, discussing, and understanding our RNA seq data was the driving force for the progress achieved in the last phase of my PhD. Dear Gon, without you, nothing would have made sense.

I would like to express my special thanks to two lab angels, Hanne Linda Nakkestad and Mette Haugen, who truly had important roles during my study. I really appreciate Hanne Linda's patience and cheerful character even when I was bothering her with my endless orders. I am thankful for Mette's excellent help in the lab, for always being supportive, and for listening to both scientific and personal matters. You two made a warm and welcoming atmosphere that I always wanted to be part of.

I am so grateful to have been able to work with Dr. Manja Schubert. Her knowledge, experience, and vision had a great impact on the project. Dear Manja, I have learned and enjoyed a lot from our conversations during those late evenings working in the lab.

A warm thank you to all my wonderful colleagues, particularly, Dr. Xiao Liang, Cecilie Kristiansen, Atefeh Kianian, Dr. Cecilie Totland and the members of Prof. Tzoulis group, especially, Dr. Christian Dölle and Nelson Osuagwu, whose supports and valuable scientific input and contribution added a lot to this project value.

I would like to express my sincere gratitude to our collaborators, and co-authors; people from prof. Tronstad's lab, prof. Sullivan's group, and prof. Ziegler's lab, for their valuable contributions to this work.. I would also like to express my appreciation for the excellent technical assistance from the members of Flow cytometry and MIC core facilities; Brith Bergum, Endy Sprite, and especially, Hege Avnes Dale who did not leave me alone even during the time that the whole faculty was closed due to the Covid-19.

A great thank you to two awesome people Ida Herdlevær and Janani Sandersan who at the beginning were my officemates, but soon they became great friends of mine. Your presence and support for both scientific and personal matters have been always appreciated.

My PhD journey was full of ups and downs, and passing through those rough moments without positive energy would be impossible. I believe that I am so blessed to have access to an unlimited source of positive energy, which is refilled constantly by great people such as my friends; Hoda and Sadaf, who became my sisters in Bergen; my brother, Alireza, and my sister in law, Anna that never stopped supporting me; my life coach, Dr. Foojan Zeine, who I learned a lot from her; and my Norwegian family, Kari and Kjell Randa, and lovely Besten that their encouragements meant a lot to me.

There is one person that I cannot find any word to explain his influence on this journey. He was the one in whose arms I found comfort. The only person who could lift me up when I was completely broken. In fact, his role in this episode of my life was invaluable. Thank you for believing in me, my love, Øyvind!

Bergen 2021

Sepideh Mostafavi

Abstract

Background: More than 90% of the energy required to sustain life is provided by mitochondria through the process of oxidative phosphorylation (OXPHOS). The role of mitochondria, however, is not restricted to supplying cellular energy; they are also involved in many other cellular processes including differentiation and cell death. Mitochondrial functional impairment is also associated with a wide spectrum of devastating diseases known as mitochondrial diseases.

Among the most common mitochondrial disorders are POLG-related diseases. These comprise a large number of different phenotypes with age of onset ranging from infancy to adulthood. These complicated and incurable disorders are caused by mutations in the *POLG* gene which encodes the catalytic subunit of DNA polymerase gamma (POLG). The enzyme POLG is involved in mitochondrial DNA (mtDNA) replication, and despite being present in all cells, the main disease manifestations show tissue and cell type-specificity. The patho-mechanisms underlying POLG-disease remain poorly documented mostly due to the lack of reliable animal models and limited access to affected tissues. Human induced pluripotent stem cells (iPSC) with the capacity of self-renewal and differentiation into all relevant tissues provide a promising tool for modeling POLG-related diseases and investigating possible treatments.

Primary clinical experiments have shown that the high energy demanding tissues such as brain, liver and skeletal muscle are severely affected, however, cardiac tissue appear clinically unaffected. Understanding this paradox is important as it can increase our understanding of the tissue specific nature of these diseases.

Aim: The main aim of this project was to model POLG-related disease using iPSCs derived from patient fibroblasts and differentiated into different cell types. We planned to differentiate them to cardiac and neuronal cells to investigate the impact of POLG mutations on mitochondrial function.

Methods: In paper I, we modified neuronal differentiation protocols to generate neural stem cells (NSC), and investigate the impact of POLG mutation on mitochondrial function by comparing different mitochondrial parameters in control and mutant NSCs. We employed different methods including flow cytometry, PCR, western blotting and

Liquid Chromatography/Mass Spectrophotometry (LC/MS) to investigate the mitochondrial content, mtDNA level, respiratory chain complexes and NAD⁺ metabolism, ROS generation and activation of mitophagy. In the second project, we established a high throughput method for differentiating cardiomyocytes in 96well plate format in order to monitor mitochondrial changes during early stages of cardiac differentiation (paper 2). In the third paper, we differentiated human pluripotent stem cells (PSC) towards mesoderm, cardiac progenitors and later to cardiomyocytes using the protocol established in paper II. We used this to investigate changes of mitochondrial content and mtDNA copy number during early stages of mesoderm differentiation using different methods including flowcytometry and qPCR. We also studied mitochondrial function and metabolic remodeling by seahorse analysis and flow cytometry.

Results: The comparison of different mutant and control cell types including fibroblasts, iPSCs and NSCs in paper 1 showed that only NSCs manifested all the features that were seen in patient post-mortem tissues including mtDNA depletion and complex I deficiency. Using our iPSC-derived NSC model, we also showed the impact of POLG mutation on the overproduction of ROS and impairment of NAD⁺ metabolism, and how this led to increased cellular senescence.

In the second part of the study, we established a high-throughput cardiomyocyte differentiation protocol with low variation of differentiation efficiency between wells and between runs of differentiation. We also showed that the differentiated cardiomyocytes generated by our micro plate format were fully functional and expressed the correct cardiomyocyte markers. We used this protocol in the third project to study the mitochondrial changes during early mesoderm differentiation towards cardiac lineage. We confirmed the previous reported metabolic remodeling during mesoderm differentiation, however, in contrast to previous studies, and our expectations, we showed that mitochondrial content and mtDNA copy number decreased during the early stages of cardiomyocyte differentiation.

Conclusion: Our NSC model of POLG disease is the first that faithfully replicates the findings observed in patient post mortem tissues. Using this model, we showed that NSC developed mtDNA depletion and complex 1 deficiency and we confirmed the metabolic impact of this by demonstrating the changes in the NAD⁺/NADH ratio. We could also

examine the downstream consequences of POLG mutation on aspects of mitochondrial function such as ROS production and show that the combined effects led to increased cellular senescence. Considering the regenerative capacity of NSCs, our aim is to use this robust model system for drug screening and identification of possible treatment for POLG diseases.

In our work with cardiomyocytes, we showed that our method using the 96 well microplate format was robust and efficient with low inter well variation. This means that it too can be used for high throughput experiments such as studying the early stages of cardiac development and drug screening.

In contrast to earlier reports, we detected a significant reduction in mitochondrial mass and mtDNA level during mesoderm differentiation towards cardiac lineage. Despite the remarkable mitochondrial reduction, we showed that differentiated cells nevertheless had a higher capacity to generate energy through OXPHOS. Overall our results suggested a unique mitochondrial remodeling process in which the metabolic switch from glycolysis to OXPHOS occurs without an increase in mitochondrial mass and mtDNA level. In the other words, metabolic remodeling is associated with mitochondrial maturation and increased mitochondrial activity rather than elevated mitochondrial mass and mtDNA level.

List of publications

- 1- LIAN, K. X., KRISTIANSEN, C. K., **MOSTAFAVI, S.**, VATNE, G. H., ZANTINGH, G. A., KIANIAN, A., TZOULIS, C., HØYLAND, L. E., ZIEGLER, M., PEREZ, R. M., FURRIOL, J., ZHANG, Z., BALAFKAN, N., HONG, Y., SILLER, R., SULLIVAN, G. J. & BINDOFF, L. A. 2020. *Disease-specific phenotype in iPSC-derived neural stem cells with POLG mutations*. EMBO Molecular Medicine, 12, e12146.
- 2- BALAFKAN, N, **MOSTAFAVI, S.**, SCHUBERT, M, SILLER, R, LIAN, K, X, SULLIVAN, G, BINDOFF, L, A. (2020). *A method for differentiating human induced pluripotent stem cells toward functional cardiomyocytes in 96-well microplates*. Scientific Reports 10(1):18498.
- 3- **MOSTAFAVI, S.**, BALAFKAN, N, NITSCHKE PETERSEN, I, K., NIDO, G. S., SILLER, R, TZOULIS, C, SULLIVAN, G.J, BINDOFF, L.A. (2021). *Distinct mitochondrial remodeling during early cardiomyocyte development in a human-based stem cell model*. Frontiers; Cell and Developmental Biology 9:744777. doi: 10.3389/fcell.2021.744777

The papers were published in online free and open access journals and available for reuse for non-commercial purposes, through open access publishing

List of Abbreviation

| | |
|-------------|---|
| ADP | Adenosine diphosphate |
| ATP | Adenosine triphosphate |
| APP | Amyloid Beta Precursor Protein |
| BMP | Bone morphogenetic protein |
| BSA | Bovine Serum Albumin |
| CCCC | Carbonyl cyanide m-chlorophenyl hydrazone |
| CDH5 | Cadherin 5 |
| cDNA | Complementary DNA |
| CHIR99021 | Inhibitor of Glycogen synthase kinase3 (name of the small molecule) |
| Connexin 43 | Gap Junction protein Alpha 1 |
| DA neuron | Dopaminergic neuron |
| DCFDA | 2',7'-dichlorofluorescein diacetate |
| DKK1 | Dickkopf WNT signaling pathway inhibitor 1 |
| EB | Embryonic body |
| ECAR | Extracellular acidification rate |
| ESC | Embryonic Stem Cell |
| ETC | Electron Transport Chain |
| FAD | Flavin Adenine Dinucleotide |
| FCCP | Carbonyl cyanide-p-trifluoromethoxyphenylhydrazone |
| PSC | Pluripotent Stem cell |
| ICM | Inner Cell Mass |
| iPSC | Induced Pluripotent Stem cell |
| IWP2 | Inhibitor of WNT production-2 |
| MEA | Microelectrode arrays |
| MMP | Mitochondrial Membrane Potential |
| MSCAE | Mitochondrial spinocerebellar ataxia with epilepsy |
| mtDNA | Mitochondrial DNA |
| MTDR | MitoTracker Deep Red |

| | |
|------------------|--|
| MTG | MitoTracker Green |
| NAD ⁺ | Nicotinamide Adenine Dinucleotide |
| NSC | Neural Stem cell |
| OCR | Oxygen consumption Rate |
| OXPPOS | Oxidative phosphorylation |
| POLGA | DNA Polymerase Gamma, Catalytic subunit; known as POLG |
| POLGB | DNA Polymerase Gamma 2, Accessory subunit; known as POLG2 |
| PSC | Pluripotent Stem Cell |
| ROS | Reactive Oxygen species |
| S1 | Differentiation Stage 1; Undifferentiated cells (D0) |
| S2 | Differentiation Stage 2; Mesendoderm cells (Day 1-2) |
| S3 | Differentiation Stage 3; Cardiac mesoderm cells (Day 3) |
| S4 | Differentiation Stage 4; Cardiac progenitors (Day 5-7) |
| S5 | Differentiation Stage 5; Functional cardiomyocytes (Day 12-15) |
| SSBP | Single stranded Binding Protein |
| TCA | Tricarboxylic acid; Krebs cycle |
| TFAM | Mitochondrial Transcription Factor A |
| TMRM | Tetramethylrhodamine methyl |
| TMRE | tetramethylrhodamine ethyl ester |
| TOMM20 | Translocase of Outer Mitochondrial Membrane 20 |
| VDAC-1 | Voltage Dependent Anion Channel 1 |
| Wnt | Wingless/INT signaling pathway |

1. Introduction

1.1. Mitochondria

Mitochondria are double-membrane organelles found in almost all eukaryotic cells that are known as the cellular powerhouse. Beside ATP generation, they are involved in a wide spectrum of cellular processes such as apoptosis, calcium signaling, and stem cell fate and differentiation¹⁻³. It is believed that mitochondria originated from a proteobacterial ancestor that became an endosymbiont with a eukaryotic cell, in which it facilitated ATP generation and oxygen detoxification for the host^{4,5}. This theory is supported by the findings that mitochondria contain their own independent genome, which is small and circular and has a genetic code similar to the bacterial code⁶. In addition, the mitochondrial translation machinery is similar to prokaryotes and intramitochondrial protein synthesis is inhibited by antibiotics such as oxazolidinones and chloramphenicol⁷. Mitochondrial number and morphology vary depending on cell type⁸⁻¹⁰ and energy demand. For example, in cardiomyocytes they occupy approximately 22-37% cardiomyocyte volume¹¹.

1.1.1. Mitochondrial structure

Mitochondria possess two membranes, which are different in composition, structure and function. While the outer membrane envelopes the organelle and regulates transport between cytosol and mitochondrial inter membrane space, the inner membrane invaginates to form a baffle-like structure, known as cristae. Cristae accommodate large number of different proteins involved in ATP generation such as electron transport chain complexes (complexes I-IV) and ATP synthase (complex V)¹²⁻¹⁴, as well as those involved in the transport of specific proteins and metabolites between mitochondrial intermembrane space and matrix. Mitochondria are highly dynamic organelles and their number, size, shape and structure vary based on both cell type and metabolic conditions (For review see¹⁵). For instance, in cardiac cells, mitochondria are more abundant and larger, and contain more cristae per surface unit of mitochondria than is observed in liver, brain and kidney cells^{8,10,16}. Moreover, cristae undergo structural modifications,

such as changes in length, width, and tightness, in response to change in bioenergetic state, substrate availability, and metabolic stresses (hypoxia), glucose depletion, increased ROS or other toxicity¹⁵.

Stem cell studies show that mitochondrial structure can switch between an elongated and interconnected network to fragmented state during reprogramming and cell differentiation to meet changing energy and metabolic demands^{17,18}.

1.1.2. Mitochondrial bioenergetics

The major enzymatic system for generating ATP, the respiratory chain, is embedded in the inner mitochondrial membrane. Cellular substrates such as carbohydrates, lipids, and proteins are broken down via intermediary metabolism and mostly converted into acetyl-CoA, which then enters the citric acid cycle, also known as tricarboxylic acid (TCA) or Krebs cycle. Acetyl-CoA is oxidized to carbon dioxide and water and energy conserved as electrons that are transferred to cofactors nicotinamide adenine dinucleotide, (NAD⁺) and flavin adenine dinucleotide (FAD)^{19,20}.

The reduced cofactors NADH and FADH₂ donate electrons to the electron transport chain (ETC) mainly complexes I and II²⁰⁻²² and the final electron acceptor is oxygen, which is reduced to water (Figure. 1). The ETC comprises several redox reactions that conserve the energy of electron transport and use it to pump protons from mitochondrial matrix to the intermembrane space, generating a pH and electrical potential across the inner mitochondrial membrane, known as mitochondrial membrane potential (MMP), ($\Delta\Psi_m$). ATP synthase (complex V) discharges this electrochemical potential to drive the phosphorylation of ADP and ATP production. This is the process of oxidative phosphorylation, OXPHOS²².

In addition to ATP generation, the MMP plays a fundamental role in cell homeostasis and cell fate. It is the driving force of importing compounds, such as mitochondrial proteins, and cations like Ca²⁺ and Fe²⁺ into mitochondria^{2,23-27}.

Moreover, the membrane potential is a determining factor involved in the mitochondrial quality control process known as mitophagy, in which mitochondria with low membrane potential are eliminated and recycled without inducing the cell death cascade^{28,29}.

Mitochondrial membrane potential is the result of controlled mechanisms that balance both the operation of the proton pumps and the membrane potential discharge. For instance, under hypoxic condition when oxidative phosphorylation stops, cells hydrolyze ATP to keep membrane potential.

Maintaining the high electrical field is energetically expensive for cells and can be associated with proton and electron leakage and increased ROS production, which can damage the cell (See section 1.1.3)^{30,31}. On the other hand, a low MMP means ATP depletion and mitochondrial depolarization that can trigger the release of cations and cytochrome c and the cascade of cell death³².

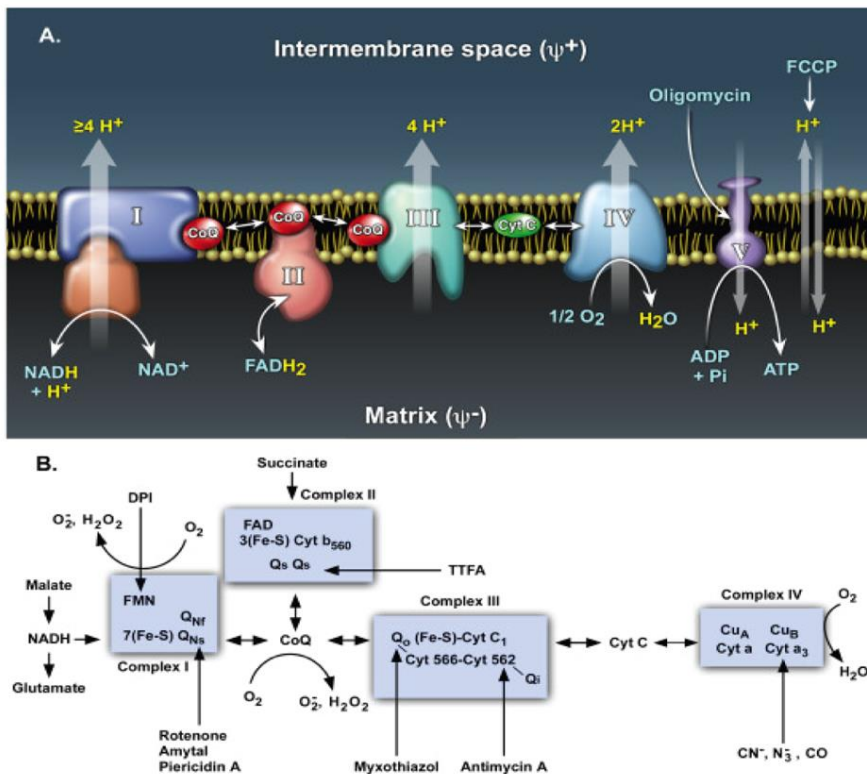


Figure 1. Mitochondrial Electron transport chain, ETC, and oxidative phosphorylation process. A) Schematic diagram of the ETC and the sites of proton translocation. $NADH$ and $FADH_2$ carry the electrons and deliver them to the complex I and II and oxidize to NAD^+ and FAD respectively. The high energy electrons are then passed down to complex III, via coenzyme Q. Ultimately, Complex III donates its electrons to complex IV which in turn reduces

molecular oxygen with the formation of water. Electrons are transferred between complexes in a “staircase” manner i.e. their free energy decreases when they transfer from one complex to another. The energy released by electron transport is used to drive protons out of the matrix into the mitochondrial intermembrane space. The last step of mitochondrial oxidative phosphorylation is catalyzed by complex V, which reverses proton flows across the inner membrane and utilizes the free energy to catalyze phosphorylation of ADP to ATP. B) Shows the Fe-S groups present in the ETC complexes that convey electrons. It also shows the sites of action of common respiratory inhibitors and ROS generation sites. The picture is adapted from an open access article ³³, and is available via license: [CC BY 2.0](https://creativecommons.org/licenses/by/2.0/).

1.1.3. Reactive Oxygen Species (ROS)

Oxygen is the ultimate recipient of respiratory chain electrons and is converted to water by Complex IV, also known as cytochrome *c* oxidase. Despite the presence of an excellent electrical insulator, i.e. mitochondrial inner membrane, high energy electrons can escape from the electron transport chain complexes and transfer directly to oxygen (Figure. 1). Partial reduction of oxygen forms the anionic free radical such as superoxide ($O_2^{\cdot -}$) and hydroxyl radical ($\cdot OH$), and non-radical oxidants, such as hydrogen peroxide (H_2O_2) and singlet oxygen (1O_2) ³⁴. While several sites for mitochondrial ROS generation have been proposed, complexes I and III are considered the major ones ³⁵⁻³⁷. Despite the presence of antioxidant defense systems including Superoxide dismutase (SODs), highly reactive molecules can cause irreversible damage to cells through oxidation of cellular compounds such as fatty acids, proteins, RNA and DNA, and by deactivating enzymes through the oxidation of co-factors. Accumulation of ROS, either due to excessive ROS production or disabled ROS scavengers, can lead to oxidative stress, which has been proposed to be involved in disease process of wide spectrum disorders including neurodegenerative diseases ³⁸. Moreover, free radical induced damage can trigger cell senescence and apoptosis ³⁹.

While ROS may cause damage, they are also involved in signaling especially during cell differentiation and cell growth ³⁴. For example, the type of reactive oxygen species produced and site of generation dictates their role; i.e. to participate in cell signaling or result in oxidative damage ^{35,40}.

1.1.4. Mitochondrial DNA (mtDNA)

The mitochondrial genome is a circular, double stranded DNA molecule of about 16.6 kb. MtDNA encodes 2 rRNA, 22 tRNA and 13 polypeptides that are all subunits of respiratory chain complexes ⁴¹⁻⁴³. Similar to the prokaryotic genome, mitochondrial genes do not contain introns, intergenetic sequences are absent or limited to a few bases ⁴², and the genetic code is different from that used for translation in the cytosol ⁶. The mammalian mitochondrial genome is inherited through the female germ line, and does not follow the rules of conventional Mendelian genetics ^{44,45}.

The mitochondrial genome is present in multiple copies in every cell. The mtDNA copy number varies from ~100 copies in sperm to >10⁵ in oocytes. Since mtDNA is present in multiple copies, genomes with mtDNA pathological variants and wild type genomes can coexist within a single cell: this is known as heteroplasmy.

Mitochondria DNA is organized into compact, small structures known as nucleoids. A number of different proteins involved in mtDNA replication and transcription are associated with the nucleoid including DNA polymerase gamma (POL γ), the mitochondrial helicase (Twinkle), mitochondrial single-stranded binding proteins (SSBPs), and mitochondrial transcription factor A (TFAM) ⁴⁶. TFAM is a 24-kDa protein that binds mtDNA through two DNA binding domains. The amount of bound TFAM is proportional to the mtDNA copy number ^{47,48}.

1.1.4.1. DNA Polymerase Gamma (POLG)

Mitochondrial DNA replication relies on products encoded by the nuclear genome. It is initiated by the formation of a replisome machinery containing mitochondrial DNA polymerases (such as POLG and PrimPol), Twinkle, SSBP, mitochondrial RNA polymerase, TFAM, and Type I and II topoisomerases.

The mitochondrial DNA polymerase γ (POLG) is a heterotrimer comprising one α and two β subunits encoded on chromosomes 15 and 17 respectively. The catalytic alpha subunit, known as POLG or POLG A, catalyzes both 5'→3' polymerase and 3'-5' exonuclease proofreading activities ⁴⁹ whereas the beta subunit (POLG B or POLG2) is

thought to act as “processivity factor” important for DNA binding ⁵⁰. Mutations in POLG are associated with a large number of different phenotypes that are described later (section 1.2).

Replication of mtDNA is regulated at different levels including by the controlled expression of proteins involved in mtDNA replication such as SSBP and TFAM, and apparently through epigenetic control ⁵¹⁻⁵³. Moreover, it has been shown that DNA polymerase activity is stimulated and regulated by binding of SSBP to the exposed single-stranded mtDNA, which is required for maintenance of mtDNA integrity ⁵⁴.

1.1.4.2. Regulation of mtDNA levels in different tissues

Mitochondrial DNA integrity and copy number play an important role in the maintenance of mitochondrial function and metabolic homeostasis. Mitochondrial DNA copy number is highly regulated in a tissue- specific manner ⁵⁵. Post-mitotic tissues with high-energy demand that are highly reliant on oxidative phosphorylation for ATP production have a higher mtDNA copy number, suggesting copy number and energy profile are linked ⁵⁵⁻⁵⁷. It has been shown that there is a threshold for mtDNA copy number for each cell type ⁵¹ and there is a balance between replication and degradation of mtDNA to keep its levels constant in a cell ⁵⁸. Failure to maintain mtDNA copy number or its integrity can lead to both impaired mitochondrial function and diseases ⁵⁸⁻⁶¹.

1.2. Mitochondrial disease / POLG-related disease

Despite the presence of an independent genome, mitochondria are not independent entities and rely heavily on gene products encoded in the nucleus for their function and homeostasis. Thus, inherited defects in both the nuclear and mitochondrial genomes can cause a mitochondrial disease. Mitochondrial disorders can arise from defects in proteins involved in mtDNA replication, OXPHOS activity, mitochondrial biogenesis, mitochondrial structure i.e. mitochondrial fission and fusion processes, and maintenance of dNTP pool.

Mitochondrial diseases are heterogeneous disorders and challenging diagnostically ⁶². Although neurological symptoms are often the most dramatic, involvement of other organs such as the eye, liver and skeletal muscle are also common. One of the most common genetic defects appears to involve the catalytic subunit of DNA polymerase gamma, *POLG* ⁶³.

Pathogenic mutations in *POLG* are associated with a large number of different phenotypes including PEO ⁶⁴, an infantile hepato-cerebral disorder, Alpers' syndrome ⁶⁵, parkinsonism ⁶⁶ and the syndrome of mitochondrial spinocerebellar ataxia with epilepsy (MSCAE) ⁶⁷⁻⁷¹, which subsequent research shows are part of a continuum ⁷². At the cellular level, it appears that the primary consequence of *POLG* mutation can be either qualitative (point mutation or multiple deletions) or quantitative (depletion) abnormalities of mtDNA. Which of these changes occur appears, in part, to be tissue dependent i.e. mtDNA depletion has been commonly found in liver and occurs also in the brain ⁶⁰, while multiple deletions of mtDNA appear most consistently in skeletal muscle ^{71,73}. Despite the presence of *POLG* mutation in all cells, disease manifestations are much more profound in neurons and hepatocytes than for example in skeletal muscle or heart.

The c.1399 G>A (p.A467T, located in the thumb domain) and the c.2243G>C (p.W748S, located in the linker region), are two of the most common *POLG* mutations. The thumb domain of the catalytic subunit binds template DNA and substrate nucleotide triphosphate and interacts with the accessory subunits. The A467T mutation leads to reduced template binding and lower processivity ⁷⁴. The linker region is located between the polymerase and exonuclease domains of the catalytic subunit and is the site where the accessory subunits bind ^{53,75,76}.

1.2.1. The W748S and A467T animal models

A number of different animal studies have been performed to elucidate the structure and function of the *POLG* protein. Studies in *Drosophila* showed that A467T mutation led to alteration in enzyme activity, processivity, and/or DNA binding affinity ⁷⁷. Studies in D257A *knock-in* mice, in which an alanine is substituted with aspartate residue in second

exonuclease domain of POLGA, showed that defects in POLG A proofreading resulted in a threefold to fivefold increase in mtDNA point mutations and mtDNA deletions. Interestingly, however, the phenotype was not similar to the human and showed reduced lifespan and premature ageing with weight loss, reduced subcutaneous fat, alopecia (hair loss), abnormalities in bones, anemia, reduced fertility and heart enlargement ⁷⁸. Thus far, animal models have not reproduced phenotypes similar to POLG-related disease in humans and this has hindered better understanding of the mechanisms behind these diseases and the finding of possible treatments.

1.3. Stem cells

The early stage of embryogenesis involves separation of the embryonic and extra-embryonic tissues i.e. blastocyst formation. Blastocysts contains three cell types: epiblast, which will develop into the embryo; visceral endoderm (VE), also called hypoblast; and trophectoderm (TE), which will participate in placenta formation. Epiblasts consist of compact cell mass, known as inner cell mass, (ICM): these cells are pluripotent and are able to give rise to all three germ layers; ectoderm, mesoderm, and endoderm, and later differentiate into different multipotent and unipotent cells to form the whole body of the embryo ⁷⁹.

Pluripotent stem cells (PSCs) are recognized by two critical features: the ability to self-renew indefinitely and the ability to differentiate into cells from all three embryonic germ layers. PSCs replenish their own population through asymmetric cell division in which two daughter cells are generated, one differentiated cell and one stem cell. These two daughter cells are not identical and do not have the same developmental potential ⁸⁰.

Differentiation of PSCs entails the loss of their pluripotency, when they differentiate into multipotent lineage progenitors and commit to form new lineages such as cardiomyocyte progenitors and neural stem cells (NSCs). While these multipotent progenitors lose their capacity for indefinite cell division, they are still able to give rise to several cell types. A limited number of progenitors reside in every adult tissue and have a critical role in tissue homeostasis.

It has been shown that cells from ICM can be isolated and cultured *in vitro* ⁸¹. These cells, known as “embryonic stem cells” (ESC), exhibit two critical features reflecting their pluripotent origin; indefinite self-renewal and the ability to differentiate into almost all cell types in the body. ESCs are categorized as an allogenic resource of pluripotent stem cells. Therefore, their clinical application for tissue regeneration is limited due to the potential induction of the immune response. In addition, generation of ESC involves the destruction of blastocyst, which raises ethical issues ⁸².

To overcome these limitations, alternative methods have been developed including somatic cell nuclear transfer ^{82,83} and somatic cell reprogramming ⁸⁴⁻⁸⁶.

Somatic cell nuclear transfer is a cloning method that involves the replacement of an oocyte nucleus with a nucleus derived from a somatic cell. Application of this technique for generation of PSCs for therapeutic purposes in human is hampered by the low efficiency of this technique, low quality of the generated line and presence of chromosomal mutations, inadequate supply of human oocyte, and induction of immune response due to the presence of mtDNA in oocyte cytoplasm. ^{82,83}.

In 2006, reprogramming of mouse fibroblasts by co-transduction of retroviral vectors harboring transcription factors *Oct3/4*, *Sox2*, *c-Myc*, and *Klf4*, introduced new technique for generation of pluripotent stem cells ⁸⁴. Reprogrammed cells using this technique, known as induced pluripotent stem cells (iPSCs), were morphologically similar to ESC, and were able to renew themselves, express the ESC surface markers and generate embryoid bodies. In 2007, iPSC were generated from human fibroblasts paving the way for patient and disease specific stem cells that could be used for disease modeling, drug screening, and regenerative medicine ⁸⁶. Reservations concerning human iPSCs generation and their later applications, such as low efficiency of the programming, introduction of an oncogene, *c-Myc* for reprogramming, and integration of four to six retroviral vectors in the host genome remained, however. To overcome such, the *c-Myc* oncogene was substituted with *Lin28* ⁸⁷, and Sendai virus vector was used to avoid integration of foreign genes into the host genome ⁸⁸. Furthermore, the use of microRNA ⁸⁹ and small molecules ⁹⁰⁻⁹³ can replace the use of reprogramming genes and can also improve reprogramming efficiency.

Initially, human stem cells research was restricted by several fundamental challenges including problems with large-scale expansion of PSCs and the exposure of stem cells to animal pathogens during propagation. The emergence of new methods for maintenance⁹⁴, xeno-free culturing medium and feeder-free culture systems⁹⁵⁻⁹⁷, in addition to more efficient differentiation protocols, allowed the translation of human pluripotent stem cell science into clinical studies. However, challenges such as clone variation^{98,99} still need to be addressed. Further, since donor age is reset during reprogramming¹⁰⁰, these cells retain their fetal-stage properties making them more appropriate for developmental studies and modeling early-onset-disorder. Different approaches to incorporate an ageing component to these cells include manipulating telomerase activity¹⁰¹, inducing of Progerin expression¹⁰² and triggering mitochondrial stress and increasing cellular ROS¹⁰³.

1.3.1. Mitochondrial changes during development and differentiation

As cells in the female germline develop, mtDNA copy number increases and reaches its highest number, $>2 \times 10^5$, in mature oocytes. Following the fertilization and during preimplantation, mtDNA replication is inactive and therefore, mtDNA level falls, as mtDNA copies segregate into the newly dividing daughter cells, and reaches to its lowest level in the blastocyst ICM cells^{104,105}. Current understanding suggests an increase in mitochondrial number and mtDNA copy number while stem cells differentiate into functional cells in order to meet the increased demand for energy associated with newly acquired specialized function¹⁰⁶⁻¹¹⁰ (Figure. 2). However, the exact timing of mitochondrial and mtDNA expansion remains unknown.

Studies have shown that undifferentiated PSC contain a relatively undeveloped mitochondrial network with just a few spherical and immature mitochondria with poorly developed cristae located around the nucleus^{106,111}. Low expression of *TFAM* and *POLG*, and low mtDNA level were reported in mouse ESCs¹⁰⁷ and human ESCs¹¹¹. A consistently low level of mitochondria with immature morphology, high glucose uptake and glycolytic metabolism, and low oxygen consumption has also been reported in human pluripotent stem cells¹¹². It has been shown that hypoxia not only promotes

reprogramming¹¹³, but also supports normal growth and maintenance of pluripotency¹¹⁴. In addition, during course of reprogramming, fragmentation of mitochondria occurs¹¹⁵ which is accompanied with reverse transition from OXPHOS to glycolysis and exhibit an immature mitochondrial morphology^{116,117}.

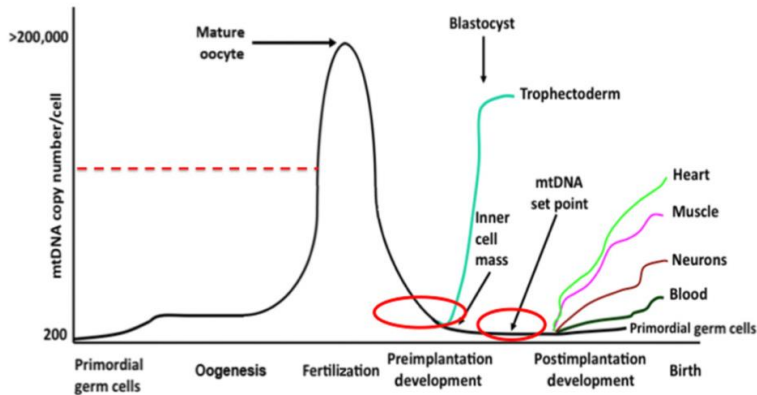


Figure 2. An overview of mtDNA copy number changes during development. During oogenesis, mtDNA copy number increases and reaches its peak in mature oocyte. During preimplantation, mtDNA copy number drops and the lowest level is seen in cells of the blastocyst. As stem cells of ICM start to differentiate, it is assumed that the number of mtDNA increases to meet the demand for higher energy production through OXPHOS. Reprinted from Annals of the New York Academy of Sciences, Licence No. 5103220883681¹¹⁸.

Stem cells rely heavily on glycolysis for maintenance and self-renewal. High glucose uptake and glycolysis not only provide ATP in hypoxic environment, in which most stem cells reside, but also provide substrates for anabolic processes while keeping ROS production low¹¹⁹⁻¹²². The core “stemness” circuitry, including the OCT4, SOX2, and NANOG, shares points of convergence with STAT3, a metabolic regulator that facilitates the oxidative to glycolytic switch¹²³. Moreover, glycolytic metabolites such as acetyl CoA, promote stemness by blocking stem cell differentiation through inhibition of histone deacetylation¹²⁴.

Differentiation describes the process from proliferation to specialization in which pluripotent stem cells lose their capacity for self-renewal and acquire specialized functions. Differentiation is associated with significant cellular and molecular changes including cell morphology, membrane potential, metabolic activity, and responsiveness to signals.

Different cell types require specific metabolic programs to meet the unique bioenergetic needs underlying their specialized functions. During differentiation, stem cells down regulate stemness genes and remodel metabolism from glycolysis to mitochondrial oxidative phosphorylation; this is accompanied by increased mitochondrial biogenesis and expansion of mitochondrial network^{106,108,109,111,125,126}. Studies in mice¹²⁷ and humans^{125,128} demonstrated that defects in mitochondria impair the differentiation process.

1.4. Cardiogenesis

The heart is the first functional organ in the embryo and its development can be subdivided into distinct phases that are partially overlapping; a) differentiation of cardiac progenitors and formation of the linear, almost symmetrical heart tube that beats in a peristaltic motion, b) cardiac looping, chamber formation, septation and maturation. Cardiac progenitor cells differentiate from the precardiac mesoderm layer that is detectable by expression of T-box transcription factor brachyury (*T*) in the posterior half of the epiblast in the pre-streak stage. Soon after gastrulation, these cells give rise to precardiac mesodermal cells expressing the Mesoderm Posterior Protein 1 (Mesp 1) that expand rapidly and migrate bilaterally through primitive streak and form heart fields contain prospective endocardial and myocardial cell¹²⁹. Mesp1 acts as a key activator of genes involved in cardiovascular lineage and at the same time, suppresses genes essential for hematopoietic cell lineage.¹³⁰⁻¹³³ In addition, Mesp1⁺ cells can also give rise to derivatives of the paraxial mesoderm and skeletal muscle of the head and neck¹³⁴. Cardiac progenitor cells are multipotent cells that can give rise to cardiomyocytes, smooth muscle cells and endothelial cells^{133,135}. These progenitors can be identified by the expression of transcription factors including LIM-homeodomain transcription factor

Islet-1 (Isl1)¹³⁶, Nk2 homeobox (Nkx2-5)¹³⁷, and GATA binding protein 4 (GATA4)¹³³.

Lineage tracing experiments demonstrated the critical role of Isl1 and Nkx 2-5 in cardiac development^{135,138}. Isl1 expresses transiently in cardiac progenitors, while later in development, the expression of Isl1 is downregulated and completely absent in fully differentiated cells^{139,140}. Nkx 2-5 is expressed in cells of both heart fields and elimination of Nkx 2-5 in mice led to arrest of cardiac development, particularly left ventricular and vascular channel.^{137,141} Furthermore, impaired Nkx 2-5 function is associated with abnormal neonatal heart development¹⁴² and atrial electrophysiological remodeling¹⁴³. In addition to Isl1 and Nkx 2-5, induction of the expression of two cardiac transcription factors, GATA4 and Tbx5 was sufficient for direct trans-differentiation of mouse mesoderm to cardiomyocytes¹⁴⁴.

Troponin T, TNNT2, regulates the function of actin filaments in a calcium dependent manner in the cardiomyocyte population^{145,146}. Myosin heavy chain proteins (MYH6) and (MYH7) are expressed in early stages of heart development, and mutations in these genes are associated with congenital heart defects, particularly, atrial septal defects¹⁴⁷⁻¹⁴⁹.

Patterning and regional specification of cardiac muscle cells with distinct electrophysiological properties is also governed by region and time- dependent expression of proteins including myosin light chain 2, MLC2v, and myosin light chain 7, MLC2a. Murine embryogenesis studies revealed that the expression of MLC2a is restricted to the atrial chamber while MLC2v is expressed in the ventricular chamber. Furthermore, expression of MLC2a is initiated before MLC2v, implicating that atrial chamber formation occurs before formation of ventricular chamber¹⁵⁰. These studies identified the genes involved in heart formation and offered a reliable marker to monitor the cardiomyocyte differentiation process¹⁵¹.

1.4.1. Signaling pathways involved in cardiogenesis

Cardiogenesis is orchestrated by different signaling pathways including Hedghog (Hh), wingless/INT (Wnt), Wnt/beta-catenin, bone morphogenetic protein (BMP), fibroblast

growth factor (FGF), and transforming growth factor beta (TGF- β)¹⁵². It has been shown that under defined growth condition, Wnt signaling is essential and sufficient for cardiogenesis induction in human PSCs¹⁵³. Canonical Wnt signaling involves the multifunctional β -catenin protein. In the absence of Wnt ligand, β -catenin is phosphorylated and degraded by proteasome after interacting with the destruction complex composed of axin, APC protein and glycogen synthase kinase 3 beta (GSK3 β). When present, the Wnt ligand interferes with assembly of the destruction complex and stabilizes the β -catenin protein, which can enter the nucleus and regulate target genes involved in cell division, proliferation, polarity and migration.

Wnt signaling has a biphasic function during cardiogenesis¹⁵⁴. It is essential for induction of mesoderm generation at the early stage of cardiac development, but negatively influences the cardiac precursor cell specification. Studies have shown that cardiac progenitor cells generation depends on upregulation of Wnt/ β -catenin signaling inhibitors such as Dkk1¹⁵⁵ or secreted Frizzled-related proteins Sfrp1 or Sfrp5, in order to downregulate pluripotency and promote differentiation of cardiac progenitor cells¹⁵⁶⁻¹⁵⁸. During cardiac lineage specification Wnt signaling supports cell proliferation and positively affects the development of second heart field- derived structures in maturing heart¹⁵⁹. Subsequently, terminal differentiation of cardiac progenitors to mature cardiomyocytes is inhibited by canonical Wnt signaling. Overall, Wnt signaling contributes to cardiac specification and differentiation through four phases: 1) generation of mesodermal germ layer, in which Wnt signaling is active, 2) generation of multipotent cardiac progenitors that canonical Wnt/ β -catenin signaling needs to be low, 3) Proliferation and expansion of several specific cardiac progenitors that requires active Wnt signaling, and 4) terminal differentiation that Wnt/ β -catenin signaling has to be low¹⁵⁸.

1.4.2. Generating cardiomyocytes in vitro from stem cells

Initial attempts to differentiate human PSC into cardiomyocytes involved cultivating cells in medium containing fetal calf serum and first generating embryoid bodies (EBs). This technique generated differentiated cells from all three germ layers and

cardiomyocyte yield was less than 1% ¹⁶⁰. The use of serum-free medium and temporal addition of growth factors such as fibroblast growth factor 2 (FGF2), transforming growth factor β (TGF- β), superfamily growth factors activin A and BMP4, vascular endothelial growth factor and the Wnt inhibitor DKK-1 improved the differentiation efficiency to 50% ^{161,162}, but high levels of heterogeneity in size, quality and number of EBs remained. In addition, not all the human ESCs that grow in feeder-free culture system are able to form EBs. These problems were addressed by the use of monolayer-based methods, which are more efficient; more than 80% ¹⁵³, and are more controllable and reproducible. These because PSCs growth uniformly in these systems and therefore, there is no barrier for diffusion and delivery of the growth factors and small molecules during differentiation process. Furthermore, the procedural steps are reduced in monolayer protocols by removing the replanting steps, which reduced the consumption of tissue culture and manpower supplies. In these protocols, cardiomyocyte differentiation is induced by treating cells with either BMP4 or sequential activation followed by inhibition of Wnt signaling pathway ^{153,163,164}.

Cardiomyocytes yield can be increased further by genetic selection based on expression of cardiac specific markers such as Nkx2-5 ¹⁶⁵ or Isl1 ¹⁶⁶, sorting the cardiomyocyte using surface markers ^{165,167}, and cardiac selection based on their mitochondrial content ¹⁶⁸. Despite many improvements, however, human PSC-derived cardiomyocytes remained largely immature ¹⁵¹ and this stimulated the search for other methods to improve maturity such as biophysical and electrical stimulation of the cardiomyocyte, metabolic remodeling, and transplantation of differentiated cells in animal models that have shown some success in generating more mature cardiomyocytes ¹⁶⁹.

1.5. Generation of neural stem cells (NSC)

All the cells of central nervous system (CNS) are derived from the ectodermal germ layer through the process that begins with Neurulation. Neurulation is a morphogenetic process described as formation of neural tube from a flat sheet of neuroepithelial cells, known as neural plate, which rolls up into an elongated tube. Neuroepithelial cells function as neural stem cells (NSCs) that are able to renew themselves and to

differentiate into three main lineages; neurons, astrocytes, and oligodendrocytes. Initially, neural development entails the proliferation of neuroectodermal NSCs that differentiate into the first wave of neurons and other types of NSCs including the neural rosette NSCs, which populate the early neural tube. Subsequently, neural rosette NSCs differentiate into another type of progenitors known as radial glial cells that are able to give rise to most of types of neurons in the CNS¹⁷⁰. NSCs are present in both the developing fetal brain and adult brain where they are involved in adult neurogenesis to develop, repair and modulate nervous system functions. Interestingly, NSC dysfunction is thought to lead to a variety of neurological and psychiatric disorders¹⁷¹.

CNS development is regulated by many transcription factors such as paired box (Pax) transcription factor (Pax6) that has a crucial role in central nervous system (CNS)¹⁷², eyes¹⁷³, nose¹⁷⁴; although it is expressed in pancreas, and pituitary gland^{175,176}. Pax6 has several important functions, including the specification, differentiation, and migration and maintenance of neurons^{172,177,178}. Pax6 determines neurogenesis in proliferating radial glia in humans and abolishing Pax6 expression in this region of the fetal forebrain leads to a significant decrease in the number of neurons at later stages of differentiation¹⁷⁹. Moreover, establishment of specific brain territories, corticogenesis, and development of neocortex are regulated by Pax6 during brain development¹⁷². It has been shown that loss of pax6 function leads to premature neurogenesis and impaired corticogenesis results in development of microcephaly and neurodevelopmental disorders, such as intellectual disability, attention deficit-hyper activity disorder, and autism spectrum disorder¹⁷⁸.

pax6 expression initiates at early stages of neurulation around the time of neural plate induction and in proliferating NSCs, and continues postnatally in neurons from different parts of the brain regions such as olfactory bulb, amygdala, thalamus, and cerebellum¹⁷⁸. Molecular structure of Pax6 is highly conserved and contains two DNA binding domains: a paired box-domain and a homeodomain. Pax6 regulates brain development through direct regulation of transcription of many downstream gene; such as *FABP7* (B-FABP/brain lipid binding protein, and *Ngn2*. It also interacts with various transcription factors such as Sox2 and synergistically regulates the expression of target genes such as

fibroblast growth factor 4 (Fgf4) and *nestin*, which play important role in neuronal development¹⁷².

Nestin is a neuroepithelial cytoskeletal, intermediate filament that plays a critical role in stem cell proliferation, differentiation and migration by affecting asymmetric cell division. Asymmetric cell division involves the asymmetric inheritance of cellular components that dictates different cellular fates for each daughter cell¹⁸⁰. Although Nestin was first characterized in NSCs, Nestin⁺ cells have been identified in skeletal muscle (satellite cells;¹⁸¹, testis¹⁸², and bone marrow¹⁸³. Studies in Nestin^{-/-} mice showed a dramatic reduction in NSC survival and self-renewal due to apoptosis and loss of Nestin was embryonically lethal (at day E8.5)¹⁸⁴. These studies emphasized the role of Nestin in regulating self-renewal of NSC rather than differentiation, since NSCs started the process of differentiation despite the down regulation of Nestin¹⁸⁵.

1.5.1. Signaling pathways involved in NSCs generation

The neural plate is formed through a highly conserved process known as neural induction, in which suppression of an epidermal fate is driven by a signal from the organizer region located in dorsal mesoderm^{186,187}. Explant culture studies showed that the default state of these ectodermal cells is neuronal rather than epidermal¹⁸⁸. Moreover, studies show that the core compounds that direct epidermal formation are BMP ligands that bind and activate their receptors, which in turn transduce a signal by intracellular cascade of phosphorylation events that ultimately alter the activities of SMAD proteins. Therefore, inhibition of BMP signaling pathway by BMP antagonists such as Chordin, Follistatin and Noggin, is sufficient for neural induction^{189,190}. In addition to BMP inhibitors, other neural inducers such as fibroblast growth factor (FGF) signal through the MAP kinase cascade. It has been suggested that FGF signaling inhibits BMP either through suppression of BMP gene expression or by repressing the SMAD-dependent BMP signal transduction in the cytoplasm^{191,192}.

1.5.2. Generating NSCs in vitro from stem cells

Several protocols for generating NSCs have been developed. Similar to cardiomyocyte differentiation, early protocols relied on embryoid body formation, stromal feeder co-culture, and/ or selective survival conditions. Most of these protocols suffer from low efficiency, poorly defined culture condition, high variation and low reproducibility, and prolonged differentiation process. These drawbacks motivated development of 2D protocols based on adherent culture systems that eliminated the EB formation step, and generated more uniform culture that is easier to maintain, freeze and refreeze, as well to use for performing experiments such as exposure to specific substances ^{193,194}. Introduction of dual inhibition of SMAD signaling for efficient neural induction ¹⁹⁵ followed by identification of different growth factors and small molecules for differentiation of NSCs into different type of neurons has provided the tools for studying complex neurodegenerative disorders such as mitochondrial diseases. However, limitations of monolayer culture in mimicking the micro-environment, in which NSCs are exposed to other cells and extracellular matrix, leads to development of new technology of 3D cell culture systems, known as organoids. These systems have a great capacity for in vivo characteristics tissue organization, preservation of embryonic neuronal differentiation and cell type diversity, in addition to increased neuronal differentiation yield ¹⁹⁶.

2. Aims

From earlier studies in patients and post-mortem tissues, it became clear that mutations in the *POLG* gene affects some tissues more than others. For example, the *POLG*-related disorders are more likely to affect neurons and hepatocytes than heart cells.

Despite being informative, post-mortem studies usually reflect end stage disease and do not allow us to study disease mechanism(s). Moreover, the lack of an animal model that faithfully replicated the human disease, the inaccessibility of affected human tissues, and the fact that cultured primary cells often show no phenotype has hampered our understanding of the pathophysiological mechanisms involved in this disease and prevented the development of treatments.

Thus, the major aim of these studies was to generate iPSC-derived neurons and cardiomyocytes – i.e. one affected and one unaffected tissue, and use these *in vitro* cell-systems to investigate disease mechanisms and potential treatments.

The specific aims of the study were:

- 1) To generate stem cell-based models using iPSCs. Ultimately, this had to be restricted due to time and cost restraints to the study of neuronal and cardiac lineages.
- 2) To develop robust and reproducible methods for differentiating different tissues from iPSCs and robust methods for measuring mitochondrial dysfunction in these cells
- 3) To investigate the disease phenotype in neurons and if possible compare this to what happens in cardiomyocytes
- 4) To investigate mitochondrial biogenesis during cardiomyocyte differentiation

3. Methods

3.1. Biological samples

3.1.1. Generating human induced pluripotent stem cell lines (iPSC)

All the human induced pluripotent stem cell lines were generated by Dr. Gareth Sullivan's group at the University of Oslo. The use of cell lines derived from patient fibroblasts was approved by the Western Norway Committee for Ethics in Health Research (REK nr. 2012/919). Patients gave written consent prior to skin biopsy. Fibroblasts from one patient homozygous for c.2243G>C, p.W748S/W748S (WS5A) and one who was compound heterozygous c.1399G>A/c.2243G>C, p.A467T/W748S (CP2A) were cultured in DMEM/F12, GlutaMAX™ (Thermo Fisher Scientific) containing 10% (v/v) FBS (Sigma-Aldrich), 20 mM glutamine (Sigma-Aldrich), 10 mM sodium pyruvate (Invitrogen), and 0.5 mM uridine (Sigma-Aldrich).

Three different control skin fibroblasts were used. The first was derived from a 44-year old female (AG05836) were obtained from the Coriell Institute ([RRID:CVCL2B58](https://www.ncbi.nlm.nih.gov/RRID/RRID:CVCL2B58)) whereas CCD-1079SK (CRL-2097™, Fibroblast line derived from a normal new-born male and Detroit 551 (CCL-110™, Fibroblast from fetal female), were purchased from the American type Culture Collection, ATCC. Control fibroblasts were cultured in DMEM/F12, GlutaMAX™ (Thermo Scientific) containing 10% (v/v) FBS. All the patient fibroblasts and control ATCC fibroblasts were reprogrammed using integrative retroviral vectors containing the Yamanaka factors (*Oct4*, *Sox2*, *Klf4*, and *c-Myc*) described by ¹⁹⁷. AG05836 fibroblast was reprogrammed by an integration free method using CytoTune™-iPS 2.0 Sendai Reprogramming kit (Thermo Fisher Scientific) harboring Yamanaka factors.

The resulting iPSC lines were characterized comprehensively, as previously described in ¹⁹⁷⁻¹⁹⁹. Expression level of induction factors was assessed by RT-qPCR performed on iPSC collected after passage 10 and exogenous pluripotency factor silencing was confirmed.

The morphology of the iPSC clones was compared with the morphology of well-established ESC lines and the presence of ESC-like morphology was confirmed

microscopically. The pluripotency of iPSC lines was assessed by the expression of pluripotency markers and their potential to differentiate into the cells from three germ layers; neurons (ectoderm), cardiomyocyte (mesoderm), hepatocyte (endoderm).

The expression of pluripotency markers was assessed at both the mRNA and protein levels using RT-qPCR, immunofluorescence microscopy and flow cytometry. In order to check the iPSC for genomic abnormalities, karyotyping was performed using G banding and KaryoLite™ BoBs™ analysis. G banding karyotyping of 20 chromosomes fixed in metaphase was performed using the G banding and Leishman stain, and the cells were analyzed based on the Clinical Cytogenetic Standards and Guidelines²⁰⁰.

Furthermore, DNA samples for KaryoLite™ BoBs™ analysis were shipped to the Turku Centre of Biotechnology, Finland and the presence of aneuploidies, gains and losses in both p and q arms of all 24 chromosomes was assessed. This method is a molecular cytogenetic technique composed of fluorescent beads that are tagged with bacterial DNA. Bacterial probes are complementary to the different regions of the chromosomes and are distinguishable by flow cytometric multiplex bead array detection system^{201,202}. Validated iPSC were tested for Mycoplasma using the MycoAlert™ Mycoplasma Detection Kit (Lonza) prior banking in liquid nitrogen. In addition, iPSC samples from each frozen lot were randomly checked for the expression of pluripotent markers after thawing and prior to performing the experiments.

3.1.2. Human embryonic stem cell lines (ESC)

Two human ESC lines - H1 (male) and H9 (female)²⁰³ - purchased from the WiCell Research Institute, and two others - 360 (male) and 429 (female)²⁰⁴ were obtained from the Karolinska Institute and characterized and validated as described above prior to use in any studies.

3.1.3. Human pluripotent stem cell (PSC) culture

All the human PSC lines including iPSC and ESC lines were cultivated under feeder-free condition using Geltrex (Invitrogen) and fed with Essential E8™ medium (Thermo Fisher) every day in 6 well plates as described in Paper I-III.

In order to authenticate our cell lines, we sequenced the hypervariable regions of mtDNA (HV1 and HV2) using BigDye direct cycle sequencing (Thermo Fisher Scientific). It is known that noncoding segments of mtDNA, known as the control region, contains two hypervariable regions HV1 (located between base number 16024 and 16383), and HV2 (located between base number 57 and 372) that are mutational hotspots for both germline and somatic mtDNA mutations²⁰⁵. It has been shown that the level of polymorphism in HV1 genetic locus is high enough to be used as a tool for studying human evolution and population genetic history²⁰⁶, and also human identification in forensic case works²⁰⁷.

The sequence of primer sets used for sequencing are as below:

HV1-F: TGTAACGACGGCCAGTATCGGAGGACAACCAGTAAG

HV1-R: CAGGAAACAGCTATGACCAGGGTGATAGACCTGTGATC

HV2-F: TGTAACGACGGCCAGTCTCAACTATCACACATCAACTG

HV2-R: CAGGAAACAGCTATGACCAGATACTGCGACATAGGGTG

3.1.4. Tissue studies

In the first study, we used brain tissue from patients with POLG mutation and neurologically healthy controls that were demographically matched to investigate the mtDNA level and ETC complexes. Samples were dissected at autopsy and either snap-frozen immediately in liquid nitrogen pre-cooled isopentane, and stored at -80°C , or fixed in formaldehyde. Fixed samples were embedded in paraffin blocks according to standard procedures. Fresh frozen samples were used for mtDNA analysis and formalin-fixed samples for mitochondrial complex I immunohistochemistry as described in Paper I and⁶⁰.

3.2. Human pluripotent stem cells differentiation and characterization

3.2.1. Human pluripotent stem cell differentiation

3.2.1.1. Neural induction and generation of NSCs

Both control and patient iPSC lines were induced to NSCs using a modified protocol described previously²⁰⁸. The iPSC culture was split and cultured on Geltrex and fed by E8 essential medium, and after 24 h the medium was changed to neural induction medium, which is the Chemically Defined Medium (CDM), supplemented with small molecules SB431542 (Tocris Bioscience), N Acetyl L cysteine (NAC, Sigma-Aldrich), and AMPK inhibitor Compound C (EMD Millipore). Cells were fed daily using induction medium for 5 days. After 5 days, cells were detached and spheres are formed and culture in StemPro™ NSC medium supplemented with 1× GlutaMAX™, bFGF, and EGF (Thermo Fisher) at 37°C on an orbital shaker (Fisher Scientific) for 2-3-days. After 2-3 days, spheres were broken down into single cells using TrypLE™ Express plated on Geltrex and fed by StemPro NSC medium in 6 well plates. Differentiated NSCs passaged using TrypLE™ Express. All the experiments were performed on NSCs with passage number 4-9. The presence of specific POLG mutation in NSC-derived from patient iPSC lines were confirmed by sequencing (The details of the neural induction process are well explained in the Paper. I).

3.2.1.2. Generating dopaminergic neurons (DA)

In order to generate DA progenitors, spheres were kept in CDM supplemented with 100 ng/ml FGF8b (R&D systems) for one week followed by another week of maintenance in CDM supplemented with 1 µM PM (EMD Millipore) and 100 ng/ml FGF-8b. Spheres were broken down into single cells gently using TrypLE™ Express and were plated on culture vessels coated by POLY-L-ornithine (Sigma-Aldrich) and laminin (Sigma-Aldrich). DA neurons were cultured in DA medium containing CDM supplemented with 10 ng/ml BDNF (PeproTech) and 10 ng/ml GDNF (PeproTech).

3.2.1.3. Cardiomyocyte differentiation

In order to differentiate human PSC into cardiomyocytes through a scale-down platform with high efficiency and reproducibility, we developed a method presented as Paper-II. Briefly, ESCs/iPSCs were treated with 0.5 mM EDTA to produce a homogeneous cell suspension. Human PSCs were seeded at 2.4 x 10⁴ cells/cm and propagated on Geltrex

under feeder-free conditions in Essential 8 Medium (E8) supplemented with 10 μ M Rock inhibitor (Y27632, Tocris Bioscience) for 24 h. After 24 h, the medium was changed with a fresh E8 medium every day until cells reached the optimum confluency, 60 to 70%; within 2-3 days, for initiation of the cardiomyocyte differentiation process. Differentiation was started by applying the GSK3 inhibitor, CHIR99021 (Tocris Bioscience) in RPMI 1640 (Thermo Fisher Scientific) medium supplemented with B27 minus insulin (RPMI/B27⁻) (Thermo Fisher Scientific), in a concentration-cell-dependent manner; for ESC 8 μ M and for iPSCs, 6 μ M CHIR99021 was added. After 24 h, the medium was changed to RPMI/B27⁻ without CHIR99021. The differentiation process was continued by adding 5 μ M inhibitor of WNT production-2, IWP2, (Tocris Bioscience) diluted in RPMI/B27⁻, 72 h post differentiation induction for 48 h. Fresh RPMI/B27⁻ medium was provided on day 5, and from day 7 cells were fed with fresh RPMI medium supplemented with B27 with insulin (Thermo Fisher Scientific), RPMI/B27⁺, without extra supplement) every two other days.

3.2.1.4. Hepatocyte differentiation

Hepatocyte differentiation and characterization was performed by our collaborator Gareth Sullivan at the University of Oslo based on the protocol previously described^{197,198}.

3.2.2. Characterization of PSCs and differentiated cells

In order to ensure correct differentiation, we used gene expression analysis and immunocytochemistry to investigate the expression of key stage-specific markers corresponding to different stages of differentiation. For neuronal differentiation, we analysed the following specific markers: for iPSC; NANOG, SOX2, SSEA4, and OCT4, NSCs; Pax6 and Nestin, DA neurons; Tyrosine hydroxylase, TH, Beta III Tubulin, and MAP2 as described in paper I.

For cardiomyocyte differentiation, we monitored the expression of markers for pluripotency state Day0 (D0), germ layer specification (D3), progenitor state (D5), and

committed cardiomyocytes (D15). For gene expression, we checked 20 markers including pluripotency markers as described in paper II.

In order to investigate the electrophysiological properties of beating cardiomyocyte we used Microelectrode arrays (MEA) a highly sensitive, non-invasive method for studying the physiological properties of electrically active cells. The MEA records electrical waveform signals that are called extracellular field potentials (FPs), which in cardiac cells represent the action potential and reflect, to some extent, the electrocardiogram recording.

We recorded FPs while we challenged the differentiated cells with different cardiac drugs including Isoproterenol; β_1 and β_2 adrenoreceptor agonist, E4031; a potassium channel antagonist, Tetrodotoxin, TTX; sodium channel antagonist, Nifedipine; L-type calcium channel antagonist, and Mosapride; 5-hydroxytryptamine (serotonin) receptor -HT4 agonist and HT3 antagonist. Finally, we investigated the presence of other cell populations in the cardiac culture. We stained the cells with antibodies against smooth muscle and endothelial specific markers and assessed the percentage of these cell populations in our culture using flow cytometry.

3.2.2.1. Gene expression analysis via real-time PCR

We used the high throughput automated MagMax express 96 -platform to extract RNA. RNA for gene expression studies was isolated using the MagMAX-96 Total RNA Isolation Kit (Thermo Fisher Scientific) and performed according to the manufacturer's instructions. In order to eliminate carry-over contamination and increase the accuracy of the experiment, we used EXPRESS One-Step Superscript qRT-PCR, in which both cDNA synthesis and amplification reactions occur in the same tube, without unnecessary pipetting. This was done according to the manufacturer's instructions. All qPCR reactions were performed in triplicate and assessed using the comparative $\Delta\Delta C_t$ method, in which reaction C_t values are normalized to the geometric mean of *ACTB* and *GAPDH* as endogenous control genes and assessed by normalizing differentiated cells to undifferentiated pluripotent stem cells. Results presented as the mean of three

independent differentiation runs and error bars showed the standard deviation of the mean.

3.2.2.2. Immunocytochemistry and immunofluorescence (ICC/IF)

Differentiated cells were characterized based on the expression of cell-specific markers that are listed in paper I-III. In the first study, cells were cultured on coverslips, whereas in cardiomyocyte studies (Paper II and III), cells were culture in 96well plates. Cells from a single well were then transferred onto glass coverslips or onto Millicell EZ SLIDES (Merck Millipore) for staining. Staining comprised fixing with 4% PFA, permeabilization, blocking in the blocking buffer, incubation with primary antibody solutions overnight at 4°C, and finally, incubation with secondary antibody solutions at RT. Nuclei staining was performed prior to taking pictures either by Zeiss LSM 510 META or Leica TCS SP5 at Molecular Imaging Center (MIC), University of Bergen. Data analysis and image editing were done with Fiji as described in paper I, II, and III. For Neuro-sphere staining, following a quick wash with PBS spheres were fixed with 4% (v/v) PFA. After two washes in PBS, spheres were incubated in 20% sucrose solution in PBS overnight at 4°C then blocked with blocking buffer for 2 h at room temperature and incubated with primary antibodies overnight at 4°C. Following washing for 3 h in PBS, spheres were stained with secondary antibodies diluted in blocking buffer overnight at 4°C in a humid and dark chamber. Slides were prepared for imaging by mounting coverslips using Fluoromount-G (Southern Biotech).

3.2.2.3. Microelectrode array measurement (MEA)

Between day 11 and 14 of differentiation, when cardiomyocytes show visible beating, but are young enough to be easily detached, cells were collected and transferred into the precoated MEA chamber and fed by RPMI-B27 with insulin medium. After 12 h of incubation at 37 °C cardiomyocytes were anchored over the electrode field using a glass-coated steel ring.

Field potential, FPs, of spontaneous beating, was recorded 48 h after transfer when cells were well settled and had obvious beating. Before the application of drugs, FPs were

recorded for 5 min under the control conditions. All the drugs were diluted in the same culture medium and used at the concentrations mentioned in Paper-II. Electrophysiological parameters including positive (pPA) and negative peak amplitude (nPA), field potential duration (FPD), and amplitude (FPA), as well as a beat interval (BI), were evaluated using the MC-Rack software (Version 4.6.2; Multichannel system). All data sets are represented as mean \pm SD compiling 5 randomly chosen electrodes of at least 5 independent experiments. The chemical compound data were normalized to control for each experiment.

3.2.2.4. Quantification of cell composition in cardiac culture

Using flow cytometry, we investigated the presence of different cell populations during a course of differentiation; undifferentiated cells (D0, S1), cardiac progenitors (D5-7, S4), and at the later stage of differentiation (D12-19, S5): cardiomyocytes, endothelial smooth muscle cells. In paper II, We used intracellular markers, TNNT2 and MYL7, and extracellular markers; CD140b and CD144, to assess the percentages of cardiac and non-cardiac cell populations respectively. Since cardiomyocytes form strong connections at later stages of differentiation (D12-19, S5), we used Multi Tissue Dissociation Kit 3 to avoid losing cells trapped in the cell clumps. However, we could not detect the signals of extracellular antigens in the samples collected by this method possibly because the Multi Tissue Dissociation Kit 3 caused changes in the structure of extracellular antigens that affected antibody detection causing loss of signal in flow cytometry. We therefore used TrypLE Express enzyme for the detection of extracellular antigens. We counted dissociated cells using either of these methods and could not detect a significant difference in their dissociation efficiency, however, the Multi Tissue Dissociation Kit 3 dissociated more mature cells faster. The details of the sample preparation using any of these methods are described in paper II. At least 30,000 events were collected for each sample with a 100 μ m nozzle by a Sony cell sorter SH800 (Sony Biotechnology Inc.) and data were analyzed and visualized using FlowJo V.10.5.0 (FlowJo LLC, OR, USA) software (www.FlowJo.com).

3.2.2.4.1. Quality assurance for polychromatic flow cytometry

In these studies, we used recombinant pre-conjugated antibodies whenever it was available to minimize cell loss caused by extra washing steps. In addition, to reduce the background and increase the signal-to-noise ratio, we used human recombinant antibodies. The presence of mutated Fc region in these antibodies avoids non-specific binding via Fc receptors on the cells.

In order to minimize the batch to batch variation, the flow cytometer was calibrated prior to each run of quantitative fluorescence intensity assessment by using Molecules of Equivalent Soluble Fluorochrome (MESF) microsphere (Quantum™ Alexa Fluor® 488 MESF, Bangs Laboratories, Inc.). These beads are labeled with a certain quantity of fluorochrome that can be used as an external standard for fluorescence intensity units. Furthermore, flow cytometer alignment and performance were routinely verified using the 8-peaks Rainbow Calibration Particles (Biolegend).

Since we co-stained the cells with different fluorochrome, Fluorescence minus one control (FMO), proper Isotype control, and compensation beads were included for gating the positive cells.

3.3. Assessment of mitochondrial biogenesis and mitochondrial function

We evaluated the mtDNA copy number, mitochondrial mass, and energy profile of the cells including mitochondrial respiration and mitochondrial membrane potential, and cellular Redox status in human PSC and differentiated progenies.

3.3.1. Mitochondrial DNA (mtDNA) assessment

We calibrated mtDNA content to mitochondrial mass rather than cell number or total protein. Mitochondrial DNA copy number level was investigated by two methods: qPCR quantification relative to nuclear gene Amyloid Beta Precursor Protein (*APP*), and flow cytometric analysis of TFAM protein level. The latter assay was based on the

direct link between TFAM protein and mtDNA ⁴⁶. We assessed TFAM using flow cytometry both as a direct measure of a matrix mitochondrial protein and since it provided an indirect measure of the level of mtDNA within each cell population. Using flow cytometry to estimate mtDNA content, we could estimate the mtDNA level per mitochondrion by calculating the ratio of TFAM: TOMM20, in which TFAM is representative of mtDNA level and TOMM20 corresponds to mitochondrial mass.

3.3.1.1. Mitochondrial DNA quantification and deletion assessment using polymerase chain reaction (PCR)

Using qPCR, we quantified mtDNA level and investigated the presence of mtDNA deletions using the method described previously ^{60,70}. In this, three probes are used; one complementary to the MT-ND4 (the region in major arc of mtDNA that is commonly deleted), the second is complementary to MT-ND1 (the region in the major arc but rarely subjected to deletion), and a third targeting a single-copy nuclear gene *APP*. A triplex reaction was performed with amplification of MT-ND1, MT-ND4, and *APP* measured in the same well using a 7500 fast sequence detection system (Thermo Fisher Scientific). Total mitochondrial DNA copy number per cell and mtDNA deletion level were calculated by the ratio of ND1/*APP* and ND4/ND1 respectively. In addition, we ran a long-range polymerase chain reaction, Long-PCR, using the method described previously ⁶⁰ to confirm the presence/absence of mtDNA deletion in the samples.

3.3.1.2. Assessment of mtDNA level per mitochondrion

In order to assess TFAM level in specific cell types in a heterogeneous cell population, we chose to use flow cytometry and not western blotting since flow allowed us to investigate the level of protein of interest per single cell. This was particularly important in our studies of cardiomyocyte differentiation in which we investigated TFAM level in two cell populations; cardiomyocytes and non-cardiac cells at the later stage of differentiation (S5 in Paper III). TFAM was ratioed to TOMM20, an outer membrane protein, to assess level per mitochondrion.

Single cells were fixed in paraformaldehyde, PFA, at RT and permeabilized with ice-cold 90% methanol at -20 °C. To avoid non-specific binding, cells were blocked using blocking buffer prior to staining with conjugated antibodies. In the third study, in order to discriminate live, dead, and dying cells (stressed cells), we used Zombie Red™ Fixable Viability Kit (BioLegend) prior to fixation with PFA.

3.3.2. Assessment of metabolic state and mitochondrial function

In paper III, we measured the oxygen consumption rate (OCR) and membrane potential in PSC and differentiated cardiomyocytes to monitor the changes of mitochondrial oxidative activity during differentiation. In paper I, in order to evaluate the effect of *POLG* mutation on mitochondrial function, we compared the level of respiratory chain complexes, mitochondrial membrane potential, ROS, ATP level, and NAD⁺ metabolism in patient and control iPSCs, fibroblasts and NSCs.

3.3.2.1. Comparing metabolic state of PSC- derived cardiomyocyte with their undifferentiated origin using Seahorse XF-96 analyzer

We used the Seahorse XF-96 analyzer to measure OCR at multiple time points during a mitochondrial stress test in which OCR is measured in the presence of OXPHOS inhibitors including oligomycin, carbonyl cyanide-4 (trifluoromethoxy) phenylhydrazone (CCCP), rotenone, and antimycin A. Glycolytic activity was evaluated using extracellular acidification rate (ECAR).

In order to measure PSC and their differentiated cardiomyocyte progeny, under the same experimental conditions, both cell types were seeded in the same XF96 assay plate. Given the higher proliferation rate of PSC, we adjusted cell density for seeding each cell type: 3×10^3 cells/well for PSC and 2×10^5 cells/well for cardiomyocytes). This gave a similar cell confluency, almost 90%, when we evaluated OCR. The experimental procedure and material concentrations are explained in paper III.

Oxygen consumed during ATP generation (ATP-linked respiration) and proton leakage were measured following the application of oligomycin; an ATPase synthase inhibitor.

This blocks the proton channel of the F₀ subunit of complex V and not only inhibits ATP synthesis, but also affects electron transport throughout complexes I–IV.

Maximal respiratory capacity was evaluated by the administration of CCCP, which uncouples mitochondrial respiration from ATP synthesis. CCCP discharge the electrochemical gradient uncoupling electron transport from complex V activity and increasing oxygen consumption to the maximum level. Defining the optimal concentration of CCCP is crucial for the experiment; at high concentrations of CCCP the mitochondrial inner membrane collapses, while at low concentrations, mitochondria do not reach their maximal respiration leading to misleading results.

Finally, mitochondrial respiration is completely halted by rotenone, a complex I inhibitor, and antimycin A, a complex III inhibitor. The application of these inhibitors reveals the remaining oxygen consumption that is independent of electron transport chain activity and known as non-mitochondrial oxygen consumption.

Since we compared two different cell types with different cell sizes, we corrected the final results for the total protein level in each well. Using the BCA protein assay Kit, the total protein of each well was isolated and the OD was measured at 280 nm, and the results were reported as $\text{pmol} \cdot \text{min}^{-1} \cdot \text{OD}_{280\text{nm}}$.

3.3.2.2. Measurement of mitochondrial membrane potential (MMP)

Mitochondrial membrane potential (MMP) reflects electron transport chain (ETC) activity and cells capacity to generate ATP through OXPHOS. Fluorescent lipophilic cationic dyes such as tetramethylrhodamine methyl (TMRM) and ethyl ester (TMRE) are used to measure the charge gradient, $\Delta\psi_m$, across the inner mitochondrial membrane. These dyes aggregate within mitochondria due to their electrical charge and solubility in the mitochondrial membrane. Dye accumulation is in inverse proportion to $\Delta\psi_m$ according to the Nernst equation; the more polarized mitochondria (the more negative matrix), the higher concentration of dye inside the mitochondrial matrix. Ultimately, the fluorescent signal can be detected optically²⁰⁹. We selected TMRM for the cardiomyocyte study (paper III) and TMRE in Paper I, and used flow cytometry to assess MMP per single cell. The dye selection was based on their properties, which are

low toxicity for cells and mitochondria, low inhibitory effect for ETC, quick equilibration, and not binding to the mitochondrial membrane or matrix proteins. Emitted fluorescence is not solely from the loaded probe into mitochondria, however, but also reflects accumulated dye in the cytoplasm, which is dependent on the plasma membrane potential and the size of the cells. Thus, we measured the fluorescence signal intensity at the presence and absence of a protonophore uncoupler, FCCP, to correct the results for the cell size and potential differences in plasma membrane potential between different cell populations.

Following FCCP treatment MMP is diminished and accumulated dye loads into cytoplasm until reaches equilibrium. The fluorescent intensity collected at the presence of uncoupler will be a function of plasma membrane potential and cell size. By subtracting the fluorescent signal in the presence of FCCP from the signal collected from the untreated sample we can avoid the interfering factors in our MMP measurement system. For staining procedure details please check the material and method parts in Paper I and III.

3.3.2.3. Assessment of *POLG* mutation effect on cellular redox state

In order to investigate the impact of *POLG* mutations on the redox state of iPSCs and differentiated cells, we measured the expression of respiratory chain complexes particularly complex I, the level of ROS, the NAD⁺/NADH ratio, and ATP level, and compared control and patient cell lines.

3.3.2.3.1. Assessment of electron transport chain (ETC) level in cells and tissues

We compared the protein levels of complexes I, II, IV in patients and controls in different cell types including iPSCs, fibroblasts, and iPSC-derived NSCs using flow cytometry. In addition, we performed immunohistochemistry⁶⁰ on 4- μ m sections of formalin-fixed, paraffin-embedded brain tissues of *POLG* patients and neurologically healthy controls to assess complex I level.

3.3.2.3.2. Measurement of ROS level and cellular senescence

In order to measure the cellular ROS level in live cells, we used flow cytometry to measure the fluorescence intensity of different fluorescent probes. Using 2',7'-dichlorofluorescein diacetate (DCFDA), we measured the levels of reactive oxygen species (ROS) including hydroxyl, peroxy, and others. DCFDA diffuses into the cells, where it is deacetylated by cellular esterases to a non-fluorescent compound. Subsequently, oxidation of this non-fluorescent compound by ROS leads to the formation of the highly fluorescent 2', 7' –dichlorofluorescein (DCF), which can be detected by flow cytometry. In addition, we employed the MitoSOX Red probe to detect the level of superoxide radicals generated specifically in mitochondria. MitoSOX Red is a cationic derivative of hydroethidine that selectively penetrates into actively respiring mitochondria via electrophoretic driving force. Oxidation of MitoSOX Red indicator by superoxide leads to the formation of 2-hydroxyethidium, which exhibits fluorescence properties different from the oxidized ethidium products generated by reactive oxygen species other than superoxide. Using these properties, we were able to discriminate mitochondrial superoxide from other reactive oxygen species. Co-staining of the cells with these probes and the mitochondrial tracker dyes, we evaluated ROS level in relation to mitochondrial volume.

We used a Senescence β -galactosidase Staining Kit (Cell Signaling) to detect one of the known characteristics of senescent cells, which is β -galactosidase activity at pH 6. Cells were cultured on coverslips in 6 well plates in their normal medium for 24 h. Cells were fixed with 1 \times fixative solution and incubated with the β -galactosidase staining solution overnight at 37°C in a dry incubator without CO₂ and images were taken using Nikon TE2000 fluorescence microscope.

3.3.2.3.3. Comparison of NAD⁺ metabolism between patient and control cell lines

We assessed redox homeostasis using Liquid Chromatography- Mass Spectrophotometry (LC/MS) to measure the level of NAD⁺, NADH, and the NAD⁺/NADH ratio. Details of the chromatography procedure are explained in the method section of Paper I and the analysis was performed by Prof.essor Mathias Ziegler

lab for analysis. We confirmed the LC/MS results using a commercial NAD⁺/NADH Quantitation Colorimetric Kit (BioVision) according to the manufacturer's instructions.

3.3.2.3.4. Assessment of ATP level

We compared the level of ATP in the patient and control cells using the Luminescent ATP Detection Assay Kit, which measures luminescent generated from the reaction of luciferin and ATP catalyzed by the luciferase enzyme.

Cells were seeded in 96 well flat, clear bottom, white wall plate and fed with normal medium. ATP measurement was performed on 90% confluent culture based on the manufacturer protocol. Luminescent signal was measure using Victor® XLight Multimode Plate Reader (PerkinElmer), and the ATP value was normalized to the cell number. We assess the number of the cells by culturing the cells in the same condition, following the incubation with Janus Green cell normalization stain (Abcam) and measuring the OD_{595 nm} by Labsystems Multiskan® Bichromatic plate reader (Titertek Instruments, USA).

3.3.3. Assessment of mitochondrial ultrastructure

We investigated mitochondrial ultrastructure using Transmission Electron Microscopy. NSCs derived from patient and control iPSCs and samples at different stages of cardiomyocyte differentiation were collected. Following a quick wash in DPBS, cells were dissociated into single cells using TrypLE™ Express Enzyme for 10-20 minutes at 37 °C and collected in the microcentrifuge tube for spinning down. Cell pellets were fixed in 2,5% glutaraldehyde (diluted in a 0,1M sodium cacodylate buffer) for 24 h at 4°C and delivered to the MIC facility at the University of Bergen. Details of post-fixation steps are well described in the method section of Paper III.

3.4. RNA sequencing

Total RNA was extracted using MagMAX™-96 Total RNA Isolation Kit, and RNA quality control, RNA library preparation, and data extraction were performed on two different RNA collections; data sets A and B. Data set A was composed of RNA sequences from both ESC and iPSC lines from two different stages of cardiac differentiation - undifferentiated cells (D0) and cardiac progenitors (D7). This data contained three replicates of two ESC lines (429 and 360), two replicates of Detroit551-7 and CRL 2097-R8, and one replicate of Detroit 551-10. Dataset B contained RNA sequences from four stages (D0, D2, D5, and D15) from three differentiation runs of the one ESC line, H1.

RNA samples were sequenced and analyzed independently: RNA from data set A were sequenced at the Finnish Microarray and Sequencing Centre's analysis service and Biocenter Finland, while RNA sequencing for data set B was performed at the HudsonAlpha Genome Sequencing Center, USA. The average RNA integrity number, RIN, of both data sets was above 7. RNA samples underwent sequencing using Illumina HiSeq 3000 instrument and single-read sequencing at 1 x 50 bp single-ended. Illumina's standard bcl2fastq2 software was applied for base calling and the raw data was assessed using fastQC version 0.11.8²¹⁰ followed by read quantification using Salmon version 1.3.0²¹¹. The data sets presented in paper III are accessible online in the European Nucleotide Archive (ENA) with accession number PRJEB47044, and the code to reproduce the RNA-seq analyses is available at <https://git.app.uib.no/gni042/cardiomyocytes-rna-seq>.

Briefly, R package tximport version 1.14.2²¹² was used to import transcript quantification and collapsing to gene-level. Low-expressed genes were filtered out (See method section paper III) resulting in 19,273 genes in dataset A, of which 80% annotated as protein-coding and 22,480 in dataset B, 73% annotated as protein-coding. the DESeq2 R package version 1.26²¹³ with default parameters was used for differential gene expression analysis. Multiple hypothesis testing was performed with the default automatic filtering of DESeq2. Thereafter, the false discovery rate (FDR) was calculated by the Benjamini-Hochberg procedure. Two data

sets were analyzed independently. Genes were scored based on their significance by transforming the p-values to account for the direction of change. Subsequently, genes were tested for enrichment with the complete Gene Ontology (GO) database annotation²¹⁴, the KEGG database²¹⁵, and a curated version of mitocarta^{216,217} (For more details see the method section of Paper III).

3.5. Statistical analysis

Due to the presence of intra-clonal heterogeneity, we included several clones of each cell line in the study published in Paper I. All experiments comprised more than three biological repeats for each clone and data were presented as mean \pm standard error of the mean (SEM). The Shapiro–Wilk test was applied to test the normal distribution of the data, and interquartile range (IQR) and Tukey’s Hinges test were used to detect outliers. The statistical significance was assessed by application of the two-sided Student’s t-test and Mann–Whitney U-test for variables with normal and non-normal distributions respectively. Data were analyzed by SPSS software (SPSS v.25, IBM), and presented by GraphPad Prism software (Prism 7.0, GraphPad Software, Inc).

In the cardiomyocyte studies, data were expressed as mean or median for the normally distributed populations, and as 95% confidence interval (CI) of the mean or median for non-normally distributed data. Normal distribution was confirmed by three normality tests including D’Agostino-Pearson omnibus test, Shapiro-Wilk test, and Kolmogorov-Smirnov test. The parametric tests were used only when the normality of the distribution was confirmed by all three tests. The statistical tests and number of biological replicates used for each assay are listed in method section of paper III. Data were analyzed and presented using GraphPad Prism software (Prism 7.0, GraphPad Software, Inc).

4. Results and Discussion

4.1. Paper I; “Disease-specific phenotypes in iPSC-derived neural stem cells with *POLG* mutations”

Since the respiratory chain, the enzyme pathway responsible for phosphorylation of ADP to ATP, has components encoded by both nuclear and mtDNA, mutation in either genome may cause mitochondrial dysfunction. One example of the interplay between nuclear and mitochondrial genomes is DNA polymerase gamma (*POLG*): both subunits of this enzyme are encoded by nuclear genes, but mutations affecting its function lead to defects in mtDNA. Pathogenic mutations in *POLG*, the gene encoding the catalytic subunit, are moreover, the most common cause of inherited mitochondrial disease.

Currently, *POLG*-related diseases are incurable and our understanding of the underlying mechanism(s) is poor. In part this due to the lack of reliable disease models and the inaccessibility of the affected tissues⁶⁰. We therefore generated an in vitro cellular model based on stem cells.

We reprogrammed patients fibroblast harboring two of the most common *POLG* mutations (c.2243G>C; p.W748S and c.1399G>A; p.A467T) to iPSCs and then differentiated these toward neuronal lineage. We found that mutant NSCs, but not patient fibroblasts or iPSCs replicated what was found in post-mortem brain tissues including mtDNA depletion and complex I deficiency. Associated with the complex I deficiency, we also found overproduction of ROS and defective NAD⁺ metabolism in our stem cell model and our data also suggested induction of cellular senescence with upregulation of UCP2 and downregulation SirT1 pathway and mitophagy activation.

While previous studies have generated *POLG*-iPSCs and investigated valproate toxicity in iPSC-derived hepatocytes²¹⁸⁻²²⁰, our study is the first replicate the *POLG* related neuro-pathological process in vitro.

4.1.1. Mutant fibroblasts and iPSCs partially manifest the mitochondrial abnormalities

Fibroblasts from a patient homozygous for W748S (called WS5A) and one compound heterozygous A467T/W748S (called CP2A) and controls were reprogrammed using a retroviral or Sendai virus systems. The iPSCs exhibited the same karyotype as their original fibroblasts and no chromosomal abnormalities were detected after reprogramming (Figure. EV1). Furthermore, the morphology of both patient and control iPSCs colonies were similar to those seen with ESCs and, like ESCs, they were able to differentiate into all three germ layers; hepatocyte (endoderm), cardiomyocyte (mesoderm), and neurons (ectoderm) (Figure. 2). All iPSCs expressed pluripotency markers such as *LIN28A*, *NANOG*, *SSEA4*, *POU5F1*. However, the expression of mRNA and protein levels of each of these markers was not the same in all clones particularly in patient iPSCs compared to ESCs (Figure.1 and Figure EV2). In order to compensate for this inter-clone variation, we included several clones of each cell line in further experiments. We compared different mitochondrial parameters in patients and control fibroblasts and their reprogrammed iPSCs lines.

In order to address the impact of *POLG* mutations on mitochondrial structure and content, we stained cells with MitoTracker Green (MTG) and showed that both patient and control fibroblasts and iPSCs contained the same mitochondrial mass (Figure. 2 and 5). These results were confirmed by assessment of another mitochondrial marker, TOMM20, in iPSCs (Figure. 2 and 6). By always including a mitochondrial mass or volume measurement (MTG or TOMM20), we were able to control for mitochondrial content in all subsequent assessments.

Since *POLG* is essential for mtDNA replication, we investigated mtDNA copy number using two different approaches; direct qPCR measurement of total mtDNA level and an indirect flow cytometry method. The indirect methods was based on the knowledge that TFAM binds mtDNA in molar quantities and its amount should therefore reflect mtDNA content. Both approaches detected no significant difference in mtDNA level between patients and controls fibroblasts and iPSCs (Figure. 2 and 6).

We employed flow cytometry to evaluate subunits of respiratory chain complexes I, II, and IV. Complex II has no mtDNA encoded subunits and thus functions as a control. No significant differences were seen in any of these complexes in fibroblasts and iPSCs (Figure. 7). Since mitochondrial dysfunction is a major source of intracellular ROS, particularly complex I dysfunction, we investigated ROS levels by dual staining the cells with 2',7'-dichlorodihydrofluorescein diacetate (DCFDA) and MitoTracker Deep Red (MTDR). Our results showed no major differences in total or specific ROS (DCFDA ratioed to MTDR) between patient and control fibroblasts and iPSCs except CP2A, which produced a lower level of ROS (Figure, EV4).

TMRE is useful not only to assess mitochondrial morphology, but also for measuring mitochondrial membrane potential; since MTG uptake into mitochondria is supposed not to be reliant on membrane potential, we used the ratio TMRE:MTG to provide a measure of MMP per mitochondrion, termed specific MMP. These experiments showed a significant increase in both total and specific MMP in patient fibroblasts, however, reprogrammed patients iPSCs had the same MMP as the control iPSCs (Figure. 2 and 5). Interestingly, when we evaluated the level of ATP in live cells, both patient cell types; fibroblast and iPSC, showed a lower level of ATP compared to control lines (Figure. 2 and 5).

Our findings are consistent with previous studies performed on iPSCs with mtDNA mutations suggesting that the mutant phenotype is rescued at the pluripotent stage²²¹. Stem cells and fibroblasts rely heavily on glycolysis rather than mitochondrial respiration for ATP generation, and glycolysis not only produces ATP in a hypoxic environment, but also maintains a low level of ROS. Further, the low ATP level in both patient iPSCs and fibroblasts and the suggestion of mitochondrial hyperpolarization in fibroblasts is also similar to previous studies²²². It suggests that either these cells hydrolyze ATP to maintain the membrane potential by reversing the proton flow in complex V²²³ or by downregulation of oxygen consumption through complex II by co-inhibition of complexes II, III, IV and V activity²²⁴.

4.1.2. Neuronal differentiated cells; NSCs and DA neurons, manifest greater mitochondrial function impairment compared with iPSCs and parental fibroblasts

We differentiated both patient and control iPSCs towards NSCs using a modified dual inhibition protocol²⁰⁸ and confirmed the expression of specific markers at each stage of differentiation (Figure. 3). The purity of cultures was checked by flow cytometry (Appendix Fig S3) and the presence of particular *POLG* mutation in NSCs- derived from patient iPSCs was confirmed (Figure. 4). In addition, we demonstrated that the generated NSCs had the potential to differentiate into neurons and glial subtypes including dopaminergic neurons and astrocytes (Figure. 4).

We applied the same experimental approach to study NSCs as was used for iPSCs and fibroblasts. Mitochondrial ultrastructure was similar in patients and control NSCs (Figure. 5), however, MTG staining suggested that WS5A NSCs had a lower mitochondrial content than controls, while mitochondrial mass in CP2A NSCs was similar to controls NSCs (Figure. 5). Investigation of mitochondrial mass using TOMM20 did not confirm these results (Figure. 6). Double staining with MTG and TMRE showed that total membrane potential was decreased in both mutant NSC lines, although there were no significant changes in specific membrane potential between patients and controls. When we measured ATP levels, however, we found that these were lower than control in both mutant NSCs suggesting that the low MMP was real (Figure.5).

Assessment of mtDNA level by qPCR and flow cytometry revealed a significant decrease in mutant NSCs (Figure. 6). We also checked the quality of the mtDNA and could not detect mtDNA deletions in patient cells (Figure. 6). The lack of qualitative mtDNA damage supported our earlier conclusion⁶⁰ that these types of mutations were cumulative and represented an “accelerated aging”. Patient NSCs differentiated into dopaminergic neurons also showed significant mtDNA depletion (Figure. 6) replicating the findings from microdissected neurons of patients with *POLG* diseases (Figure. 7)⁶⁰. In addition to the reduced mtDNA level, we also confirmed significantly lower complex I in mutant NSCs. Immunostaining showed no significant changes in

Complex II subunits in mutant NSCs compared to control, however, complex IV was significantly lower in WS5A, but not CP2A NSCs, compared to control.

Our findings reveal a cell specificity associated with POLG disease; different cell types respond differently to the same bioenergetic challenge. Given that differentiation and maintenance of neurons is time-consuming and these cells have limited expansion potential, we considered NSCs to be a precise and reliable cell type for disease modeling. NSCs not only manifest exactly the same mitochondrial impairment we detected in patient tissues but can be expanded, banked, and, potentially be used for high-throughput drug screening.

4.1.3. Changes in cellular redox status occur only in mutant NSCs

Since mitochondrial respiratory chain dysfunction is a major source of intracellular ROS, we investigated intracellular ROS levels. We used dual staining with 2',7'-dichlorodihydrofluorescein diacetate (DCFDA) and MitoTracker Deep Red (MTDR) and calculated "specific ROS" level using the ratio of total ROS (DCFDA) to total mitochondrial mass (measured by MTDR signal) in each cell. Whereas we found no significant increase in either fibroblasts or iPSCs (Figure EV4), both total and specific ROS production level was clearly elevated in both mutant NSCs compared to control. To ensure that mitochondria were the source of this increased ROS, we co-stained the cells with the ROS-sensitive fluorescent dye, MitoSox and MTG and quantified both total and specific mitochondrial ROS. This confirmed mitochondria as the source of the increased ROS (Figure. 8).

Loss of complex I and neurodegeneration in the substantia nigra has long been associated with Parkinson's disease (PD)²²⁵. However, it has been shown that neuronal complex I deficiency is a widespread phenomenon in the PD brain and can occur independently of mtDNA damage²²⁶. Moreover, a previous study in mtDNA maintenance disorders, including POLG-related disease, suggested that complex I deficiency was a compensatory response to reduce the oxidative damage to neurons²²⁷. Mitochondrial ROS has been linked to neurodegenerative diseases, including PD²²⁸ and Alzheimer's disease (AD)²²⁹. Nevertheless, the relationship between increased ROS

and loss of complex I, and subsequently cell death is not clear, specifically in mitochondrial disease. Irrespective of the pathological or compensatory role of complex I deficiency and elevated ROS, these features are clearly associated with the POLG disorder and can be used for monitoring treatment or other interventions.

Complex I is vital for the re-oxidization of NADH and maintenance of the cellular NAD⁺/NADH ratio. We, therefore, investigated the impact of POLG mutations on the redox status of the cell using LC/MS. Despite variation of NAD⁺ and NADH levels in mutant NSCs, we observed a significant decrease in the NAD⁺/NADH ratio in both mutant NSC lines compared to controls (Figure 8). These results were confirmed using a commercial NAD⁺/NADH assay (Appendix Fig S8). Evaluation of redox status in iPSCs revealed an increase in NAD⁺/NADH, while NAD⁺ and NADH exhibited a decreased pattern in patient iPSCs compared to control iPSCs and only the CP2A line reached significance (Figure. 8).

4.1.4. UCP2/SirT1- regulated cellular senescence and BNIP3 pathway-mediated mitophagy are involved in the pathogenesis of mutant NSCs

In light of the association between disrupted NAD⁺ metabolism and increased ROS with aging^{230,231}, we evaluated cellular senescence and mitophagy our NSCs. We performed staining of β -galactosidase and measure p16INK4 protein level by flow cytometry and found significant increased β -galactosidase activity and p16INK4 in patient NSCs. These results are consistent with the previous studies showing that mitochondrial dysfunction may promote cellular senescence both in vivo and in vitro. Given that different mitogenic mechanisms are involved in induction of cellular senescence, we investigated the possible molecular pathways triggering the process of senescence. Irreversible reduction of membrane potential by overproduction of mitochondrial uncoupler protein 2 (UCP2) has been shown to induce senescence-like morphology and result in the loss of cellular ATP, elevated ROS production, and metabolic change²³². Moreover, *UCP2* gene expression is suppressed by SirT1, a NAD⁺-dependent protein deacetylase²³³. We evaluated UCP2 and phosphorylated SirT1 by western blotting and found upregulation of UCP2 and decreased activity of SirT1 in mutant NSCs.

Since it has been shown that mitochondrial turnover through mitophagy/autophagy can stimulate and inhibit senescence, we evaluated the expression of mitophagy markers such as PINK1, Parkin, BNIP3, and LC3B by western blot. While the expression of PINK1 and Parkin was similar to control, the expression of BNIP3 and the ratio of LC3BII/LC3BI were increased, but in only CP2A NSCs. These data support the association of POLG dysfunction with cellular senescence and activation of autophagy/mitophagy. Multiple studies have suggested a role for impaired mitophagy in neurodegenerative diseases such as PD ²³⁴, AD ²³⁰, and Huntington's disease ²³⁵. Consistent with these studies, our observations suggest that POLG disease in the brain is associated with the activation of BNIP3-mediated autophagy/mitophagy.

In conclusion, this study showed that we can faithfully recapitulate the findings made in post-mortem POLG-brains, namely mtDNA depletion and complex I deficiency in a robust and tractable model. Further, our results provide insight into the cellular mechanisms involved in the neuronal death, including the loss of ATP and membrane potential, the changes in redox potential, overproduction of ROS and the activation of mitophagy. All these leads to neuronal dysfunction and eventually neuronal loss.

4.2. Paper II; “A method for differentiating human induced pluripotent stem cells toward functional cardiomyocytes in 96-well microplates”

One of the main objectives of these studies was to develop a platform for monitoring mitochondrial changes during the early stages of cardiomyocyte development. Therefore, our primary task was to establish a differentiation platform that recapitulated cardiomyocyte early development *in vitro*. Earlier methods such as spontaneous differentiation using EBs yielded low level of cardiomyocytes (<10%) and high levels of heterogeneity^{161,162}. The more recent methodology, monolayer-directed differentiation, have significantly enhanced the efficiency of cardiomyocyte differentiation (>80%) by using defined media, small molecules, and purifying methods for enriching cardiomyocytes^{153,164}. We chose monolayer-directed differentiation since this method is more controllable and reproducible, and does not need extra re-plating steps.

In order to maximize time and resources we decided to establish the protocol in a 96 well format. Available protocols usually generated cardiomyocytes in large formats and then seeded them into 96-well plate^{236,237}. Thereafter, increased efficiency was obtained through genetic or metabolic manipulation^{238,239}. We modified a well-established monolayer protocol¹⁶⁴ to develop a high throughput, efficient and robust protocol that started in a 96 well format and did not require modification or post purification.

4.2.1. Optimizing cardiomyocyte differentiation in 96 well format

In order to develop the differentiation protocol in 96-well plates, we first investigated the impact of parameters such as PSC quality, the matrix, media, small molecules, cell density and cell confluency. To do this, we used two human ESC (H1 and H9) and two iPSC (Detroit 551-A and AG05836B-15) lines. We changed Matrigel for Geltrex, which is a cheaper and a more defined extracellular matrix, and we substituted the mTeSR1 medium with the simpler Essential 8 medium. These modifications reduced the cost of the differentiation process, while the yield of cardiomyocyte differentiation was

unaffected. We investigated the impact of confluency prior to initiation of differentiation and found that the optimal confluency of PSCs was 60-70% compared to 80-90% required for the 12-well format^{153,240} (Figure. 2). We also estimated the optimal cell density for seeding in order to reach 60-70% confluency within a minimum of 2 days (Supplementary Fig. S1). This period was set to provide enough time for the cells to recover from the effect of Y27632 and for them to reach the desired confluency in the shortest time. Different cell lines may need more time to reach the optimal confluency, for instance H9 became 60-70% confluent within 3 days, while Detroit 551-A needed 2 days. Finally, we adjusted the concentration of small molecule CHIR99021, the GSK3 inhibitor, based on the confluency and cell line and found that 8 μ M was optimal for ESCs while iPSCs required 6 μ M CHIR99021 to give high levels of cardiomyocytes on D15. Seventy two hours post differentiation induction, cells were cultured in medium containing the inhibitor of WNT production-2, IWP2, for 48 h. On day 5, the medium was changed to fresh (RPMI/B-27 without insulin), and from day 7 cells were fed with fresh RPMI/B-27 (with insulin) every two days. Beating cardiomyocytes appeared in the culture usually by day 7 (Figure. 1).

4.2.2. Monitoring cardiomyocyte differentiation process

We confirmed that differentiation followed the correct developmental route i.e. pluripotency state at day 0 (D0), germ layer specification (D3), progenitor state (D5) and committed cardiomyocytes (D15) by monitoring the expression level of key markers. We demonstrated the decreased expression of pluripotency genes *NANOG* and *POU5F1*, and the appearance of early mesodermal markers such as *MESPI*, *MIXL1*, and *T* at the highest level on D3 of differentiation. Increased expression of *ISL1* and *TEMEM88* confirmed the presence of cardiac progenitors on D5 and the expression of *TBX5*, *TNNT2*, *MYH6* and *MYL7* on D15 defined the emergence of committed cardiomyocytes (Figure. 3 and Supplementary Fig. S2-S3). Using this method, we were able to culture the cardiomyocytes in 96well plate format for more than 2 months. The expression of *HOPX*, *MYH6*, and *MYH7* at later stages of

differentiation proved the development of mature cardiomyocytes in the culture (Supplementary Fig.S4).

Gene expression results were confirmed using immunocytochemistry. We detected expression of Isl1 and Nkx 2-5 on day 6 and the cardiomyocyte marker, TNNT2, on day 10 of differentiation. Moreover, the co-localization of myosin light chain 7 (MYL7), and connexin 43 (GJA1) in the cells expressing TNNT2 and TNNI3, revealed the presence of cardiac sarcomeres and the gap junctions structures in TNNT2⁺ cells on D10-12 of differentiation (Figure. 4).

4.2.3. Assessment of cell composition in the culture and yield of differentiation

Since cardiovascular progenitors can differentiate into cardiomyocytes, smooth muscle and endothelial cells ²⁴¹, we investigated the presence of different cell populations at later stages of differentiation using flow cytometry. Co-staining of the cells collected within D12-D19 of differentiation with TNNT2 and MYL7 revealed a high percentage of cells were committed cardiomyocytes; $82 \pm 7\%$ TNNT2⁺ and $60 \pm 10\%$ MYL7⁺ in H1 cultures while $85.7 \pm 3\%$ and $79.7 \pm 3\%$ were positive in Detroit551-A cells (Figure. 5). The poor differentiation capacity of H9; 47% TNNT2 positive and 45% MYL7-positive cells is consistent with a previous study ²⁴² and might be explained by the high expression of Isl-1 through H9 differentiation (Figure 5 and supplementary Fig. S3). Using antibodies against CDH5 (a marker for the endothelial lineage) and ACTA2 (smooth muscle), we confirmed the presence of endothelial and smooth muscles on day 15 of culture. To evaluate the relative proportions, we co-stained cells for the surface markers CD144 and CD140b and found that iPSC-derived cultures contained a higher percentage of smooth muscle cells than ES cells, 18.45% in Detroit 551-A and 21% in AG05836B-15, whereas endothelial cell composition was lower in the iPSC lines compared to H1 (Figure. 5).

4.2.4. Electrophysiological validation of PSC-derived cardiomyocyte

The electrophysiological activity of cardiomyocytes depends on the correct expression and function of various ion channels including sodium, potassium, and calcium channels. We investigated these properties using microelectrode arrays (MEA), which record the extracellular field potential (FP) simultaneously in multiple sites from the whole culture. The wave form FP signals represent the cardiac action potential and reflects, to some extent, the electrocardiogram recording. Typically, the signal starts with a rapid upstroke corresponding to the Na⁺ influx (R/Q peak) and membrane depolarization followed by a slow wave/plateau phase, which is thought to correspond to the Ca²⁺ influx, and ultimately a repolarization phase corresponding to a predominant K⁺ efflux (T peak). Beating cardiomyocytes were transferred to the chamber and we recorded all the parameters in the absence and presence of specific drugs including β_1 and β_2 adrenoreceptor agonist (isoproterenol), potassium channel antagonist (E4031), sodium channel antagonist tetrodotoxin (TTX), L-type calcium channel antagonist (nifedipine), and the 5-hydroxytryptamine (serotonin) receptor, T4, 5HT4, agonist and 5HT3 antagonist (Mosapride). While there was variation between H1 and Detroit-derived cardiomyocytes, both cultures reacted similarly to the drugs confirming that both had electrophysiological properties consistent with those expected (Figure.7 and Table 1).

4.2.5. Investigation of inter-well heterogeneity

In order to investigate the inter-well variation in one culture plate, we extracted RNA from multiple wells and performed qPCR to assess the expression of *TNNT2* and *NKX 2-5* relative to a housekeeping gene *GAPDH* in each well of 96 well-plate. We selected up to twelve wells of a differentiation run at random and isolated total RNA using the MagMAX isolation kit. We looked at two differentiation runs of H1; for the first run, we analysed 12 wells of one plate while for the second run, we analysed 12 wells selected from 3 different plates. We also isolated total RNA of multiple wells from 3 different plates of one run of Detroit 551-A differentiation. We calculated the expression of *NKX*

2-5 and *TNNT2* relative to *GAPDH* using the ratio of the Ct value of each of these genes. The calculated coefficient of variation of the $Ct_{NKX2-5} : Ct_{GAPDH}$, and $Ct_{TNNT2} : Ct_{GAPDH}$ showed a variation between 1.96 and 7.30%, which confirmed the presence of similar numbers of cardiomyocytes in each well (Figure. 6).

In conclusion, we have successfully developed a scale-down platform for efficient cardiac differentiation that reduces both workload and cost, while improving reproducibility and precision. Since all steps of differentiation from PSC to functional tissue are performed in 96-well format, this protocol is suitable for both developmental and disease modeling studies, and also for high throughput investigations such as drug screening.

4.3. Paper III; “Distinct mitochondrial remodeling during mesoderm differentiation in a human-based stem cell model”

The last part of the project was an investigation of mitochondrial changes during early stages of mesodermal layer differentiation towards cardiomyocytes and other derivatives of cardiovascular progenitors. The general assumption is that pluripotent stem cells rely on glycolysis for ATP generation and once they exit pluripotency, they shift from glycolysis to OXPHOS to meet the higher energy demand that specialized functions require^{119,121,243}. This metabolic switch is also associated with mitochondrial remodeling from a fragmented state with lower mtDNA and mass in pluripotent stem cells to high level of elongated mitochondria with increased level of mtDNA in differentiated cells^{106,111,244,245}.

Interestingly, recent evidence shows that the metabolic shift is germ layer specific; the metabolic switch from glycolysis to OXPHOS occurs during the transition to mesoderm and endoderm while during early ectoderm commitment glycolysis is still active and is essential for early ectoderm specification²⁴⁶. In addition, it has been reported that mtDNA level and mitochondrial volume fall in the early phase of neuronal differentiation, particularly during the transition of human PSCs towards neural precursor cells (NPCs)^{247,248}. This is followed by an expansion of mitochondrial mass and mtDNA level along with increased in OXPHOS at later stages of neuronal differentiation²⁴⁹. Despite the reported increase in mitochondrial mass, and mtDNA level and the activation of metabolic remodeling during human PSC differentiation into hepatocyte¹⁰⁹, skeletal muscle²⁵⁰ and cardiomyocyte¹¹¹, conflicting results have raised questions concerning the accepted mitochondrial remodeling pattern during mesoderm and endoderm differentiation. For instance, the decreased expression of mitochondrial transcription factors A, B1, B2, nuclear respiratory factor 1 and polymerase gamma have been reported during cardiomyocyte differentiation¹¹¹.

In this study, we investigated the mitochondrial properties including mitochondrial mass, ultrastructure, membrane potential, and respiratory complex activity during differentiation and maturation of cardiomyocytes derived from both human embryonic stem cells (ESC) and induced pluripotent stem cells (iPSC). In contrast to previous

reports, we detected a significant reduction in mitochondrial biomass and mtDNA levels during mesoderm differentiation towards cardiac progenitors and even to functional cardiomyocytes. Despite the marked reduction in mitochondrial content, differentiated cardiomyocytes maintained a similar basal oxygen consumption rate relative to undifferentiated PSCs, made the metabolic transition from glycolysis to OXPHOS, and showed ultrastructure remodeling. Overall, we show that despite a fall in mitochondrial volume, developing cardiomyocytes still increased their mitochondrial efficiency and levels of ATP-linked respiration, which compensated for the lower number of mitochondria.

4.3.1. Investigation of mitochondrial changes during cardiomyocyte differentiation

We differentiated human PSCs towards cardiomyocyte using the protocol developed in paper II (Figure. 1). For comparative purposes, we divided the differentiation process into phases based on the expression of specific markers (Figure. 1): pluripotent state (Day0, S1), mesendoderm cells (Day 1-2, S2), precardiac mesoderm (Day3, S3), cardiac progenitor cells (Day 5-7, S4), functional cardiomyocyte (Day 8-15, S5). The correct mesoderm differentiation route was confirmed based on the expression of stage specific markers at both RNA and protein level (Figure.1 and Supplementary Fig. 1 and 2). In order to know the proportion of cardiomyocytes versus other cell types, we assessed the purity of cultures at different stages of differentiation. Undifferentiated and cardiac progenitor cultures (S1 and S4 respectively) represented a relatively pure culture, while culture at S5 comprises two different cell populations ; cardiomyocytes (20% \pm 13 TNNT2+) and non-cardiomyocyte (TNNT2-) cell populations (Figure. 1). We investigated mtDNA level, mitochondrial mass, mitochondrial function and structure at different stages of cardiomyocyte differentiation.

4.3.2. Mitochondrial content falls progressively during mesoderm differentiation

We assessed mtDNA copy number using a qPCR assay developed earlier⁶⁰ and found a clear and progressive reduction of mtDNA (of up to 85%) during differentiation of both iPSCs and ESCs to mesodermal lineage (Figure. 2). We found no evidence of mtDNA deletion at any stage of differentiation (Supplementary Fig. 3). For comparative purposes, we also compared the level of mtDNA in post-mortem human heart tissue using the same method. While this may not accurately reflect the mtDNA level in life, it confirmed that mtDNA level in the mature tissue is at least 11- 44 times higher than PSCs and differentiated cells at S5 (Figure. 2).

We evaluated the expression of the genes involved in mtDNA homeostasis and replication using bulk RNA-seq datasets. Consistent with reduction of mtDNA level, transcriptomic analysis showed decreased expression of the majority of genes involved in mtDNA replication during differentiation (Figure. 2). This was particularly clear for mitochondrial genome maintenance exonuclease1, MGME1, single-stranded DNA binding protein, SSBP, mitochondrial transcription factor A, TFAM and mtDNA helicase, TWNK. Interestingly, DNA polymerase gamma, POLG mRNA level remained unchanged through differentiation. The progressive reduction of SSBP mRNA level and unchanged expression of POLG were confirmed using qPCR (Supplementary Fig. 3). The significant reduction in mtDNA during cardiomyocyte differentiation contrasts with previous studies, but may reflect the use of different methods for differentiation or mtDNA detection^{106,111}. For example, in earlier studies, PCR for mtDNA was performed on bulk lysates using cells generated through embryonic bodies development and mitochondrial mass measured in the same lysates using western blotting.

In order to assess mtDNA level in living cells, we employed the link between TFAM protein and mtDNA^{251,252}. It is known that TFAM, one of the key components that participates in nucleoid structure, binds mtDNA in molar quantities; 1000 TFAM molecules per mtDNA^{52,253,254}. Therefore, TFAM protein level provides an indirect measure of mtDNA level within a single cell. We used flow cytometry and co-stained

cells with antibodies against stage-specific markers and TFAM, and Zombie Red as a cell viability dye. We found a 58% reduction in mtDNA in cardiac progenitors (S4) relative to pluripotent cells (S1). Further, while the level of TFAM in cells at S5 was lower than S1, the level was ca. 10% higher than progenitors at stage S4. We also found a significant difference in TFAM level between TNNT2+ and TNNT2- population suggesting a higher level of mtDNA in cardiac cells relative to non-cardiac (Figure. 2). Both methods confirmed the mtDNA reduction during differentiation. Reduction of mtDNA level in cardiac progenitor was aligned with the recent findings reported lowest mtDNA level in neuronal progenitor cells during ectoderm differentiation²⁴⁷ and during hematopoietic differentiation²⁵⁵. Nevertheless, the low level of mtDNA in functional cardiomyocytes, S5, was not expected.

The reduction in mtDNA raised the question of whether this was restricted to mtDNA, e.g. a reflection of mtDNA segregation into daughter cells, or a consequence of mitochondria loss during differentiation. Transcriptomic results showed a significant reduction of *VDAC1* suggesting a decrease in mitochondrial volume (Supplementary Fig. S3). We validated this by evaluating TOMM20 using flow cytometry. TOMM20 fell from S1 to S4 (43% below S1) and reached its lowest level at S5 (60%) (Figure. 2). As expected, the level of TOMM20 was lower (~40%) in non-cardiac cells compared with cardiomyocytes indicating a lower level of mitochondria in non-cardiac cells relative to cardiomyocytes (Figure. 2). The significant reduction of mitochondrial content was surprising for two reasons. Firstly, the demand for energy is expected to be higher in differentiated cells, and second, because of the relationship between the cell size and mitochondrial mass²⁴⁹; differentiated cells at S5 are much bigger than PSCs at S1 and expected therefore to contain more mitochondria compared to undifferentiated cells.

While protein levels of TFAM and TOMM20 generally showed a similar pattern, we did not observe an increase in TOMM20 from S4 to S5 as was seen with TFAM. These results raise questions concerning the link between mtDNA level and mitochondrial content during cardiac differentiation. To assess changes in mtDNA level relative to mitochondrial content, we plotted the TFAM level (an indirect marker of mtDNA) against the TOMM20 level (a direct marker for mitochondrial content). We found that

this ratio increased significantly from progenitors (S4) to differentiated (S5) cells (Figure. 2) suggesting that cardiac progenitors contain the lowest mtDNA per unit of mitochondria, which rose in the more differentiated stage. Together, these results not only suggest a progressive fall of mitochondrial content during mesoderm differentiation, but also suggest that mtDNA level can change independently of mitochondrial mass. These studies also show that it is important to use complementary methods to evaluate mitochondrial volume and level of mtDNA.

4.3.3. Despite lower mitochondrial mass, differentiated cells at S5 contain mature mitochondria that can generate more energy through TCA rather than glycolysis

Bulk RNA sequencing revealed a decrease in the expression of genes encoded by mtDNA from PSCs to cardiac progenitors, S4, followed by a significant increase at S5 suggesting that differentiated cells, both cardiomyocytes and non-cardiomyocytes, were more reliant on OXPHOS (Figure. 3). We confirmed this using the Seahorse XF-96 extracellular flux analyzer. Despite a lower mitochondrial volume in S5 cells, basal OCR (~137 pmol/min) was similar to undifferentiated PSCs (S1) (~ 148 pmol/min) (Figure. 3) while maximal OCR and spare capacity showed a slight increase during differentiation (Figure. 3 and supplementary Fig. S5). The percentage of the oxygen consumed through OXPHOS for ATP synthesis, known as coupling efficiency, was also significantly higher in S5 than S1 (Figure. 3). Thus, although differentiated cells at S5 had significantly lower mitochondrial content, we found that these cells had a clear increase in mitochondrial ATP generating capacity with no change in basal respiration. In addition to the increase in ATP generating capacity, the ratio of OCR to extracellular acidification rate (ECAR), which reflects the amount of lactate produced through glycolysis, showed a clear shift from glycolysis to OXPHOS. The finding of a 50% increase in OCR:ECAR ratio at the basal level, and more than a 2.5-fold increase at maximal level suggests that differentiated cells at S5 are much more reliant on OXPHOS than undifferentiated PSCs (Figure. 3). This change from glycolysis to OXPHOS was

supported by a significant increase in expression of all the genes that code for ETC complex subunits and TCA cycle enzymes (Appendix Figures 1-4).

We also investigated mitochondrial membrane potential (MMP) as a marker for mitochondrial activity using TMRM and single-cell flow cytometry. Unexpectedly, we observed a significant fall in median fluorescent intensity (MFI) of TMRM at S5 relative to undifferentiated PSCs. Although mitochondrial membrane potential is an excellent marker for assessing mitochondrial function ²⁵⁶, it also reflects mitochondrial volume. Thus, to avoid misinterpreting low MMP, we corrected for cellular mitochondrial content by normalizing TMRM fluorescent intensity to that of TOMM20. This showed a more than two-fold increase in MMP level per unit of mitochondrial mass in S5 cells relative to undifferentiated PSCs (Figure. 3) confirming that mitochondria in differentiated cells were more efficient in generating ATP.

4.3.4. Cristae remodeling during cardiomyocytes differentiation

The transcriptomic profile of differentiated cells at S5 showed a significant increase in the expression of genes regulating mitochondrial respiration including PPARA, PPARG, PGC-1A, and ESSRA (Figure. 3). Since we did not detect any increase in mitochondrial content, we hypothesized that this upregulation might be involved in the remodeling of mitochondrial ultrastructure. We examined S1, S4, and S5 cells by transmission electron microscopy (TEM) and found that mitochondria in PSCs (S1), which are spherical and fragmented with an abundant matrix, underwent a remodeling with the formation of more compact cristae and clearer matrix in S5 (Figure. 3). These findings are consistent with previous studies showing the formation of cristae and mitochondrial permeability transition pore (mPTP) closure in differentiated cardiomyocytes as signs of mitochondrial maturation during cardiomyocyte differentiation ²⁵⁷⁻²⁵⁹.

In conclusion, our results are aligned with previous reports showing the metabolic remodeling during mesoderm and endoderm differentiation. However, our data revealed that switching from glycolysis to OXPHOS occurs independent from mitochondrial

content expansion. Reduction of mitochondrial biomass and mtDNA level in cardiac progenitors was expected since it has been reported during the neuronal differentiation, particularly during transition of PSCs towards the neural precursor cells (NPCs)^{247,248}, however, further reduction of mitochondrial mass and mtDNA in differentiated cells including beating cardiomyocytes was not expected. Recent studies also reported reduction of mitochondrial mass in hematopoietic stem cells, which are also of mesodermal origin²⁵⁵. All together these findings suggested that a unique mitochondrial and metabolic path during mesodermal differentiation. In addition, our data suggested that mitochondria in terminally differentiated cells are more mature and more efficient in ATP production that can compensate for the mitochondrial reduction in these cells.

5. Concluding remarks and future perspectives

The main aim of this project was to develop iPSC-based models to investigate the mechanisms underlying POLG-related disease. We successfully established a patient-specific neuronal model and demonstrated that this provided an excellent platform to explore tissue specific mechanisms. In our neuronal model, we showed that mutant NSCs recapitulated the disease phenotypes that we saw in post-mortem brain tissues including mtDNA depletion, complex I deficiency. We also showed the presence of energy failure, high levels of mitochondrial reactive oxygen species (ROS) and the upregulation of senescence. This is the first stem cell based model for the neurological disease caused by POLG mutations and this work is now being extended and adapted to generate a platform for use in drug screening experiments.

Since we know that there are multiple mutations in the POLG gene, we can also develop our model to include patient lines carrying other POLG mutations to investigate the impact of different POLG mutations on mitochondrial function and cell survival. In addition, the differentiation of iPSCs into different types of neurons and glial cells may help to reveal the impact of POLG mutations on the function of various parts of the brain. Lastly, when considering the limitation of monolayer culture, it would be of interest to develop 3D neuronal differentiation protocols to understand better how POLG mutations influence neuronal development and interconnections.

One of the main technical issues that must be addressed is the lack of isogenic controls. Despite being aware of available gene editing techniques such as CRISPR Cas9, we decided to compare age/gender-matched controls from healthy individuals as disease comparators instead of gene-corrected isogenic controls and we included more clones in our study to minimize the phenotypic diversity caused by inter-clonal heterogeneity. This decision was based partly on the presence of a compound heterozygous patient (CP2A) and the difficulties for introducing compound mutations using CRISPR. Nevertheless, we understand that gene-corrected isogenic controls or rescue experiments will be necessary to validate studies including our looking at POLG loss of function.

In the second study, we successfully developed a scaled down platform for cardiac differentiation. We did this in order to have a tractable system to use in later experiments, e.g. investigating why heart appears less clinically involved than other tissues such as brain and liver, and one that would be amenable for high throughput screening. We also want a system that was efficient and reproducible without any genetic modification or additional enrichment processes. We showed that this platform provided an adaptable system for developmental studies e.g. monitoring the differentiation and development of cardiac tissue from very early stages to functional tissue in a 96-well format. The platform is well suited for the investigation of early disease development, and high throughput studies such as drug screening.

In the last paper, we used the platform developed in paper II to generate novel findings concerning how mitochondrial mass and mtDNA change during the early stages of mesoderm differentiation. Contrary to our expectations, we found reduction in mitochondria and mtDNA, but were able to show that this was more than compensated for by a higher level of mitochondrial membrane potential, higher coupling efficiency, and a switch from glycolysis to OXPHOS.

Given that our protocol allows us to keep cells in culture for longer, it would be interesting and informative to investigate how further maturation of cardiomyocytes affects mtDNA level, mitochondrial content and function. In our study, we did not explain the mechanism underlying the mitochondrial loss during cardiomyocyte differentiation. For example, transcriptomic data did not show an increase in the expression of genes involved in mitophagy. However, a recent study revealed the importance of BNIP3- mediated mitophagy process in cardiomyocyte differentiation, and this can be investigated in more detail as a possible mechanism. Recent new data has revealed that mitochondrial loss also occurs during hematopoietic differentiation, another lineage with mesodermal origin. Thus, it would be of interest to establish whether this phenomenon is limited to mesoderm or also seen in cells originating from endoderm.

Considering that our studies are in vitro, it would be interesting to know whether this phenomenon also occurs during early embryonic developmental stages. Due to the ethical problems surrounding work on human embryos, this could initially be studied in

animal models. Several studies have reported mitochondrial reduction during the formation of blastocyst, and high level of mitochondria at later stages of development during heart formation. However, it remains unclear how and when the increased mitochondrial content occurs. Therefore, it is necessary to investigate the stages between the blastocyst and mature heart in the embryo to fill the gap and address how mitochondria change during development.

6. References

- 1 Sinha, K., Das, J., Pal, P. B. & Sil, P. C. Oxidative stress: the mitochondria-dependent and mitochondria-independent pathways of apoptosis. *Archives of Toxicology* **87**, 1157-1180, doi:10.1007/s00204-013-1034-4 (2013).
- 2 Rizzuto, R., De Stefani, D., Raffaello, A. & Mammucari, C. Mitochondria as sensors and regulators of calcium signalling. *Nature Reviews Molecular Cell Biology* **13**, 566-578, doi:10.1038/nrm3412 (2012).
- 3 Zhang, H., Menzies, K. J. & Auwerx, J. The role of mitochondria in stem cell fate and aging. *Development* **145**, doi:10.1242/dev.143420 (2018).
- 4 Andersson, S. G. E. *et al.* The genome sequence of *Rickettsia prowazekii* and the origin of mitochondria. *Nature* **396**, 133-140, doi:10.1038/24094 (1998).
- 5 Martijn, J., Vosseberg, J., Guy, L., Offre, P. & Ettema, T. J. G. Deep mitochondrial origin outside the sampled alphaproteobacteria. *Nature* **557**, 101-105, doi:10.1038/s41586-018-0059-5 (2018).
- 6 Ott, M., Amunts, A. & Brown, A. Organization and Regulation of Mitochondrial Protein Synthesis. *Annu Rev Biochem* **85**, 77-101, doi:10.1146/annurev-biochem-060815-014334 (2016).
- 7 McKee, E. E., Ferguson, M., Bentley, A. T. & Marks, T. A. Inhibition of mammalian mitochondrial protein synthesis by oxazolidonones. *Antimicrob Agents Chemother* **50**, 2042-2049, doi:10.1128/AAC.01411-05 (2006).
- 8 Collins, T. J., Berridge, M. J., Lipp, P. & Bootman, M. D. Mitochondria are morphologically and functionally heterogeneous within cells. *Embo j* **21**, 1616-1627, doi:10.1093/emboj/21.7.1616 (2002).
- 9 Cheng, A. *et al.* Involvement of PGC-1 α in the formation and maintenance of neuronal dendritic spines. *Nature Communications* **3**, 1250, doi:10.1038/ncomms2238 (2012).
- 10 Birkedal, R., Shiels, H. A. & Vendelin, M. Three-dimensional mitochondrial arrangement in ventricular myocytes: from chaos to order. *Am J Physiol Cell Physiol* **291**, C1148-1158, doi:10.1152/ajpcell.00236.2006 (2006).
- 11 Barth, E., Stämmler, G., Speiser, B. & Schaper, J. Ultrastructural quantitation of mitochondria and myofilaments in cardiac muscle from 10 different animal species including man. *J Mol Cell Cardiol* **24**, 669-681, doi:10.1016/0022-2828(92)93381-s (1992).
- 12 Sousa, J. S., D'Imprima, E. & Vonck, J. in *Membrane Protein Complexes: Structure and Function* (eds J. Robin Harris & Egbert J. Boekema) 167-227 (Springer Singapore, 2018).
- 13 Sazanov, L. A. A giant molecular proton pump: structure and mechanism of respiratory complex I. *Nature Reviews Molecular Cell Biology* **16**, 375-388, doi:10.1038/nrm3997 (2015).
- 14 Kühlbrandt, W. Structure and function of mitochondrial membrane protein complexes. *BMC Biol* **13**, 89, doi:10.1186/s12915-015-0201-x (2015).
- 15 Baker, N., Patel, J. & Khacho, M. Linking mitochondrial dynamics, cristae remodeling and supercomplex formation: How mitochondrial structure can

- regulate bioenergetics. *Mitochondrion* **49**, 259-268, doi:<https://doi.org/10.1016/j.mito.2019.06.003> (2019).
- 16 Benard, G. *et al.* Physiological diversity of mitochondrial oxidative phosphorylation. *Am J Physiol Cell Physiol* **291**, C1172-1182, doi:10.1152/ajpcell.00195.2006 (2006).
- 17 Noguchi, M. & Kasahara, A. Mitochondrial dynamics coordinate cell differentiation. *Biochem Biophys Res Commun* **500**, 59-64, doi:<https://doi.org/10.1016/j.bbrc.2017.06.094> (2018).
- 18 Seo, B. J., Yoon, S. H. & Do, J. T. Mitochondrial Dynamics in Stem Cells and Differentiation. *Int J Mol Sci* **19**, doi:10.3390/ijms19123893 (2018).
- 19 Fernie, A. R., Carrari, F. & Sweetlove, L. J. Respiratory metabolism: glycolysis, the TCA cycle and mitochondrial electron transport. *Curr Opin Plant Biol* **7**, 254-261, doi:10.1016/j.pbi.2004.03.007 (2004).
- 20 Nolfi-Donagan, D., Braganza, A. & Shiva, S. Mitochondrial electron transport chain: Oxidative phosphorylation, oxidant production, and methods of measurement. *Redox biology* **37**, 101674-101674, doi:10.1016/j.redox.2020.101674 (2020).
- 21 Guo, R., Gu, J., Zong, S., Wu, M. & Yang, M. Structure and mechanism of mitochondrial electron transport chain. *Biomed J* **41**, 9-20, doi:10.1016/j.bj.2017.12.001 (2018).
- 22 Zhao, R. Z., Jiang, S., Zhang, L. & Yu, Z. B. Mitochondrial electron transport chain, ROS generation and uncoupling (Review). *Int J Mol Med* **44**, 3-15, doi:10.3892/ijmm.2019.4188 (2019).
- 23 Pinton, P., Giorgi, C., Siviero, R., Zecchini, E. & Rizzuto, R. Calcium and apoptosis: ER-mitochondria Ca²⁺ transfer in the control of apoptosis. *Oncogene* **27**, 6407-6418, doi:10.1038/onc.2008.308 (2008).
- 24 Baughman, J. M. *et al.* Integrative genomics identifies MCU as an essential component of the mitochondrial calcium uniporter. *Nature* **476**, 341-345, doi:10.1038/nature10234 (2011).
- 25 Gunter, T. E. & Pfeiffer, D. R. Mechanisms by which mitochondria transport calcium. *Am J Physiol* **258**, C755-786, doi:10.1152/ajpcell.1990.258.5.C755 (1990).
- 26 Paul, B. T., Manz, D. H., Torti, F. M. & Torti, S. V. Mitochondria and Iron: current questions. *Expert Rev Hematol* **10**, 65-79, doi:10.1080/17474086.2016.1268047 (2017).
- 27 Zorov, D. B. *et al.* The mitochondrion as janus bifrons. *Biochemistry (Mosc)* **72**, 1115-1126, doi:10.1134/s0006297907100094 (2007).
- 28 Jin, S. M. *et al.* Mitochondrial membrane potential regulates PINK1 import and proteolytic destabilization by PARL. *J Cell Biol* **191**, 933-942, doi:10.1083/jcb.201008084 (2010).
- 29 Yan, C. *et al.* PHB2 (prohibitin 2) promotes PINK1-PRKN/Parkin-dependent mitophagy by the PARL-PGAM5-PINK1 axis. *Autophagy* **16**, 419-434, doi:10.1080/15548627.2019.1628520 (2020).
- 30 Starkov, A. A. & Fiskum, G. Regulation of brain mitochondrial H₂O₂ production by membrane potential and NAD(P)H redox state. *J Neurochem* **86**, 1101-1107, doi:10.1046/j.1471-4159.2003.01908.x (2003).

- 31 Grivennikova, V. G. & Vinogradov, A. D. Generation of superoxide by the mitochondrial Complex I. *Biochim Biophys Acta* **1757**, 553-561, doi:10.1016/j.bbabi.2006.03.013 (2006).
- 32 Gottlieb, E., Armour, S. M., Harris, M. H. & Thompson, C. B. Mitochondrial membrane potential regulates matrix configuration and cytochrome c release during apoptosis. *Cell Death Differ* **10**, 709-717, doi:10.1038/sj.cdd.4401231 (2003).
- 33 Liu, Y. & Schubert, D. R. The specificity of neuroprotection by antioxidants. *J Biomed Sci* **16**, 98-98, doi:10.1186/1423-0127-16-98 (2009).
- 34 Shadel, G. S. & Horvath, T. L. Mitochondrial ROS signaling in organismal homeostasis. *Cell* **163**, 560-569, doi:10.1016/j.cell.2015.10.001 (2015).
- 35 Quinlan, C. L., Perevoshchikova, I. V., Hey-Mogensen, M., Orr, A. L. & Brand, M. D. Sites of reactive oxygen species generation by mitochondria oxidizing different substrates. *Redox Biology* **1**, 304-312, doi:<https://doi.org/10.1016/j.redox.2013.04.005> (2013).
- 36 Vinogradov, A. D. & Grivennikova, V. G. Oxidation of NADH and ROS production by respiratory complex I. *Biochimica et Biophysica Acta (BBA) - Bioenergetics* **1857**, 863-871, doi:<https://doi.org/10.1016/j.bbabi.2015.11.004> (2016).
- 37 Zorov, D. B., Juhaszova, M. & Sollott, S. J. Mitochondrial reactive oxygen species (ROS) and ROS-induced ROS release. *Physiol Rev* **94**, 909-950, doi:10.1152/physrev.00026.2013 (2014).
- 38 Islam, M. T. Oxidative stress and mitochondrial dysfunction-linked neurodegenerative disorders. *Neurol Res* **39**, 73-82, doi:10.1080/01616412.2016.1251711 (2017).
- 39 Orrenius, S., Gogvadze, V. & Zhivotovsky, B. Mitochondrial oxidative stress: implications for cell death. *Annu Rev Pharmacol Toxicol* **47**, 143-183, doi:10.1146/annurev.pharmtox.47.120505.105122 (2007).
- 40 Hamanaka, R. B. & Chandel, N. S. Mitochondrial reactive oxygen species regulate cellular signaling and dictate biological outcomes. *Trends Biochem Sci* **35**, 505-513, doi:10.1016/j.tibs.2010.04.002 (2010).
- 41 Young, M. J. & Copeland, W. C. Human mitochondrial DNA replication machinery and disease. *Curr Opin Genet Dev* **38**, 52-62, doi:10.1016/j.gde.2016.03.005 (2016).
- 42 Yasukawa, T. & Kang, D. An overview of mammalian mitochondrial DNA replication mechanisms. *J Biochem* **164**, 183-193, doi:10.1093/jb/mvy058 (2018).
- 43 Barshad, G., Marom, S., Cohen, T. & Mishmar, D. Mitochondrial DNA Transcription and Its Regulation: An Evolutionary Perspective. *Trends Genet* **34**, 682-692, doi:10.1016/j.tig.2018.05.009 (2018).
- 44 Kaneda, H. *et al.* Elimination of paternal mitochondrial DNA in intraspecific crosses during early mouse embryogenesis. *Proceedings of the National Academy of Sciences* **92**, 4542, doi:10.1073/pnas.92.10.4542 (1995).
- 45 Sutovsky, P., Navara, C. S. & Schatten, G. Fate of the Sperm Mitochondria, and the Incorporation, Conversion, and Disassembly of the Sperm Tail

- Structures during Bovine Fertilization. *Biology of Reproduction* **55**, 1195-1205, doi:10.1095/biolreprod55.6.1195 (1996).
- 46 Farge, G. & Falkenberg, M. Organization of DNA in Mammalian Mitochondria. *International journal of molecular sciences* **20**, 2770, doi:10.3390/ijms20112770 (2019).
- 47 Kukat, C. *et al.* Cross-strand binding of TFAM to a single mtDNA molecule forms the mitochondrial nucleoid. *Proceedings of the National Academy of Sciences* **112**, 11288, doi:10.1073/pnas.1512131112 (2015).
- 48 Kukat, C. & Larsson, N. G. mtDNA makes a U-turn for the mitochondrial nucleoid. *Trends Cell Biol* **23**, 457-463, doi:10.1016/j.tcb.2013.04.009 (2013).
- 49 Yakubovskaya, E., Chen, Z., Carrodeguas, J. A., Kisker, C. & Bogenhagen, D. F. Functional human mitochondrial DNA polymerase gamma forms a heterotrimer. *J Biol Chem* **281**, 374-382, doi:10.1074/jbc.M509730200 (2006).
- 50 Fan, L. *et al.* A novel processive mechanism for DNA synthesis revealed by structure, modeling and mutagenesis of the accessory subunit of human mitochondrial DNA polymerase. *J Mol Biol* **358**, 1229-1243, doi:10.1016/j.jmb.2006.02.073 (2006).
- 51 Lee, W. *et al.* Mitochondrial DNA copy number is regulated by DNA methylation and demethylation of POLGA in stem and cancer cells and their differentiated progeny. *Cell Death Dis* **6**, e1664-e1664, doi:10.1038/cddis.2015.34 (2015).
- 52 Ekstrand, M. I. *et al.* Mitochondrial transcription factor A regulates mtDNA copy number in mammals. *Human Molecular Genetics* **13**, 935-944, doi:10.1093/hmg/ddh109 (2004).
- 53 Kaguni, L. S. DNA Polymerase γ , The Mitochondrial Replicase. *Annual Review of Biochemistry* **73**, 293-320, doi:10.1146/annurev.biochem.72.121801.161455 (2004).
- 54 Ciesielski, G. L. *et al.* Mitochondrial Single-stranded DNA-binding Proteins Stimulate the Activity of DNA Polymerase γ by Organization of the Template DNA*. *Journal of Biological Chemistry* **290**, 28697-28707, doi:<https://doi.org/10.1074/jbc.M115.673707> (2015).
- 55 Kelly, R. D. W., Mahmud, A., McKenzie, M., Trounce, I. A. & St John, J. C. Mitochondrial DNA copy number is regulated in a tissue specific manner by DNA methylation of the nuclear-encoded DNA polymerase gamma A. *Nucleic acids research* **40**, 10124-10138, doi:10.1093/nar/gks770 (2012).
- 56 Williams, R. S. <1986-Mitochondrial Gene Expression in Mammalian Striated Muscle .pdf>. *journal of Biological chemistry* **261**, 12390-12349 (1986).
- 57 Tang, Y. *et al.* Rearrangements of Human Mitochondrial DNA (mtDNA): New Insights into the Regulation of mtDNA Copy Number and Gene Expression. *Molecular Biology of the Cell* **11**, 1471-1485, doi:10.1091/mbc.11.4.1471 (2000).
- 58 Clay Montier, L. L., Deng, J. J. & Bai, Y. Number matters: control of mammalian mitochondrial DNA copy number. *Journal of Genetics and Genomics* **36**, 125-131, doi:[https://doi.org/10.1016/S1673-8527\(08\)60099-5](https://doi.org/10.1016/S1673-8527(08)60099-5) (2009).

- 59 Stringer, H. A. J., Sohi, G. K., Maguire, J. A. & Côté, H. C. F. Decreased skeletal muscle mitochondrial DNA in patients with statin-induced myopathy. *Journal of the Neurological Sciences* **325**, 142-147, doi:<https://doi.org/10.1016/j.jns.2012.12.023> (2013).
- 60 Tzoulis, C. *et al.* Molecular pathogenesis of polymerase γ -related neurodegeneration. *Ann Neurol* **76**, 66-81, doi:10.1002/ana.24185 (2014).
- 61 Moraes, C. T. *et al.* mtDNA depletion with variable tissue expression: a novel genetic abnormality in mitochondrial diseases. *Am J Hum Genet* **48**, 492-501 (1991).
- 62 Chinnery, P. F. Mitochondrial Disorders overview. *GeneReviews* (2014).
- 63 Rahman, S. & Copeland, W. C. POLG-related disorders and their neurological manifestations. *Nature Reviews Neurology* **15**, 40-52, doi:10.1038/s41582-018-0101-0 (2019).
- 64 Lamantea, E. *et al.* Mutations of mitochondrial DNA polymerase gammaA are a frequent cause of autosomal dominant or recessive progressive external ophthalmoplegia. *Ann Neurol* **52**, 211-219 (2002).
- 65 Ferrari, G. *et al.* Infantile hepatocerebral syndromes associated with mutations in the mitochondrial DNA polymerase-gammaA. *Brain* **128**, 723-731, doi:10.1093/brain/awh410 (2005).
- 66 Luoma, P. *et al.* Parkinsonism, premature menopause, and mitochondrial DNA polymerase gamma mutations: clinical and molecular genetic study. *Lancet* **364**, 875-882, doi:10.1016/S0140-6736(04)16983-3 (2004).
- 67 Tzoulis, C. & Bindoff, L. A. Acute mitochondrial encephalopathy reflects neuronal energy failure irrespective of which genome the genetic defect affects. **135**, 3627-3634, doi:10.1093/brain/aws223 (2012).
- 68 Tzoulis, C. *et al.* The spectrum of clinical disease caused by the A467T and W748S POLG mutations: a study of 26 cases. *Brain* **129**, 1685-1692, doi:10.1093/brain/awl097 (2006).
- 69 Tzoulis, C. *et al.* Localized cerebral energy failure in DNA polymerase gamma-associated encephalopathy syndromes. **133**, 1428-1437, doi:10.1093/brain/awq067 (2010).
- 70 Tzoulis, C. *et al.* Severe nigrostriatal degeneration without clinical parkinsonism in patients with polymerase gamma mutations. **136**, 2393-2404, doi:10.1093/brain/awt103 (2013).
- 71 Winterthun, S. *et al.* Autosomal recessive mitochondrial ataxic syndrome due to mitochondrial polymerase gamma mutations. *Neurology* **64**, 1204-1208, doi:10.1212/01.Wnl.0000156516.77696.5a (2005).
- 72 Hikmat, O. *et al.* Simplifying the clinical classification of polymerase gamma (POLG) disease based on age of onset; studies using a cohort of 155 cases. *J Inherit Metab Dis* **43**, 726-736, doi:10.1002/jimd.12211 (2020).
- 73 Tzoulis, C.
- 74 Chan, S. S. L., Longley, M. J. & Copeland, W. C. The Common A467T Mutation in the Human Mitochondrial DNA Polymerase (POLG) Compromises Catalytic Efficiency and Interaction with the Accessory Subunit*. *Journal of Biological Chemistry* **280**, 31341-31346, doi:<https://doi.org/10.1074/jbc.M506762200> (2005).

- 75 Lee, Y.-S., Kennedy, W. D. & Yin, Y. W. Structural Insight into Processive Human Mitochondrial DNA Synthesis and Disease-Related Polymerase Mutations. *Cell* **139**, 312-324, doi:<https://doi.org/10.1016/j.cell.2009.07.050> (2009).
- 76 Chan, S. S. L., Longley, M. J. & Copeland, W. C. Modulation of the W748S mutation in DNA polymerase gamma by the E1143G polymorphism in mitochondrial disorders. *Human molecular genetics* **15**, 3473-3483, doi:10.1093/hmg/ddl424 (2006).
- 77 Luo, N. & Kaguni, L. S. Mutations in the Spacer Region of Drosophila Mitochondrial DNA Polymerase Affect DNA Binding, Processivity, and the Balance between Pol and Exo Function*. *Journal of Biological Chemistry* **280**, 2491-2497, doi:<https://doi.org/10.1074/jbc.M411447200> (2005).
- 78 Trifunovic, A. *et al.* Premature ageing in mice expressing defective mitochondrial DNA polymerase. *Nature* **429**, 417-423, doi:10.1038/nature02517 (2004).
- 79 Molè, M. A., Weberling, A. & Zernicka-Goetz, M. in *Current Topics in Developmental Biology* Vol. 136 (ed Lilianna Solnica-Krezel) 113-138 (Academic Press, 2020).
- 80 Shenghui, H., Nakada, D. & Morrison, S. J. Mechanisms of Stem Cell Self-Renewal. *Annual Review of Cell and Developmental Biology* **25**, 377-406, doi:10.1146/annurev.cellbio.042308.113248 (2009).
- 81 Czechanski, A. *et al.* Derivation and characterization of mouse embryonic stem cells from permissive and nonpermissive strains. *Nature Protocols* **9**, 559-574, doi:10.1038/nprot.2014.030 (2014).
- 82 Hipp, J. & Atala, A. Sources of stem cells for regenerative medicine. *Stem Cell Rev* **4**, 3-11, doi:10.1007/s12015-008-9010-8 (2008).
- 83 Brambrink, T., Hochedlinger, K., Bell, G. & Jaenisch, R. ES cells derived from cloned and fertilized blastocysts are transcriptionally and functionally indistinguishable. *Proc Natl Acad Sci U S A* **103**, 933, doi:10.1073/pnas.0510485103 (2006).
- 84 Yamanaka, S. Induction of Pluripotent Stem Cells from Mouse Embryonic and Adult Fibroblast Cultures by Defined Factors. *Cell* **126**, doi:<https://doi.org/10.1016/j.cell.2006.07.024> (2006).
- 85 Yamanaka, S. Induced Pluripotent Stem Cells: Past, Present, and Future. *Cell Stem Cell* **10**, 678-684, doi:10.1016/j.stem.2012.05.005 (2012).
- 86 Takahashi, K. *et al.* Induction of Pluripotent Stem Cells from Adult Human Fibroblasts by Defined Factors. *Cell* **131**, 861-872, doi:10.1016/j.cell.2007.11.019 (2007).
- 87 Yu, J. *et al.* Induced Pluripotent Stem Cell Lines Derived from Human Somatic Cells. *Science* **318**, 1917, doi:10.1126/science.1151526 (2007).
- 88 Fusaki, N., Ban, H., Nishiyama, A., Sasaki, K. & Hasegawa, M. Efficient induction of transgene-free human pluripotent stem cells using a vector based on Sendai virus, an RNA virus that does not integrate into the host genome. *Proc Jpn Acad Ser B Phys Biol Sci* **85**, 348-362, doi:10.2183/pjab.85.348 (2009).

- 89 Judson, R. L., Babiarz, J. E., Venere, M. & Blelloch, R. Embryonic stem cell-specific microRNAs promote induced pluripotency. *Nature Biotechnology* **27**, 459-461, doi:10.1038/nbt.1535 (2009).
- 90 Shi, Y. *et al.* Induction of Pluripotent Stem Cells from Mouse Embryonic Fibroblasts by Oct4 and Klf4 with Small-Molecule Compounds. *Cell Stem Cell* **3**, 568-574, doi:<https://doi.org/10.1016/j.stem.2008.10.004> (2008).
- 91 Li, W. *et al.* Identification of Oct4-activating compounds that enhance reprogramming efficiency. *Proceedings of the National Academy of Sciences* **109**, 20853, doi:10.1073/pnas.1219181110 (2012).
- 92 Li, Y. *et al.* Generation of iPSCs from mouse fibroblasts with a single gene, Oct4, and small molecules. *Cell Research* **21**, 196-204, doi:10.1038/cr.2010.142 (2011).
- 93 Huangfu, D. *et al.* Induction of pluripotent stem cells by defined factors is greatly improved by small-molecule compounds. *Nature Biotechnology* **26**, 795-797, doi:10.1038/nbt1418 (2008).
- 94 Marli Silva *et al.* Generating iPSCs: Translating Cell Reprogramming Science into Scalable and Robust Biomanufacturing Strategies. doi: <http://dx.doi.org/10.1016/j.stem.2014.12.013> (2015).
- 95 Desai, N., Rambhia, P. & Gishto, A. Human embryonic stem cell cultivation: historical perspective and evolution of xeno-free culture systems. *Reproductive Biology and Endocrinology* **13**, 9, doi:10.1186/s12958-015-0005-4 (2015).
- 96 Chen, Y.-M. *et al.* Xeno-free culture of human pluripotent stem cells on oligopeptide-grafted hydrogels with various molecular designs. *Scientific Reports* **7**, 45146, doi:10.1038/srep45146 (2017).
- 97 Chen, G. *et al.* Chemically defined conditions for human iPSC derivation and culture. *Nature methods* **8**, 424-429, doi:10.1038/nmeth.1593 (2011).
- 98 Narsinh, K. H. *et al.* Single cell transcriptional profiling reveals heterogeneity of human induced pluripotent stem cells. *The Journal of Clinical Investigation* **121**, 1217-1221, doi:10.1172/JCI44635 (2011).
- 99 Abyzov, A. *et al.* Somatic copy number mosaicism in human skin revealed by induced pluripotent stem cells. *Nature* **492**, 438-442, doi:10.1038/nature11629 (2012).
- 100 Mahmoudi, S. & Brunet, A. Aging and reprogramming: a two-way street. *Curr Opin Cell Biol* **24**, 744-756, doi:10.1016/j.ceb.2012.10.004 (2012).
- 101 Vera, E., Bosco, N. & Studer, L. Generating Late-Onset Human iPSC-Based Disease Models by Inducing Neuronal Age-Related Phenotypes through Telomerase Manipulation. *Cell Rep* **17**, 1184-1192, doi:10.1016/j.celrep.2016.09.062 (2016).
- 102 Miller, J. D. *et al.* Human iPSC-based modeling of late-onset disease via progerin-induced aging. *Cell Stem Cell* **13**, 691-705, doi:10.1016/j.stem.2013.11.006 (2013).
- 103 Studer, L., Vera, E. & Cornacchia, D. Programming and Reprogramming Cellular Age in the Era of Induced Pluripotency. *Cell Stem Cell* **16**, 591-600, doi:10.1016/j.stem.2015.05.004 (2015).
- 104 Pikó, L. & Taylor, K. D. Amounts of mitochondrial DNA and abundance of some mitochondrial gene transcripts in early mouse embryos. *Developmental*

- Biology* **123**, 364-374, doi:[https://doi.org/10.1016/0012-1606\(87\)90395-2](https://doi.org/10.1016/0012-1606(87)90395-2) (1987).
- 105 Cao, L. *et al.* The mitochondrial bottleneck occurs without reduction of mtDNA content in female mouse germ cells. *Nature Genetics* **39**, 386-390, doi:10.1038/ng1970 (2007).
- 106 Cho, Y. M. *et al.* Dynamic changes in mitochondrial biogenesis and antioxidant enzymes during the spontaneous differentiation of human embryonic stem cells. *Biochem Biophys Res Commun* **348**, 1472-1478, doi:<https://doi.org/10.1016/j.bbrc.2006.08.020> (2006).
- 107 Facucho-Oliveira, J. M., Alderson, J., Spikings, E. C., Egginton, S. & St. John, J. C. Mitochondrial DNA replication during differentiation of murine embryonic stem cells. *Journal of Cell Science* **120**, 4025-4034, doi:10.1242/jcs.016972 (2007).
- 108 Agostini, M. *et al.* Metabolic reprogramming during neuronal differentiation. *Cell Death & Differentiation* **23**, 1502-1514, doi:10.1038/cdd.2016.36 (2016).
- 109 Wanet, A. *et al.* Mitochondrial remodeling in hepatic differentiation and dedifferentiation. *The International Journal of Biochemistry & Cell Biology* **54**, 174-185, doi:<https://doi.org/10.1016/j.biocel.2014.07.015> (2014).
- 110 Lukyanenko, V., Chikando, A. & Lederer, W. J. Mitochondria in cardiomyocyte Ca²⁺ signaling. *The International Journal of Biochemistry & Cell Biology* **41**, 1957-1971, doi:<https://doi.org/10.1016/j.biocel.2009.03.011> (2009).
- 111 St. John, J. C. *et al.* The Expression of Mitochondrial DNA Transcription Factors during Early Cardiomyocyte In Vitro Differentiation from Human Embryonic Stem Cells. *Cloning and Stem Cells* **7**, 141-153, doi:10.1089/clo.2005.7.141 (2005).
- 112 Gu, W. *et al.* Glycolytic Metabolism Plays a Functional Role in Regulating Human Pluripotent Stem Cell State. *Cell Stem Cell* **19**, 476-490, doi:<https://doi.org/10.1016/j.stem.2016.08.008> (2016).
- 113 Mathieu, J. *et al.* Hypoxia-Inducible Factors Have Distinct and Stage-Specific Roles during Reprogramming of Human Cells to Pluripotency. *Cell Stem Cell* **14**, 592-605, doi:<https://doi.org/10.1016/j.stem.2014.02.012> (2014).
- 114 Chen, H.-F. *et al.* A reduced oxygen tension (5%) is not beneficial for maintaining human embryonic stem cells in the undifferentiated state with short splitting intervals. *Human Reproduction* **24**, 71-80, doi:10.1093/humrep/den345 (2009).
- 115 Prieto, J. *et al.* Early ERK1/2 activation promotes DRP1-dependent mitochondrial fission necessary for cell reprogramming. *Nature Communications* **7**, 11124, doi:10.1038/ncomms11124 (2016).
- 116 Prigione, A., Fauler, B., Lurz, R., Lehrach, H. & Adjaye, J. The Senescence-Related Mitochondrial/Oxidative Stress Pathway is Repressed in Human Induced Pluripotent Stem Cells. *STEM CELLS* **28**, 721-733, doi:<https://doi.org/10.1002/stem.404> (2010).
- 117 Folmes, C. D., Dzeja, P. P., Nelson, T. J. & Terzic, A. Metabolic plasticity in stem cell homeostasis and differentiation. *Cell Stem Cell* **11**, 596-606, doi:10.1016/j.stem.2012.10.002 (2012).

- 118 Lee, W. T. Y. & John, J. S. The control of mitochondrial DNA replication during development and tumorigenesis. *Ann N Y Acad Sci* **1350**, 95-106, doi:10.1111/nyas.12873 (2015).
- 119 Zhang, J., Nuebel, E., Daley, G. Q., Koehler, C. M. & Teitell, M. A. 589-595 (Cambridge, MA :, 2012).
- 120 Rafalski, V. A., Mancini, E. & Brunet, A. Energy metabolism and energy-sensing pathways in mammalian embryonic and adult stem cell fate. *Journal of Cell Science* **125**, 5597-5608, doi:10.1242/jcs.114827 (2012).
- 121 Varum, S. *et al.* Energy metabolism in human pluripotent stem cells and their differentiated counterparts. *PloS one* **6**, e20914-e20914, doi:10.1371/journal.pone.0020914 (2011).
- 122 Vander Heiden, M. G., Cantley, L. C. & Thompson, C. B. Understanding the Warburg effect: the metabolic requirements of cell proliferation. *Science* **324**, 1029-1033, doi:10.1126/science.1160809 (2009).
- 123 Chen, X. *et al.* Integration of External Signaling Pathways with the Core Transcriptional Network in Embryonic Stem Cells. *Cell* **133**, 1106-1117, doi:<https://doi.org/10.1016/j.cell.2008.04.043> (2008).
- 124 Moussaieff, A. *et al.* Glycolysis-Mediated Changes in Acetyl-CoA and Histone Acetylation Control the Early Differentiation of Embryonic Stem Cells. *Cell Metabolism* **21**, 392-402, doi:<https://doi.org/10.1016/j.cmet.2015.02.002> (2015).
- 125 Xinde Zheng, L. B., Mingji Jin, Jerome Mertens, Yongsung Kim, Li Ma, Li Ma, Michael Hamm, Fred H Gage. Metabolic reprogramming during neuronal differentiation from aerobic glycolysis to neuronal oxidative phosphorylation. *eLife*, doi:DOI: 10.7554/eLife.13374 (2016).
- 126 Chen, C.-T., Shih, Y.-R. V., Kuo, T. K., Lee, O. K. & Wei, Y.-H. Coordinated Changes of Mitochondrial Biogenesis and Antioxidant Enzymes During Osteogenic Differentiation of Human Mesenchymal Stem Cells. *STEM CELLS* **26**, 960-968, doi:<https://doi.org/10.1634/stemcells.2007-0509> (2008).
- 127 Ghazvini Zadegan, F. *et al.* Cardiac differentiation of mouse embryonic stem cells is influenced by a PPAR γ /PGC-1 α —FNDC5 pathway during the stage of cardiac precursor cell formation. *European Journal of Cell Biology* **94**, 257-266, doi:<https://doi.org/10.1016/j.ejcb.2015.04.002> (2015).
- 128 Spitkovsky, D. *et al.* Activity of complex III of the mitochondrial electron transport chain is essential for early heart muscle cell differentiation. *The FASEB Journal* **18**, 1300-1302, doi:<https://doi.org/10.1096/fj.03-0520fje> (2004).
- 129 Wittig, J. G. & Münsterberg, A. The Early Stages of Heart Development: Insights from Chicken Embryos. *J Cardiovasc Dev Dis* **3**, 12, doi:10.3390/jcdd3020012 (2016).
- 130 Bondue, A. & Blanpain, C. Mesp1: a key regulator of cardiovascular lineage commitment. *Circ Res* **107**, 1414-1427, doi:10.1161/circresaha.110.227058 (2010).
- 131 Saga, Y., Kitajima, S. & Miyagawa-Tomita, S. Mesp1 expression is the earliest sign of cardiovascular development. *Trends Cardiovasc Med* **10**, 345-352, doi:10.1016/s1050-1738(01)00069-x (2000).

- 132 Kouskoff, V., Lacaud, G., Schwantz, S., Fehling, H. J. & Keller, G. Sequential development of hematopoietic and cardiac mesoderm during embryonic stem cell differentiation. *Proc Natl Acad Sci U S A* **102**, 13170-13175, doi:10.1073/pnas.0501672102 (2005).
- 133 Van Vliet, P., Wu, S. M., Zaffran, S. & Puc at, M. Early cardiac development: a view from stem cells to embryos. *Cardiovascular Research* **96**, 352-362, doi:10.1093/cvr/cvs270 (2012).
- 134 Saga, Y. *et al.* MesP1 is expressed in the heart precursor cells and required for the formation of a single heart tube. *Development* **126**, 3437-3447 (1999).
- 135 Moretti, A. *et al.* Multipotent embryonic isl1+ progenitor cells lead to cardiac, smooth muscle, and endothelial cell diversification. *Cell* **127**, 1151-1165, doi:10.1016/j.cell.2006.10.029 (2006).
- 136 Moretti, A., Lam, J., Evans, S. M. & Laugwitz, K. L. Biology of Isl1+ cardiac progenitor cells in development and disease. *Cell Mol Life Sci* **64**, 674-682, doi:10.1007/s00018-007-6520-5 (2007).
- 137 Tanaka, M., Chen, Z., Bartunkova, S., Yamasaki, N. & Izumo, S. The cardiac homeobox gene Csx/Nkx2.5 lies genetically upstream of multiple genes essential for heart development. *Development* **126**, 1269-1280 (1999).
- 138 Sun, Y. *et al.* Islet 1 is expressed in distinct cardiovascular lineages, including pacemaker and coronary vascular cells. *Developmental Biology* **304**, 286-296, doi:<https://doi.org/10.1016/j.ydbio.2006.12.048> (2007).
- 139 Quaranta, R. *et al.* Revised roles of ISL1 in a hES cell-based model of human heart chamber specification. *eLife* **7**, doi:10.7554/elife.31706 (2018).
- 140 Gao, R. *et al.* Pioneering function of Isl1 in the epigenetic control of cardiomyocyte cell fate. *Cell Research*, doi:10.1038/s41422-019-0168-1 (2019).
- 141 Mommersteeg, M. T. *et al.* Pitx2c and Nkx2-5 are required for the formation and identity of the pulmonary myocardium. *Circ Res* **101**, 902-909, doi:10.1161/circresaha.107.161182 (2007).
- 142 Serpooshan, V. *et al.* Nkx2.5+ Cardiomyoblasts Contribute to Cardiomyogenesis in the Neonatal Heart. *Scientific reports* **7**, 12590-12590, doi:10.1038/s41598-017-12869-4 (2017).
- 143 Chen, J. *et al.* Nkx2.5 insufficiency leads to atrial electrical remodeling through Wnt signaling in HL-1 cells. *Exp Ther Med* **18**, 4631-4636, doi:10.3892/etm.2019.8134 (2019).
- 144 Takeuchi, J. K. & Bruneau, B. G. Directed transdifferentiation of mouse mesoderm to heart tissue by defined factors. *Nature* **459**, 708-711, doi:10.1038/nature08039 (2009).
- 145 Ahmad, F. *et al.* The role of cardiac troponin T quantity and function in cardiac development and dilated cardiomyopathy. *PLoS one* **3**, e2642-e2642, doi:10.1371/journal.pone.0002642 (2008).
- 146 England, J., Pang, K. L., Parnall, M., Haig, M. I. & Loughna, S. Cardiac troponin T is necessary for normal development in the embryonic chick heart. *J Anat* **229**, 436-449, doi:10.1111/joa.12486 (2016).

- 147 Budde, B. S. *et al.* Noncompaction of the Ventricular Myocardium Is Associated with a De Novo Mutation in the β -Myosin Heavy Chain Gene. *PLOS ONE* **2**, e1362, doi:10.1371/journal.pone.0001362 (2007).
- 148 Ching, Y.-H. *et al.* Mutation in myosin heavy chain 6 causes atrial septal defect. *Nature Genetics* **37**, 423-428, doi:10.1038/ng1526 (2005).
- 149 Rutland, C. S. *et al.* Knockdown of embryonic myosin heavy chain reveals an essential role in the morphology and function of the developing heart. *Development* **138**, 3955-3966, doi:10.1242/dev.059063 (2011).
- 150 Brien, T. X., Lee, K. J. & Chien, K. R. Positional specification of ventricular myosin light chain 2 expression in the primitive murine heart tube. *Proceedings of the National Academy of Sciences* **90**, 5157, doi:10.1073/pnas.90.11.5157 (1993).
- 151 Friedman, C. E. *et al.* Single-Cell Transcriptomic Analysis of Cardiac Differentiation from Human PSCs Reveals HOPX-Dependent Cardiomyocyte Maturation. *Cell Stem Cell* **23**, 586-598.e588, doi:10.1016/j.stem.2018.09.009 (2018).
- 152 Brand, T. Heart development: molecular insights into cardiac specification and early morphogenesis. *Developmental Biology* **258**, 1-19, doi:[https://doi.org/10.1016/S0012-1606\(03\)00112-X](https://doi.org/10.1016/S0012-1606(03)00112-X) (2003).
- 153 Lian, X. *et al.* Cozzarelli Prize Winner: Robust cardiomyocyte differentiation from human pluripotent stem cells via temporal modulation of canonical Wnt signaling. **109**, E1848-E1857, doi:10.1073/pnas.1200250109 (2012).
- 154 Naito, A. T. *et al.* Developmental stage-specific biphasic roles of Wnt/ β -catenin signaling in cardiomyogenesis and hematopoiesis. *Proc Natl Acad Sci U S A* **103**, 19812-19817, doi:10.1073/pnas.0605768103 (2006).
- 155 Lindsley, R. C. *et al.* Mesp1 coordinately regulates cardiovascular fate restriction and epithelial-mesenchymal transition in differentiating ESCs. *Cell Stem Cell* **3**, 55-68, doi:10.1016/j.stem.2008.04.004 (2008).
- 156 Chen, V. C., Stull, R., Joo, D., Cheng, X. & Keller, G. Notch signaling respecifies the hemangioblast to a cardiac fate. *Nat Biotechnol* **26**, 1169-1178, doi:10.1038/nbt.1497 (2008).
- 157 Kwon, C. *et al.* A regulatory pathway involving Notch1/ β -catenin/Isl1 determines cardiac progenitor cell fate. *Nat Cell Biol* **11**, 951-957, doi:10.1038/ncb1906 (2009).
- 158 Mohamed, I. A., El-Badri, N. & Zaher, A. Wnt Signaling: The double-edged sword diminishing the potential of stem cell therapy in congenital heart disease. *Life Sciences* **239**, 116937, doi:<https://doi.org/10.1016/j.lfs.2019.116937> (2019).
- 159 Ai, D. *et al.* Canonical Wnt signaling functions in second heart field to promote right ventricular growth. *Proc Natl Acad Sci U S A* **104**, 9319-9324, doi:10.1073/pnas.0701212104 (2007).
- 160 Kehat, I. *et al.* Human embryonic stem cells can differentiate into myocytes with structural and functional properties of cardiomyocytes. *J Clin Invest* **108**, 407-414, doi:10.1172/jci12131 (2001).

- 161 Yang, L. *et al.* Human cardiovascular progenitor cells develop from a KDR+ embryonic-stem-cell-derived population. *Nature* **453**, 524-528, doi:10.1038/nature06894 (2008).
- 162 Kattman, S. J. *et al.* Stage-specific optimization of activin/nodal and BMP signaling promotes cardiac differentiation of mouse and human pluripotent stem cell lines. *Cell Stem Cell* **8**, 228-240, doi:10.1016/j.stem.2010.12.008 (2011).
- 163 Laflamme, M. A. *et al.* Cardiomyocytes derived from human embryonic stem cells in pro-survival factors enhance function of infarcted rat hearts. *Nat Biotechnol* **25**, 1015-1024, doi:10.1038/nbt1327 (2007).
- 164 Lian, X. *et al.* Directed cardiomyocyte differentiation from human pluripotent stem cells by modulating Wnt/ β -catenin signaling under fully defined conditions. *Nature Protocols* **8**, 162-175, doi:10.1038/nprot.2012.150 (2013).
- 165 Elliott, D. A. *et al.* NKX2-5(eGFP/w) hESCs for isolation of human cardiac progenitors and cardiomyocytes. *Nat Methods* **8**, 1037-1040, doi:10.1038/nmeth.1740 (2011).
- 166 Bu, L. *et al.* Human ISL1 heart progenitors generate diverse multipotent cardiovascular cell lineages. *Nature* **460**, 113-117, doi:10.1038/nature08191 (2009).
- 167 Uosaki, H. *et al.* Efficient and scalable purification of cardiomyocytes from human embryonic and induced pluripotent stem cells by VCAM1 surface expression. *PLoS One* **6**, e23657, doi:10.1371/journal.pone.0023657 (2011).
- 168 Hattori, F. *et al.* Nongenetic method for purifying stem cell-derived cardiomyocytes. *Nat Methods* **7**, 61-66, doi:10.1038/nmeth.1403 (2010).
- 169 Karbassi, E. *et al.* Cardiomyocyte maturation: advances in knowledge and implications for regenerative medicine. *Nat Rev Cardiol* **17**, 341-359, doi:10.1038/s41569-019-0331-x (2020).
- 170 Mertens, J., Marchetto, M. C., Bardy, C. & Gage, F. H. Evaluating cell reprogramming, differentiation and conversion technologies in neuroscience. *Nat Rev Neurosci* **17**, 424-437, doi:10.1038/nrn.2016.46 (2016).
- 171 Li, L., Chao, J. & Shi, Y. Modeling neurological diseases using iPSC-derived neural cells : iPSC modeling of neurological diseases. *Cell Tissue Res* **371**, 143-151, doi:10.1007/s00441-017-2713-x (2018).
- 172 Osumi, N., Shinohara, H., Numayama-Tsuruta, K. & Maekawa, M. Concise Review: Pax6 Transcription Factor Contributes to both Embryonic and Adult Neurogenesis as a Multifunctional Regulator. *STEM CELLS* **26**, 1663-1672, doi:<https://doi.org/10.1634/stemcells.2007-0884> (2008).
- 173 Remez, L. A. *et al.* Pax6 is essential for the generation of late-born retinal neurons and for inhibition of photoreceptor-fate during late stages of retinogenesis. *Dev Biol* **432**, 140-150, doi:10.1016/j.ydbio.2017.09.030 (2017).
- 174 Nomura, T., Haba, H. & Osumi, N. Role of a transcription factor Pax6 in the developing vertebrate olfactory system. *Development, Growth & Differentiation* **49**, 683-690, doi:<https://doi.org/10.1111/j.1440-169X.2007.00965.x> (2007).

- 175 Dohrmann, C., Gruss, P. & Lemaire, L. Pax genes and the differentiation of hormone-producing endocrine cells in the pancreas. *Mech Dev* **92**, 47-54, doi:10.1016/s0925-4773(99)00324-x (2000).
- 176 Kioussi, C. *et al.* Pax6 is essential for establishing ventral-dorsal cell boundaries in pituitary gland development. *Proc Natl Acad Sci U S A* **96**, 14378-14382, doi:10.1073/pnas.96.25.14378 (1999).
- 177 Arocena, M., Rajnicek, A. M. & Collinson, J. M. Requirement of Pax6 for the integration of guidance cues in cell migration. *Royal Society Open Science* **4**, 170625, doi:10.1098/rsos.170625 (2017).
- 178 Kikkawa, T. *et al.* The role of Pax6 in brain development and its impact on pathogenesis of autism spectrum disorder. *Brain Research* **1705**, 95-103, doi:<https://doi.org/10.1016/j.brainres.2018.02.041> (2019).
- 179 Mo, Z. & Zecevic, N. Is Pax6 Critical for Neurogenesis in the Human Fetal Brain? *Cerebral Cortex* **18**, 1455-1465, doi:10.1093/cercor/bhm181 (2007).
- 180 Horvitz, H. R. & Herskowitz, I. Mechanisms of asymmetric cell division: Two Bs or not two Bs, that is the question. *Cell* **68**, 237-255, doi:[https://doi.org/10.1016/0092-8674\(92\)90468-R](https://doi.org/10.1016/0092-8674(92)90468-R) (1992).
- 181 Day, K., Shefer, G., Richardson, J. B., Enikolopov, G. & Yablonka-Reuveni, Z. Nestin-GFP reporter expression defines the quiescent state of skeletal muscle satellite cells. *Developmental Biology* **304**, 246-259, doi:<https://doi.org/10.1016/j.ydbio.2006.12.026> (2007).
- 182 Jiang, M. H. *et al.* Characterization of Nestin-positive stem Leydig cells as a potential source for the treatment of testicular Leydig cell dysfunction. *Cell research* **24**, 1466-1485, doi:10.1038/cr.2014.149 (2014).
- 183 Méndez-Ferrer, S. *et al.* Mesenchymal and haematopoietic stem cells form a unique bone marrow niche. *Nature* **466**, 829-834, doi:10.1038/nature09262 (2010).
- 184 Park, D. *et al.* Nestin is required for the proper self-renewal of neural stem cells. *Stem Cells* **28**, 2162-2171, doi:10.1002/stem.541 (2010).
- 185 Mignone, J. L., Kukekov, V., Chiang, A. S., Steindler, D. & Enikolopov, G. Neural stem and progenitor cells in nestin-GFP transgenic mice. *J Comp Neurol* **469**, 311-324, doi:10.1002/cne.10964 (2004).
- 186 Colas, J. F. & Schoenwolf, G. C. Towards a cellular and molecular understanding of neurulation. *Dev Dyn* **221**, 117-145, doi:10.1002/dvdy.1144 (2001).
- 187 Spemann & Mangold. Uber Induktion von Embryonalanlagen durch Implantation artfremder Organisatoren. (1924).
- 188 Sato, S. M. & Sargent, T. D. Development of neural inducing capacity in dissociated *Xenopus* embryos. *Dev Biol* **134**, 263-266, doi:10.1016/0012-1606(89)90096-1 (1989).
- 189 Niehrs, C. Regionally specific induction by the Spemann-Mangold organizer. *Nat Rev Genet* **5**, 425-434, doi:10.1038/nrg1347 (2004).
- 190 Dang, L. & Tropepe, V. Neural induction and neural stem cell development. *Regen Med* **1**, 635-652, doi:10.2217/17460751.1.5.635 (2006).
- 191 Bainter, J. J., Boos, A. & Kroll, K. L. Neural induction takes a transcriptional twist. *Dev Dyn* **222**, 315-327, doi:10.1002/dvdy.1210 (2001).

- 192 Kuroda, H., Fuentealba, L., Ikeda, A., Reversade, B. & De Robertis, E. M. Default neural induction: neuralization of dissociated *Xenopus* cells is mediated by Ras/MAPK activation. *Genes & development* **19**, 1022-1027, doi:10.1101/gad.1306605 (2005).
- 193 D'Aiuto, L. *et al.* Large-scale generation of human iPSC-derived neural stem cells/early neural progenitor cells and their neuronal differentiation. *Organogenesis* **10**, 365-377, doi:10.1080/15476278.2015.1011921 (2014).
- 194 Cho, M. S., Hwang, D. Y. & Kim, D. W. Efficient derivation of functional dopaminergic neurons from human embryonic stem cells on a large scale. *Nat Protoc* **3**, 1888-1894, doi:10.1038/nprot.2008.188 (2008).
- 195 Chambers, S. M. *et al.* Highly efficient neural conversion of human ES and iPSC cells by dual inhibition of SMAD signaling. *Nature biotechnology* **27**, 275-280, doi:10.1038/nbt.1529 (2009).
- 196 Chukwurah, E., Osmundsen, A., Davis, S. W. & Lizarraga, S. B. All Together Now: Modeling the Interaction of Neural With Non-neural Systems Using Organoid Models. *Frontiers in Neuroscience* **13**, doi:10.3389/fnins.2019.00582 (2019).
- 197 Siller, R. *et al.* Development of a rapid screen for the endodermal differentiation potential of human pluripotent stem cell lines. **6**, 37178, doi:10.1038/srep37178 (2016).
- 198 Siller, R., Greenhough, S., Naumovska, E. & Gareth. Small-Molecule-Driven Hepatocyte Differentiation of Human Pluripotent Stem Cells. **4**, 939-952, doi:10.1016/j.stemcr.2015.04.001 (2015).
- 199 Mathapati, S. *et al.* Small-Molecule-Directed Hepatocyte-Like Cell Differentiation of Human Pluripotent Stem Cells. *Curr Protoc Stem Cell Biol* **38**, 1g.6.1-1g.6.18, doi:10.1002/cpsc.13 (2016).
- 200 Meisner, L. F. & Johnson, J. A. Protocols for cytogenetic studies of human embryonic stem cells. *Methods* **45**, 133-141, doi:10.1016/j.ymeth.2008.03.005 (2008).
- 201 Gross, S. J. *et al.* Rapid and novel prenatal molecular assay for detecting aneuploidies and microdeletion syndromes. *Prenat Diagn* **31**, 259-266, doi:10.1002/pd.2674 (2011).
- 202 Vialard, F. *et al.* Prenatal BACs-on-Beads™ : a new technology for rapid detection of aneuploidies and microdeletions in prenatal diagnosis. *Prenat Diagn* **31**, 500-508, doi:10.1002/pd.2727 (2011).
- 203 Thomson, J. A. *et al.* Embryonic stem cell lines derived from human blastocysts. *Science* **282**, 1145-1147, doi:10.1126/science.282.5391.1145 (1998).
- 204 Ström, S., Holm, F., Bergström, R., Strömberg, A. M. & Hovatta, O. Derivation of 30 human embryonic stem cell lines--improving the quality. *In Vitro Cell Dev Biol Anim* **46**, 337-344, doi:10.1007/s11626-010-9308-0 (2010).
- 205 Stoneking, M. Hypervariable sites in the mtDNA control region are mutational hotspots. *Am J Hum Genet* **67**, 1029-1032, doi:10.1086/303092 (2000).
- 206 Vigilant, L., Stoneking, M., Harpending, H., Hawkes, K. & Wilson, A. C. African populations and the evolution of human mitochondrial DNA. *Science* **253**, 1503, doi:10.1126/science.1840702 (1991).

- 207 Holland, M. M. & Parsons, T. J. Mitochondrial DNA Sequence Analysis -
Validation and Use for Forensic Casework. *Forensic Sci Rev* **11**, 21-50 (1999).
- 208 Stacpoole, S. R. L. *et al.* Efficient derivation of NPCs, spinal motor neurons
and midbrain dopaminergic neurons from hESCs at 3% oxygen. *Nature*
protocols **6**, 1229-1240, doi:10.1038/nprot.2011.380 (2011).
- 209 Szabadkai, G. & Duchen, M. R. Mitochondria: The Hub of Cellular Ca²⁺
Signaling. *Physiology* **23**, 84-94, doi:10.1152/physiol.00046.2007 (2008).
- 210 Andrews, S. *FastQC: a quality control tool for high throughput sequence data.*
, <[https://www.bioinformatics.babraham.ac.uk/projects/fastqc/RNA-
Seq_fastqc.html](https://www.bioinformatics.babraham.ac.uk/projects/fastqc/RNA-Seq_fastqc.html)> (2010).
- 211 Patro, R., Duggal, G., Love, M. I., Irizarry, R. A. & Kingsford, C. Salmon
provides fast and bias-aware quantification of transcript expression. *Nature*
Methods **14**, 417-419, doi:10.1038/nmeth.4197 (2017).
- 212 Sonesson, C., Love, M. I. & Robinson, M. D. Differential analyses for RNA-seq:
transcript-level estimates improve gene-level inferences. *F1000Res* **4**, 1521,
doi:10.12688/f1000research.7563.2 (2015).
- 213 Love, M. I., Huber, W. & Anders, S. Moderated estimation of fold change and
dispersion for RNA-seq data with DESeq2. *Genome Biology* **15**, 550,
doi:10.1186/s13059-014-0550-8 (2014).
- 214 Ashburner, M. *et al.* Gene ontology: tool for the unification of biology. The
Gene Ontology Consortium. *Nat Genet* **25**, 25-29, doi:10.1038/75556 (2000).
- 215 Kanehisa, M. & Goto, S. KEGG: kyoto encyclopedia of genes and genomes.
Nucleic Acids Res **28**, 27-30, doi:10.1093/nar/28.1.27 (2000).
- 216 Calvo, S. E., Clauser, K. R. & Mootha, V. K. MitoCarta2.0: an updated
inventory of mammalian mitochondrial proteins. *Nucleic Acids Res* **44**, D1251-
1257, doi:10.1093/nar/gkv1003 (2016).
- 217 Gaare, J. J. *et al.* Rare genetic variation in mitochondrial pathways influences
the risk for Parkinson's disease. *Mov Disord* **33**, 1591-1600,
doi:10.1002/mds.64 (2018).
- 218 Chumarina, M. *et al.* Cellular alterations identified in pluripotent stem cell-
derived midbrain spheroids generated from a female patient with progressive
external ophthalmoplegia and parkinsonism who carries a novel variation
(p.Q811R) in the POLG1 gene. *Acta Neuropathol Commun* **7**, 208,
doi:10.1186/s40478-019-0863-7 (2019).
- 219 Li, S. *et al.* Valproic acid-induced hepatotoxicity in Alpers syndrome is
associated with mitochondrial permeability transition pore opening-dependent
apoptotic sensitivity in an induced pluripotent stem cell model. *Hepatology* **61**,
1730-1739, doi:10.1002/hep.27712 (2015).
- 220 Zurita, F. *et al.* Generation of a human iPSC line from a patient with a defect of
intergenomic communication. *Stem Cell Res* **16**, 120-123,
doi:10.1016/j.scr.2015.12.016 (2016).
- 221 Ma, H. *et al.* Metabolic rescue in pluripotent cells from patients with mtDNA
disease. *Nature* **524**, 234-238, doi:10.1038/nature14546 (2015).
- 222 Lorenz, C. *et al.* Human iPSC-Derived Neural Progenitors Are an Effective
Drug Discovery Model for Neurological mtDNA Disorders. *Cell Stem Cell* **20**,
659-674.e659, doi:10.1016/j.stem.2016.12.013 (2017).

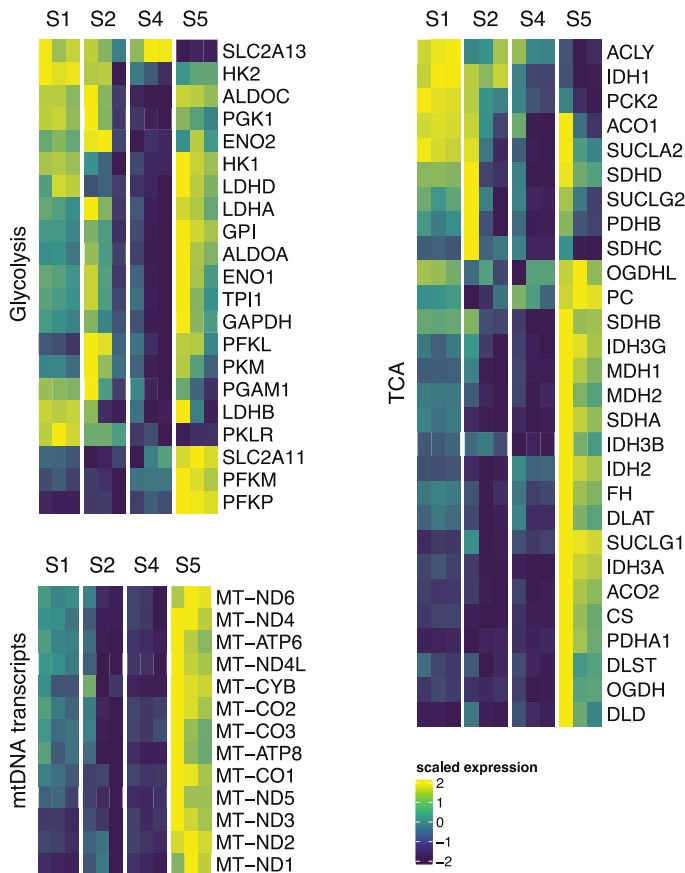
- 223 Abramov, A. Y. *et al.* Mechanism of neurodegeneration of neurons with mitochondrial DNA mutations. *Brain* **133**, 797-807, doi:10.1093/brain/awq015 (2010).
- 224 Forkink, M. *et al.* Mitochondrial hyperpolarization during chronic complex I inhibition is sustained by low activity of complex II, III, IV and V. *Biochim Biophys Acta* **1837**, 1247-1256, doi:10.1016/j.bbabi.2014.04.008 (2014).
- 225 Schapira, A. H. *et al.* Mitochondrial complex I deficiency in Parkinson's disease. *Lancet* **1**, 1269, doi:10.1016/s0140-6736(89)92366-0 (1989).
- 226 Flønes, I. H. *et al.* Neuronal complex I deficiency occurs throughout the Parkinson's disease brain, but is not associated with neurodegeneration or mitochondrial DNA damage. *Acta Neuropathol* **135**, 409-425, doi:10.1007/s00401-017-1794-7 (2018).
- 227 Palin, E. J., Paetau, A. & Suomalainen, A. Mesencephalic complex I deficiency does not correlate with parkinsonism in mitochondrial DNA maintenance disorders. *Brain* **136**, 2379-2392, doi:10.1093/brain/awt160 (2013).
- 228 Schapira, A. H. Mitochondria in the aetiology and pathogenesis of Parkinson's disease. *Lancet Neurol* **7**, 97-109, doi:10.1016/s1474-4422(07)70327-7 (2008).
- 229 Leuner, K. *et al.* Mitochondrion-derived reactive oxygen species lead to enhanced amyloid beta formation. *Antioxid Redox Signal* **16**, 1421-1433, doi:10.1089/ars.2011.4173 (2012).
- 230 Fang, E. F. *et al.* Mitophagy inhibits amyloid- β and tau pathology and reverses cognitive deficits in models of Alzheimer's disease. *Nat Neurosci* **22**, 401-412, doi:10.1038/s41593-018-0332-9 (2019).
- 231 Johnson, S. & Imai, S.-I. NAD (+) biosynthesis, aging, and disease. *F1000Research* **7**, 132-132, doi:10.12688/f1000research.12120.1 (2018).
- 232 Nishio, K. & Ma, Q. Effect of Overproduction of Mitochondrial Uncoupling Protein 2 on Cos7 Cells: Induction of Senescent-like Morphology and Oncotic Cell Death. *Curr Aging Sci* **9**, 229-238, doi:10.2174/1874609809666160211125332 (2016).
- 233 Bordone, L. *et al.* Sirt1 regulates insulin secretion by repressing UCP2 in pancreatic beta cells. *PLoS Biol* **4**, e31, doi:10.1371/journal.pbio.0040031 (2006).
- 234 Ryan, B. J., Hoek, S., Fon, E. A. & Wade-Martins, R. Mitochondrial dysfunction and mitophagy in Parkinson's: from familial to sporadic disease. *Trends Biochem Sci* **40**, 200-210, doi:10.1016/j.tibs.2015.02.003 (2015).
- 235 Khalil, B. *et al.* PINK1-induced mitophagy promotes neuroprotection in Huntington's disease. *Cell Death Dis* **6**, e1617, doi:10.1038/cddis.2014.581 (2015).
- 236 Zwartsen, A. *et al.* Cardiotoxicity screening of illicit drugs and new psychoactive substances (NPS) in human iPSC-derived cardiomyocytes using microelectrode array (MEA) recordings. *Journal of Molecular and Cellular Cardiology*, doi:10.1016/j.yjmcc.2019.09.007 (2019).
- 237 McPheeters, M. T., Wang, Y. T., Werdich, A. A., Jenkins, M. W. & Laurita, K. R. An infrared optical pacing system for screening cardiac electrophysiology in human cardiomyocytes. *PLOS ONE* **12**, e0183761, doi:10.1371/journal.pone.0183761 (2017).

- 238 Dubois, N. C. *et al.* SIRPA is a specific cell-surface marker for isolating cardiomyocytes derived from human pluripotent stem cells. *Nature Biotechnology* **29**, 1011-1018, doi:10.1038/nbt.2005 (2011).
- 239 Hattori, F. *et al.* Nongenetic method for purifying stem cell-derived cardiomyocytes. *Nature methods* **7**, 61-66, doi:10.1038/nmeth.1403 (2010).
- 240 BurrIDGE, P. W. *et al.* Chemically defined generation of human cardiomyocytes. *Nature methods* **11**, 855-860, doi:10.1038/nmeth.2999 (2014).
- 241 Sturzu, A. C. & Wu, S. M. Developmental and Regenerative Biology of Multipotent Cardiovascular Progenitor Cells. *Circulation Research* **108**, 353-364, doi:10.1161/circresaha.110.227066 (2011).
- 242 Sepac, A. *et al.* Comparison of Cardiomyogenic Potential among Human ESC and iPSC Lines. *Cell Transplantation* **21**, 2523-2530, doi:10.3727/096368912X653165 (2012).
- 243 Locasale, J. W. & Cantley, L. C. Metabolic flux and the regulation of mammalian cell growth. *Cell Metab* **14**, 443-451, doi:10.1016/j.cmet.2011.07.014 (2011).
- 244 Sercel, A. J., Carlson, N. M., Patananan, A. N. & Teitell, M. A. Mitochondrial DNA Dynamics in Reprogramming to Pluripotency. *Trends Cell Biol* **31**, 311-323, doi:10.1016/j.tcb.2020.12.009 (2021).
- 245 Belmonte, S. & Morad, M. Shear Fluid-induced Ca²⁺ Release and the Role of Mitochondria in Rat Cardiac Myocytes. *Ann N Y Acad Sci* **1123**, 58-63, doi:10.1196/annals.1420.007 (2008).
- 246 Cliff, T. S. *et al.* MYC Controls Human Pluripotent Stem Cell Fate Decisions through Regulation of Metabolic Flux. *Cell Stem Cell* **21**, 502-516.e509, doi:10.1016/j.stem.2017.08.018 (2017).
- 247 Lees, J. G., Gardner, D. K. & Harvey, A. J. Mitochondrial and glycolytic remodeling during nascent neural differentiation of human pluripotent stem cells. *Development* **145**, dev168997, doi:10.1242/dev.168997 (2018).
- 248 Birket, M. J. *et al.* A reduction in ATP demand and mitochondrial activity with neural differentiation of human embryonic stem cells. *Journal of Cell Science* **124**, 348, doi:10.1242/jcs.072272 (2011).
- 249 Zheng, X. *et al.* Metabolic reprogramming during neuronal differentiation from aerobic glycolysis to neuronal oxidative phosphorylation. *Elife* **5**, doi:10.7554/eLife.13374 (2016).
- 250 Malinska, D., Kudin, A. P., Bejtka, M. & Kunz, W. S. Changes in mitochondrial reactive oxygen species synthesis during differentiation of skeletal muscle cells. *Mitochondrion* **12**, 144-148, doi:<https://doi.org/10.1016/j.mito.2011.06.015> (2012).
- 251 Larsson, N.-G., Oldfors, A., Holme, E. & Clayton, D. A. Low levels of mitochondrial transcription factor A in mitochondrial DNA depletion. *Biochemical and biophysical research communications* **200**, 1374-1381 (1994).
- 252 Larsson, N.-G. *et al.* Mitochondrial transcription factor A is necessary for mtDNA maintenance and embryogenesis in mice. *Nature genetics* **18**, 231-236 (1998).

- 253 Kaufman, B. A. *et al.* The mitochondrial transcription factor TFAM coordinates the assembly of multiple DNA molecules into nucleoid-like structures. *Molecular biology of the cell* **18**, 3225-3236 (2007).
- 254 Kukat, C. & Larsson, N.-G. mtDNA makes a U-turn for the mitochondrial nucleoid. *Trends in cell biology* **23**, 457-463 (2013).
- 255 de Almeida, M. J., Luchsinger, L. L., Corrigan, D. J., Williams, L. J. & Snoeck, H.-W. Dye-Independent Methods Reveal Elevated Mitochondrial Mass in Hematopoietic Stem Cells. *Cell Stem Cell* **21**, 725-729.e724, doi:<https://doi.org/10.1016/j.stem.2017.11.002> (2017).
- 256 Perry, S. W., Norman, J. P., Barbieri, J., Brown, E. B. & Gelbard, H. A. Mitochondrial membrane potential probes and the proton gradient: a practical usage guide. *Biotechniques* **50**, 98 (2011).
- 257 Hom, J. R. *et al.* The permeability transition pore controls cardiac mitochondrial maturation and myocyte differentiation. *Developmental cell* **21**, 469-478 (2011).
- 258 Dai, D.-F., Danoviz, M. E., Wiczer, B., Laflamme, M. A. & Tian, R. Mitochondrial Maturation in Human Pluripotent Stem Cell Derived Cardiomyocytes. *Stem Cells International* **2017** (2017).
- 259 Teixeira, F. K. *et al.* ATP synthase promotes germ cell differentiation independent of oxidative phosphorylation. *Nature cell biology* **17**, 689-696 (2015).

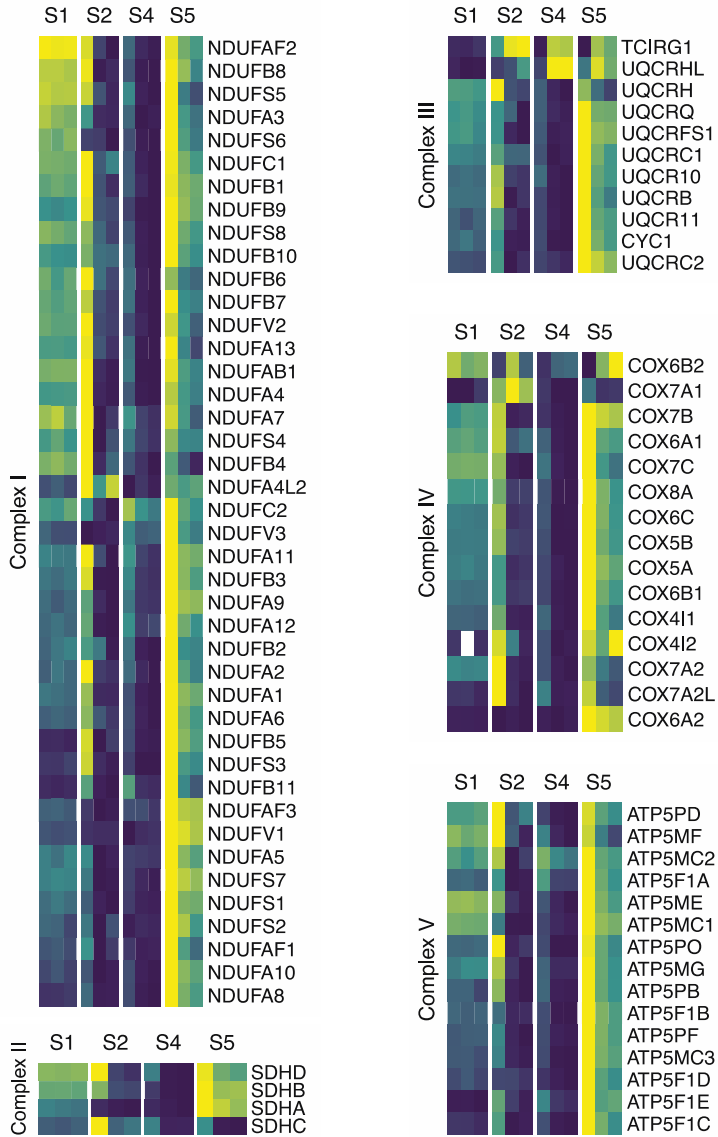
7. Appendix Figures

Appendix Figure 1.



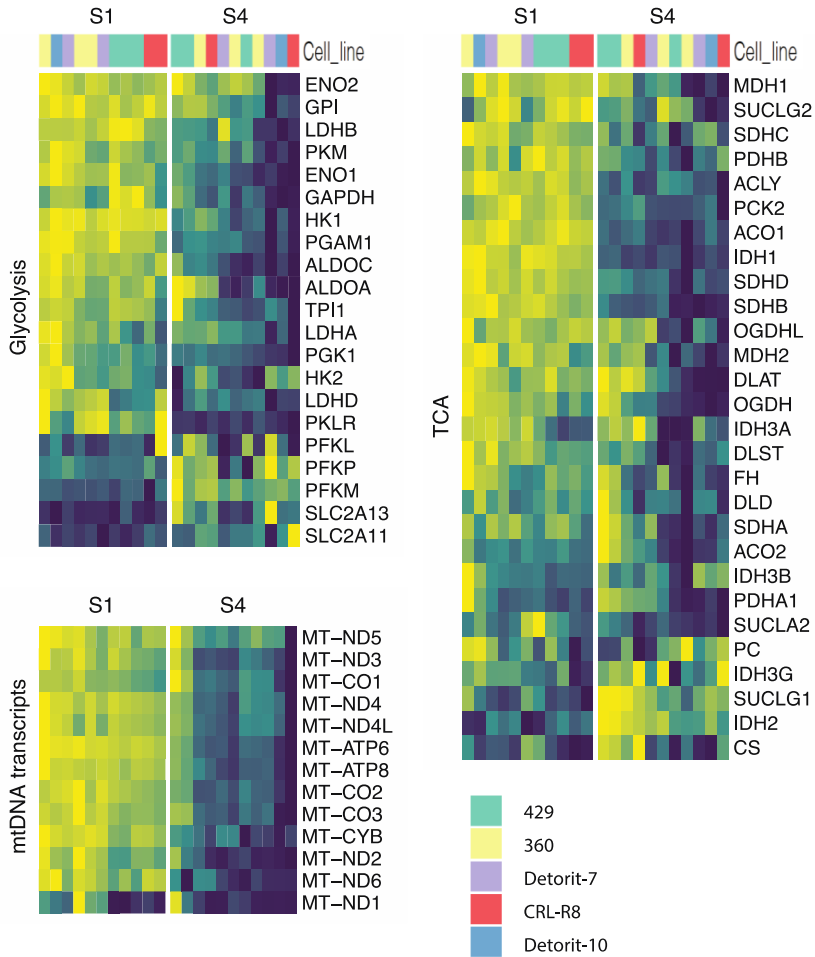
Appendix Figure 1. Scaled expression levels of genes involved in glycolysis, TCA cycle and mitochondrial transcripts at different stages of H1 differentiation towards functional cardiomyocytes (S1-S5; Dataset B).

Appendix Figure 2.



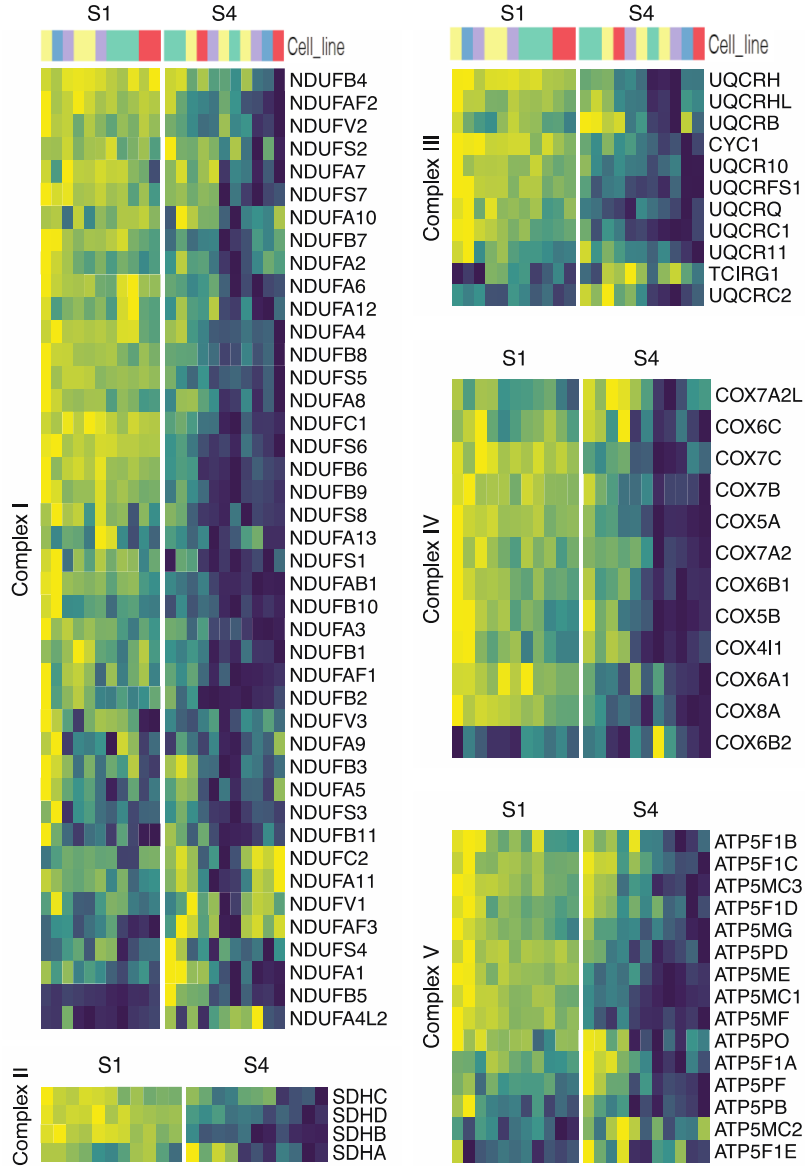
Appendix Figure 2. Scaled expression levels of genes encoding ETC complexes during differentiation of H1 to committed cardiomyocyte (S1-S5; Dataset B).

Appendix Figure 3.



Appendix Figure 3. Scaled expression levels of genes involved in glycolysis, TCA cycle and mitochondrial transcripts during differentiation of PSCs to cardiac progenitors (S1,S4; Dataset A).






Appendix Figure 4.



Appendix Figure 4. Scaled expression levels of genes encoding the ECT complexes during differentiation of PSCs to cardiac progenitors (S1, S4; Dataset A).



Disease-specific phenotypes in iPSC-derived neural stem cells with *POLG* mutations

Kristina Xiao Liang^{1,2,†,*} , Cecilie Katrin Kristiansen^{2,†}, Sepideh Mostafavi², Guro Helén Vatne², Gina Alien Zantingh³, Atefeh Kianian², Charalampos Tzoulis^{1,2}, Lena Elise Høyland⁴, Mathias Ziegler⁴ , Roberto Megias Perez⁴ , Jessica Furriol^{2,5}, Zhuoyuan Zhang^{6,7}, Novin Balafkan², Yu Hong^{1,2}, Richard Siller^{8,9}, Gareth John Sullivan^{8,9,10,11,12}  & Laurence A Bindoff^{1,2,**} 

Abstract

Mutations in *POLG* disrupt mtDNA replication and cause devastating diseases often with neurological phenotypes. Defining disease mechanisms has been hampered by limited access to human tissues, particularly neurons. Using patient cells carrying *POLG* mutations, we generated iPSCs and then neural stem cells. These neural precursors manifested a phenotype that faithfully replicated the molecular and biochemical changes found in patient post-mortem brain tissue. We confirmed the same loss of mtDNA and complex I in dopaminergic neurons generated from the same stem cells. *POLG*-driven mitochondrial dysfunction led to neuronal ROS overproduction and increased cellular senescence. Loss of complex I was associated with disturbed NAD⁺ metabolism with increased UCP2 expression and reduced phosphorylated Sirt1. In cells with compound heterozygous *POLG* mutations, we also found activated mitophagy via the BNIP3 pathway. Our studies are the first that show it is possible to recapitulate the neuronal molecular and biochemical defects associated with *POLG* mutation in a human stem cell model. Further, our data provide insight into how mitochondrial dysfunction and mtDNA alterations influence cellular fate determining processes.

Keywords mitochondria; mitophagy; neural stem cells; *POLG*; reactive oxygen species

Subject Categories Genetics, Gene Therapy & Genetic Disease; Neuroscience; Stem Cells & Regenerative Medicine

DOI 10.15252/emmm.202012146 | Received 12 February 2020 | Revised 30 July 2020 | Accepted 31 July 2020 | Published online 25 August 2020

EMBO Mol Med (2020) 12: e12146

Introduction

Mitochondria are membrane enclosed, intracellular organelles involved in multiple cellular functions, but best known for generating adenosine triphosphate (ATP). Mitochondria are the only organelles besides the nucleus that possess their own DNA (mitochondrial DNA; mtDNA) and their own machinery for synthesizing RNA and proteins. DNA polymerase gamma, Poly, is a heterotrimeric protein that catalyzes the replication and repair of the mitochondrial genome. The holoenzyme is a heterotrimer composed of one catalytic subunit (*POLG*) with the size of 122 kDa, encoded by the *POLG* gene, and a dimer of two accessory subunits (*POLG2*) of 55 kDa encoded by *POLG2*.

Mutations in *POLG* cause a wide variety of diseases that vary in age of onset and severity. More than 200 disease-causing mutations are known, and these cause diverse phenotypes including devastating early onset encephalopathy syndromes such as Alpers' syndrome (Naviaux & Nguyen, 2004; Ferrari *et al.*, 2005) or severe adult onset disorders with progressive spinocerebellar ataxia and epilepsy (Van Goethem *et al.*, 2004; Hakonen *et al.*, 2005; Winterthun *et al.*, 2005). Other phenotypes include progressive external ophthalmoplegia (PEO) (Lamantea *et al.*, 2002) and parkinsonism (Luoma *et al.*, 2004). Mitochondrial dysfunction is also

1 Neuro-SysMed, Center of Excellence for Clinical Research in Neurological Diseases, Haukeland University Hospital, Bergen, Norway

2 Department of Clinical Medicine, University of Bergen, Bergen, Norway

3 Leiden University Medical Centre, Leiden University, Leiden, The Netherlands

4 Department of Biomedicine, University of Bergen, Bergen, Norway

5 Department of Medicine, Haukeland University Hospital, Bergen, Norway

6 State Key Laboratory of Oral Diseases, West China School of Stomatology, Sichuan University, Chengdu, China

7 Department of Head and Neck Cancer Surgery, West China School of Stomatology, Sichuan University, Chengdu, China

8 Department of Molecular Medicine, Institute of Basic Medical Sciences, University of Oslo, Oslo, Norway

9 Norwegian Center for Stem Cell Research, Oslo University Hospital and University of Oslo, Oslo, Norway

10 Institute of Immunology, Oslo University Hospital, Oslo, Norway

11 Hybrid Technology Hub - Centre of Excellence, Institute of Basic Medical Sciences, University of Oslo, Oslo, Norway

12 Department of Pediatric Research, Oslo University Hospital, Oslo, Norway

*Corresponding author. Tel: +47 55 97 50 96; E-mail: Xiao.Liang@uib.no

**Corresponding author. Tel: +47 55 97 57 04; E-mail: Laurence.Bindoff@uib.no

[†]These authors contributed equally to this work

implicated in the pathophysiology of common forms of neurodegeneration, such as Parkinson's disease. Studying the effect of *POLG* mutation on mitochondrial function and cellular homeostasis is, therefore, relevant to a wide spectrum of diseases.

Our previous studies using post-mortem human brain revealed that while *POLG*-related disease caused widespread damage in the brain, dopaminergic neurons of the substantia nigra were particularly affected (Tzoulis *et al*, 2014). In addition to progressive loss, nigral neurons also showed an age-related progressive accumulation of mtDNA deletions and point mutations (Tzoulis *et al*, 2014). While informative, post-mortem studies often represent the end stage of disease and are not tractable. The need for models to study disease mechanisms is, therefore, clear, and since mouse models often fail to recapitulate the human neural phenotype, we chose to examine the potential of induced pluripotent stem cells (iPSCs). iPSCs retain the potential to differentiate into any cell type and, while still at an early developmental stage, carry the disease mutation and the patients' own genetic background, giving us the possibility to study disease during tissue development (Marchetto *et al*, 2011).

Primary neural stem cells (NSCs) provide a continued source of neurons and glial cells in the brain that further serve as a foundation for development, repair, and functional modulations of human adult neurogenesis. It is not surprising, therefore, that dysfunction of neural precursor cells contributes to an assortment of neurological disorders (Li *et al*, 2018). While primary NSCs derived from patients have the ability to circumvent immune rejection, they are hard to acquire and display a limited expansion and engraftment capacity. A solution to this problem is the neural induction of iPSCs to NSCs, either through an intermediate rosette-like stage or directly by application of a cocktail of small molecules (Lorenz *et al*, 2017). Since iPSC-derived NSCs are relatively straightforward to generate, they provide an alternative to primary NSCs for disease-relevant phenotype studies and drug development (Griffin *et al*, 2015; Lorenz *et al*, 2017; Li *et al*, 2018). Others have also suggested that NSC models might provide new insights into mtDNA disorders (Kim *et al*, 2013).

Mitochondria conserve the energy generated by substrate oxidation and use this to generate a membrane potential. The proton electrochemical gradient, termed the mitochondrial membrane potential (MMP), provides the energy that drives ATP synthesis. The MMP also regulates mitochondrial calcium sequestration, import of proteins into the mitochondrion and mitochondrial membrane dynamics. Mitochondria are the major producer of superoxide and other downstream reactive oxygen species (ROS) in the cell (Bae *et al*, 2011), with the main sites of mitochondrially derived superoxide being complexes I and III (Brand, 2016). Mitochondrially generated ROS can mediate redox signaling or, in excess, affect replication and transcription of mtDNA and result in a decline in mitochondrial function, which in turn, can further enhance ROS production (Cui *et al*, 2012).

Accumulating evidence demonstrates that ROS plays a critical role in induction and maintenance of cellular senescence (Davalli *et al*, 2016; Zheng *et al*, 2018). This state of stable cell cycle arrest, in which proliferating cells become resistant to growth-promoting stimuli, typically occurs in response to DNA damage. Cellular senescence also appears to cause mitochondrial dysfunction including loss of membrane potential, decreased respiratory coupling, and

increased ROS production, and these changes were associated with altered mitophagy (Korolchuk *et al*, 2017). Mitophagy is the autophagic pathway involved in mitochondrial quality control that removes damaged mitochondria and regulates mitochondrial number to match metabolic demand. In mammals, more than 20 proteins have been associated with this process, including PTEN-induced kinase 1 (PINK1), parkin, serine/threonine-protein kinase ULK1 (ULK1), BCL2/adenovirus E1B 19 kDa protein-interacting protein 3-like (BNIP3L/NIX), and serine/threonine-protein kinase TBK1 (TBK1) (Kerr *et al*, 2017). Alterations in mitophagy have been linked to neurodegenerative diseases such as Alzheimer's disease (AD) (Fang *et al*, 2019). Mitophagy also plays a vital role in neuronal function and survival by maintaining a healthy mitochondrial pool and inhibiting neuronal death (Fang *et al*, 2019). The role of mitophagy in mitochondrial disease such as those caused by *POLG* mutation remains, however, unclear.

In the present study, we generated an experimental model for *POLG*-related brain disease using iPSCs reprogrammed from patient fibroblasts that were differentiated to NSCs. NSCs showed defective ATP production and increased oxidative stress reflected by elevated levels of intracellular and mitochondrial ROS. In addition, we found depletion of mtDNA and loss of mitochondrial respiratory chain complex I, findings that precisely recapitulate those from post-mortem tissue studies. Further mechanistic studies showed that these neural cells had disturbed NAD⁺ metabolism-mediated UCP2/Sirt1 and increased cellular senescence and BNIP3-mediated mitophagy, which may contribute to pathological mechanisms involved in this form of mitochondrial neurodegeneration.

Results

Generating iPSCs from patient cells carrying *POLG* mutations

We generated iPSCs from parental fibroblasts from two patients carrying *POLG* mutations, one homozygous for c.2243G>C; p.W748S (WS5A) and one compound heterozygous c.1399G>A/c.2243G>C; p.A467T/W748S (CP2A). The clinical symptoms of both patients included ataxia, peripheral neuropathy, stroke-like episodes, and PEO (Tzoulis *et al*, 2006, 2014). Fibroblast lines Detroit 551, CCD-1079Sk and AG05836 were reprogrammed as disease-free controls, and two different human embryonic stem cells, H1 (ESC1) and line 360 (ESC2), were used as internal controls for iPSC generation and characterization.

All fibroblasts were reprogrammed into iPSCs using a retroviral or Sendai virus system. Four retrovirus viral particles including *hOCT4*, *hSOX2*, *hKLF4*, and *hCMYC* were transduced at an MOI of 5 according to a previously described report (Siller *et al*, 2016). In order to account for clonal variation arising during iPSC reprogramming, 2–4 clones from each iPSC line were selected and used for further investigation (Appendix Table S1).

The Detroit 551 control and patient fibroblast (WS5A, CP2A) derived iPSCs displayed typical ESC morphology with well-defined sharp edges and contained tightly packed cells (Fig 1A). No obvious different appearance was noticed in patient WS5A and CP2A iPSCs compared to iPSCs generated from Detroit 551 control (Fig 1A). In order to confirm normal karyotypes for all the reprogrammed iPSC

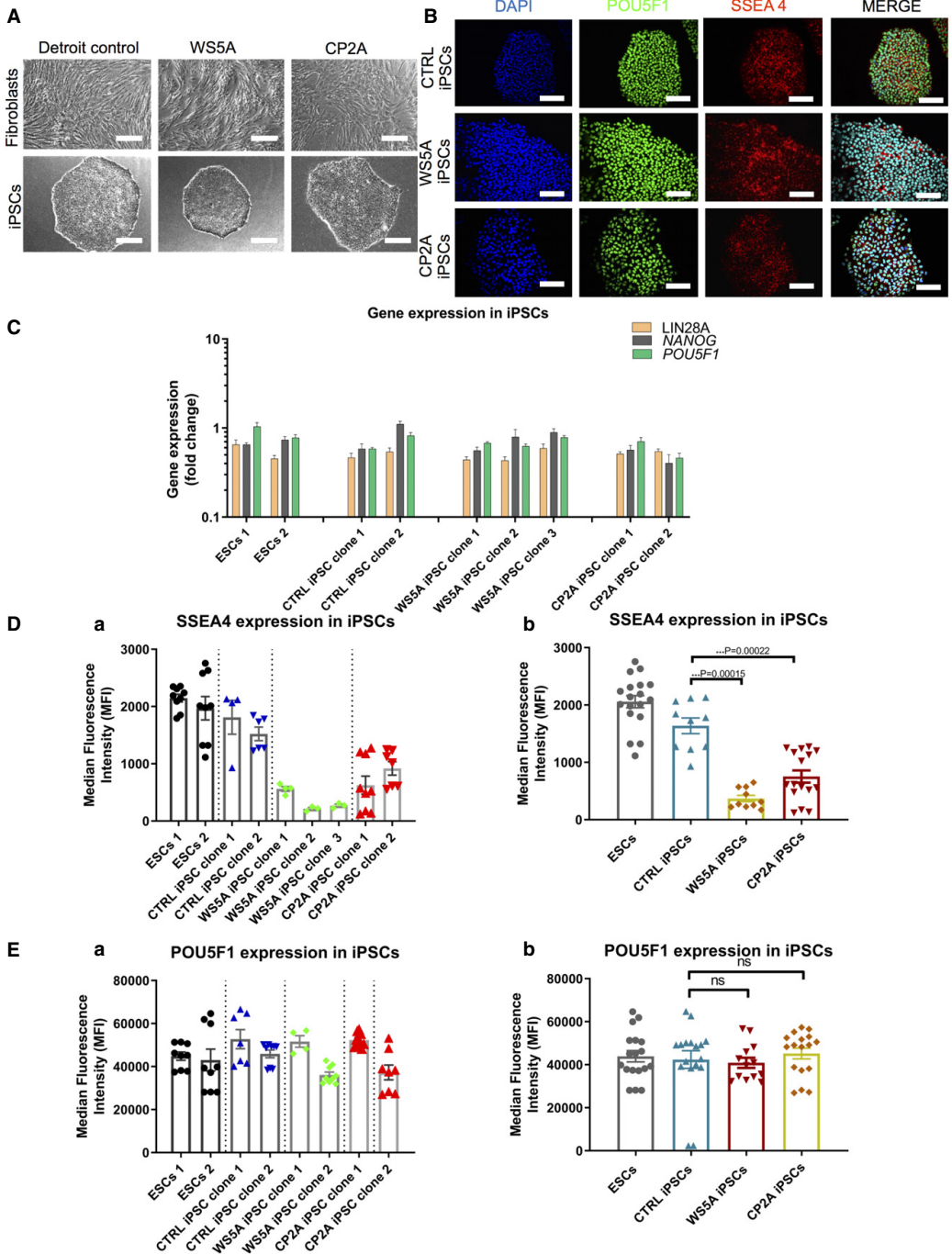


Figure 2.

Figure 1. iPSCs generated from patient fibroblasts carrying homozygous and heterozygous *POLG* mutations.

- A Morphology on phase contrast microscopy for parental fibroblast lines (upper panel) and iPSCs (lower panel) from Detroit 551 control, WS5A, and CP2A *POLG* patients (scale bars, 50 μ m).
- B Immunofluorescence staining of stem cell markers POU5F1 (green) and SSEA4 (red): upper panel—Detroit 551 control iPSCs, middle panel—WS5A iPSCs, and lower panel—CP2A iPSCs (Scale bar, 100 μ m). Nuclei are stained with DAPI (blue).
- C RT-qPCR quantification of gene expression for *LIN28A*, *NANOG*, and *POU5F1* for all iPSCs from Detroit 551 control, WS5A, and CP2A *POLG* patients ($n = 7$, technical replicates per line for ESCs; $n = 4$, technical replicates per clone for control, WS5A, and CP2A iPSCs). The gene expression of the individual clones is assessed with fold change using the comparative $\Delta\Delta C_t$ method by normalizing iPSCs to ESC1.
- D, E Flow cytometric quantification of expression level of SSEA4 (D, $n = 9$, technical replicates per line for ESCs; $n = 5$, technical replicates per clone for control iPSCs; $n = 3$, technical replicates per clone for WS5A iPSCs, $n = 8$, technical replicates per clone for CP2A iPSCs) and POU5F1 (E, $n = 9$, technical replicates per line for ESCs; $n = 5$, technical replicates per clone for control iPSCs; $n = 3$, technical replicates per clone for WS5A iPSCs, $n = 8$, technical replicates per clone for CP2A iPSCs) for ESCs and iPSCs for both ESC control lines and iPSCs generated from Detroit 551 control, WS5A and CP2A fibroblasts.
- Data information: The data presented in C–E were generated from 2 distinct ESC lines, 2 iPSC clones from Detroit 551 control, 3 different clones from WS5A patient, and 2 different clones from CP2A patient iPSCs. Data in D and E are presented as individual (a) and combination as a group (b). Data are presented as mean \pm SEM for the number of samples. Mann–Whitney *U*-test was used for the data presented. Significance is denoted for *P* values of less than 0.05. *****P* < 0.001. Source data are available online for this figure.

lines, G banding analysis was used. We showed that all iPSC lines presented with the same karyotype as their parental human fibroblasts after reprogramming, with no evidence of chromosomal abnormalities (Fig EV1).

Next, we characterized the reprogrammed iPSCs for their pluripotency using immunostaining and flow cytometry for protein expression and RT-qPCR analysis for gene expression. Immunostaining confirmed that all the iPSCs expressed the specific pluripotent markers POU5F1 and SSEA4 (Fig 1B). RT-qPCR analysis showed similar mRNA expression levels in terms of *LIN28A*, *POU5F1*, and *NANOG* in iPSC clones from Detroit 551 control, WS5A, CP2A, and ESC lines (Fig 1C). In addition, we measured expression of pluripotent transcription factors POU5F1, *NANOG* and pluripotent surface markers SSEA4, TRA-1-60, and TRA-1-81 and quantified these using flow cytometric analysis. Using this technique, we observed that both the ESC and iPSC lines exhibited over 98% of POU5F1-positive cells and over 88% of the cells showed positive staining for SSEA4 (Appendix Fig S1). Interestingly, we detected a lower level of the three pluripotent surface markers SSEA4 (Fig 1D(a and b)), TRA-1-60 (Fig EV2A(a and b)), and TRA-1-81 (Fig EV2B(a and b)) in both WS5A and CP2A iPSCs compared to the two ESC lines and control iPSC line. However, no changes were observed in the expression of POU5F1 (Fig 1E(a and b)). We observed a higher expression of *NANOG* in WS5A compared to control but not in CP2A lines (Fig EV2C(a and b)). In addition, clonal variations for the protein level and mRNA expression were noticed (Figs 1C and D(a), E(a) and EV2A(a), B(a), C(a)). In order to minimize the phenotypic diversity caused by intracolon heterogeneity, multiple clones were included in the further analysis.

Next, we demonstrated that the iPSCs we generated retained the potential to differentiate into cell types associated with all three germ layers. We generated hepatocytes (endoderm) with positive expression of albumin and HNF4A (Fig 2A(a)), cardiomyocytes (mesoderm) with positive expression of TNNT2 (Fig 2A(b)) and neurons (ectoderm), specifically dopaminergic neuronal cells with positive expression of Tyrosine hydroxylase (TH) and MAP2 (Fig 2A(c)).

These data confirm that it is possible to generate patient-specific iPSCs with *POLG* mutations by reprogramming of patient fibroblasts.

***POLG* iPSCs manifest a partial phenotype**

Next, we asked whether iPSCs generated from *POLG* patients showed changes in mitochondrial structure or function. Since clonal variations were detected between ESCs and other iPSC lines during neuronal differentiation, we compared three homozygous WS5A iPSC clones and two heterozygous CP2A iPSC clones to four clones from two different control iPSC lines to investigate mitochondrial morphology, MMP, and intracellular ATP production. In addition, we quantified the mtDNA using two approaches (i) indirectly using flow cytometry and (ii) PCR quantification. ESCs were excluded for the investigation of the disease-related phenotypes due to the difference between ESC and other iPSCs lines.

Mitochondrial morphology was analyzed by fluorescence microscopy and mitochondrial activity by flow cytometry. First, we double-stained cells with MitoTracker Green (MTG) and tetramethylrhodamine ethyl ester (TMRE) (Agnello et al, 2008) and identified a similar appearance of mitochondrial morphology in both patient and control iPSCs under confocal microscopy (Fig 2B).

TMRE, a cationic, lipophilic compound, can be used to measure MMP in live cells as it reversibly accumulates in the highly negatively charged mitochondrial matrix. Thus, membrane potential can be measured dynamically; release of TMRE after mitochondrial depolarization and its reuptake after repolarization can be quantified (Krohn et al, 1999). In order to understand the relationship between MMP and the volume of mitochondria present in live cells, we combined MTG and TMRE staining and measured the relative fluorescence intensity of each by flow cytometry. This ratio gives a relative measure of MMP independent of mitochondrial mass that we call specific MMP. To establish this assay, we first had to evaluate the relationship between MTG and MMP fluorescence particularly since MTG fluorescence has been reported to be both independent of (Doherty & Perl, 2017) and sensitive to MMP (Pendergrass et al, 2004). We titrated different concentrations of TMRE against 150 nM MTG in control iPSCs. We saw no significant difference in MTG fluorescence in the TMRE concentration range of 5–100 nM (Appendix Fig S2). Higher TMRE concentrations (over 100 nM) caused a decrease in MTG fluorescence (Appendix Fig S2). Thus, we chose 100 nM TMRE and 150 nM MTG to estimate the specific MMP. Mitochondrial volume measured by MTG (Fig 2C), total MMP measured by TMRE alone

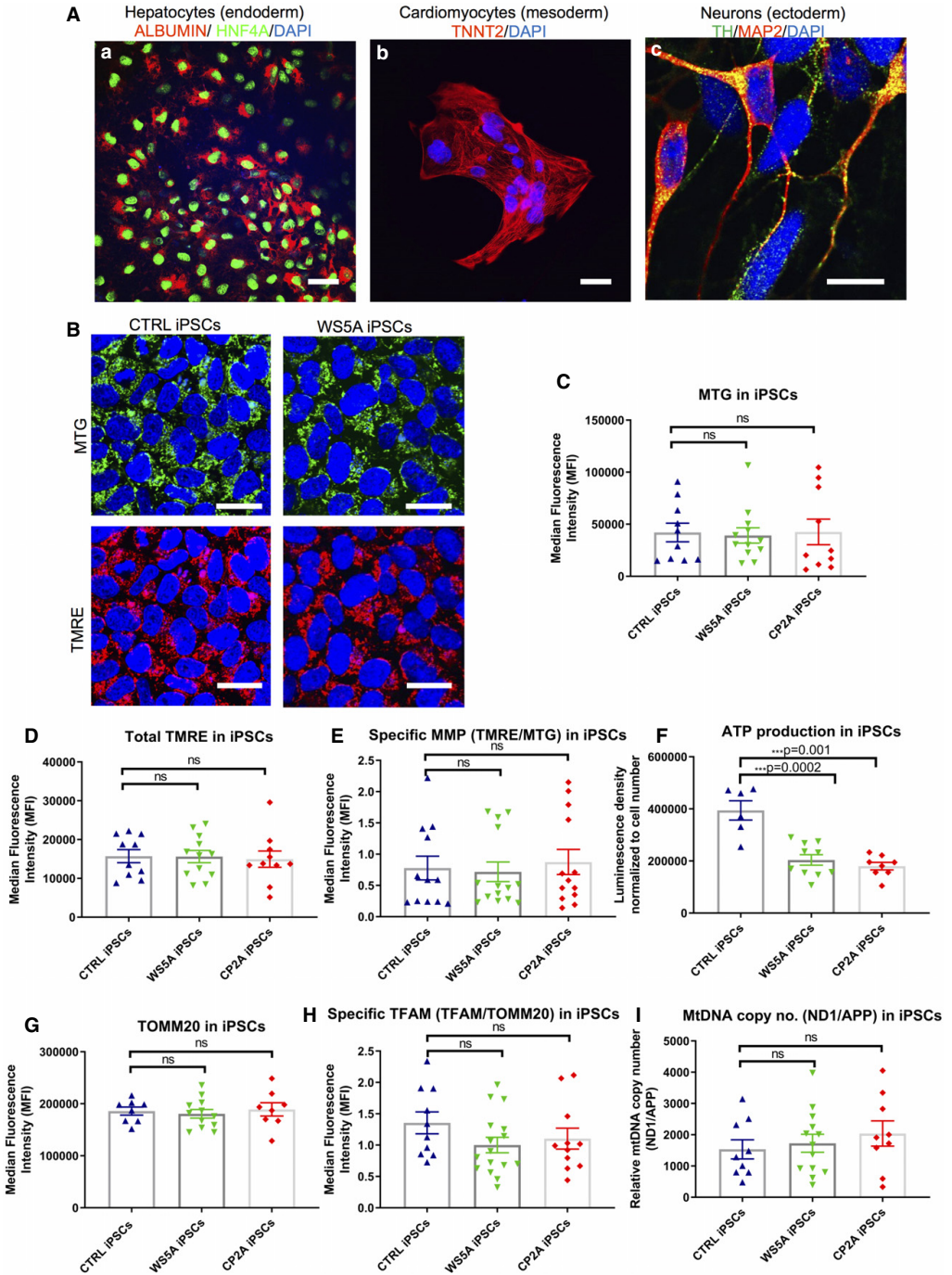


Figure 2.

Figure 2. POLG iPSCs manifested a partial phenotype presenting with energy depletion.

- A Representative confocal images of iPSC lineage-specific differentiation into germ layers of endoderm-derived hepatocytes with positive expression of ALBUMIN (red) and HNF4A (green) (a) (scale bar, 100 μ m), mesodermal-derived cardiomyocytes with positive expression of TNNT2 (red) (b) (scale bar, 100 μ m), and ectodermal-derived dopaminergic neurons with positive expression of TH (green) and MAP2 (red) (c) (scale bar, 10 μ m). Nuclei are stained with DAPI (blue).
- B Confocal images of mitochondrial morphology for iPSC lines with co-staining of MTG (upper panel) and TMRE (lower panel) (scale bars, 25 μ m). Nuclei are stained with DAPI (blue).
- C–E Flow cytometric analysis of iPSCs generated from Detroit 551, WSSA, and CP2A fibroblasts for mitochondrial volume (MTG) (C, $n = 6$, technical replicates per clone for control and CP2A; $n = 5$, technical replicates per clone for WSSA), total MMP (TMRE) (D, $n = 6$, technical replicates per clone for control and CP2A; $n = 5$, technical replicates per clone for WSSA) and specific MMP (E, $n = 6$, technical replicates per clone for control and CP2A; $n = 5$, technical replicates per clone for WSSA) calculated by dividing median fluorescence intensity (MFI) for total TMRE expression by MTG.
- F Intracellular ATP production in iPSCs generated from Detroit 551, WSSA, and CP2A fibroblasts ($n = 3$, technical replicates per clone for control and WSSA; $n = 4$, technical replicates per clone for CP2A).
- G, H Flow cytometric analysis of TOMM20 expression level (G, $n = 4$, technical replicates per clone) and specific TFAM level (total TFAM/TOMM20) (H, $n = 4$, technical replicates per clone).
- I Relative mtDNA copy number in Detroit 551, WSSA and CP2A iPSCs by RT-qPCR analysis using ND1 and APP ($n = 5$, technical replicates per clone for control; $n = 5$, technical replicates per clone for WSSA and CP2A). Values are presented as Log_2 of the ratio between the expression values of ND1 in relation to APP.

Data information: The data presented in C–I were generated from 2 different iPSC clones from Detroit 551 control, 3 different clones from WSSA patient iPSCs, and 2 different clones from CP2A patient iPSCs. Data are presented as mean \pm SEM for the number of samples. Mann–Whitney U -test was used for the data presented in C and E. Two-sided Student's t -test was used for the data presented in D and F–I. Significance is denoted for P values of less than 0.05. *** $P < 0.001$. Source data are available online for this figure.

(Fig 2D), and specific MMP calculated by TMRE/MTG using the combined assay (Fig 2E) showed no differences between patient WSSA and CP2A and control iPSCs. We next assessed ATP production per cell using a live cell luminescence assay and found significantly lower ATP levels in both WSSA and CP2A iPSCs compared to control iPSCs (Fig 2F).

We investigated mtDNA copy number using two different approaches: first, with flow cytometry to assess the level of mitochondrial transcription factor A (TFAM), which binds mtDNA in molar quantities and second, using RT-qPCR to quantify the mtDNA copy number. We performed flow cytometric quantification using antibodies against TFAM and mitochondrial import receptor subunit TOM20 (TOMM20), a mitochondrial outer membrane protein, in order to correlate this to mitochondrial mass. We found no difference in TOMM20 expression (Fig 2G) and TFAM protein levels corrected for mitochondrial content in patients versus control (Fig 2H). Lastly, quantification of mtDNA copy number was performed by RT-qPCR using the relative method. Mitochondrial and nuclear DNA quantities were measured amplifying genomic regions of ND1 and APP genes, respectively. The ratio of mtDNA/nDNA (ND1/APP) was calculated and showed no difference between iPSC clones in WSSA and CP2A patient and control (Fig 2I).

Our findings reveal an energy failure with loss of ATP production in POLG-specific iPSCs, but no change in mitochondrial volume, membrane potential, or mtDNA level. This suggests that the pluripotent stage is not suitable for modeling mitochondrial disease caused by POLG mutation.

Neural induction and derivation of neural stem cells carrying POLG mutations

Primary NSCs serve as a source of different types of neurons and glial cells *in vivo* and play a vital role in development, repair, and the functional modulation of human adult neurogenesis. In addition, NSC dysfunction may contribute to an assortment of neurological disorders (Li *et al.*, 2018). We therefore explored whether NSCs derived from these two patients showed defective mitochondrial function.

We employed a modified dual SMAD protocol (Fig 3A) to differentiate NSCs from both control and patient iPSCs. A three-stage induction protocol (Fig 3A and B) was applied. Briefly, we utilized the iPSCs and ESCs with high quality and showing no sign of differentiation to initiate the neural induction. After 5 days neural induction using a chemically defined medium (CDM) supplemented with SB431542, AMPK inhibitor Compound C and N-acetylcysteine (NAC), iPSCs (Fig 3B(a)) progressed to a neural epithelial stage exhibiting clear neural rosette structures (Fig 3B(b)). Neurospheres were generated by lifting neural epithelium at day 5, and these were round, well-defined spheres of small to medium size in suspension culture (Fig 3B(c)). NSCs were then produced by dissociating neurospheres into single cells and then replating in monolayers. NSCs in monolayers showed a clear neural progenitor appearance (Fig 3B(d)).

We confirmed the specific stages of neural induction with immunostaining: iPSCs showed SSEA4 and POU5F1 expression (Fig 3B(e)); neural epithelial cells showed rosette structures that uniformly expressed PAX6 and NESTIN (Fig 3B(f)); neurospheres showed positive NESTIN expression (Fig 3B(g)); and NSCs stained positively for PAX6 (Fig 3B(h)). Using flow cytometric quantification, we demonstrated that POU5F1 expression decreased during the induction process, while the neural progenitor markers NESTIN and PAX6 increased during neural induction over the 5 days (Fig 3C). To minimize intraclonal variation, we included two different ESC lines, four independent clones from Detroit 551 fibroblasts, one clone from CCD-1079Sk, one clone from control AG05836, three independent clones from WSSA, and two independent clones generated from CP2A fibroblasts. Each line was subjected to neural induction, on three independent occasions, generating a total of 33 NSC lines which were used in further investigations.

Next, we used immunostaining and flow cytometry to investigate relevant protein markers and RT-qPCR to evaluate gene expression to characterize the NSC lines. Immunostaining demonstrated that iPSC-derived NSCs were positive for NESTIN and PAX6 (Fig 3D). RT-qPCR analysis for neural progenitor markers *SOX2*, *NESTIN*, and *PAX6* revealed similar patterns of gene expression for all NSCs

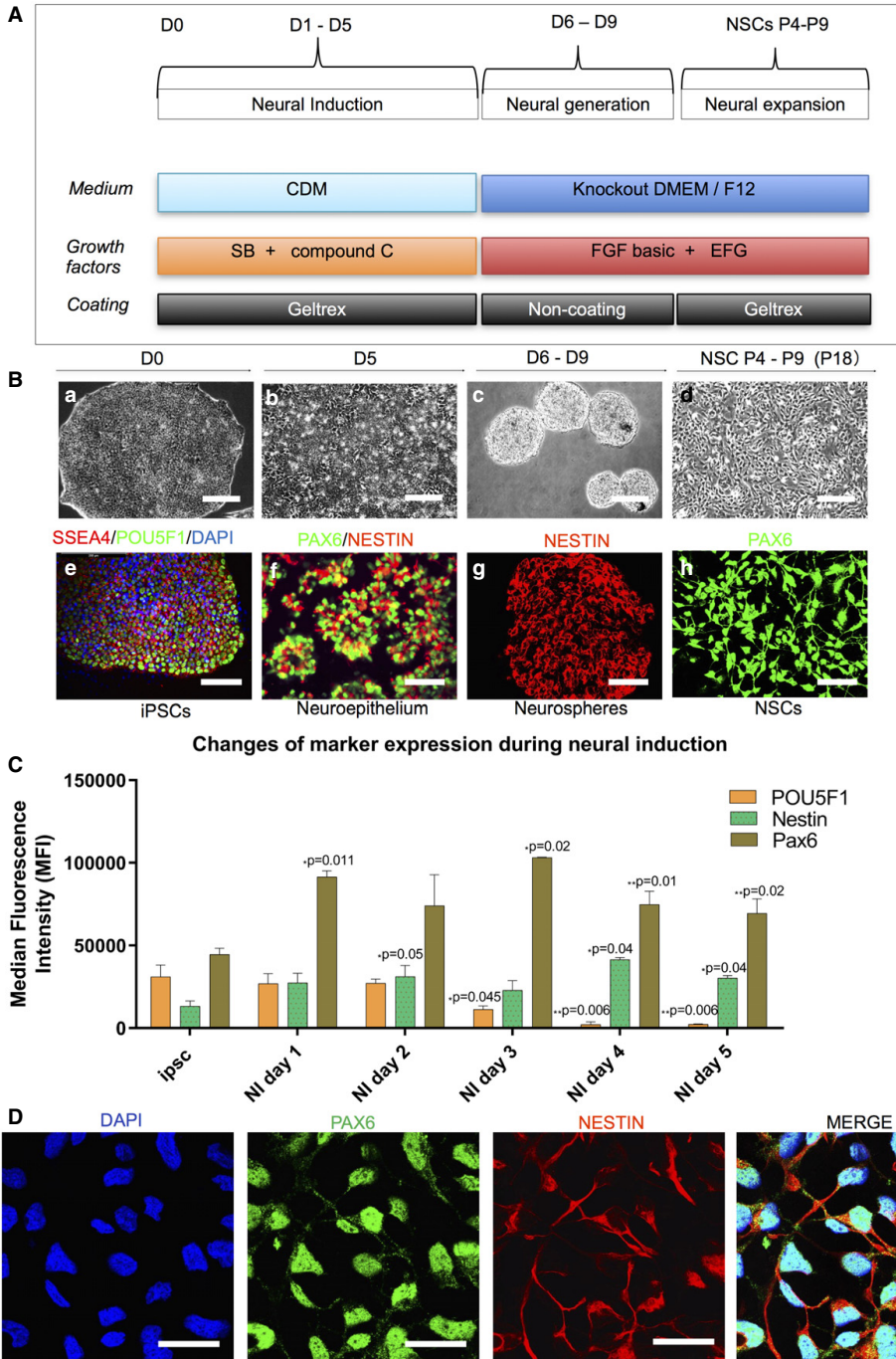


Figure 3.

Figure 3. Validation of patient-specific NSCs.

- A Schematic of dual differentiation and seeding paradigm for NSCs via the dual SMAD protocol.
- B Representative phase contrast images (upper panel) and immunostaining for specific stages during neural induction from iPSCs to NSCs. Upper panel displays the morphology in culture of different cell types during neural induction to NSCs from iPSCs including iPSCs (a); neuroepithelium with rosette-like structures (b); neurospheres with defined round shapes in suspension culture (c); and NSCs in monolayers (d) (scale bars, 50 μ m). Lower panel demonstrates the representative phase contrast images for the immunostaining corresponding to the specific stages in the upper panel: iPSCs with positive staining of SSEA4 (red) and POU5F1 (green) (e) (scale bar, 50 μ m); neuroepithelium with rosette-like structures with positive staining of PAX6 (green) and NESTIN (red) (f) (scale bar, 50 μ m); neurospheres with positive staining of NESTIN (red) (g) (scale bar, 100 μ m); NSCs with positive staining of PAX6 (green) (h) (scale bar, 50 μ m).
- C Flow cytometric assessment of stemness marker POU5F1 and NSC markers NESTIN and PAX6 during neural induction from day 0 to day 5 ($n = 3$, technical replicates).
- D Representative images of the immunofluorescent labeling for NSC markers SOX2 (green) and NESTIN (red) (scale bar, 25 μ m) from Detroit 551 control iPSC-derived NSCs. Nuclei are stained with DAPI (blue).

Data information: The data presented in C were generated from one iPSC clones (clone 1) from Detroit 551 control. Data are presented as mean \pm SEM for the number of samples. Mann–Whitney *U*-test was used to test the significant difference in the expressions of days 1–5 compared to day 0. Significance is denoted for *P* values of less than 0.05. **P* < 0.05; ***P* < 0.01.

Source data are available online for this figure.

(Fig 4A). Since quantification using immunostaining is challenging, we performed flow cytometry to analyze the purity of our NSC cell populations. All NSCs showed positive protein expression of NSC markers PAX6 (Fig 4B) and NESTIN (Fig 4C), with over 94% of the population positive for NESTIN (Appendix Fig S3). In addition, our data showed that the protein expression level for PAX6 (Fig EV3A) exhibited a peak on passage 7 and dropped afterward, and the pluripotency marker POU5F1 (Fig EV3B) remained unchanged during long-term cultivation. Thus, all the NSCs used for further investigation were limited to passages 4–9.

We confirmed that the NSCs generated from patients maintained the same *POLG* gene profile of the parental cells by demonstrating that they retained the same mutation as the original fibroblasts (Fig 4D). Thereafter, we showed that these NSCs had the potential to differentiate into glial subtypes and neurons, including astrocytes which expressed glial fibrillary acidic protein (GFAP, Fig 4E(a)), S100 calcium-binding protein β (S100 β) (Appendix Fig S4), excitatory amino acid transporter 1 (EAAT1), and glutamine synthetase (Appendix Fig S5); oligodendrocytes via expression of galactocerebroside (GALC, Fig 4E(b)), oligodendrocyte transcription factor (OLIG2) and myelin basic protein (MBP) (Appendix Fig S6), and dopaminergic (DA) neurons which were positive for TH and tubulin beta III (TUJ1) (Fig 4E(c)).

These findings indicate that it is possible to generate patient-specific, *POLG*-mutated NSCs with reasonable purity and efficiency. We also confirm that our iPSC-derived NSCs faithfully retained the original genotype (Ma et al, 2015; Kang et al, 2016) and carried the sequencing with the relevant *POLG* exons.

POLG NSCs showed a greater impairment of mitochondrial function compared to iPSCs and parental fibroblasts

We applied the same experimental approaches as described above to investigate mitochondrial function in NSCs. We compared a panel of different NSCs generated from three homozygous WS5A iPSC clones and two heterozygous CP2A iPSC clones to three clones from Detroit 551 iPSCs, one clone from CRL2097, and one clone from AG05836 control, to investigate mitochondrial morphology, MMP, and intracellular ATP production. In addition, we assessed the original patient fibroblast lines to determine whether a phenotype was present.

We assessed mitochondrial morphology by transmission electron microscopy and found similar morphology in both patient and

control NSCs, displaying normal and well-developed cristae (Fig 5A).

Using the TMRE/MTG double staining approach described above, we found that mitochondrial volume was less in WS5A, but similar in CP2A NSCs compared to control lines (Fig 5B). While the total MMP (Fig 5C) appeared decreased in mutant NSCs as compared to control, no significant difference was detected in the specific MMP level, i.e. MMP per mitochondrial volume (total TMRE/MTG) (Fig 5D). In fibroblasts, similar mitochondrial volumes were found in mutant and control cells based on MTG level (Fig 5F). However, a significantly increased total (Fig 5G) and specific MMP (Fig 5H) was seen in fibroblasts from both WS5A and CP2A mutants versus control lines.

Direct measurement of intercellular ATP production revealed a significant defect in both WS5A and CP2A NSCs compared to control (Fig 5E). Interestingly, this was also seen in the parental fibroblasts (Fig 5I) and iPSCs (Fig 2F). Fibroblasts, however, appeared capable of maintaining and indeed increasing their membrane potential (Lorenz et al, 2017), possibly by hyperpolarization, while NSCs did not.

Our data indicate a cell lineage/tissue specificity in response to *POLG* mutation. Energy depletion is seen in both NSCs and fibroblasts, but the effect on MMP differed. This differential response suggests that neurons are selectively vulnerable to the mitochondrial changes induced by *POLG* mutation.

POLG NSCs manifest mtDNA depletion, but not mtDNA deletion

We assessed mtDNA both qualitatively and quantitatively. As previously, we used both flow cytometric analysis of TFAM and qPCR. We detected a significant decrease of specific TFAM protein level (TFAM/TOMM20) in both WS5A and CP2A NSCs compared to control (Fig 6B), whereas no changes were observed at TOMM20 expression level (Fig 6A). Quantification based on RT-qPCR measurements of the ND1/APP ratio also revealed a significant reduction of mtDNA copy number in patient WS5A and CP2A NSCs (Fig 6C). In contrast, TOMM20 (Fig 6D) and TFAM levels (Fig 6E), as well as mtDNA copy number (Fig 6F), were not significantly changed in patient fibroblasts. These findings further demonstrate the differential response between patient NSCs (Fig 6A–C), iPSCs (Fig 2G–I), and parental fibroblasts (Fig 6D–F). The fact that mtDNA depletion arises in neural lineage indicates that NSCs are a

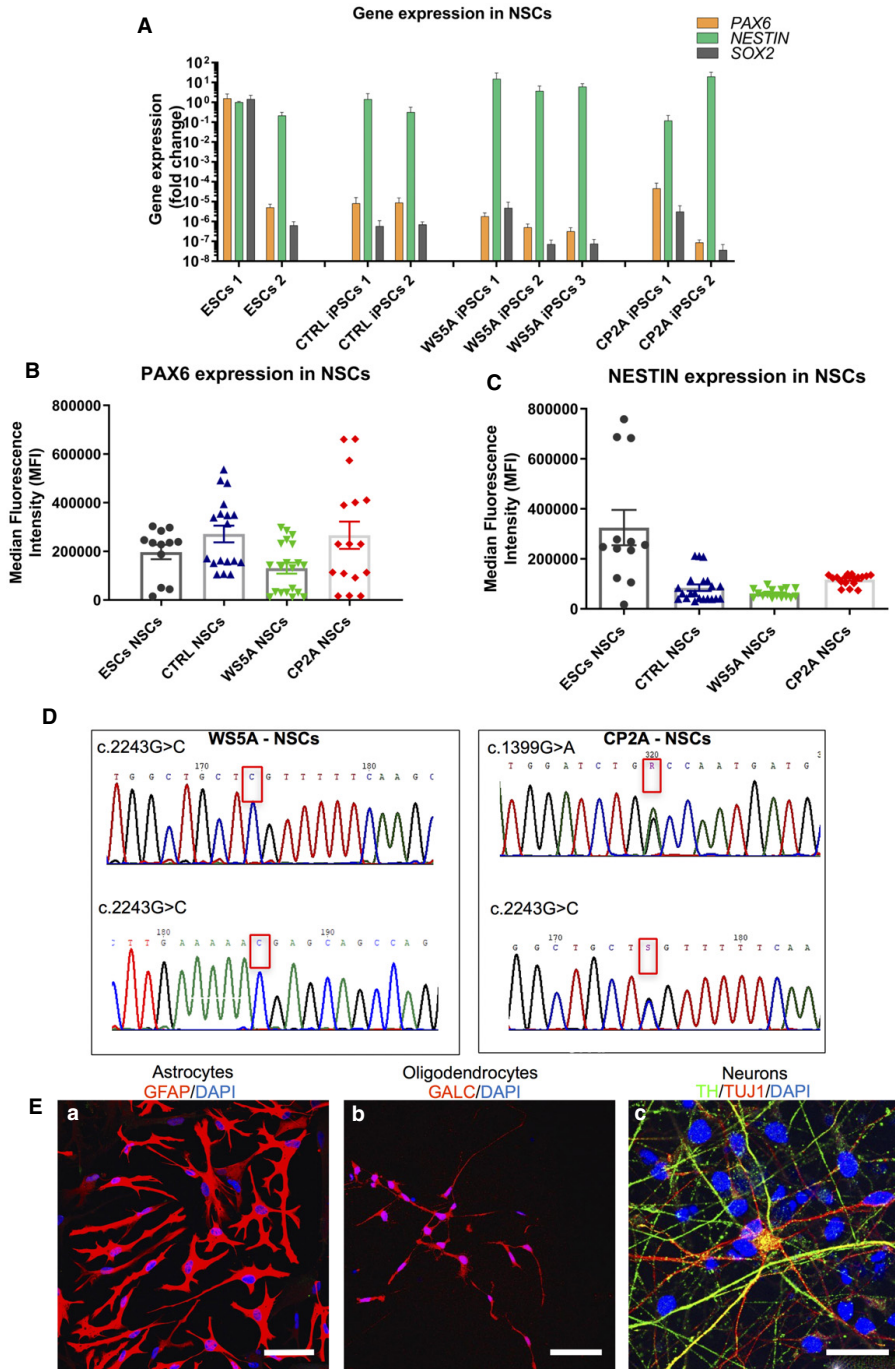


Figure 4.

Figure 4. NSCs retained the original genotype and sequence.

- A Quantification of gene expression for NSC markers *PAX6*, *NESTIN*, and *SOX2* for all NSCs from RT-qPCR analysis. The expression of the neural stem cell markers is assessed with fold change using the comparative $\Delta\Delta C_t$ method by normalizing NSCs to iPSCs ($n = 3$, technical replicates per ESC line or iPSC clone).
- B, C Quantification of protein expression level for *PAX6* (B, $n = 6$, technical replicates per line for ESCs; $n = 7$, technical replicates per clone for control; $n = 8$, technical replicates per clone for W55A; $n = 9$, technical replicates per clone for CP2A) and *NESTIN* (C, $n = 6$, technical replicates per line for ESCs; $n = 7$, technical replicates per clone for control; $n = 8$, technical replicates per clone for W55A; $n = 9$, technical replicates per clone for CP2A) for iPSC-derived NSCs using flow cytometry.
- D Sequencing chromatogram showing the homozygous c.2243G>C variation in *POLG* in W55A iPSC-derived NSCs and the heterozygous c.1399G>A and c.2243G>C variation in *POLG* in CP2A iPSC-derived NSCs.
- E Representative confocal images showing glial and neuronal lineages derived from NSCs. (a) Immunostaining of NSC-derived astrocytes with GFAP (red) staining (scale bar, 50 μm). (b) Immunostaining of oligodendrocytes showing GALC (red)-positive labeling (scale bar, 50 μm). (c) Dopaminergic neurons showing TH (green) and TUJ1 (red)-positive staining (scale bar, 25 μm). Nuclei are stained with DAPI (blue).

Data information: The data points in A–C represent NSCs generated from 2 ESC lines, 3 different control iPSCs including 2 different clones from Detroit 551 control, one clone from control AG05836, 3 different clones from W55A patient, and 2 different clones from CP2A patient iPSCs. Data are presented as mean \pm SEM for the number of samples.

Source data are available online for this figure.

relevant model system for mtDNA-associated disease with *POLG* mutation.

Since we previously identified mtDNA deletions in post-mortem neurons from patients (Tzoulis *et al*, 2014), we used long range PCR to investigate whether qualitative mtDNA damage also occurred in NSCs. Deletions were not detectable in the mtDNA of patient NSCs and nor were they found in the parental fibroblasts (Fig 6G). Thus, the accumulation of mtDNA deletions appears time dependent, both in aging tissues (Kazachkova *et al*, 2013) and in neurons of *POLG* patients (Tzoulis *et al*, 2014).

These findings indicate that NSCs but not fibroblasts or iPSC faithfully replicate the mtDNA depletion found in post-mortem neurons. Deletions of mtDNA, which only accumulate slowly over time, were not found.

POLG dopaminergic (DA) neurons confirm mtDNA findings in NSCs

As DA neurons of the substantia nigra were one of the most affected cell types in *POLG* disease (Tzoulis *et al*, 2014), we generated this specific neuronal type to investigate whether we could replicate the pathological findings seen in NSCs.

We applied DA neuron differentiation based on the dual SMAD method with the addition of FGF-8 and Sonic hedgehog (SHH) agonist purmorphamine (PM), modified from a previous report (Stacpoole *et al*, 2011). This procedure included, Phase I: the first stage of differentiation from stem cells to neural rosette-like colonies, and the second stage of differentiation from neural rosette-like colonies to neurospheres by dual inhibition of SMAD signaling with SB431542 and dorsomorphin/Compound C. Phase II and III: caudalization of neurospheres with addition of FGF-8 and further ventralization to dopaminergic progenitors using the combination of FGF-8 and the SHH agonist PM. Phase IV: DA neuron maturation from DA progenitors by adding BDNF and GDNF. Using this protocol, both control and *POLG* mutant iPSCs efficiently differentiated into mature DA neurons as shown by both TH and MAP2 expression (Fig 6H), and the yield of TH-positive neurons was over 97% in both control and *POLG* cultures (Fig 6I).

We then investigated alterations of TFAM level and mtDNA copy number in both W55A and CP2A DA neurons. We found that mutant DA neurons displayed similar defects to those seen in NSCs

(Fig 6B and C), with both lower TFAM level (Fig 6J) and mtDNA copy number (Fig 6K) than control DA neurons.

Our findings confirm that different cell types respond differently to the same bioenergetic challenge. However, considering neurons are difficult to acquire and display limited expansion potential, it would be preferential to use NSCs as they are feasible to expand, bank, and can potentially enable high-throughput drug screening. Since we found that NSCs manifest *POLG* disease phenotypes, NSCs were considered as a precise and reliable cell type and applied for further studies of disease mechanisms.

Respiratory chain complex I loss, NAD⁺/NADH redox changes and ROS excess occur in *POLG* NSCs, but not iPSCs

We showed previously that respiratory chain complex I was lost in *POLG* affected frontal and cerebellar neurons (Tzoulis *et al*, 2014), and we confirmed these findings in this current study. We studied occipital neurons collected from fresh frozen brain tissue taken from patients with *POLG* mutations ($n = 5$) and controls ($n = 5$). The *POLG* mutations were as follows: A467T/G303R (AL-1B); A467T/A467T (AT-1A); A467T/A467T (AT-2A); W748S/W748S (WS-10A), and W748S/W748S (WS-3A). In agreement with our previous study, immunohistochemistry demonstrated clear complex I deficiency in occipital neurons of *POLG* patients (Fig 7A(a–c)). Further, relative quantification of mtDNA from microdissected occipital neurons showed significantly decreased mtDNA copy number in the patient neurons compared to controls (Fig 7A(d)).

We then investigated whether this also occurred in *POLG* cells. To quantify complex I level, we used Anti-NDUFB10, the same antibody as was used in post-mortem studies. Co-staining with TOMM20 was used to correlate complex level to mitochondrial mass. We found a similar level of complex I in both patient and control iPSCs (Fig 7F). Levels of complex II (Fig 7G) and IV (Fig 7H) were also similar in iPSCs. In NSCs, however, we observed a significant decrease in mitochondrial complex I assessed by both immunostaining (Fig 7B) and flow cytometry (Fig 7C). This was not seen in either iPSCs (Fig 7F) or fibroblasts (Fig 7I). Although no significant changes in mitochondrial complex II (Fig 7D) or IV subunits (Fig 7E) were found in mutant NSCs or fibroblasts (Fig 7J and K) as compared to control lines, lower complex IV subunit was found in W55A NSCs compared to control (Fig 7E). These data

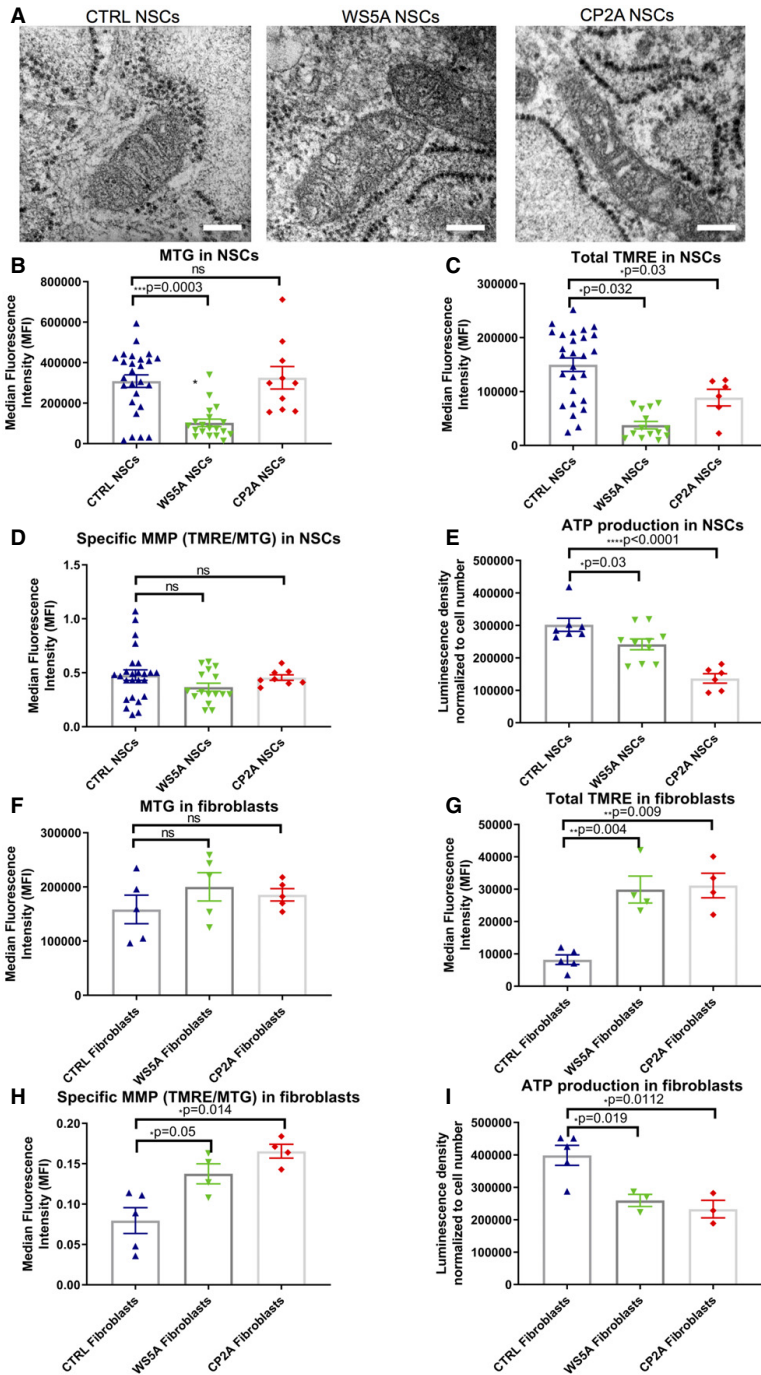


Figure 5.

Figure 5. POLG NSCs exhibited impaired mitochondrial function, which was partly presented in fibroblasts.

A Representative transmission electron microscopy images of mitochondrial structures in Detroit 551 control, W55A, and CP2A NSCs (scale bar, 400 nm).

B–D Flow cytometric analysis of mitochondrial volume (MTG) (B, $n = 5$, technical replicates per clone), total MMP (TMRE) (C, $n = 5$, technical replicates per clone), and specific MMP (D, $n = 5$, technical replicates per clone), calculated by dividing median fluorescence intensity (MFI) for total TMRE expression by MTG in NSCs generated from control lines, W55A, and CP2A iPSCs.

E Intracellular ATP production in NSCs ($n = 3$, technical replicates per clone).

F–H Flow cytometric analysis of mitochondrial volume (MTG) (F, $n = 6$, technical replicates for control; $n = 5$, technical replicates for W55A and CP2A), total MMP (TMRE) (G, $n = 5$, technical replicates for control; $n = 4$, technical replicates for W55A and CP2A), and specific MMP (TMRE/MTG) (H, $n = 5$, technical replicates for control; $n = 4$, technical replicates for W55A and CP2A) in Detroit 551, W55A, and CP2A fibroblasts.

I Intracellular ATP production in Detroit 551, W55A, and CP2A fibroblasts ($n = 6$, technical replicates for control; $n = 3$, technical replicates for W55A and CP2A).

Data information: The data points in B–D represent NSCs generated from 5 different control iPSCs including 3 different clones from Detroit 551 control, one clone from CCD-1079Sk, one clone from control AG05836, 3 different clones from W55A patient iPSCs, and 2 different clones from CP2A patient iPSCs. The data points in E represent NSCs derived 3 different clones from Detroit 551, 3 different clones from W55A, and 2 different clones from CP2A iPSCs. Data are presented as mean \pm SEM for the number of samples. Mann–Whitney *U*-test was used for the data presented in B and C. Two-sided Student's *t*-test was used for the data presented in D–I. Significance is denoted for *P* values of less than 0.05. **P* < 0.05; ***P* < 0.01; ****P* < 0.001; *****P* < 0.0001.

Source data are available online for this figure.

indicate that, similar to both POLG patient tissues, complex I defect is present in NSCs.

Complex I function is essential for the re-oxidation of NADH and maintenance of the NAD⁺/NADH ratio, which is an important indicator of redox status and major modulator of intermediary metabolism (Houtkooper *et al*, 2010). To investigate the effect of *POLG* mutation on NAD⁺ metabolism, we measured both NAD⁺ and NADH levels using liquid chromatography–mass spectrometry (LC-MS). As expected, we found a significant decrease in the NAD⁺/NADH ratio in both patient NSCs compared with control (Fig 8A). While the levels of NAD⁺ and NADH varied in the patient NSCs (Fig 8B and C), the ratio showed disturbed NAD⁺ homeostasis in both. To confirm these findings, we performed colorimetric analysis using a commercial NAD⁺/NADH assay. Similar to the findings from LC-MS, we found a significant decrease of NAD⁺/NADH ratio in both patient NSCs versus control (Appendix Fig S8). However, we found an increase in the NAD⁺/NADH ratio (Fig 8D) and reduced level of NAD⁺ (Fig 8E) and NADH (Fig 8F) in both patient iPSCs compared with control, though only the CP2A line reached significance (Fig 8D–F).

The mitochondrial respiratory chain is considered to be a major source of intracellular ROS, and the dysfunction of complex I is particularly implicated in excess ROS production (Hayashi & Cortopassi, 2015), which potentially can damage both mitochondria and mtDNA (Cui *et al*, 2012). To investigate whether the presence of *POLG* mutation led to increased ROS production, we used dual staining with 2',7'-dichlorodihydrofluorescein diacetate (DCFDA) and MitoTracker Deep Red (MTDR). We found no major differences in ROS production (DCFDA) in patient W55A and CP2A iPSCs compared to controls (Fig EV4A). To ensure that this reflected the mitochondrial mass in each cell type, we divided total ROS by a measure of mitochondrial mass (MTDR) to give specific ROS and again found no difference between patient and control iPSCs (Fig EV4B). Interestingly, a trend toward reduced total (Fig EV4C) and specific ROS level (Fig EV4D) was detected in patient fibroblasts. In contrast, both total ROS (Fig EV4E) and specific ROS (Fig 8G), i.e., the ratio of ROS to mitochondrial volume defined by MTDR, appeared significantly higher in mutant NSCs compared to control, indicating the potential for oxidative damage in mutant NSCs. To confirm that the increased ROS was of mitochondrial origin, we used the ROS-sensitive fluorescent dye MitoSox and

quantified both total and the ratio of ROS to mitochondrial volume defined by MTG, i.e., specific ROS. Both patient NSCs showed a significant increase in the mean intensity of MitoSox fluorescence at specific level (Fig 8H), suggesting the high ROS production generated from mitochondria itself. However, the total level of mitochondrial ROS was lower in W55A patient but higher in CP2A patient compared to control (Fig EV4F).

These data suggest that complex I loss has functional consequences. The disturbance of NAD⁺ homeostasis will have major implications for neurons that are heavily dependent on glucose metabolism and thus reoxidation of NADH generated by the citric acid cycle. Increased ROS production leads potentially to a more indiscriminate damage. Both consequences are likely to contribute to the pathological mechanism of *POLG*-related diseases.

UCP2/SirT1-regulated cellular senescence and BNIP3 pathway-mediated mitophagy are involved in the pathogenesis of neuronal *POLG* diseases

In view of the changes in NAD⁺ metabolism and the known link between mitochondrial dysfunction with increased ROS production and aging (Fang *et al*, 2019), we investigated cellular senescence and mitophagy in our NSCs. We performed staining of β -galactosidase and flow cytometric measurements of cellular senescence marker p16INK4. We observed significantly increased activity for β -galactosidase in both patient W55A and CP2A NSCs compared to control NSCs (Fig 8I and J). This finding was further corroborated with flow cytometry against p16INK4 (Fig EV5).

Next, we investigated the molecular pathways linked to initiating the process of senescence. Previous studies have shown that overproduction of mitochondrial uncoupler protein 2 (UCP2) irreversibly reduces the MMP and induced a senescent-like morphology, leading to irreversible metabolic changes, loss of cellular ATP, and high ROS (Nishio & Ma, 2016). Sirtuin 1 (SirT1) is the most conserved mammalian NAD⁺-dependent protein deacetylase and is increasingly recognized as a crucial regulator of a variety of cellular processes, including energy metabolism, stress response, and senescence (Li, 2013). In addition, SirT1 has been shown to repress the *UCP2* gene by binding directly to the *UCP2* promoter (Bordone *et al*, 2006). To investigate a possible pathogenic role for UCP2 and SirT1 in *POLG*-induced senescence, we examined the expression of UCP2

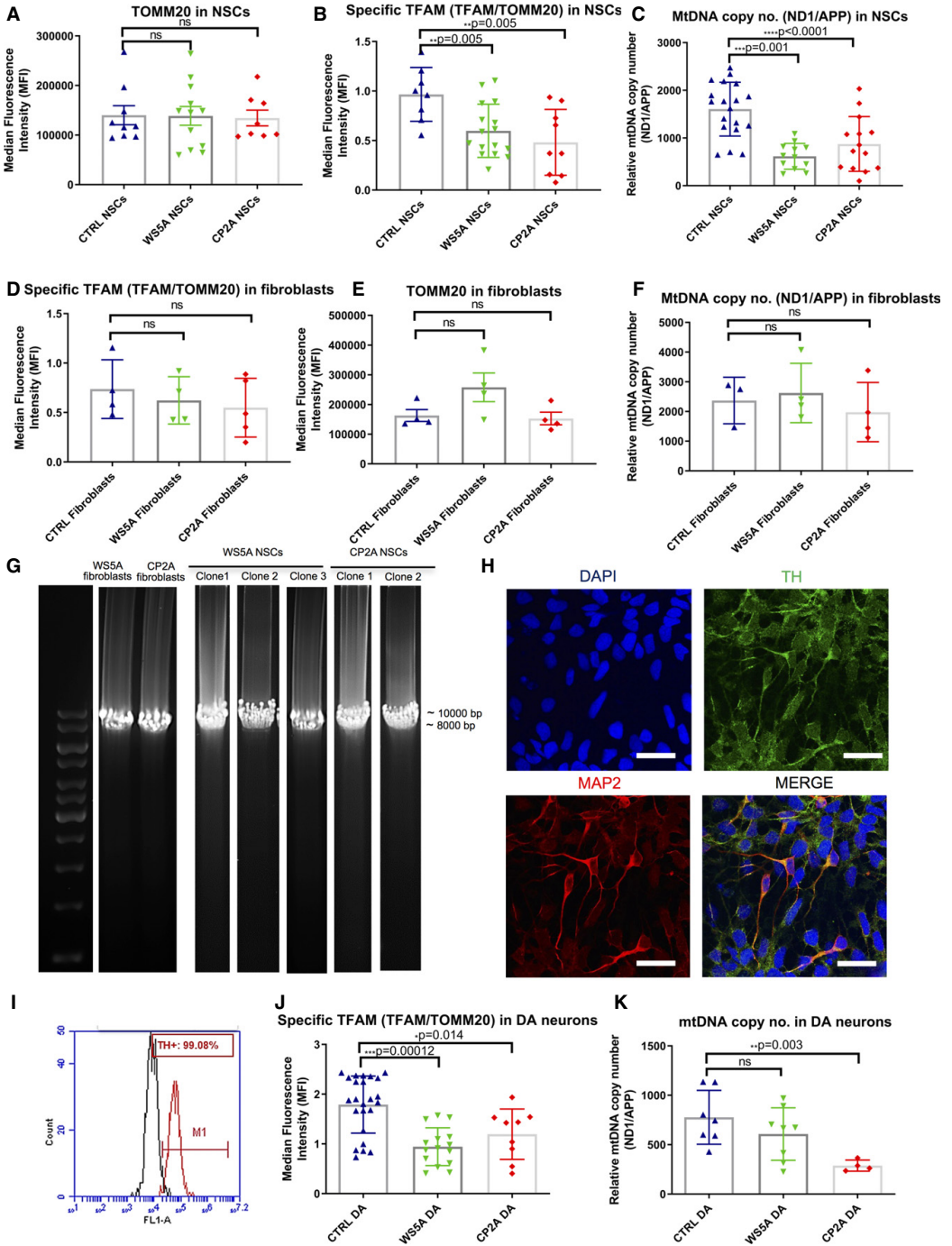


Figure 6.

Figure 6. POLG NSCs exhibited decreased TFAM level and mtDNA depletion, but not mtDNA deletion, consistent with iPSC-derived DA neurons.

- A, B Flow cytometric analysis of TOMM20 (A, $n = 3$, technical replicates per clone for control; $n = 4$, technical replicates per clone for W55A and CP2A) and TFAM protein expression (B, $n = 3$, technical replicates per clone for control and CP2A; $n = 5$, technical replicates per clone for W55A) in NSCs. Expressed as specific TFAM level (total TFAM/TOMM20).
- C Relative mtDNA copy number analyzed by RT-qPCR using primers and fluorogenic probes for regions of ND1 and nuclear gene APP in all NSCs ($n = 4$, technical replicates per clone for control; $n = 5$, technical replicates per clone for W55A; $n = 7$, technical replicates per clone for CP2A).
- D, E Flow cytometric analysis of TOMM20 expression level (D, $n = 4$, technical replicates per clone) and TFAM protein expression (E, $n = 4$, technical replicates for control and W55A; $n = 5$, technical replicates for CP2A) in fibroblasts. Expressed as specific TFAM level (total TFAM/TOMM20).
- F Relative mtDNA copy number analyzed by RT-qPCR for regions of ND1 and nuclear gene APP in fibroblasts ($n = 3$, technical replicates for control; $n = 4$, technical replicates for W55A and CP2A).
- G Long-PCR for detection of mtDNA deletions in NSCs and their parental fibroblasts from W55A and CP2A patients.
- H Representative images of confocal microscopy with immunofluorescence labeling of DA neuron-specific marker TH (green) and neuron-specific marker MAP2 (red) for iPSC-derived DA neurons (scale bars, 25 μm). Nuclei are stained with DAPI (blue).
- I Histogram of the positive cell population stained with DA marker TH in iPSC-derived DA neurons using flow cytometric analysis.
- J Flow cytometric measurement of specific TFAM level (total TFAM/TOMM20) in iPSC-derived DA neurons from Detroit 551 control, W55A, and CP2A POLG patients ($n = 8$, technical replicates per clone for control; $n = 5$, technical replicates per clone for W55A; $n = 4$, technical replicates per clone for CP2A).
- K Relative mtDNA copy number analyzed by RT-qPCR for regions of ND1 and nuclear gene APP in all iPSC-derived DA neurons ($n = 3$, technical replicates per clone).

Data information: The data points in A, B represent NSCs generated from 3 different control iPSCs including 2 different clones from Detroit 551 control, 1 clone from control AG05836, 3 clones from W55A patient iPSCs, and 2 clones from CP2A patient iPSCs. Data points in C represent NSCs from 5 different controls, including 3 clones from Detroit 551 control, 1 clone from control AG05836, 1 clone from control CCD-10795k, 3 clones from W55A patient iPSCs, and 2 clones from CP2A patient iPSCs. The data points in J and K represent DA neurons generated from 3 clones from Detroit 551 control, 3 clones from W55A patient iPSCs, and 2 clones from CP2A patient iPSCs. Data are presented as mean \pm SEM for the number of samples. Mann-Whitney *U*-test was used for the data presented in A and J. Two-sided Student's *t*-test was used for the data presented in B–F and K. Significance is denoted for *P* values of less than 0.05. **P* < 0.05; ***P* < 0.01; ****P* < 0.001; *****P* < 0.0001. Source data are available online for this figure.

and the phosphorylated phospho-SirT1 (Ser47) by western blot. We found upregulation of UCP2 expression and reduced phosphorylated SirT1 in both W55A and CP2A NSCs compared with control (Fig 8K and L(a and c)). These data suggested that decreased SirT1 activity and increased UCP2 expression might be involved in cellular senescence observed in *POLG* mutation.

Mitophagy/autophagy appeared able to both promote and inhibit senescence and senescence-associated phenotypes (Korolchuk *et al*, 2017). To investigate whether an activation of mitophagy was involved in *POLG*-related disorders, we studied the mitophagy-related proteins PINK1, Parkin, BNIP3, and LC3B using western blotting. Immunoblotting analysis showed an increased level of the autophagosome marker microtubule-associated protein 1 light chain 3 β (LC3B-II) with increased ratio of LC3BII/LC3BI in CP2A NSCs indicating autophagy activation (Fig 8K and L(b)). PINK1 and Parkin expression were similar to the control group (Fig 8K and L(d and e)), while BNIP3 accumulation was also observed in CP2A, but not W55A (Fig 8K and L(f)). Our data showed that *POLG* mutation increase cellular senescence and is associated with increased mitophagy.

Our data suggests that *POLG* mutation can induce cellular senescence and that this may be modulated via upregulation of UCP2. We also find that mitophagy is an active component of neuronal *POLG* pathogenesis, particularly in the compound heterozygote model.

Discussion

Despite the presence of mitochondria in most cells, mitochondrial disorders manifest strikingly different tissue involvement (Chinnery, 2015). *POLG*-related disorders, for example, show major involvement of the nervous system and liver. Modeling brain diseases have been hampered by the limited availability of human tissue and lack of faithful disease models. These present major obstacles to our

understanding of disease mechanisms and the development of effective treatments. Reprogramming of patient cells combined with their differentiation to the affected cell type has revolutionized the field (Kanerker *et al*, 2014; Tabar & Studer, 2014). Here, we reprogrammed patient fibroblasts carrying the two common *POLG* mutations (c.2243G>C; p.W748S and c.1399G>A; p.A467T) to iPSCs and then differentiated these to NSCs. We found that patient-specific NSCs replicated the findings of mtDNA depletion and complex I deficiency identified in post-mortem tissues. While others have generated iPSCs from patients with *POLG* mutations (Zurita *et al*, 2016; Chumarina *et al*, 2019) or investigated valproate toxicity in iPSC-derived *POLG* patient hepatocytes (Li *et al*, 2015), we believe our study is the first to confirm that the pathological changes seen in post-mortem studies are faithfully replicated in iPSC-derived NSCs. More importantly, using iPSC-derived NSCs we were able to identify cellular and molecular mechanisms involved in the disease process including the overproduction of ROS associated with suppressed complex I-driven respiration and defective NAD⁺ metabolism leading to cellular senescence via UCP2 upregulation and SirT1 downregulation pathway and mitophagy activation. These findings provided compelling evidence of the multiple cellular and molecular mechanisms contributing to the decline of neuron pool in *POLG*-related diseases and open the way for the development of novel diagnostic and therapeutic interventions.

In the present study, we found that iPSCs harboring *POLG* mutations appeared to be able to maintain their MMP, mitochondrial mass, and mtDNA replication at similar levels to control. They also appeared capable of regulating their ROS homeostasis. This suggested either that the mutant phenotypes were rescued at this stage, as was suggested by an earlier study of iPSCs with mtDNA mutations (Ma *et al*, 2015), or that, similar to fibroblasts, these cells derived proportionally more of their energy from glycolysis and maintained ROS levels by lowered respiratory chain activity. However, both mutated iPSCs and fibroblasts showed significantly lower ATP levels. In addition, ATP depletion was associated with

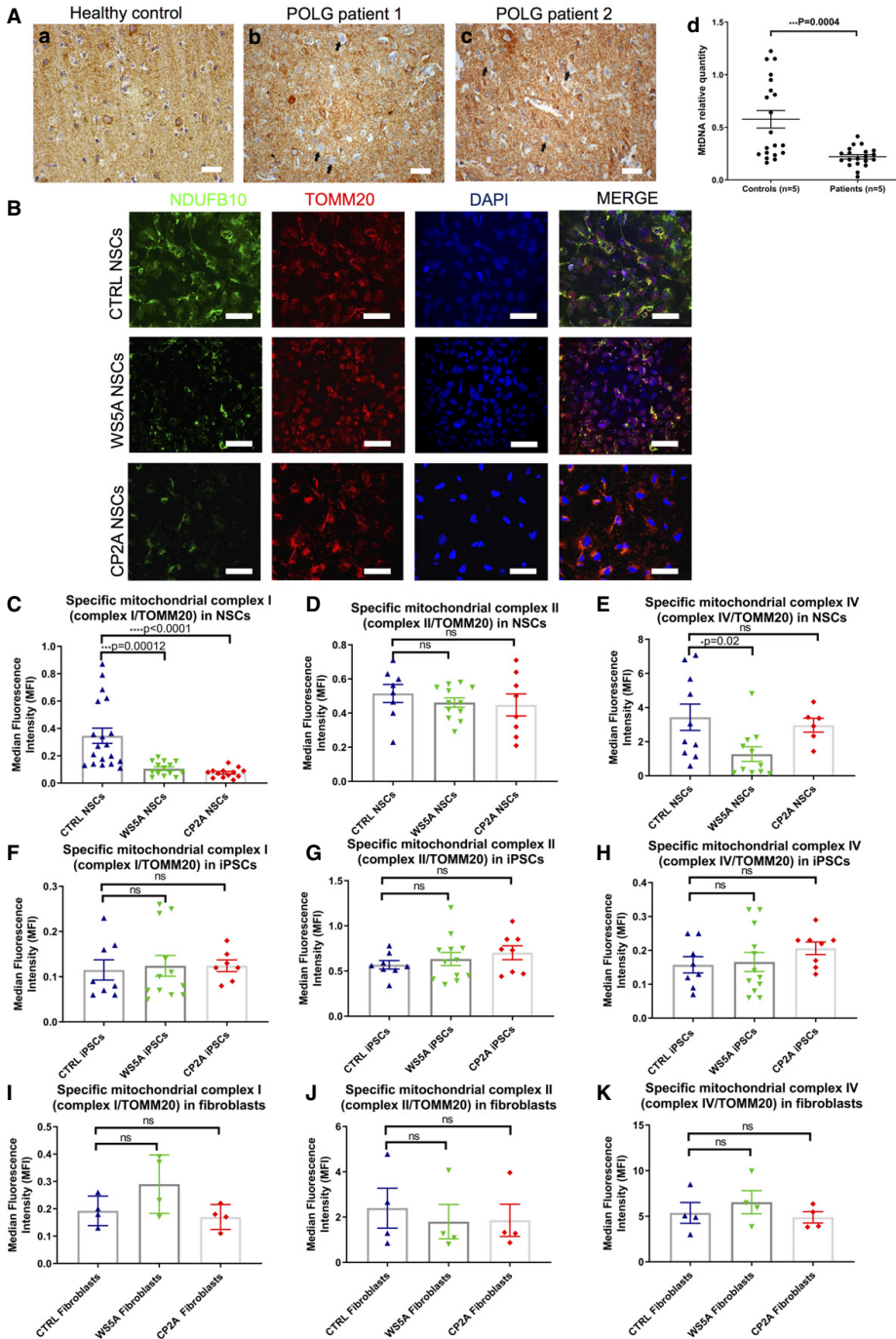


Figure 7.

Figure 7. POLG mutations induced defects in respiratory chain complex I.

- A** Complex I immunohistochemistry in the occipital cortex of a neurologically healthy control (a) and two patients with POLG disease (b and c) (Scale bar, 20 μ m). Patients have numerous complex I-negative neurons (examples marked by arrows). (d) mtDNA relative quantification in microdissected neurons from the occipital cortex of patients with POLG diseases ($n = 5$) and neurologically healthy controls ($n = 5$). Each point represents the mean value of three technical replicates from a pooled sample of 10 neurons. For the purposes of comparison, a control sample has been arbitrarily set to one. The medians of the two groups are compared by Mann–Whitney *U*-test. Data are presented as mean (horizontal bars) \pm SEM (vertical bars).
- B** Representative confocal images of immunostaining for mitochondrial complex I subunit NDUFB10 (green) and TOMM20 (red) in control, W55A, and CP2A NSCs (scale bars, 50 μ m). Nuclei are stained with DAPI (blue).
- C–E** Flow cytometric measurements of mitochondrial complex I (C, $n = 4$, technical replicates per clone), II (D, $n = 3$, technical replicates per clone for control; $n = 4$, technical replicates per clone for W55A and CP2A) and IV (E, $n = 3$, technical replicates per clone for control and CP2A; $n = 4$, technical replicates per clone for W55A) protein level in iPSC-derived NSCs. Expressed as specific complex I, II, and IV level (total complex I, II, IV level/TOMM20).
- F–H** Flow cytometric measurements of mitochondrial complex I (F, $n = 4$, technical replicates per clone), II (G, $n = 4$, technical replicates per clone) and IV (H, $n = 4$, technical replicates per clone) protein level in iPSCs. Expressed as specific complex I, II, and IV level.
- I–K** Flow cytometric measurements of mitochondrial complex I (I, $n = 4$, technical replicates), II (J, $n = 4$, technical replicates), and IV (K, $n = 4$, technical replicates) protein level in parental fibroblasts expressed as specific complex I, II, and IV level.

Data information: The data points in C represent NSCs generated from 5 different controls, including 3 clones from Detroit 551 control, 1 clone from control AG05836, 1 clone from control CCD-10795K, 3 clones from W55A patient iPSCs, and 2 clones from CP2A patient iPSCs. The data points in D, E represent NSCs generated from 3 clones from Detroit 551 control, 3 clones from W55A patient iPSCs, and 2 clones from CP2A patient iPSCs. The data points in F–H represent 2 clones from Detroit 551 iPSCs, 3 clones from W55A patient iPSCs, and 2 clones for CP2A iPSCs. Data are presented as mean \pm SEM for the number of samples. Mann–Whitney *U*-test was used for the data presented in F and J. Two-sided Student's *t*-test was used for the data presented in C–E, G–I and K. Significance is denoted for *P* values of less than 0.05. **P* < 0.05; ****P* < 0.001; *****P* < 0.0001.

Source data are available online for this figure.

mitochondrial hyperpolarization in fibroblasts. These findings are similar to those observed in another stem cell model of mitochondrial disease (Lorenz *et al*, 2017) and suggest either that these cells compensated for lower ATP production by reversing the proton flow in the F_1F_0 ATPase (Abramow *et al*, 2010) or the presence of other mechanisms such as downregulating oxygen consumption through complex II (Forkink *et al*, 2014) are active.

We successfully generated patient-specific NSCs and DA neurons. Combined with neurons being difficult to acquire and display limited expansion potential, NSCs provide a powerful tool to unravel disease mechanism and, potentially, enable high-throughput drug screening. Further, one can perform assays of mitochondrial function in “live cells”. From our previous (Tzoulis *et al*, 2014) and present studies in NSCs, we observed the following potential mechanisms. Confirmation of the loss of complex I in neurons from the occipital cortex and verification of this at the early progenitor stage and in patterned DA neurons. A key finding from our patient studies (Tzoulis *et al*, 2014) was mtDNA depletion was present in neurons from infants under 1 year of age, and this was also observed in our patient NSCs. Depletion of mtDNA was not, however, present in patient fibroblasts or the derived iPSCs. Interestingly, while depletion was clearly detected by qRT-PCR, we also observed lowered mtDNA levels using an indirect method based on flow cytometric measurement of TFAM. Methodologically, this is of major interest as it suggested that we could use this in live cells as a surrogate measure of mtDNA level. The presence of mtDNA depletion did not appear to impair cell growth; however, unlike the situation in patients, we did not expose our cells to any form of stress. Deletions of mtDNA were not observed in any of the above cell types, suggesting that these were generated over time in post mitotic tissues. The lack of qualitative mtDNA damage supported our earlier conclusion that these changes were cumulative and representative of “accelerated aging”.

Since complex I is a major site of ROS production, it has been suggested that loss of this complex is part of a response aimed at reducing the production of these damaging species (Palin *et al*, 2013). Further, Pryde *et al* (2016) provided evidence that complex I

degradation was mediated through protease-dependent inactivation. Interestingly, complex I loss was found to affect the whole brain in Parkinson's disease (Flones *et al*, 2018), not just the substantia nigra (Palin *et al*, 2013; Flones *et al*, 2018), supporting the view that loss of this complex was not itself the cause of neuronal loss, but a secondary event. Irrespective of whether neuronal complex I deficiency and elevated ROS are pathological events or a compensatory response, they are clearly important features associated with the POLG disease process in neurons and changes in level of these may be useful for monitoring treatment or other interventions. Here, we found a clear overproduction of ROS. It was attractive to postulate a causal relationship between these findings. The relationship between ROS and cell death and increased ROS and complex I loss remains unclear. Abrupt increases in ROS levels, i.e., above a physiological threshold, may be harmful and may among other events trigger cell death (Davila & Torres-Aleman, 2008). Oxidative stress has been linked to many neurodegenerative diseases, including Alzheimer's (Leuner *et al*, 2012) and Parkinson's (Schapira, 2008), but its role in mitochondrial disease remains unclear.

Cellular senescence is as a complex stress response by which proliferative cells lose the ability to divide and enter cell cycle arrest. Mounting evidence also showed accumulation of senescent cells with age, a process that may contribute to age-related phenotypes and pathologies (Byun *et al*, 2015). Dysfunctional mitochondria can induce cellular senescence both in *in vitro* culture (Moiseeva *et al*, 2009) and *in vivo* (Kang *et al*, 2013; Wiley *et al*, 2016). Some studies have implicated mitochondrial ROS in this process since ROS are capable of damaging nuclear DNA and thus activating a DNA damage response to induce senescence (Moiseeva *et al*, 2009). Redox changes, reflected by a lower NAD^+ /NADH ratio, were also likely to induce a senescence arrest (Lee *et al*, 2012). We showed that dysfunctional mitochondria due to POLG mutation could drive ROS overproduction and lower the NAD^+ /NADH ratio, raising the possibility that both were involved in generating the senescence response in POLG NSCs.

A previous study reported that the NAD^+ -dependent deacetylase SirT1 played an important role in the acceleration of cellular

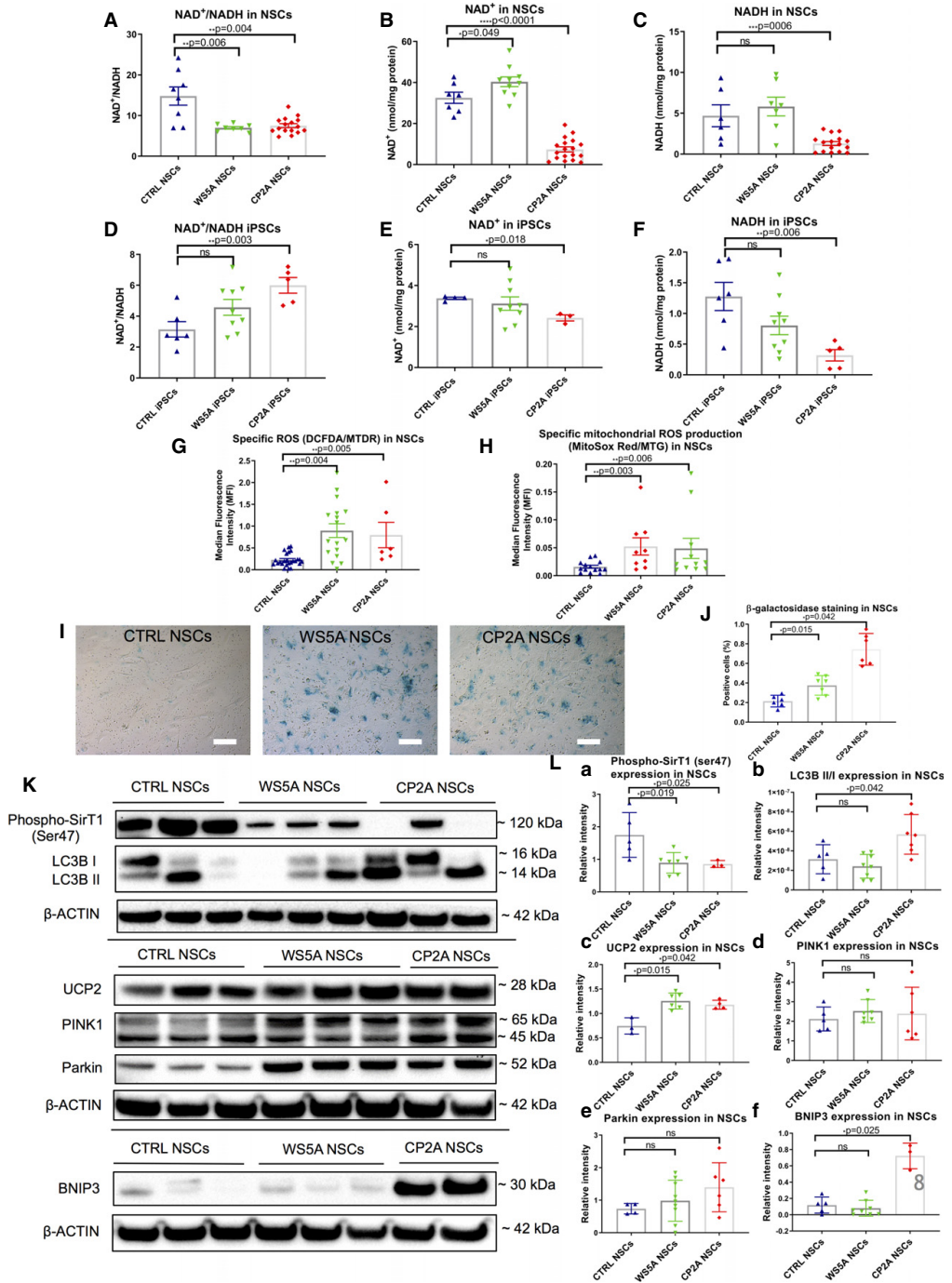


Figure 8.

Figure 8. NAD⁺ metabolism, ROS overproduction, exhibition of a senescence phenotype through UCP2/SirT1 and mitophagy activation via BNIP3.

A–C LC-MS-based metabolomics for quantitative measurements of NAD⁺/NADH ratio (A, $n = 3$, technical replicates per clone), NAD⁺ (B, $n = 3$, technical replicates per clone), and NADH (C, $n = 3$, technical replicates per clone) level in NSCs.
 D–F LC-MS-based metabolomics for quantitative measurement of NAD⁺/NADH ratio (D, $n = 3$, technical replicates per clone), NAD⁺ (E, $n = 3$, technical replicates per clone), and NADH (F, $n = 3$, technical replicates per clone) level in iPSCs.
 G Intracellular ROS production measurements of the specific ROS level calculated by total ROS/MTDR in control, WSSA, and CP2A iPSC-derived NSCs using DCFDA and MTDR ($n = 6$, technical replicates per clone for control; $n = 5$, technical replicates per clone for WSSA; $n = 3$, technical replicates per clone for CP2A).
 H Flow cytometric measurements of mitochondrial ROS production at the specific ROS level in Detroit 551, WSSA, and CP2A iPSC-derived NSCs calculated by total ROS (MitoSox Red)/MTG ($n = 4$, technical replicates per clone for control and CP2A; $n = 3$, technical replicates per clone for WSSA).
 I, J Representative images of senescence β -galactosidase staining (scale bars, 20 μ m) (I) and quantification by calculating the percentage of positively stained cells by division of the negative cells from I (J, $n = 3$, technical replicates per clone).
 K, L Representative images (K) and quantification (L) for western blotting with Phospho-SirT1 (Ser47), LC3B, UCP2, PINK1, Parkin, BNIP3, and β -ACTIN. Three independent experiments are included.

Data information: The data points in A–F and H represent iPSCs or iPSC-derived NSCs from 2 different clones from Detroit 551 control, 3 different clones from WSSA patient iPSCs, and 2 different clones from CP2A patient iPSCs. The data points in G represent NSCs generated from 5 different control iPSCs including 4 clones from Detroit 551 control and one clone from control AG05836, 3 clones from WSSA patient iPSCs, and 2 clones from CP2A patient iPSCs. The data points in J represent NSCs generated from 2 different clones from Detroit 551 control, 2 different clones from WSSA patient iPSCs, and 2 different clones from CP2A patient iPSCs. The data points in L represent NSCs generated from 2 to 3 different clones from Detroit 551 control and 3 different clones from WSSA patient iPSCs and 2–3 different clones from CP2A patient iPSCs. Data are presented as mean \pm SEM for the number of samples. Mann–Whitney *U*-test was used for the data presented in G, L, e, and L, f. Two-sided Student's *t*-test was used for the data presented in A–F, H, J, and L, a–d. Significance is denoted for *P* values of less than 0.05. **P* < 0.05; ***P* < 0.01; ****P* < 0.001; *****P* < 0.0001.

Source data are available online for this figure.

senescence induced by oxidative stress via p53 acetylation (Furukawa *et al.*, 2007). Further, it has been reported that SirT1 represses expression of the UCP2 gene by binding directly to the UCP2 promoter (Amat *et al.*, 2007). UCP2, a mitochondrial transporter present in the inner mitochondrial membrane, plays an important role in uncoupling oxidative phosphorylation and decreasing mitochondrial O₂ consumption by regulating the MMP. UCP2 overproduction following total loss of cellular ATP was found to induce irreversible metabolic changes and senescent-like morphology (Nishio & Ma, 2016). Here, we showed that SirT1 signaling decreased, while UCP2 signaling increased in POLG-mutated cells, suggesting that senescence may indeed contribute to neuronal loss in POLG-related diseases.

Mitophagy plays a role in maintaining mitochondrial health throughout life and preventing age-related disease. Mitophagy can either specifically eliminate damaged or dysfunctional mitochondria or clear all mitochondria during specialized developmental stages. Accumulating evidence suggests that mitophagy is associated with neurodegenerative disorders, including Parkinson's (Ryan *et al.*, 2015), Huntington's (Khalil *et al.*, 2015), and Alzheimer's disease (Fang *et al.*, 2019). Recent progress in mitophagy studies revealed that mitochondrial priming was mediated either by the PINK1-Parkin signaling pathway (Shiba-Fukushima *et al.*, 2012) or by the mitophagic receptors Nix (Vo *et al.*, 2019) and BNIP3 (Tang *et al.*, 2019). Our finding on the upregulation of BNIP3 protein levels and occurrence of mitochondrial autophagosomes in NSCs with heterozygous *POLG* mutations suggested active degradation through mitophagy. This evidence suggested that BNIP3-mediated autophagy/mitophagy may be involved in POLG-related pathogenesis.

There are two technical questions pertaining to our study that require discussion. Firstly, isogenic controls were not used. We recognize that the current state of the art is to compare patient samples to gene-corrected isogenic controls, usually made by CRISPR-based gene editing. In our studies, however, we considered that the use of multiple, age-matched controls ($n = 5$) remained a viable alternative. This choice was, in part, driven by the presence of a compound heterozygous patient (CP2A patient). Further, we

would point out that many studies still use age/gender-matched controls from healthy individuals as disease comparators as exemplified by the recent study of another *POLG* mutation, p.Q811R (Chumarina *et al.*, 2019). Nevertheless, in cases of loss of function mutations and to minimize background-specific confounding factors, we agree that gene-corrected isogenic controls or a well-executed rescue experiment should be conducted.

Secondly, we used retroviral reprogramming to generate most of the cell lines studied. Since the first experiments using integrating retroviral vectors, various approaches to deliver the reprogramming genes have been described, most notably newer integration-free and viral-free methods (Stadtfeld & Hochedlinger, 2010; Bellin *et al.*, 2012; Robinton & Daley, 2012). These new techniques avoid insertional mutagenesis and transgene reactivation and can minimize variability between reprogrammed cell lines. While non-integrating methods can benefit both disease modeling and the future use in cell transplantation therapies, many excellent studies of disease modeling have used the retroviral system (Bellin *et al.*, 2012). This may, in part, be explained by the limited protocol efficiencies of the new methods. Among the newer techniques, episomal plasmids and Sendai virus are the more commonly used (Okita *et al.*, 2011; Chumarina *et al.*, 2019), but reprogramming using synthetic mRNAs is also possible. As the non-integrating reprogramming technology improves, these technologies will be preferred in future studies.

In conclusion, our previous studies on patient tissues showed that *POLG* mutations lead to neuronal mtDNA depletion and, given sufficient time, point mutations and deletions (Tzoulis *et al.*, 2013, 2014). Our current studies confirm that there is loss of ATP and membrane potential that we believe leads to changes in redox potential and excess ROS production. We also find activation of mitophagy. Our hypothesis is that neuronal death occurs by two mechanisms: Firstly, the initiation of seizures in already stressed neurons exceeds the capacity of this neuron to maintain cellular energy production and thus cellular integrity and leads to acute neuronal death. Secondly, the loss of ATP with changes in redox potential and ROS production lead to neuronal dysfunction that eventually leads to chronic neuronal loss (Fig 9).

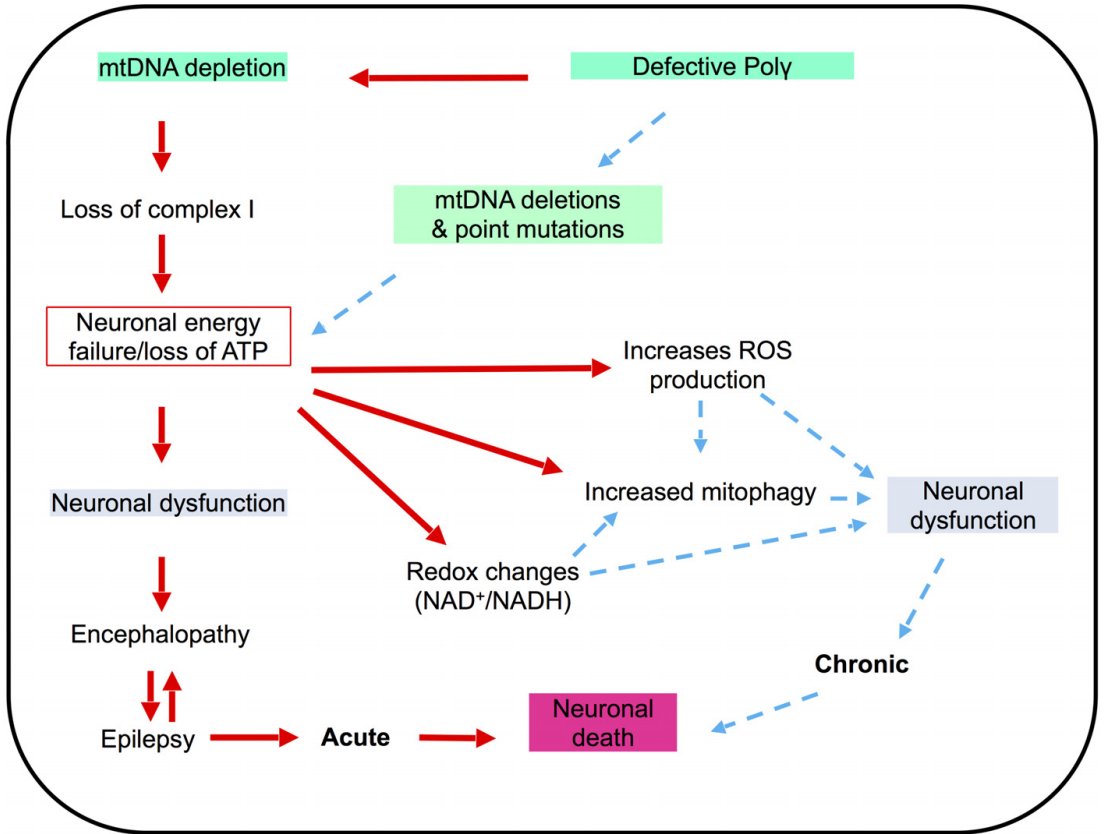


Figure 9. Summary of the possible disease mechanisms in neuronal cells with *POLG* mutations.

We believe that our studies are the first that show that it is possible to recapitulate the biochemical and molecular findings associated with the common mutations in *POLG*. Further, we believe that these studies demonstrate that iPSC-derived neural stem cells provide a robust model system in which to study tissue-specific mitochondrial disease manifestations. Since NSCs can be grown in large numbers in smaller formats, we hope to use this system to establish a high-throughput screening system in order to identify therapies for these devastating diseases. Our studies indicate further that the health potential of targeting NAD⁺ homeostasis will inform clinical study design to identify nutraceutical approaches for combating *POLG* disease.

Materials and Methods

Ethics approval

The project was approved by the Western Norway Committee for Ethics in Health Research (REK nr. 2012/919). Tissues were

acquired with written informed consent from all patients, and the experiments conformed to the principles set out in the WMA Declaration of Helsinki and the Department of Health and Human Services Belmont Report.

Derivation of iPSCs

Skin fibroblasts from one homozygous c.2243G>C, p.W748S/W748S (WS5A) and one compound heterozygous c.1399G>A/c.2243G>C, p.A467T/W748S (CP2A) patient were collected by punch biopsy and cultured in DMEM/F12, GlutaMAX™ (Thermo Fisher Scientific, cat. no. 10565018) with 10% (*v/v*) FBS (Sigma-Aldrich, cat. no. 12103C), 20 mM glutamine (Sigma-Aldrich, cat. no. G7513), 10 mM sodium pyruvate (Invitrogen, cat. no. 11360 070), and 0.5 mM uridine (Sigma-Aldrich, cat. no. U 3003). Detroit 551 (control 1, ATCC® CCL 110™, human normal fetal female fibroblast), CCD-1079Sk (control 2, ATCC® CRL-2097™, human normal new-born male fibroblast), and AG05836 (control 3, RRID:CVCL2B58, 44-year-old female fibroblasts) were used as controls. Control fibroblasts were grown in

DMEM/F12, GlutaMAX™ (Thermo Scientific, cat. no. 35050061) with 10% (*v/v*) FBS.

We reprogrammed Detroit 551 and CCD-1079Sk control fibroblasts, and patient fibroblasts using retroviral vectors encoding POU5F1, SOX2, Klf4, and c Myc as previously described (Siller *et al*, 2016). AG05836 control fibroblasts were reprogrammed by Sendai virus vectors. We also employed two human embryonic stem cell lines (hESCs) as controls: The hESC line 360 (male) was obtained from the Karolinska Institute, Sweden, (Strom *et al*, 2010) and H1 (male) from WiCell Research Institute (Thomson *et al*, 1998).

Both iPSC and hESC lines were maintained under feeder-free conditions using Geltrex (Invitrogen, cat. no. A1413302) in E8 medium (Invitrogen, cat. no. A1517001) in 6-well plates (Thermo Scientific, cat. no. 140675). Each line was passaged with 0.5 mM EDTA (Invitrogen, cat. no. 15575038) at 70–80% confluency. The E8 was changed every day, and the cells passaged every 3–4 days. All the cells were monitored for mycoplasma contamination regularly using MycoAlert™ Mycoplasma Detection Kit (Lonza, cat. no. LT07-218).

Neural induction

Neural induction was based on a previously described method (Stacpoole *et al*, 2011) with minor modifications. Briefly, 70% confluent iPSCs were split and seeded onto feeder-free Geltrex-coated plates in E8 medium. After 24 h, the medium was changed to neural induction medium prepared by addition of 10 μM SB431542 (Tocris Bioscience, cat. no. 1614), 10 μM N Acetyl L cysteine (NAC, Sigma-Aldrich, cat. no. A7250), and 2 μM AMPK inhibitor Compound C (EMD Millipore, cat. no. US1171261 1MG) to Chemically Defined Medium (CDM) containing 50% Iscove's Modified Dulbecco's Medium (IMDM, Invitrogen, cat. no. 21980 065), 50% F12 Nutrient Mixture (Ham) liquid with GlutaMAX™, 5 mg/ml bovine serum albumin (BSA) Fraction V (Europa bioproducts ITD, cat. no. EQBAC62 1000), 1% (*v/v*) Lipid 100 X (Invitrogen, cat. no. 11905 031), 450 μM 1 thioglycerol (Sigma-Aldrich, cat. no. M6145 25ML), 7 μg/ml insulin (Roche cat. no. 11376497001), and 15 mg/ml transferrin (Roche, cat. no. 10652202001). Medium was changed daily until cells reached the neural epithelial stage at day 5. The cells were then detached by incubation with collagenase IV (Invitrogen, cat. no. 17104 019) at 37°C for 1 min. After incubation, the cells were washed with DPBS without calcium and magnesium (DPBS^{-/-}) before addition of StemPro™ NSC medium supplemented with 1× GlutaMAX™, bFGF, and EGF (Thermo Fisher, cat. no. A1050901). Spheres were then generated by scraping a grid pattern at the bottom of each well using a pipette tip, and the cell suspensions transferred into 100 mm Corning® non-treated culture dishes (Sigma-Aldrich, cat. no. CLS430591) and incubated at 37°C on an orbital shaker (Fisher Scientific, cat. no. SGM 250 030K). After 2–3 days, the spheres were collected and dissociated into single cells by incubation with TrypLE™ Express at 37°C for 10 min followed by trituration. After neutralization with DMEM with 10% (*v/v*) FBS, the cell pellet was reconstituted in StemPro NSC medium and seeded on Geltrex-coated 6-well plates as monolayer NSCs. All the NSCs used for further analysis was limited to passages 4–9 in order to maintain them as primary lines.

Mitochondrial volume and MMP measurement

To measure mitochondrial volume and MMP, cells were double-stained with 150 nM MitoTracker Green (MTG) (Invitrogen, cat. no. M7514) and 100 nM TMRE (Abcam, cat. no. ab113852) for 45 min at 37°C. Cells treated with 100 μM FCCP (Abcam, cat. no. ab120081) were used as negative control. Stained cells were washed with PBS, detached with TrypLE™ Express, and neutralized with media containing 10% FBS. The cells were immediately analyzed on a FACS BD Accuri™ C6 flow cytometer (BD Biosciences, San Jose, CA, USA). The data analysis was performed using Accuri™ C6 software. For each sample, more than 40,000 events were analyzed, and doublets or dead cells excluded.

Mitochondrial DNA quantification and deletion assessment

DNA was extracted using a QIAGEN DNeasy Blood and Tissue Kit (QIAGEN, cat. no. 69504) according to the manufacturer's protocol. MtDNA quantification and depletion assessment were performed using RT-qPCR and long range polymerase chain reaction (Long-PCR) as previously described (Tzoulis *et al*, 2014).

Hepatocyte differentiation

Hepatocyte differentiation from iPSCs was optimized for patient and control lines using a previously established approach (Siller *et al*, 2015, 2016; Siller & Sullivan, 2017). Terminal differentiation to hepatocyte-like cells was performed using the optimal conditions identified above and following a previously reported small molecule driven protocol (Siller *et al*, 2015; Mathapati *et al*, 2016).

Immunohistochemistry for identifying the hepatocytes was performed as previously described (Siller *et al*, 2015, 2016; Mathapati *et al*, 2016; Siller & Sullivan, 2017). Images were obtained using a Zeiss LSM700 Confocal microscope (Carl Zeiss Meditec AG, Germany).

Cardiomyocyte differentiation

Cardiomyocyte differentiation was done utilizing a well-established protocol for generating cardiomyocytes through sequential activation and inhibition of Wnt signaling pathway (Lian *et al*, 2013).

Karyotype analyses

Human G banding karyotyping was performed using standard methods. For each cell line, 20 chromosomes were analyzed from live or fixed cells in metaphase. The analysis was performed using G banding and Leishman stain, and the cells were analyzed according to the Clinical Cytogenetics Standards and Guidelines published by the American College of Medical Genetics (Meisner & Johnson, 2008).

Glial cells and DA neuron differentiation

For astrocyte differentiation, NSCs were plated on poly-D-lysine (PDL)-coated coverslips (Neuvitro, cat. no. GG-12-15-PDL). The following day, the cells were washed with DPBS^{-/-} and cultured in astrocyte differentiation medium: DMEM/F-12, GlutaMAX™ supplemented with 1× N2 (Invitrogen, cat. no. 17502-048), 1× B27

(Invitrogen, cat. no. 17504044-10 ml), 200 ng/ml insulin-like growth factor-I (IGF-I) (Sigma-Aldrich, cat. no. 13769-50UG), 10 ng/ml heregulin 1 β (Sigma-Aldrich cat. no. SRP3055-50UG), 10 ng/ml activin A (PeproTech, cat. no. 120-14E), 8 ng/ml FGF2 (PeproTech, cat. no. 100-18B), and 1% FBS. The medium was changed every other day for the first week, every 2 days for the second week, and every 3 days for the third and fourth week.

After 28 days of differentiation, the cells were cultured in maturation medium AGMTM Astrocyte Growth Medium BulletKitTM (Lonza, cat. no. CC-3186), including Astrocyte Basal Medium supplemented with ascorbic acid, rhEGF, Gentamicin Sulfate/Amphotericin (GA-1000), insulin, L-glutamine, and FBS for one more month.

For glial oligodendrocyte differentiation, NSCs were plated at different cell densities onto surfaces coated with PDL or 0.01% poly-L-ornithine (Sigma-Aldrich, cat. no. P4957) and 5 μ g/ml laminin (Sigma-Aldrich, cat. no. L2020). After 2 days, differentiation was performed according to commercial protocol (Invitrogen). Briefly, oligodendrocyte differentiation medium was supplemented with 1 \times Neurobasal medium (Invitrogen, cat. no.: 21103049) with 2% B27 Serum Free Supplement, 2 mM GlutaMAXTM, and 30 ng/ml triiodothyronine (T3) (Sigma-Aldrich, cat. no. D6397). Differentiating oligodendrocyte cells were kept in these conditions, and the medium was changed every other day.

For DA neuron differentiation, neurospheres generated from neural induction were maintained in CDM supplemented with 100 ng/ml FGF8b (R&D systems, cat. no. 423-F8) over a period of 7 days to initiate DA progenitor induction. The following 7 days, the medium was changed to CDM supplemented with 1 μ M PM (EMD Millipore, cat. no. 540220-5MG) and 100 ng/ml FGF-8. Termination of the suspension cultures was performed by dissociating the spheres into single cells by incubation with TrypLETM Express followed by trituration and subsequent plating into monolayers. The DA neurons were matured in DA medium: CDM supplemented with 10 ng/ml BDNF (PeproTech, cat. no. 450-02) and 10 ng/ml GDNF (PeproTech, cat. no. 450-10) on poly-L-ornithine (Sigma-Aldrich, cat. no. P4957) and laminin (Sigma-Aldrich, cat. no. L2020)-coated plates.

Immunocytochemistry and immunofluorescence (ICC/IF)

Cells were fixed with 4% (*v/v*) paraformaldehyde (PFA, VWR, cat. no. 100503 917) and blocked using blocking buffer containing 1 \times PBS, 10% (*v/v*) normal goat serum (Sigma-Aldrich, cat. no. G9023) with 0.3% (*v/v*) TritonTM X-100 (Sigma-Aldrich, cat. no. X100-100ML). The cells were then incubated with primary antibody solution overnight at 4°C and further stained with secondary antibody solution (1:800 in blocking buffer) for 1 h at RT. iPSCs were stained for pluripotent markers using the primary antibodies rabbit Anti-SOX2 (Abcam, cat. no. ab97959, 1:100), rabbit Anti-POU5F1 (Abcam, cat. no. ab19857, 1:100), and mouse Anti-SSEA4 [MC813] (Abcam, cat. no. ab16287, 1:200). NSCs were stained with rabbit Anti-PAX6 (Abcam, cat. no. ab5790, 1:100), mouse Anti-NESTIN (10c2) (Santa Cruz Biotechnology, cat. no. sc23927, 1:50), rabbit Anti-SOX2, and mitochondrial complex I subunit rabbit Anti-NDUFB10 (Abcam, cat. no. ab196019, 1:1,000). Astrocytes and oligodendrocytes were stained with chicken Anti-GFAP (Abcam cat. no. ab4674, 1:400), rabbit Anti-S100 β (Abcam cat. no. ab196442,

1:100), rabbit Anti-EAAT1 (Abcam cat. no. ab416, 1:200), mouse Anti-Glutamine Synthetase (Abcam cat. no. ab64613, 1:200), rabbit Anti-GALC (Abcam cat. no. ab2894, 1:200), rabbit Anti-OLIGO2 (Abcam cat. no. ab2453, 1:1,000), and rabbit Anti-MBP (Abcam cat. no. ab62631, 1:500) respectively. The antibodies used for DA neuron staining were rabbit Anti-tyrosine hydroxylase (Abcam, cat. no. ab75875, 1:100), mouse Anti-Beta III Tubulin (Abcam, cat. no. ab78078, 1:1,000), and chicken Anti-MAP2 (Abcam, cat. no. ab5392, 1:100). The secondary antibodies used were Alexa Flour[®] goat Anti-rabbit 488 (Thermo Fisher Scientific, cat. no. A11008, 1:800), Alexa Flour[®] goat Anti-rabbit 594 (Thermo Fisher Scientific, cat. no. A11012, 1:800), Alexa Flour[®] goat Anti-mouse 594 (Thermo Fisher Scientific, cat. no. A11005, 1:800), and Alexa Flour[®] goat Anti-chicken 594 (Thermo Fisher Scientific, cat. no. A11042, 1:800). After incubation with secondary antibodies, the coverslips were mounted onto cover slides using Prolong Diamond Antifade Mountant with DAPI (Invitrogen, cat. no. P36962).

For staining of neurospheres, spheres were spread directly onto cover slides and left at RT until completely dry and then fixed with 4% (*v/v*) PFA. After two washes with PBS, the spheres were covered in PBS with 20% sucrose, sealed with parafilm, and incubated overnight at 4°C. The spheres were blocked with blocking buffer for 2 h at RT, and the primary antibodies were added to the samples overnight at 4°C. After washing the samples for 3 h in PBS with a few changes of buffer, incubation with secondary antibodies (as described above) was conducted overnight at 4°C in a humid and dark chamber. Coverslips were mounted using Fluoromount-G (Southern Biotech, cat. no. 0100 01) before imaging was performed using the Leica TCS SP5 or SP8 confocal microscope (Leica Microsystems, Germany).

ATP generation assay

The Luminescent ATP Detection Assay Kit (Abcam, cat. no. ab113849) was used to investigate intracellular ATP production. Cells were cultured in a Corning[®] 96-well flat, clear bottom, white wall plate (Life Sciences, cat. no. 3601), and ATP measurements were performed according to the manufacturer's protocol when cells had reached 90% confluence. The kit irreversibly inactivates ATP degrading enzymes (ATPases) during the lysis step and measures the luminescent signal corresponding to the endogenous levels of ATP. Three to six replicates were measured for each sample. Luminescence intensity was monitored using the Victor[®] XLight Multi-mode Plate Reader (PerkinElmer). To normalize the value with cell number, cells grown on the same 96-well plates were incubated with Janus Green cell normalization stain after manufacturer's instructions (Abcam, cat. no. ab111622). OD 595 nm was measured using the Labsystems Multiskan[®] Bichromatic plate reader (Titertek Instruments, USA).

ROS production

Intracellular ROS production was measured by flow cytometry using dual staining of 30 μ M DCFDA (Abcam, cat. no. b11385) and 150 nM MTDR (Invitrogen, cat. no. M22426), which enabled us to assess ROS level related to mitochondrial volume. Mitochondrial ROS production was quantified using co-staining of 10 μ M Mito-SOXTM red mitochondrial superoxide indicator (Invitrogen, cat. no.

M36008) and 150 nM MTG to evaluate ROS level in relation to mitochondrial volume. Stained cells were detached with TrypLE™ Express and neutralized with media containing 10% FBS. The cells were immediately analyzed on a FACS BD Accuri™ C6 flow cytometer. For each sample, more than 40,000 events were recorded, and doublets or dead cells excluded before data analysis was performed using the Accuri™ C6 software.

NAD⁺ metabolism measurement using LC-MS analysis

Cells were washed with PBS and extracted by addition of ice-cold 80% methanol followed by incubation at 4°C for 20 min. Thereafter, the samples were stored at -80°C overnight. The following day, samples were thawed on a rotating wheel at 4°C and subsequently centrifuged at 16,000 g and 4°C for 20 min. The supernatant was added to 1 volume of acetonitrile, and the samples were stored at -80°C until analysis. The pellet was dried and subsequently reconstituted in lysis buffer (20 mM Tris-HCl (pH 7.4), 150 mM NaCl, 2% SDS, 1 mM EDTA) to allow for protein determination (BCA assay).

Separation of the metabolites was achieved with a ZIC-pHILC column (150 × 4.6 mm, 5 μm; Merck) in combination with the Dionex UltiMate 3000 (Thermo Scientific) liquid chromatography system. The column was kept at 30°C. The mobile phase consisted of 10 mM ammonium acetate pH 6.8 (Buffer A) and acetonitrile (Buffer B). The flow rate was kept at 400 μl/min, and the gradient was set as follows: 0 min 20% Buffer B, 15 min to 20 min 60% Buffer B, and 35 min 20% Buffer B. Ionization was subsequently achieved by heated electrospray ionization facilitated by the HESI-II probe (Thermo Scientific) using the positive ion polarity mode and a spray voltage of 3.5 kV. The sheath gas flow rate was 48 units with an auxiliary gas flow rate of 11 units and a sweep gas flow rate of 2 units. The capillary temperature was 256°C, and the auxiliary gas heater temperature was 413°C. The stacked-ring ion guide (S-lens) radio frequency (RF) level was at 90 units. Mass spectra were recorded with the QExactive mass spectrometer (Thermo Scientific), and data analysis was performed with the Thermo Xcalibur Qual Browser. Standard curves generated for NAD⁺ and NADH were used as reference for metabolite quantification.

NAD⁺ metabolism measurement using colorimetric analysis

The ratio of NAD⁺/NADH was quantified with a commercial NAD⁺/NADH Quantitation Colorimetric Kit (BioVision, cat. no. K337) according to the manufacturer's instructions and as previously described (Gomes *et al.*, 2012).

Protein level assessment of TFAM and mitochondrial respiratory chain complexes

Cells were detached with TrypLE™ Express, pelleted, and fixed in 1.6% (*v/v*) PFA at RT for 10 min, before permeabilization with ice-cold 90% methanol at -20°C for 20 min. The cells were blocked using buffer containing 0.3 M glycine, 5% goat serum, and 1% BSA in PBS. For TFAM expression, cells were stained with Anti-TFAM antibody conjugated with Alexa Fluor® 488 (Abcam, cat. no. ab198308, 1:400) and Anti-TOMM20 antibody conjugated with Alexa Fluor® 488 (Santa Cruz Biotechnology, cat. no. sc 17764

AF488, 1:400), separately. Staining of mitochondrial respiratory chain complexes was conducted using primary antibodies Anti-NDUFB10 (Abcam, cat. no. ab196019, 1:1,000), Anti-SDHA [2E3GC12FB2AE2] (Abcam, cat. no. ab14715, 1:1,000), and Anti-COX IV [20E8C12] (Abcam, cat. no. ab14744, 1:1,000), followed by secondary antibody incubation (1:400). The cells were immediately analyzed on BD Accuri™ C6 flow cytometer, and Accuri™ C6 software was used for data analysis. Both dot plots of SSC-H/SSC-A and FSC-H/FSC-A were used to exclude duplicates. For each sample, more than 40,000 events were recorded.

Western blotting

Extraction of protein was performed using 1× RIPA lysis buffer (Sigma-Aldrich, cat. no. R0278) supplemented with Halt™ Protease and Phosphatase Inhibitor Cocktail (Invitrogen, cat. no. 78444). Protein concentration was determined using BCA protein assay (Thermo Fisher Scientific, cat. no. 23227). The cell protein was loaded into NuPAGE™ 4–12% Bis-Tris Protein Gels (Invitrogen, cat. no. NP0321PK2) and resolved in PVDF membrane (Bio-Rad, cat. no. 1704157) using the Trans-Blot® Turbo™ Transfer System (Bio-Rad, Denmark). Membranes were blocked with 5% non-fat dry milk or 5% BSA in TBST for 1 h at RT. Membranes were then incubated overnight at 4°C with rabbit monoclonal IgG Anti-UCP2 (1:1,000, Cell Signalling, cat. no. 89326), rabbit polyclonal IgG Anti-Phospho-SirT1 (Ser47) (1:2,000, Cell Signalling, cat. no. 2314), rabbit polyclonal IgG Anti-PINK1 (1:500, Proteintech, cat. no. 23274-1-AP), rabbit polyclonal IgG Anti-Parkin (1:500, Proteintech, cat. no. 14060-1-AP), rabbit polyclonal IgG Anti-LC3B (1:3,000, Abcam, cat. no. ab51520), rabbit polyclonal Anti-BNIP3 (1:1,000, Abcam, cat. no. ab10962) or rabbit polyclonal IgG Anti-UCP2 (1:500, Proteintech, cat. no. 11081-1-AP), and mouse monoclonal IgG Anti-β-ACTIN antibody conjugated to HRP (1:5,000, Abcam, cat. no. ab49900) as a control. After washing in TBST, membranes were incubated with donkey Anti-mouse monoclonal antibody or swine Anti-rabbit monoclonal antibody conjugated to HRP secondary antibody (Jackson ImmunoResearch, 1:1,000), for 1 h at RT. Super Signal West Pico Chemiluminescent Substrate (Thermo Fisher Scientific, cat. no. 34577) was used as enzyme substrate according to manufacturer's recommendations. The membranes were visualized in SynGene scanner (VWR, USA).

β-galactosidase staining assay

β-galactosidase activity was detected by using a Senescence β-galactosidase Staining Kit (Cell Signalling, cat. no. 9860) according to the manufacturer's instructions. The cells were seeded in complete media into 6-well plates with coverslips. After 24 h-incubation, the cells were fixed with 1× fixative solution and incubated with the β-galactosidase staining solution overnight at 37°C in a dry incubator without CO₂. Afterward, cells were observed, and images were captured under Nikon TE2000 fluorescence microscope.

Tissue studies

Formalin-fixed, paraffin-embedded (FFPE), and fresh frozen brain tissues were available from patients with POLG disease (*n* = 5) and neurologically healthy controls (*n* = 5) who were demographically

matched. Informed consent was obtained from all subjects and that the experiments conformed to the principles set out in the WMA Declaration of Helsinki and the Department of Health and Human Services Belmont Report. The *POLG* mutations for these patients are A467T/G303R (AL-1B); A467T/A467T (AT-1A); A467T/A467T (AT-2A); W748S/W748S (WS-10A); and W748S/W748S (WS-3A). Patient IDs used in our previous publications were shown in parenthesis to allow comparison with results of our earlier work. There were no statistically significant differences in post-mortem interval or length of fixation between patient and control tissue. Samples were dissected at autopsy and either snap-frozen immediately in isopentane, which had been cooled in liquid nitrogen, and stored at -80°C , or fixed in formaldehyde and later embedded in paraffin blocks according to standard procedures.

Mitochondrial complex I immunohistochemistry was performed on 4- μm sections of formalin-fixed, paraffin-embedded tissue from the primary occipital cortex of three patients and two neurologically healthy controls as previously described (Tzoulis et al, 2014).

Neurons for mtDNA analysis were microdissected from frozen sections of primary occipital (Brodmann area 17) from five patients and five age-matched controls. Microdissection and cell lysis were carried out as previously described (Tzoulis et al, 2013). Only cells that could be positively identified as neurons, with a visible nucleus and normal morphological characteristics, were used. For each area, there was no significant size difference between neurons of patients and corresponding controls. A total of 400 neurons were picked from 5 patients ($n = 200$) and five age-matched controls ($n = 200$). Neurons were microdissected, avoiding carryover of glia or other cells, and pooled in 3–5 groups of 10 cells per individual. MtDNA copy number quantification was performed in microdissected neurons by qRT-PCR, using TaqMan fluorogenic probes and a 7500 fast sequence detection system (ABI) as previously described (Tzoulis et al, 2013).

Gene expression

Total RNA was isolated using MagMAX™ 96 Total RNA isolation Kit (Thermo Fisher Scientific, cat. no. AM1830). High-throughput MagMAX™ Express 96 was employed to extract RNA from the cell lysate.

EXPRESS One Step Superscript™ RT-qPCR Kit (Thermo Fisher Scientific, cat. no. 11781 200) and TaqMan™ Probes were recruited to perform cDNA synthesis and RT-qPCR in one step. Applied Biosystems 7500 Fast Real-Time PCR machine (Thermo Fisher Scientific) was used to perform qRT-PCR. TaqMan™ probes (Life Technologies) for *POU5F1* (Hs00999634), *NANOG* (Hs04260366), *PAX6* (Hs01088114), *NESTIN* (Hs04187831), and *LIN28A* (Hs00702808) were used. The average CT values of three technical replicates were normalized to the geometric mean of endogenous control gene, *Actin Beta* (ACTB; Hs01060665). The expression of the iPSC markers was assessed with fold change by using the comparative $\Delta\Delta C_t$ method by normalizing the gene level from ESC1. The expression of the NSC markers was assessed with fold change by using the comparative $\Delta\Delta C_t$ method by normalizing NSCs to iPSCs.

DNA sequencing for *POLG* mutations

Forward and backward oligonucleotide primers were used to amplify the 7 exons and 13 exons of the *POLG* gene, as reported

The paper explained

Problem

Mitochondrial diseases are the most common with inborn errors of metabolism and mutations in *POLG*, the gene encoding the catalytic subunit of the mitochondrial DNA polymerase gamma, the most common subgroup. These diseases are often associated with catastrophic involvement of the brain, and currently, there are no cures and no robust models to study disease mechanisms in neuronal tissue. We used neural stem cells (NSCs) produced from patient induced pluripotent stem cells (iPSCs) to study disease mechanisms.

Results

We generated iPSCs containing two founder mutations (W748S homozygous; W748S/A467T compound heterozygous) and differentiated these into NSCs. These neural precursors manifested features that faithfully replicated the molecular and biochemical changes found in patient post-mortem brain tissue, namely mtDNA depletion and loss of complex I. We also confirmed the same phenotypes in dopaminergic neurons generated from these iPSCs. *POLG*-driven mitochondrial dysfunction also led to neuronal ROS overproduction, increased cellular senescence, and disturbed NAD^+ metabolism, a feature that reflected the loss of complex I.

Impact

This is the first model of *POLG* disease that replicates exactly what is seen in patient tissues. Using this system, it was possible to examine the consequences of *POLG*-induced loss of mtDNA and complex I and show how *POLG* mutations affects NAD^+ metabolism and cellular fate. We believe that iPSC-derived NSCs provide a robust model system in which to study tissue specific mitochondrial disease manifestations, and we hope to use this system to establish a high-throughput screening system in order to identify therapies for these devastating diseases.

elsewhere (Hakonen et al, 2005). Automated nucleotide sequencing was performed using the Applied Biosystems™ BigDye® Terminator v3.1 Cycle Sequencing Kit (Invitrogen, cat. no. 4337454) and analyzed on an ABI3730 Genetic Analyzer with sequencing analyzer software ChromasPro (Technelysium Pty Ltd, Australia). The primers designed for seven exons in *POLG* 1 gene were: forward, 5' TGTAAAACGACGGCCAGTGAAAGAAGCTGAG GCTCCGAG 3' and reverse, 5' CAGGAAACAGCTATGACCCTACAGAGCCA GTCCACT 3'. The primers designed for 13 exons in *POLG* 1 gene were: forward, 5' TGTAAAACGACGGCCAGTATTTCCAGCTG ATGACGAC 3' and reverse, 5' CAGGAAACAGCTATGACCTGCCACCGGACT TTCATTAG 3'. DNA Chromatogram was aligned with the best matching human sequences in NCBI Trace.

Data analysis

In order to minimize the phenotypic diversity caused by intraclonal heterogeneity which is a common issue for iPSC-related studies, multiple clones in each line were included in the all the analysis and more than three biological repeats were conducted for each clone to ensure adequate power to detect a prespecified effect size. Data were presented as mean \pm standard error of the mean (SEM) for the number of samples ($n \geq 3$ per clone). Distributions were tested for normality using the Shapiro–Wilk test. Outliers were detected using interquartile range (IQR) and Tukey's Hinges test. Mann–

Whitney *U*-test was used to assess statistical significance for variables with non-normal distribution, while two-sided Student's *t*-test was applied for normal distributed variables. Data were analyzed with SPSS software (SPSS v.25, IBM), and figures were produced by GraphPad Prism software (Prism 7.0, GraphPad Software, Inc.). Significance was denoted for *P* values of less than 0.05.

Data availability

This study includes no data deposited in external repositories.

Expanded View for this article is available online.

Acknowledgements

The authors encourage all laboratory members for discussions and critical reading of the manuscript. We are grateful to the Molecular Imaging Centre, Flow Cytometry Core Facility and Genomics Core Facility in University of Bergen in Norway. This work was supported by funding from the Norwegian Research Council (project no. 229652), Rakel og Otto Kr.Bruuns legat and Meltzer (project no. 809432). GJS was partly supported by the Norwegian Research Council through its Centres of Excellence funding scheme (project number 262613).

Author contributions

KXL, LAB, and GJS conceptualized. KXL involved in methodology. KXL, CKK, SM, GHV, GAZ, AK, CT, LEH, MZ, RMP, ZZ, and NB investigated. KXL and CKK wrote original draft. KXL, CKK, MZ, YH, RS, GJS, and LAB involved in writing, review, and editing. JF performed statistical analysis. LAB, KXL, and GJS acquired funding. GJS, MZ, and LAB provided resources. KXL and LAB supervised. All authors agree to the authorship.

Conflict of interest

The authors declare that they have no conflict of interest.

References

- Abramov AY, Smulders-Srinivasan TK, Kirby DM, Acin-Perez R, Enriquez JA, Lightowlers RN, Duchon MR, Turnbull DM (2010) Mechanism of neurodegeneration of neurons with mitochondrial DNA mutations. *Brain* 133: 797–807
- Agnello M, Morici G, Rinaldi AM (2008) A method for measuring mitochondrial mass and activity. *Cytotechnology* 56: 145–149
- Amat R, Solanes G, Giralt M, Villarroya F (2007) SIRT1 is involved in glucocorticoid-mediated control of uncoupling protein-3 gene transcription. *J Biol Chem* 282: 34066–34076
- Bae YS, Oh H, Rhee SG, Yoo YD (2011) Regulation of reactive oxygen species generation in cell signaling. *Mol Cells* 32: 491–509
- Bellin M, Marchetto MC, Gage FH, Mummery CL (2012) Induced pluripotent stem cells: the new patient? *Nat Rev Mol Cell Biol* 13: 713–726
- Bordone L, Motta MC, Picard F, Robinson A, Jhala US, Apfeld J, McDonagh T, Lemieux M, McBurney M, Szilvasi A et al (2006) Sirt1 regulates insulin secretion by repressing UCP2 in pancreatic beta cells. *PLoS Biol* 4: e31
- Brand MD (2016) Mitochondrial generation of superoxide and hydrogen peroxide as the source of mitochondrial redox signaling. *Free Radic Biol Med* 100: 14–31
- Byun HO, Lee YK, Kim JM, Yoon G (2015) From cell senescence to age-related diseases: differential mechanisms of action of senescence-associated secretory phenotypes. *BMB Rep* 48: 549–558
- Chinnery PF (2015) Mitochondrial disease in adults: what's old and what's new? *EMBO Mol Med* 7: 1503–1512
- Chumarina M, Russ K, Azevedo C, Heuer A, Pihl M, Collin A, Frostner EA, Elmer E, Hyttel P, Cappelletti G et al (2019) Cellular alterations identified in pluripotent stem cell-derived midbrain spheroids generated from a female patient with progressive external ophthalmoplegia and parkinsonism who carries a novel variation (p. Q811R) in the POLG1 gene. *Acta Neuropathol Commun* 7: 208
- Cui H, Kong Y, Zhang H (2012) Oxidative stress, mitochondrial dysfunction, and aging. *J Signal Transduct* 2012: 646354
- Davalli P, Mitic T, Caporali A, Lauriola A, D'Arca D (2016) ROS, cell senescence, and novel molecular mechanisms in aging and age-related diseases. *Oxid Med Cell Longev* 2016: 3565127
- Davila D, Torres-Aleman I (2008) Neuronal death by oxidative stress involves activation of FOXO3 through a two-arm pathway that activates stress kinases and attenuates insulin-like growth factor I signaling. *Mol Biol Cell* 19: 2014–2025
- Doherty E, Perl A (2017) Measurement of mitochondrial mass by flow cytometry during oxidative stress. *React Oxyg Species (Apex)* 4: 275–283
- Fang EF, Hou Y, Palikaras K, Adriaanse BA, Kerr JS, Yang B, Lautrup S, Hasan-Olive MM, Caponio D, Dan X et al (2019) Mitophagy inhibits amyloid-beta and tau pathology and reverses cognitive deficits in models of Alzheimer's disease. *Nat Neurosci* 22: 401–412
- Ferrari G, Lamantea E, Donati A, Filosto M, Briem E, Carrara F, Parini R, Simonati A, Santer R, Zeviani M (2005) Infantile hepatocerebral syndromes associated with mutations in the mitochondrial DNA polymerase-gammaA. *Brain* 128: 723–731
- Flonas IH, Fernandez-Vizarra E, Lykouri M, Brakedal B, Skeie GO, Miletic H, Lilleng PK, Alves G, Tysnes OB, Haugarvoll K et al (2018) Neuronal complex I deficiency occurs throughout the Parkinson's disease brain, but is not associated with neurodegeneration or mitochondrial DNA damage. *Acta Neuropathol* 135: 409–425
- Forkink M, Manjeri GR, Liemburg-Apers DC, Nibbeling E, Blanchard M, Wojtala A, Smeitink JA, Wieckowski MR, Willems PH, Koopman WJ (2014) Mitochondrial hyperpolarization during chronic complex I inhibition is sustained by low activity of complex II, III, IV and V. *Biochim Biophys Acta* 1837: 1247–1256
- Furukawa A, Tada-Oikawa S, Kawanishi S, Oikawa S (2007) H₂O₂ accelerates cellular senescence by accumulation of acetylated p53 via decrease in the function of SIRT1 by NAD⁺ depletion. *Cell Physiol Biochem* 20: 45–54
- Gomes AP, Duarte FV, Nunes P, Hubbard BP, Teodoro JS, Varela AT, Jones JG, Sinclair DA, Palmeira CM, Rolo AP (2012) Berberine protects against high fat diet-induced dysfunction in muscle mitochondria by inducing SIRT1-dependent mitochondrial biogenesis. *Biochim Biophys Acta* 1822: 185–195
- Griffin TA, Anderson HC, Wolfe JH (2015) *Ex vivo* gene therapy using patient iPSC-derived NSCs reverses pathology in the brain of a homologous mouse model. *Stem Cell Reports* 4: 835–846
- Hakonen AH, Heiskanen S, Juvonen V, Lappalainen I, Luoma PT, Rantamaki M, Goethem GV, Lofgren A, Hackman P, Paetau A et al (2005) Mitochondrial DNA polymerase W748S mutation: a common cause of autosomal recessive ataxia with ancient European origin. *Am J Hum Genet* 77: 430–441
- Hayashi G, Cortopassi G (2015) Oxidative stress in inherited mitochondrial diseases. *Free Radic Biol Med* 88: 10–17

- Houtkooper RH, Canto C, Wanders RJ, Auwerx J (2010) The secret life of NAD⁺: an old metabolite controlling new metabolic signaling pathways. *Endocr Rev* 31: 194–223
- Kang S, Louboutin JP, Datta P, Landel CP, Martinez D, Zervos AS, Strayer DS, Fernandes-Alnemri T, Alnemri ES (2013) Loss of HtrA2/Omi activity in non-neuronal tissues of adult mice causes premature aging. *Cell Death Differ* 20: 259–269
- Kang E, Wang X, Tippner-Hedges R, Ma H, Folmes CD, Gutierrez NM, Lee Y, Van Dyken C, Ahmed R, Li Y et al (2016) Age-related accumulation of somatic mitochondrial DNA mutations in adult-derived human iPSCs. *Cell Stem Cell* 18: 625–636
- Kanherkar RR, Bhatia-Dey N, Makarev E, Csoka AB (2014) Cellular reprogramming for understanding and treating human disease. *Front Cell Dev Biol* 2: 67
- Kazachkova N, Ramos A, Santos C, Lima M (2013) Mitochondrial DNA damage patterns and aging: revising the evidences for humans and mice. *Aging Dis* 4: 337–350
- Kerr JS, Adriaanse BA, Greig NH, Mattson MP, Cader MZ, Bohr VA, Fang EF (2017) Mitophagy and Alzheimer's disease: cellular and molecular mechanisms. *Trends Neurosci* 40: 151–166
- Khalil B, El Fissi N, Aouane A, Cabriol-Pol MJ, Rival T, Liévins JC (2015) PINK1-induced mitophagy promotes neuroprotection in Huntington's disease. *Cell Death Dis* 6: e1617
- Kim SU, Lee HJ, Kim YB (2013) Neural stem cell-based treatment for neurodegenerative diseases. *Neuropathology* 33: 491–504
- Korolchuk VI, Miwa S, Carroll B, von Zglinicki T (2017) Mitochondria in cell senescence: is mitophagy the weakest link? *EBioMedicine* 21: 7–13
- Krohn AJ, Wahlbrink T, Pohn JH (1999) Mitochondrial depolarization is not required for neuronal apoptosis. *J Neurosci* 19: 7394–7404
- Lamantea E, Tiranti V, Bordoni A, Toscano A, Bono F, Servidei S, Papadimitriou A, Spelbrink H, Silvestri L, Casari G et al (2002) Mutations of mitochondrial DNA polymerase gammaA are a frequent cause of autosomal dominant or recessive progressive external ophthalmoplegia. *Ann Neurol* 52: 211–219
- Lee SM, Dho SH, Ju SK, Maeng JS, Kim JY, Kwon KS (2012) Cytosolic malate dehydrogenase regulates senescence in human fibroblasts. *Biogerontology* 13: 525–536
- Leuner K, Schutt T, Kurz C, Eckert SH, Schiller C, Occhipinti A, Mai S, Jendrach M, Eckert GP, Kruse SE et al (2012) Mitochondrion-derived reactive oxygen species lead to enhanced amyloid beta formation. *Antioxid Redox Signal* 16: 1421–1433
- Li X (2013) SIRT1 and energy metabolism. *Acta Biochim Biophys Sin (Shanghai)* 45: 51–60
- Li S, Guo J, Ying Z, Chen S, Yang L, Chen K, Long Q, Qin D, Pei D, Liu X (2015) Valproic acid-induced hepatotoxicity in Alpers syndrome is associated with mitochondrial permeability transition pore opening-dependent apoptotic sensitivity in an induced pluripotent stem cell model. *Hepatology* 61: 1730–1739
- Li L, Chao J, Shi Y (2018) Modeling neurological diseases using iPSC-derived neural cells: iPSC modeling of neurological diseases. *Cell Tissue Res* 371: 143–151
- Lian X, Zhang J, Azarin SM, Zhu K, Hazeltine LB, Bao X, Hsiao C, Kamp TJ, Palecek SP (2013) Directed cardiomyocyte differentiation from human pluripotent stem cells by modulating Wnt/beta-catenin signaling under fully defined conditions. *Nat Protoc* 8: 162–175
- Lorenz C, Lesimple P, Bukowiecki R, Zink A, Inak G, Mlody B, Singh M, Semtner M, Mah N, Aure K et al (2017) Human iPSC-derived neural progenitors are an effective drug discovery model for neurological mtDNA disorders. *Cell Stem Cell* 20: 659–674 e659
- Luoma P, Melberg A, Rinne JO, Kaukonen JA, Nupponen NN, Chalmers RM, Oldfors A, Rautakorpi I, Peltonen L, Majamaa K et al (2004) Parkinsonism, premature menopause, and mitochondrial DNA polymerase gamma mutations: clinical and molecular genetic study. *Lancet* 364: 875–882
- Ma H, Folmes CD, Wu J, Morey R, Mora-Castilla S, Ocampo A, Ma L, Poulton J, Wang X, Ahmed R et al (2015) Metabolic rescue in pluripotent cells from patients with mtDNA disease. *Nature* 524: 234–238
- Marchetto MC, Brennand KJ, Boyer LF, Gage FH (2011) Induced pluripotent stem cells (iPSCs) and neurological disease modeling: progress and promises. *Hum Mol Genet* 20: R109–R115
- Mathapati S, Siller R, Impellizzeri AA, Lycke M, Vegheim K, Almaas R, Sullivan GJ (2016) Small-molecule-directed hepatocyte-like cell differentiation of human pluripotent stem cells. *Curr Protoc Stem Cell Biol* 38: 1G 6.1–1G 6.18
- Meisner LF, Johnson JA (2008) Protocols for cytogenetic studies of human embryonic stem cells. *Methods* 45: 133–141
- Moiseeva O, Bourdeau V, Roux A, Deschenes-Simard X, Ferbeyre G (2009) Mitochondrial dysfunction contributes to oncogene-induced senescence. *Mol Cell Biol* 29: 4495–4507
- Naviaux RK, Nguyen KV (2004) POLG mutations associated with Alpers' syndrome and mitochondrial DNA depletion. *Ann Neurol* 55: 706–712
- Nishio K, Ma Q (2016) Effect of overproduction of mitochondrial uncoupling protein 2 on Cos7 cells: induction of senescent-like morphology and oncotic cell death. *Curr Aging Sci* 9: 229–238
- Okita K, Matsumura Y, Sato Y, Okada A, Morizane A, Okamoto S, Hong H, Nakagawa M, Tanabe K, Tezuka K et al (2011) A more efficient method to generate integration-free human iPS cells. *Nat Methods* 8: 409–412
- Palin EJ, Paetau A, Suomalainen A (2013) Mesencephalic complex I deficiency does not correlate with parkinsonism in mitochondrial DNA maintenance disorders. *Brain* 136: 2379–2392
- Pendergrass W, Wolf N, Poot M (2004) Efficacy of MitoTracker Green and CMXRosamine to measure changes in mitochondrial membrane potentials in living cells and tissues. *Cytometry A* 61: 162–169
- Pryde KR, Taanman JW, Schapira AH (2016) A LON-ClpP proteolytic axis degrades complex I to extinguish ROS production in depolarized mitochondria. *Cell Rep* 17: 2522–2531
- Robinton DA, Daley GQ (2012) The promise of induced pluripotent stem cells in research and therapy. *Nature* 481: 295–305
- Ryan BJ, Hoek S, Fon EA, Wade-Martins R (2015) Mitochondrial dysfunction and mitophagy in Parkinson's: from familial to sporadic disease. *Trends Biochem Sci* 40: 200–210
- Schapira AH (2008) Mitochondria in the aetiology and pathogenesis of Parkinson's disease. *Lancet Neurol* 7: 97–109
- Shiba-Fukushima K, Imai Y, Yoshida S, Ishihama Y, Kanao T, Sato S, Hattori N (2012) PINK1-mediated phosphorylation of the Parkin ubiquitin-like domain primes mitochondrial translocation of Parkin and regulates mitophagy. *Sci Rep* 2: 1002
- Siller R, Greenhough S, Naumovska E, Sullivan GJ (2015) Small-molecule-driven hepatocyte differentiation of human pluripotent stem cells. *Stem Cell Reports* 4: 939–952
- Siller R, Naumovska E, Mathapati S, Lycke M, Greenhough S, Sullivan GJ (2016) Development of a rapid screen for the endodermal differentiation potential of human pluripotent stem cell lines. *Sci Rep* 6: 37178
- Siller R, Sullivan GJ (2017) Rapid screening of the endodermal differentiation potential of human pluripotent stem cells. *Curr Protoc Stem Cell Biol* 43: 1G 7.1–1G 7.23

- Stacpoole SR, Bilican B, Webber DJ, Luzhynskaya A, He XL, Compston A, Karadottir R, Franklin RJ, Chandran S (2011) Efficient derivation of NPCs, spinal motor neurons and midbrain dopaminergic neurons from hESCs at 3% oxygen. *Nat Protoc* 6: 1229–1240
- Stadtfeld M, Hochedlinger K (2010) Induced pluripotency: history, mechanisms, and applications. *Genes Dev* 24: 2239–2263
- Strom S, Holm F, Bergstrom R, Stromberg AM, Hovatta O (2010) Derivation of 30 human embryonic stem cell lines—improving the quality. *In Vitro Cell Dev Biol Anim* 46: 337–344
- Tabar V, Studer L (2014) Pluripotent stem cells in regenerative medicine: challenges and recent progress. *Nat Rev Genet* 15: 82–92
- Tang C, Han H, Liu Z, Liu Y, Yin L, Cai J, He L, Liu Y, Chen G, Zhang Z et al (2019) Activation of BNIP3-mediated mitophagy protects against renal ischemia-reperfusion injury. *Cell Death Dis* 10: 677
- Thomson JA, Itskovitz-Eldor J, Shapiro SS, Waknitz MA, Swiergiel JJ, Marshall VS, Jones JM (1998) Embryonic stem cell lines derived from human blastocysts. *Science* 282: 1145–1147
- Tzoulis C, Engelsens BA, Telstad W, Aasly J, Zeviani M, Winterthun S, Ferrari G, Aarseth JH, Bindoff LA (2006) The spectrum of clinical disease caused by the A467T and W748S POLG mutations: a study of 26 cases. *Brain* 129: 1685–1692
- Tzoulis C, Tran GT, Schwarzlmuller T, Specht K, Haugarvoll K, Balafkan N, Lilleng PK, Miletic H, Biermann M, Bindoff LA (2013) Severe nigrostriatal degeneration without clinical parkinsonism in patients with polymerase gamma mutations. *Brain* 136: 2393–2404
- Tzoulis C, Tran GT, Coxhead J, Bertelsen B, Lilleng PK, Balafkan N, Payne B, Miletic H, Chinnery PF, Bindoff LA (2014) Molecular pathogenesis of polymerase gamma-related neurodegeneration. *Ann Neurol* 76: 66–81
- Van Goethem G, Luoma P, Rantamaki M, Al Memar A, Kaakkola S, Hackman P, Krahe R, Lofgren A, Martin JJ, De Jonghe P et al (2004) POLG mutations in neurodegenerative disorders with ataxia but no muscle involvement. *Neurology* 63: 1251–1257
- Vo MT, Smith BJ, Nicholas J, Choi YB (2019) Activation of NIX-mediated mitophagy by an interferon regulatory factor homologue of human herpesvirus. *Nat Commun* 10: 3203
- Wiley CD, Velarde MC, Lecot P, Liu S, Sarnoski EA, Freund A, Shirakawa K, Lim HW, Davis SS, Ramanathan A et al (2016) Mitochondrial dysfunction induces senescence with a distinct secretory phenotype. *Cell Metab* 23: 303–314
- Winterthun S, Ferrari G, He L, Taylor RW, Zeviani M, Turnbull DM, Engelsens BA, Moen G, Bindoff LA (2005) Autosomal recessive mitochondrial ataxic syndrome due to mitochondrial polymerase gamma mutations. *Neurology* 64: 1204–1208
- Zheng H, Huang Q, Huang S, Yang X, Zhu T, Wang W, Wang H, He S, Ji L, Wang Y et al (2018) Senescence inducer shikonin ROS-dependently suppressed lung cancer progression. *Front Pharmacol* 9: 519
- Zurita F, Galera T, Gonzalez-Paramos C, Moreno-Izquierdo A, Schneiderat P, Fraga MF, Fernandez AF, Garesse R, Gallardo ME (2016) Generation of a human iPSC line from a patient with a defect of intergenomic communication. *Stem Cell Res* 16: 120–123



License: This is an open access article under the terms of the Creative Commons Attribution 4.0 License, which permits use, distribution and reproduction in any medium, provided the original work is properly cited.

Expanded View Figures

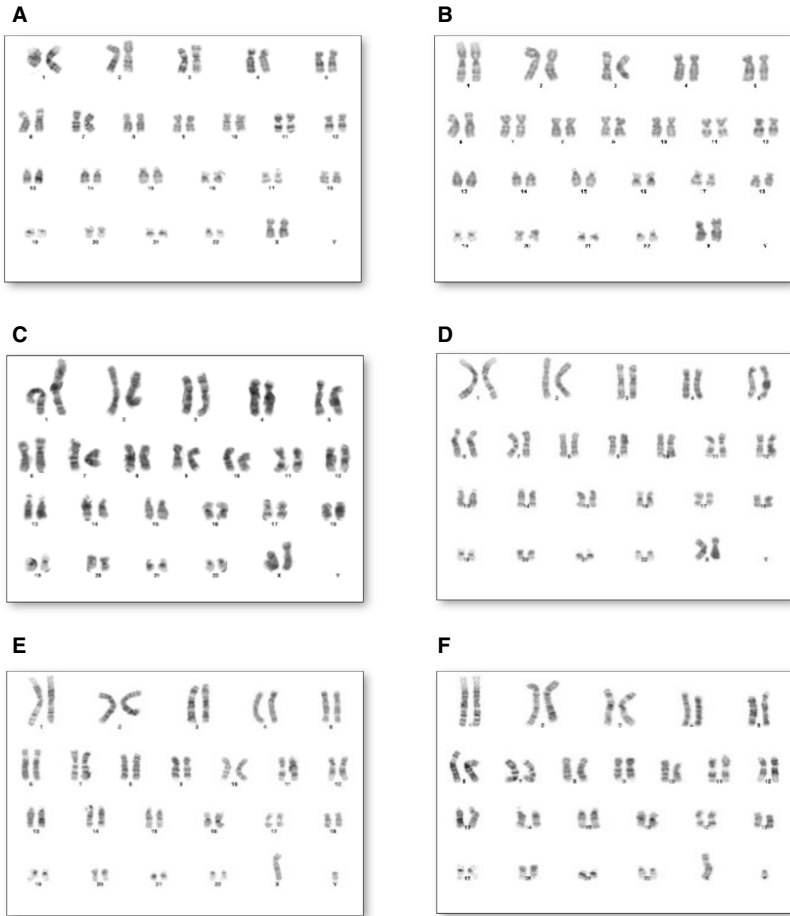


Figure EV1. Karyotype analysis for parental fibroblasts and reprogrammed iPSC lines.

A, C, E Representative karyotypes for Detroit 551 control fibroblasts (A) and WS5A and CP2A POLG fibroblasts (C, E).
B, D, F Representative karyotypes for control iPSC line (B) and POLG iPSC lines (D, F).

Figure EV2. Flow cytometric analysis of expression level of pluripotency markers TRA-1-60, TRA-1-81 and NANOG in iPSC lines.

A–C Flow cytometric analysis of expression level of pluripotency markers TRA-1-60 (A, $n = 3$, technical replicates per line/clone), TRA-1-81 (B, $n = 3$, technical replicates per line/clone), and NANOG (C, $n = 9$, technical replicates per line/clone for ESCs, control, and WS5A iPSCs; $n = 6$, technical replicates per clone for CP2A iPSCs) in ESC and iPSC lines. Data are demonstrated as individual clones (left panel, a) and combination as a group for ESCs, CTRL iPSCs, and WS5A and CP2A patient lines (right panel, b).

Data information: The data points in A–C represent 2 ESC lines, 2 different control clones from Detroit 551 iPSCs, 3 different iPSC clones from WS5A patient, and 2 different clones from CP2A patient iPSCs. Data are presented as mean \pm SEM for the number of samples. Mann–Whitney *U*-test was used for the data presented in B, b. Two-sided Student's *t*-test was used for the data presented in A, b and C, b. Significance is denoted for *P* values of less than 0.05. * $P < 0.05$; ** $P < 0.01$.

Source data are available online for this figure.

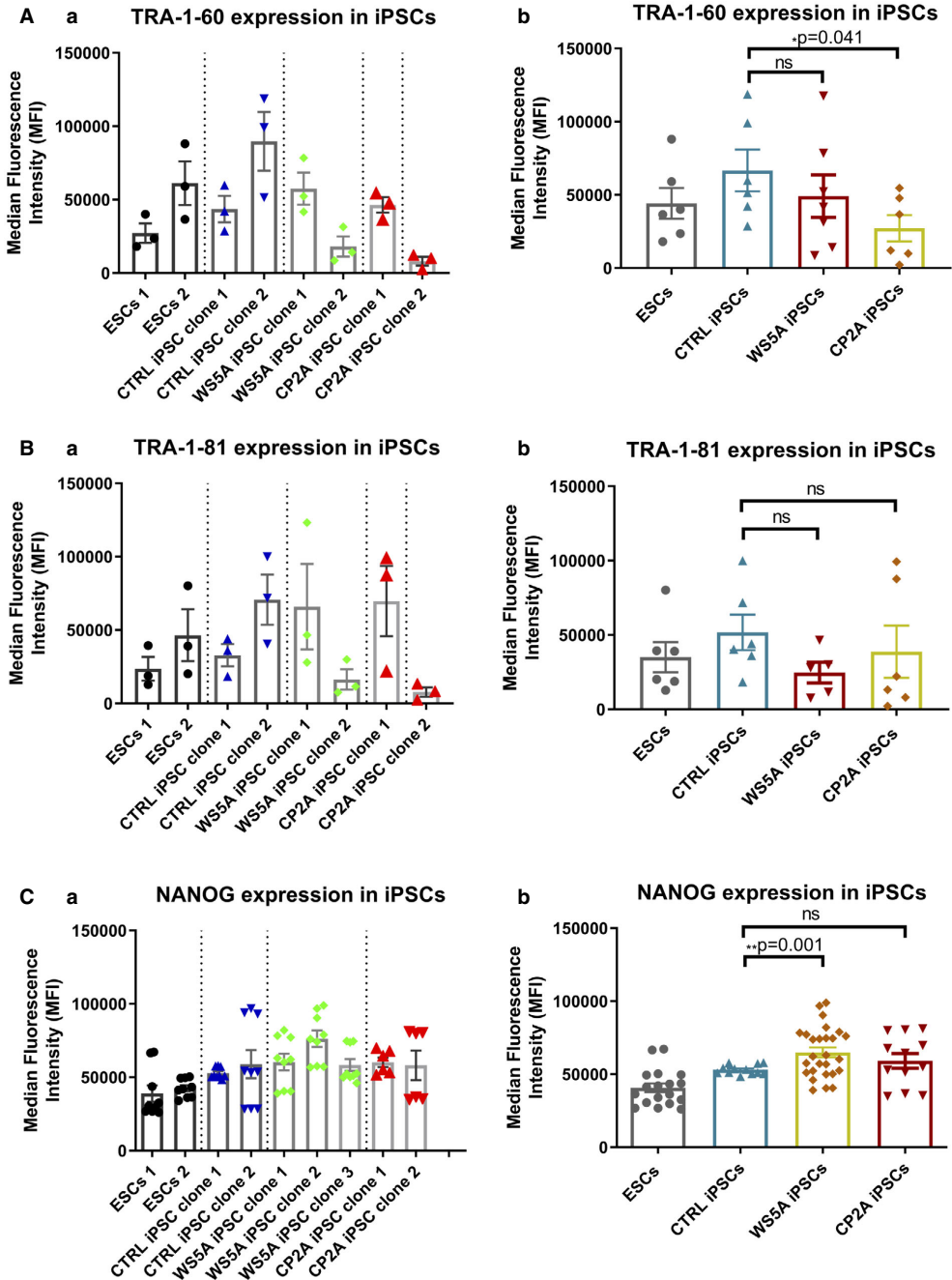


Figure EV2.

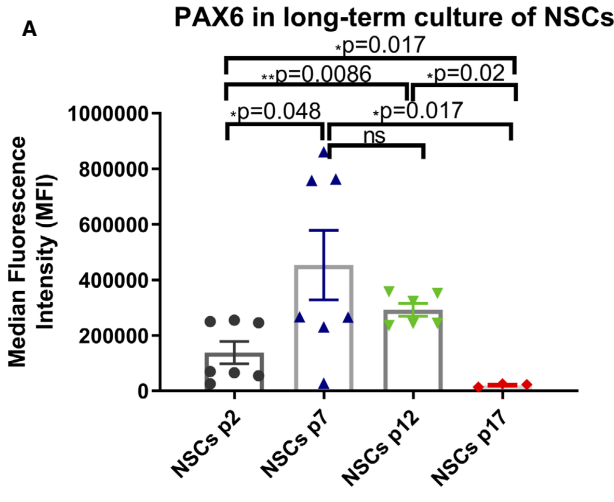


Figure EV3. Flow cytometric analysis of NSC marker PAX6 and pluripotency marker POU5F1 expression in long-term NSC culture.

A, B Representative bar graphs of NSC marker PAX6 (A, $n = 7$, technical replicates for p2; $n = 6$, technical replicates for p7, 12; $n = 3$, technical replicates for p17) and pluripotency marker POU5F1 (B, $n = 7$, technical replicates for p2; $n = 6$, technical replicates for p7, 12; $n = 3$, technical replicates for p17) in different passages during long-term NSC culture using flow cytometric analysis.

Data information: The data points in A and B represent NSCs generated from one Detroit 551 control iPSC line. Data are presented as mean \pm SEM for the number of samples. Mann–Whitney U -test was used for the data presented in A and B. Significance is denoted for P values of less than 0.05. * $P < 0.05$; ** $P < 0.01$. Source data are available online for this figure.

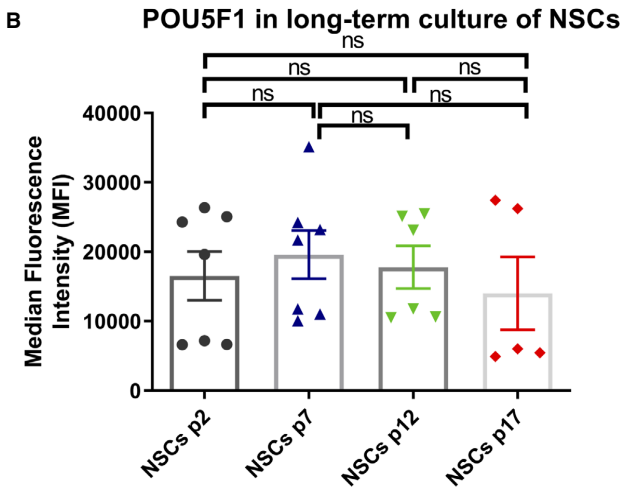


Figure EV4. Intracellular and mitochondrial ROS production in Detroit 551 control, WS5A, and CP2A fibroblasts, iPSCs, and NSCs.

- A, B Intracellular ROS production measurements of the total ROS (DFCDA) level (A, $n = 7$, technical replicates per clone for control; $n = 5$, technical replicates per clone for WS5A; $n = 8$, technical replicates per clone for CP2A) and specific ROS level (B, $n = 7$, technical replicates per clone for control; $n = 5$, technical replicates per clone for WS5A; $n = 8$, technical replicates per clone for CP2A) calculated by total DCFDA/MTDR in iPSCs.
- C, D Total intracellular ROS (C, $n = 6$, technical replicates for control; $n = 4$, technical replicates for WS5A; $n = 5$, technical replicates for CP2A) and specific ROS (D, $n = 6$, technical replicates for control; $n = 4$, technical replicates for WS5A; $n = 5$, technical replicates for CP2A) production measurements in fibroblasts.
- E, F Intracellular ROS production measurements of the total ROS level (E, $n = 6$, technical replicates per clone for control; $n = 5$, technical replicates per clone for WS5A; $n = 4$, technical replicates per clone for CP2A) and mitochondrial ROS level (F, $n = 6$, technical replicates per clone for control; $n = 5$, technical replicates per clone for WS5A; $n = 4$, technical replicates per clone for CP2A) in NSCs.

Data information: The data points in A, B and F represent iPSCs and NSCs generated from 3 different control clones including 2 different clones from Detroit 551 control, 3 different clones from WS5A patient, and 2 different clones from CP2A patient. The data points in E represent NSCs generated from 4 clones from Detroit 551 control and one clone from control AG05836, 3 clones from WS5A patient, and 2 clones from CP2A patient. Data are presented as mean \pm SEM for the number of samples. Mann–Whitney *U*-test was used for the data presented in A–C and E. Two-sided Student's *t*-test was used for the data presented in D and F. Significance is denoted for *P* values of less than 0.05. * $P < 0.05$; ** $P < 0.01$; **** $P < 0.0001$. Source data are available online for this figure.

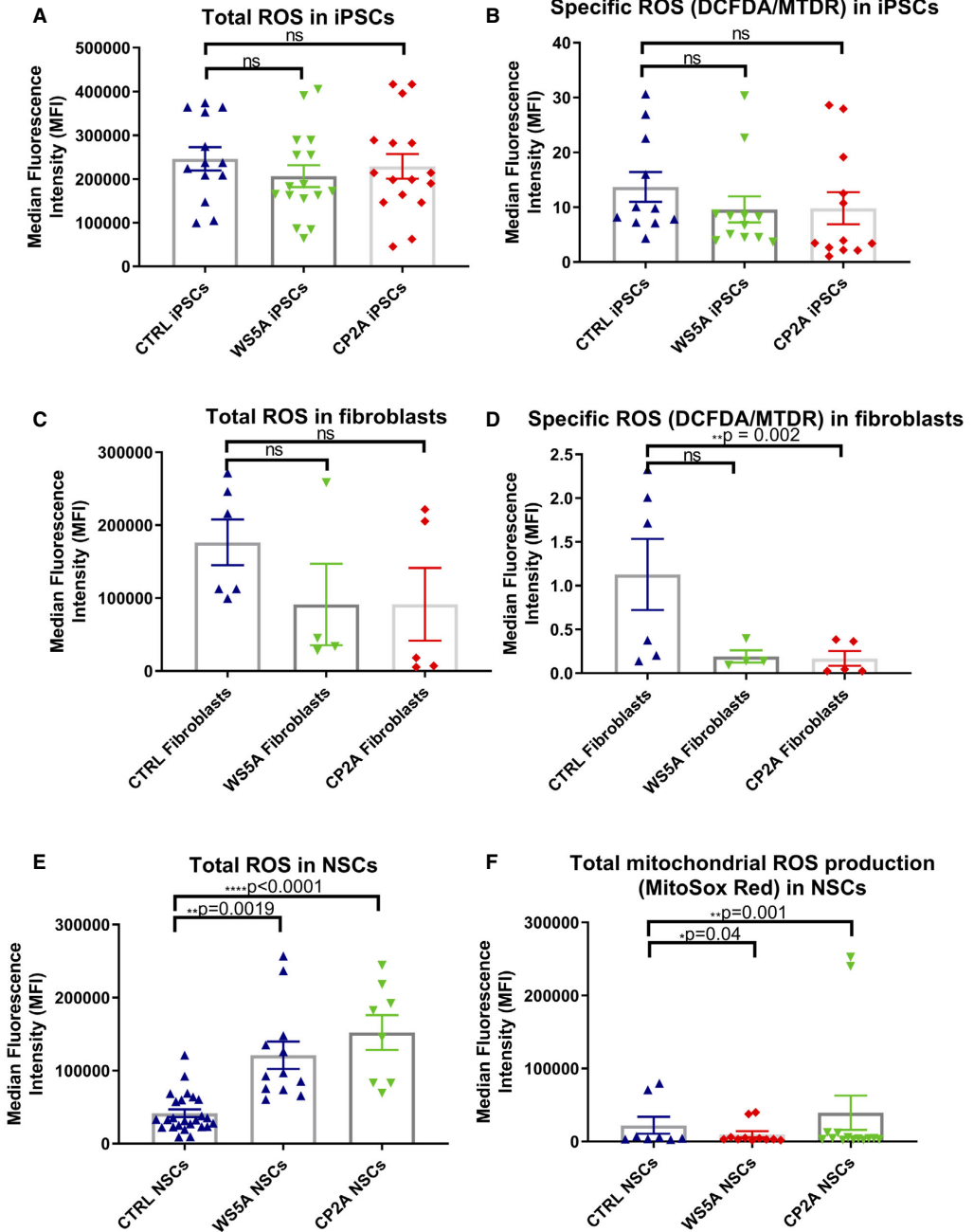


Figure EV4.

Cellular senescence marker p16INK4a in NSCs

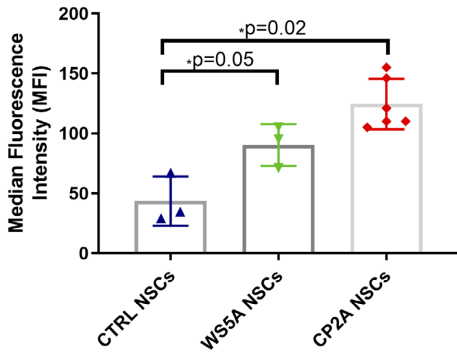


Figure EV5. Flow cytometric analysis of the expression level of cellular senescence marker p16INK4a in NSCs.

The data points represent NSCs generated from one clone from Detroit 551 control, one clone from W55A patient, and 2 different clones from CP2A patient. Data are presented as mean \pm SEM for the number of samples ($n = 3$, technical replicates per clone). Mann–Whitney U -test was used for the data presented. Significance is denoted for P values of less than 0.05. * $P < 0.05$.

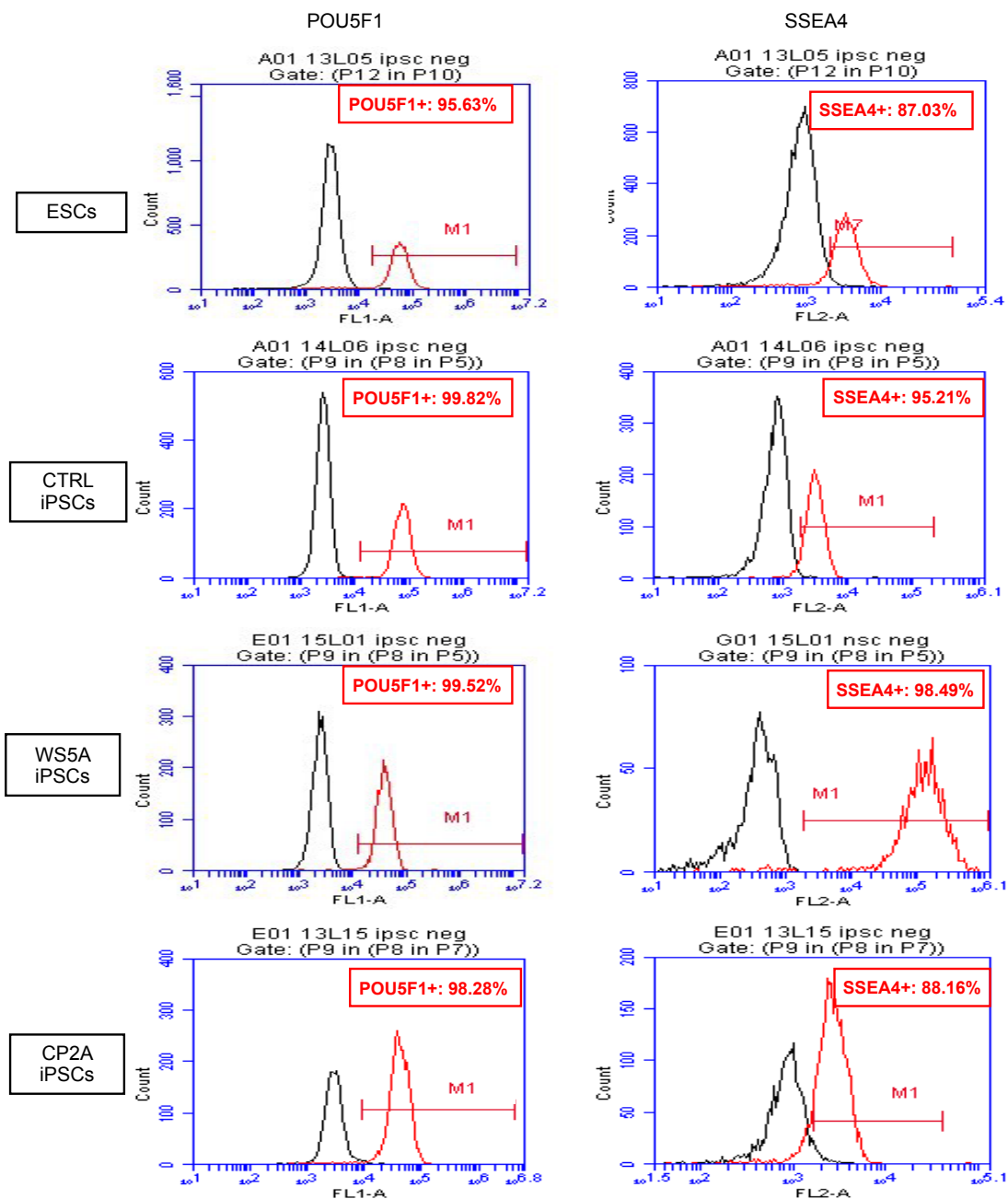
Source data are available online for this figure.

List of Contents

| | |
|--------------------|---|
| Appendix Table S1 | Summary of the iPSC or ESC clones used in the study |
| Appendix Figure S1 | Representative histograms from flow cytometric analysis of the positive cell population stained with pluripotency markers POU5F1 and SSEA4 in ESCs and iPSCs derived from Detroit 551 control, WS5A and CP2A fibroblasts. |
| Appendix Figure S2 | Flow cytometric analysis of the correlation between MTG and TMRE expression under different titrations (from 5 nM to 1 μ M) of TMRE using TMRE and 150 nM MTG dual staining of control iPSCs. |
| Appendix Figure S3 | Representative histograms of the positive staining with NSC marker NESTIN in NSCs derived from ESCs, Detroit 551 control, WS5A and CP2A iPSCs using flow cytometric analysis. |
| Appendix Figure S4 | Representative images of immunostaining for astrocyte marker S100 β from astrocytes derived from iPSC-NSCs. |
| Appendix Figure S5 | Representative images of immunostaining for astrocyte markers EAAT1 and Glutamine Synthetase from astrocytes derived from iPSC-NSCs. |
| Appendix Figure S6 | Representative images of immunostaining for OLIG2 and MBP from oligodendrocytes derived from iPSC-NSCs. |
| Appendix Figure S7 | Colorimetric analysis of measurements of the NAD ⁺ /NADH ratio in Detroit 551 control, WS5A and CP2A NSCs. |

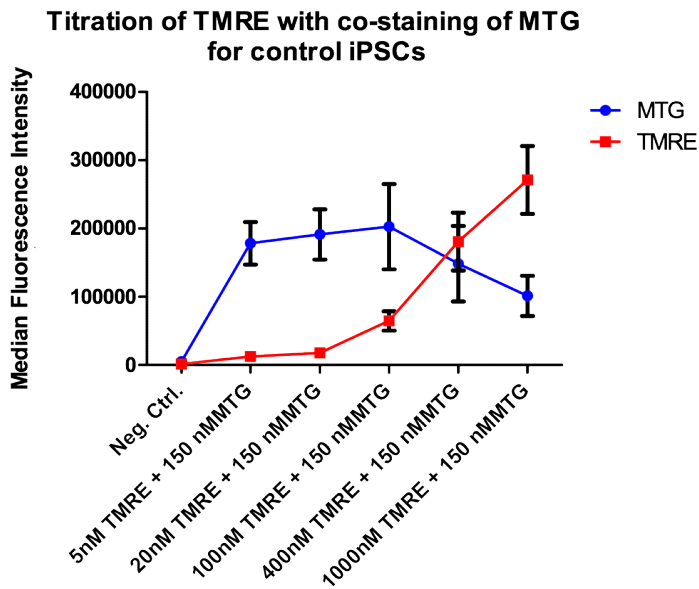
Appendix Table S1: Summary of the ESC lines and iPSC clones used in the study.

| Cell type | Clone | Application | Source |
|----------------|---------|---------------------------------------|--------------------------|
| ESC 1 | - | Differentiation | hESC line 360 |
| ESC 2 | - | Differentiation | H1 |
| Control iPSC 1 | Clone 1 | Differentiation and disease modelling | Detroit 551 fibroblasts |
| | Clone 2 | Differentiation and disease modelling | Detroit 551 fibroblasts |
| | Clone 3 | Differentiation and disease modelling | Detroit 551 fibroblasts |
| | Clone 4 | Differentiation and disease modelling | Detroit 551 fibroblasts |
| Control iPSC 2 | Clone 1 | Differentiation and disease modelling | CCD-1079Sk fibroblasts |
| Control iPSC 3 | Clone 1 | Differentiation and disease modelling | AG05836 fibroblasts |
| WS5A iPSC | Clone 1 | Differentiation and disease modelling | WS5A patient fibroblasts |
| | Clone 2 | Differentiation and disease modelling | WS5A patient fibroblasts |
| | Clone 3 | Differentiation and disease modelling | WS5A patient fibroblasts |
| CP2A iPSC | Clone 1 | Differentiation and disease modelling | CP2A patient fibroblasts |
| | Clone 2 | Differentiation and disease modelling | CP2A patient fibroblast |



Appendix Figure S1:

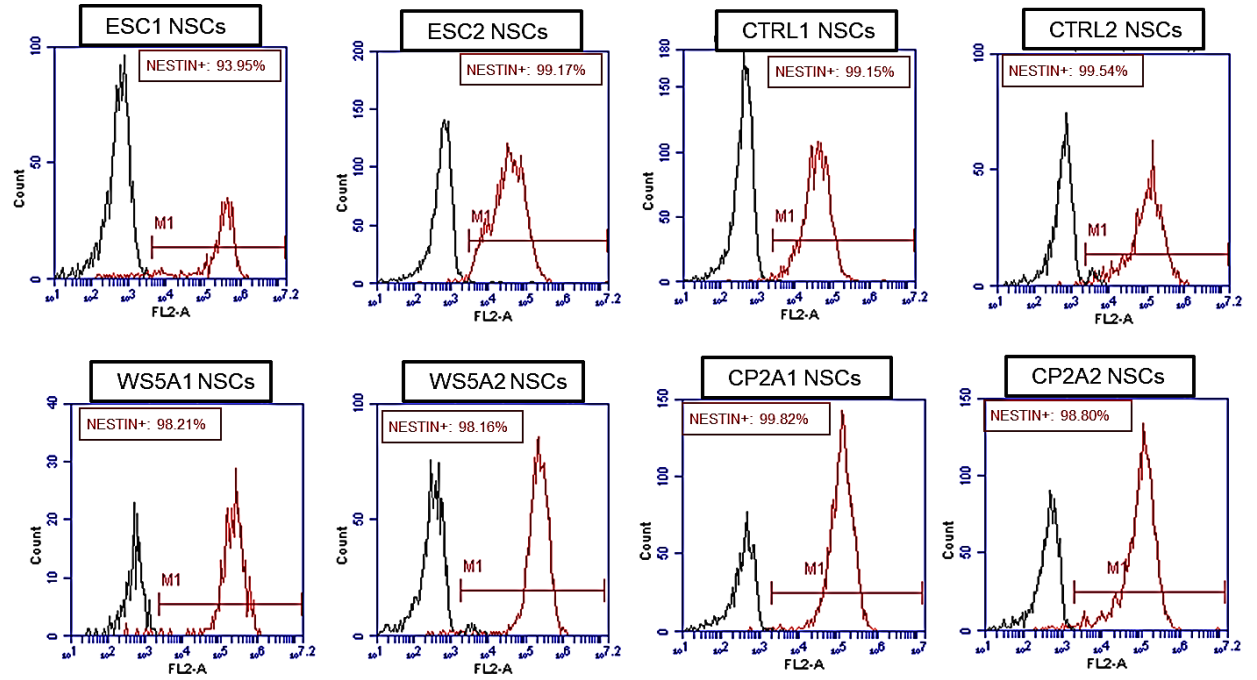
Representative histograms from flow cytometric analysis of the positive cell population stained with pluripotency markers POU5F1 and SSEA4 in ESCs and iPSCs derived from Detroit 551 control, WS5A and CP2A fibroblasts.



Appendix Figure S2:

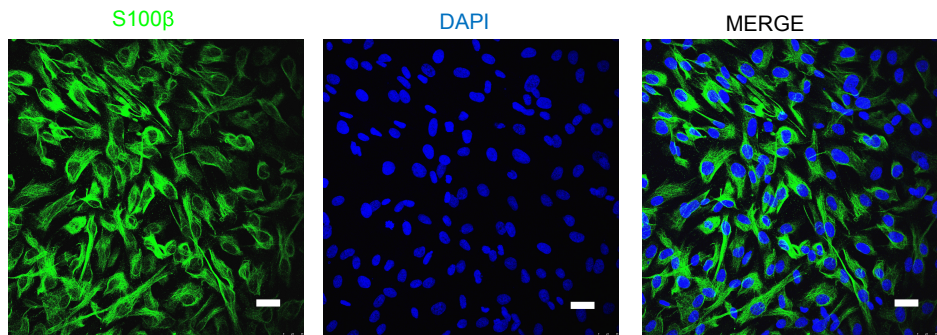
Flow cytometric analysis of the correlation between MTG and TMRE expression under different titrations (from 5 nM to 1 μ M) of TMRE using TMRE and 150 nM MTG dual staining of control iPSCs.

Data information: The data points represent iPSCs generated from one clone from Detroit 551 control. Data are presented as mean \pm SEM for the number of samples (n=3, technical replicates).



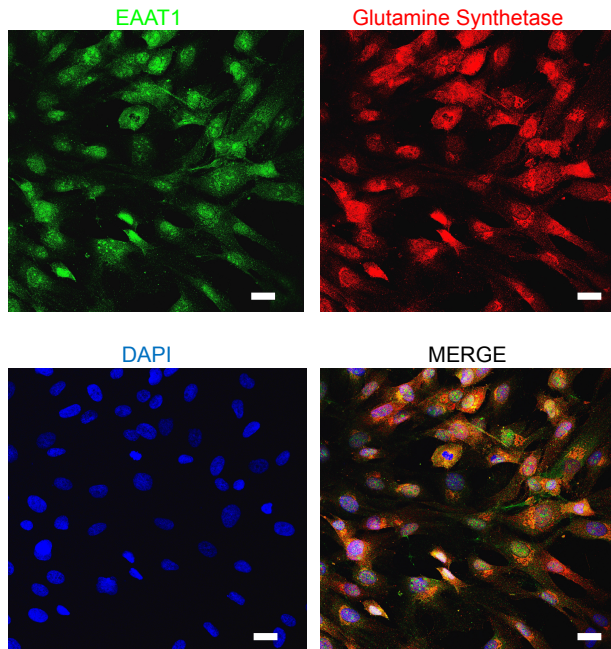
Appendix Figure S3:

Representative histograms of the positive staining with NSC marker NESTIN in NSCs derived from ESCs, Detroit 551 control, WS5A and CP2A iPSCs using flow cytometric analysis.



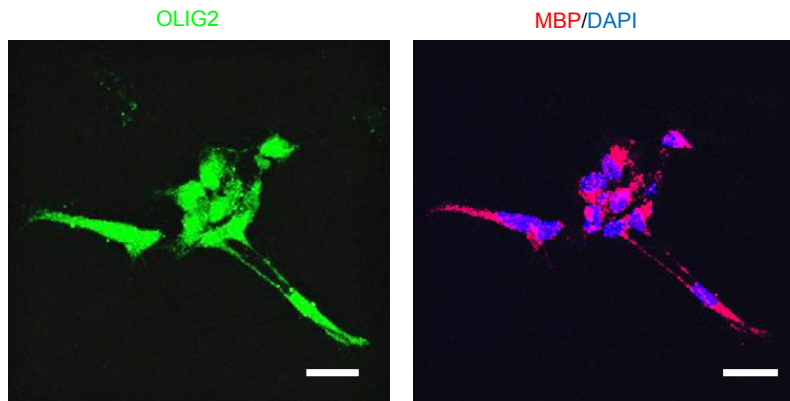
Appendix Figure S4:

Representative images of immunostaining for astrocyte marker S100 β from astrocytes derived from iPSC-NSCs (scale bar, 50 μ m). Nuclei are stained with DAPI (blue).



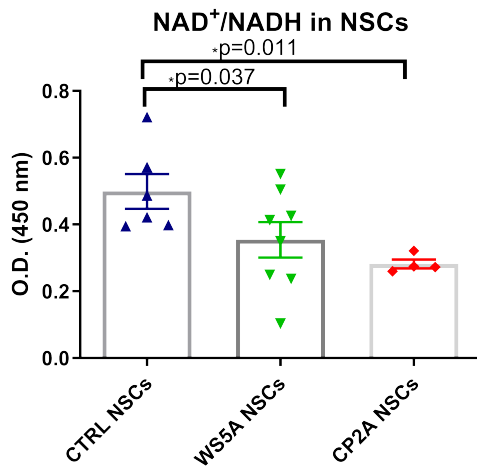
Appendix Figure S5:

Representative images of immunostaining for astrocyte markers EAAT1 and Glutamine Synthetase from astrocytes derived from iPSC-NSCs (scale bar, 50 μm). Nuclei are stained with DAPI (blue).



Appendix Figure S6:

Representative images of immunostaining for OLIG2 and MBP from oligodendrocytes derived from iPSC-NSCs (scale bar, 50 μ m). Nuclei are stained with DAPI (blue).



Appendix Figure S7 :

Colorimetric analysis of measurements of the NAD⁺/NADH ratio in Detroit 551 control, WS5A and CP2A NSCs

Data information: The data points represent NSCs generated from 2 or 3 different clones from Detroit 551 control, 3 different clones from WS5A patient and 2 different clones from CP2A patient. Data are presented as mean ± SEM for the number of samples (n=3, technical replicates per clone). Mann-Whitney U test is used. Significance is denoted for P values of less than 0.05. *P<0.05.



OPEN

A method for differentiating human induced pluripotent stem cells toward functional cardiomyocytes in 96-well microplates

Novin Balafkan^{1,8}, Sepideh Mostafavi^{1,8}, Manja Schubert², Richard Siller^{4,5}, Kristina Xiao Liang², Gareth Sullivan^{3,4,5,6} & Laurence A. Bindoff^{1,2,7}✉

The capacity of pluripotent stem cells both for self-renewal and to differentiate into any cell type have made them a powerful tool for studying human disease. Protocols for efficient differentiation towards cardiomyocytes using defined, serum-free culture medium combined with small molecules have been developed, but thus far, limited to larger formats. We adapted protocols for differentiating human pluripotent stem cells to functional human cardiomyocytes in a 96-well microplate format. The resulting cardiomyocytes expressed cardiac specific markers at the transcriptional and protein levels and had the electrophysiological properties that confirmed the presence of functional cardiomyocytes. We suggest that this protocol provides an incremental improvement and one that reduces the impact of heterogeneity by increasing inter-experimental replicates. We believe that this technique will improve the applicability of these cells for use in developmental biology and mechanistic studies of disease.

Human pluripotent stem cells, hPSCs, including human embryonic cells, ESCs and human induced pluripotent stem cells, iPSCs, are increasingly used in both drug discovery and to study disease and tissue development. An important feature of human pluripotent stem cells (hPSCs) is their ability to differentiate into virtually any cell type including cardiomyocytes^{1–3}. Previous studies have shown that stem cell-derived cardiomyocytes share characteristics and functional properties of primary human heart tissue^{4–6}. Monolayer directed differentiation, together with a combination of small molecules and well-defined culture media have enhanced the generation of cardiomyocytes at relative high purity (>80%) without the need for additional growth factors^{7–9}. Variation in differentiation efficiency and low reproducibility have nevertheless remained problematical and these have been variously ascribed to initial seeding densities and confluency and the effect of batch variability of compounds used in the differentiation process^{7,10–12}. Furthermore, inter- and intra-clonal variation in both hESC and hiPSC lines, as demonstrated by differences in gene and protein expression, DNA methylation, and differentiation potential, have a major impact on the efficiency of differentiation^{8,13–16}. To overcome such problems, and provide an enabling platform for studying etiology of the disease in early developmental stages, we investigated cardiomyocyte differentiation using defined media and small molecules in a 96-well plate format. Compared with larger plate formats, the 96-well plate format allows an increased number of replicates, giving a greater potential for reproducibility, while still being cost-effective.

¹Department of Clinical Medicine (K1), University of Bergen, Bergen, Norway. ²Department of Neurology, Haukeland University Hospital, 5021 Bergen, Norway. ³Department of Molecular Medicine, Institute of Basic Medical Sciences, University of Oslo, Oslo, Norway. ⁴Norwegian Center for Stem Cell Research, Oslo University Hospital, Domus Medica, Oslo, Norway. ⁵Institute of Immunology, Oslo University Hospital-Rikshospitalet, P.O. Box 4950, 0424 Nydalen, Oslo, Norway. ⁶Hybrid Technology Hub - Centre of Excellence, Institute of Basic Medical Sciences, University of Oslo, Blindern, Oslo, Norway. ⁷Neuro-SysMed, Department of Neurology, Haukeland University Hospital, Bergen, Norway. ⁸These authors contributed equally: Novin Balafkan and Sepideh Mostafavi. ✉email: laurence.bindoff@nevro.uib.no

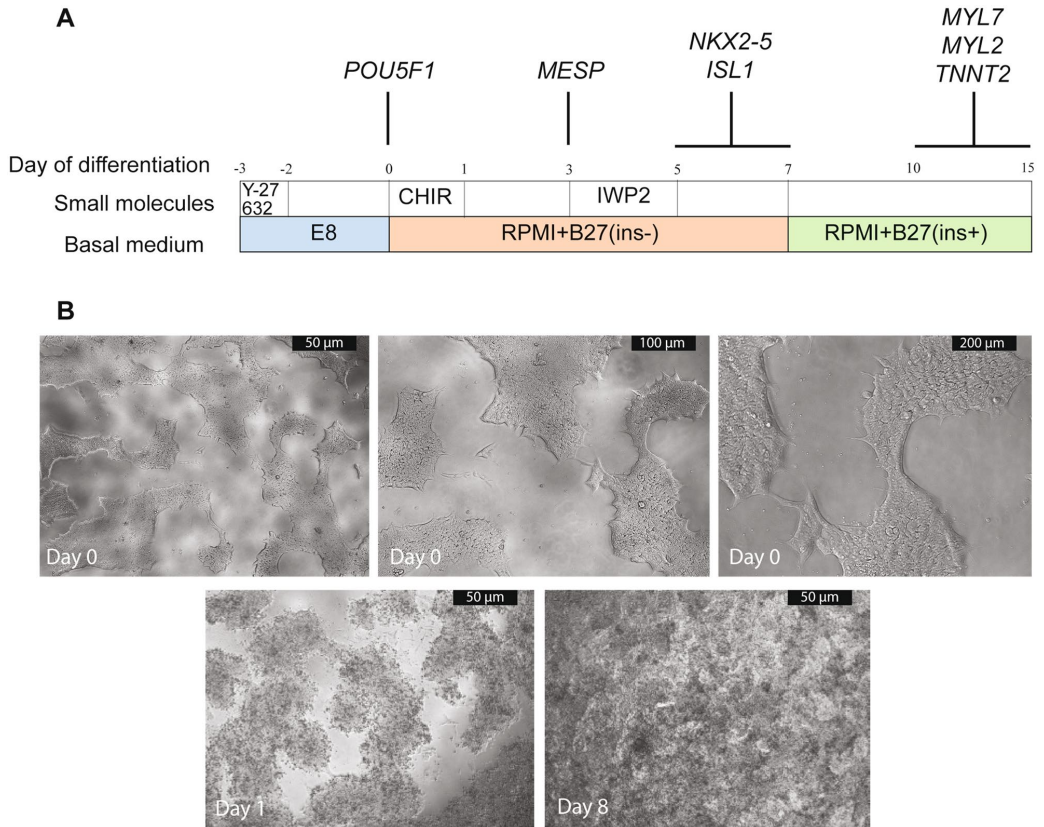


Figure 1. An overview of the protocol. (A) Schematic of representation of differentiation protocol from hPSCs to differentiated cardiomyocytes. The different media and small molecules used at each stage are shown together with the markers that define the stage of differentiation. (B) Phenotypic overview of H1 culture at different differentiation stages. Differentiation was started when the confluency of the culture reached 60–70% (Day 0). The quality of the hPSC colonies was checked visually (i.e., homogeneous appearing colonies with clear borders and the absence of obvious differentiating zones). Cells were treated with 6 μ M (hiPSCs) or 8 μ M (hESCs) CHIR99021 (CHIR) on day 1 for 24 h followed by treatment with IWP2 for 48 h on day 3. By day 8, beating islands of cardiomyocytes covered most of the space in each well. Pictures were taken using inverted light microscopy (Leica DML 1000). Scale bars, 50 μ m. The quality of the hPSC colonies was investigated with higher magnifications, 100 and 200 μ m.

Results

Optimizing cardiomyocyte differentiation in 96 well format. As differentiation yield is affected by the quality of hESCs/hiPSCs, the matrix, media, small molecules, cell density and cell confluency^{8,12,17,18}, we evaluated these factors in a 96-well format. We used two hESC lines (H1 and H9) and two hiPSC lines: Detroit 551-A and AG05836B-15^{1,19–21}. In order to account for potential differences in the reprogramming methods employed, we used a retroviral reprogrammed line (Detroit 551-A) and an integration free Sendai virus reprogrammed line (AG05836B-15). Further, we changed propagation matrix and media to Geltrex and Essential 8 Medium (E8) respectively. Figure 1 shows the time line of differentiation, the media and small molecules used, some of the developmental markers studied and colony morphology.

We investigated confluency by initiating differentiation at 30–40%, 60–70% and 80–90% confluency and found that 60–70% confluency gave rise to a culture with the highest percentage of functional cardiomyocytes on day 15 (D15) of differentiation (Fig. 2). Then, we estimated the cell density needed to cover 60–70% of the well area within a minimum of 2 days after cell seeding. Seeding involves resolving hPSC colonies into single cell suspension and/or small clumps containing two to six cells using E8 medium supplemented by Y27632. Cells were incubated at 37 °C overnight in this combination and after 24 h the medium changed to fresh E8 medium. Thus, estimating seeding density required a minimum 2 days in culture to provide enough time for the cells to recover and reach the desired confluency. We identified a density of 2.4×10^4 cells/cm² for both hESCs and hiPSCs as

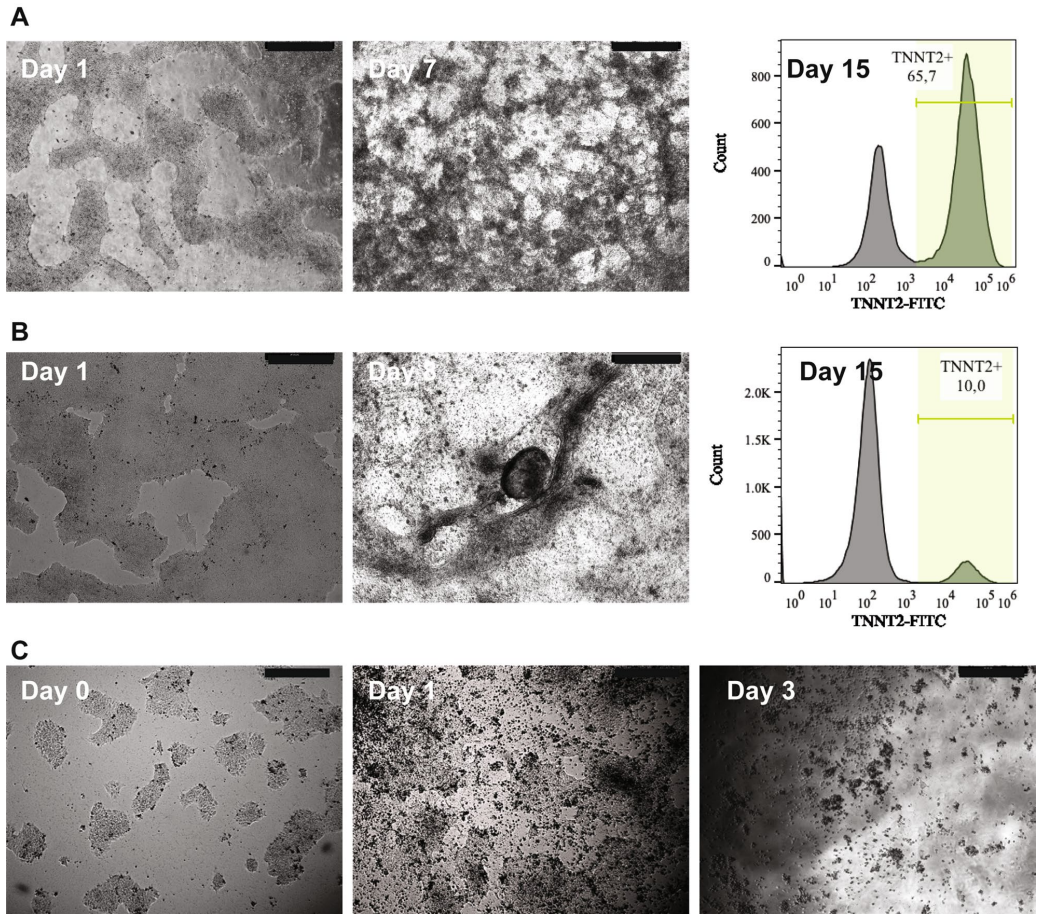


Figure 2. The impact of confluency on differentiation efficiency. The figure shows the morphology of Detroit551-A cell culture with different confluency prior to differentiation initiation and monitoring them at different stages of differentiation process. Finally estimation of TNNT2+ cells in the culture using flow cytometry. (A) Cells cultured to a confluency of 60–70% prior to differentiation initiation. Beating cardiomyocytes appeared on day 7 of differentiation and staining the cells for TNNT2 marker showed a high level of TNNT2+ cells on day 15. (B) This panel shows Detroit 551-A at a starting confluency of 80–90% on day 1 and the presence of few beating clumps on day 8 after initiation of differentiation. Flow cytometry revealed low level of TNNT2+ cells in the culture on day 15. (C) This panel shows morphology of Detroit 551-A cells, cultured to a confluency of 30–40% prior to differentiation. This initial confluency gave rise to no cardiomyocytes. Cells started to die just after 24 h treatment with CHIR99021 (day-1) and most were dead after 3 days. All Pictures were taken using inverted light microscope (Leica DML 1000). Scale bars, 500 μ m. Cardiomyocyte population were estimated using flowcytometer Sony cell sorter SH800 (Sony Biotechnology Inc.) and data were analyzed and visualized using FlowJo 10.5.0 (FlowJo LLC, OR, USA) software (www.flowjo.com).

optimal for generating areas of beating cardiomyocytes by day 7 and spontaneous contractions of larger areas by day 9 to 10 (see Supplementary Fig. S1 and Video S1). The lines used in these experiments were 60–70% confluent within 2–3 days, however, time to optimal confluency may vary for other cell lines. Further, we also noted that any deviation in confluency without reciprocal concentration adjustment of the small molecule CHIR99021 resulted in either increased cell death or low differentiation efficiency. We found that 8 μ M was optimal for hESC while for hiPSCs, 6 μ M CHIR99021 resulted in high levels of TNNT2+ cells on D15.

Human ESCs/hiPSCs were propagated on Geltrex under feeder free conditions in Essential 8 Medium (E8) at 2.4×10^4 cells/cm. Within 3 days, they reached a confluency of 60 to 70%, the ideal point to induce differentiation by applying the GSK3 inhibitor CHIR99021, in concentration-cell-dependent manner. The inhibitor of WNT production-2, IWP2, was added 72 h post differentiation induction for 48 h. Fresh medium was provided

(RPMI/B-27 without insulin) on day 5, and from day 7 cells were fed with fresh RPMI/B-27 (with insulin) every two other days (Fig. 1). We observed areas of beating cardiomyocytes by day 7 and by day 9–10, spontaneous contractions could be seen in large areas of the well (see Supplementary Video S1). Contractile cardiomyocytes were collected from day 10–15 for further analysis.

Characterizing cardiomyocytes derived from human pluripotent stem cells. *Assessment of developmental markers throughout differentiation.* Differentiation from hPSC toward the cardiac lineage involves formation of a primitive-streak-like population, from which all endodermal and mesodermal lineages develop including cardiovascular progenies i.e. cardiomyocytes, endothelial cells and smooth muscle cells. To ensure that differentiation followed the correct developmental route, we monitored the expression levels of key markers at time points corresponding to stage-specific transitions including—pluripotency state (D0), germ layer specification (D3), progenitor state (D5) and committed cardiomyocytes (D15) in the ES line H1 (Fig. 3) and we confirmed this in the Detroit IPSC line (Fig. S2). As expected, treatment of hPSC with CHIR99021 resulted in decreased expression of pluripotency genes *NANOG* and *POU5F1*, and the appearance of early mesodermal markers such as *MESPI*, *MIXL1* and *T* at the highest level on D3 of differentiation (Fig. 3, Supplementary Figs. S2 and S3A). Further differentiation of H1 and Detroit 551-A to cardiac progenitor was defined by the increased expression of *ISL1* and *TEMEM88* on D5, and to committed cardiomyocyte defined by the specific markers such as *TBX5*, *TNNT2*, *MYH6* and *MYL7* (Fig. 3, Supplementary Figs. S2 and S3A). The gene expression data revealed the gradual increase of *GATA4* and *ATP2A2* expression while cells were navigating from germ layer specification (D3) towards the committed cardiomyocytes (D15), and expression of cardiac specific markers *TNNT2* and *MYL7* coincided with maturation and contractile activity (Fig. 3, Supplementary Figs. S2 and S3A). These studies also showed the presence of *MYL2*, a marker for ventricular myocytes, from day 12 (Supplementary Fig. S3A).

To ensure that we were seeing appropriated maturation, we investigated the expression of mature cardiomyocyte markers such as *HOPX* and *MYH7*⁶ at a later stage of differentiation, D30. We showed that *HOPX* and *MYH7* increased at D30 of differentiation and *MYH6* fell (Supplementary Fig. S4).

We confirmed our gene expression findings using immunocytochemistry (Fig. 4 and Supplementary Fig. S3). We assessed the hPSCs for pluripotency and found expression of *POU5F1* and no evidence of the cardiomyocyte marker *TNNT2* in hPSC (day 0) prior to initiation of the differentiation. By day 7 of the differentiation process, we observed a marked reduction in the expression of *POU5F1* and the appearance of the cardiomyocyte marker *TNNT2* (Supplementary Fig. S3B). Next, we assessed cells committed to the cardiac lineage by evaluating the expression of *ISL1* and *NKX2-5* that define the cardiac progenitor stage. We found *ISL1* and *NKX2-5* positive cells by day 6 of the differentiation (Fig. 4A) and *TNNT2* was robustly detected by day 10 (Fig. 4A). Staining with an antibody against myosin light chain 7 (*MYL7*), a specific marker for atrial myocytes, revealed the presence of cardiac sarcomeres in the cells within D10–12 of differentiation (Fig. 4B–ii). Furthermore, we found the expression of connexin 43 (*GJA1*), a marker for the gap junctions in *TNNT2*⁺ cells on D10–12 of differentiation (Fig. 4B–iii). Co-staining of *MYL7* and troponin I3 (*TNNI3*) that is specific to the cardiac muscle cells (Fig. 4B–iv) confirmed the presence of committed cardiomyocytes in the culture on D10–12 of differentiation.

Quantification of cell composition using flow cytometric analysis. The major cell types formed during cardiac lineage differentiation are cardiomyocytes, smooth muscle and endothelial cells (for review²³). Co-staining of the cells for markers of committed cardiomyocytes (*TNNT2* and *MYL7*) at later stages of differentiation (Day12–19) revealed that 82 ± 7% and 60 ± 10% of the cells from the H1 culture were positive for these markers whereas 85.7 ± 3% of the Detroit551-A cells were positive for *TNNT2* and 79.7 ± 3% of them were positive for *MYL7* (Fig. 5A). Based on flow cytometric results, H9 had the lowest differentiation efficiency with 47 ± 13% *TNNT2*-positive and 45% *MYL7*-positive cells. We then stained cardiomyocytes for *CDH5* (a marker for the endothelial lineage) and *ACTA2* (smooth muscle) on day 15. This analysis confirmed the presence of smooth muscle and endothelial cells, which are expected to arise as a by-product during cardiac lineage differentiation (Fig. 5C).

We used flow cytometry to investigate the relative proportions of endothelial and smooth muscle cells in cardiac cultures on Day15²³. The surface markers *CD144* and *CD140b* were used to identify endothelial and smooth muscle respectively. Parallel, samples from the same 96 well plate were stained with an internal cardiomyocyte marker, *TNNT2* to provide an estimate of the number of cardiomyocytes (Fig. 5B). In the H1-derived cardiomyocyte culture 74.5 ± 8% were *TNNT2* positive cells, 9.5 ± 2.94% stained for the smooth muscle marker (*CD140b*) and only 3.71 ± 0.81% of the population expressed the endothelial marker (*CD144*) (Fig. 5B). In the Detroit 551-A culture, the proportion of *TNNT2* positive cells was 77 ± 0.18% while 18.45 ± 0.1% were *CD140b* positive cells and 5.53 ± 0.02% were endothelial cells. In the AG05836B-15 culture 67.2 ± 0.2% were *TNNT2* positive cells, while 21 ± 0.1% and 2 ± 0.007% of the cells were positive for *CD140b* and *CD144* markers respectively (Fig. 5B).

Investigating the inter-well heterogeneity. In order to investigate the heterogeneity between wells, we extracted RNA from multiple wells and performed qPCR to assess the expression of *TNNT2* and *NKX2-5* relative to a housekeeping gene *GAPDH*. We selected up to twelve wells of a differentiation run at random and isolated total RNA using the MagMAX isolation kit. We looked at 2 differentiation runs of H1 and from the first analysed 12 wells of one plate while on the second run we analysed multiple wells of 3 different plates. We also isolated total RNA of multiple wells from 3 different plates of one run of Detroit 551-A differentiation. The data is shown in supplementary table S1online. The variation is shown in Fig. 6 and we calculated the coefficient of variation between these CT values, which varied between 1.96 and 7.30% confirming that there were similar numbers of cardiomyocytes in each well.

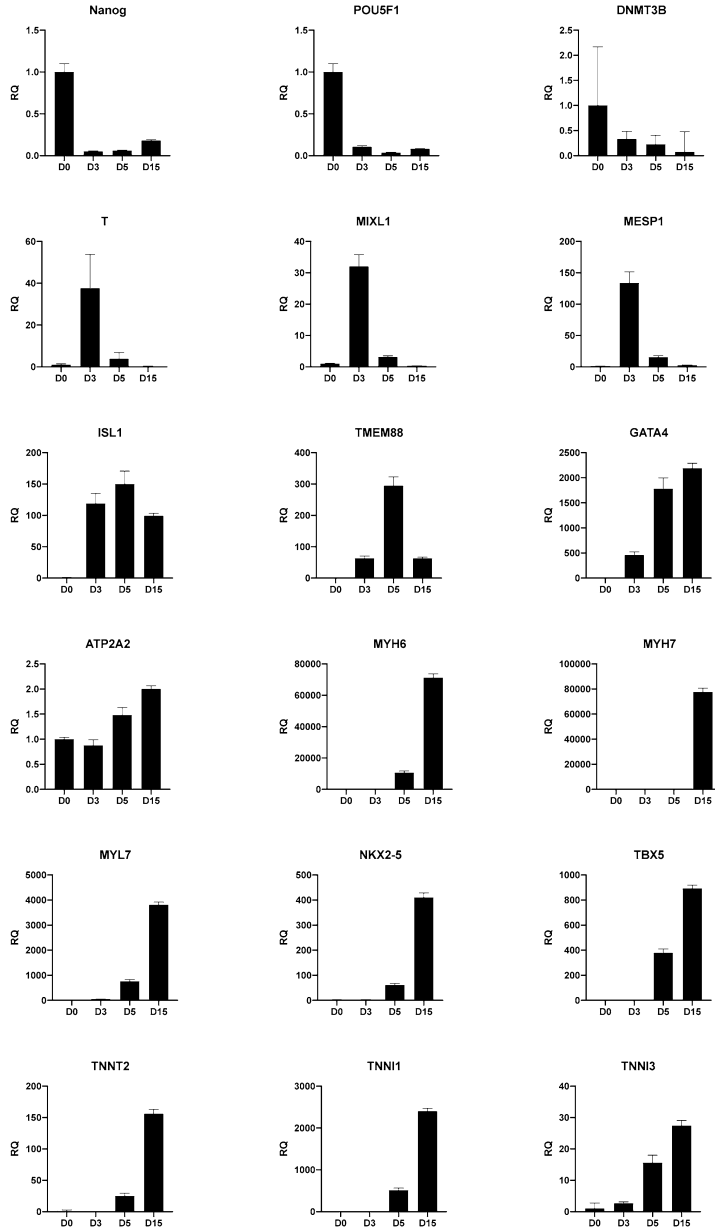


Figure 3. Characterization of h1-derived cardiomyocytes by gene expression. Relative quantification of mRNA expression profiles of 18 markers, representing the different stages of differentiation from hPSC to the cardiac lineage. Data are collected from the differentiation of hESC-H1 toward cardiomyocytes and presented as the mean of three independent differentiation runs and error bars are the standard deviation of the mean. Changes in expression level are related to the pluripotent stage, D0.

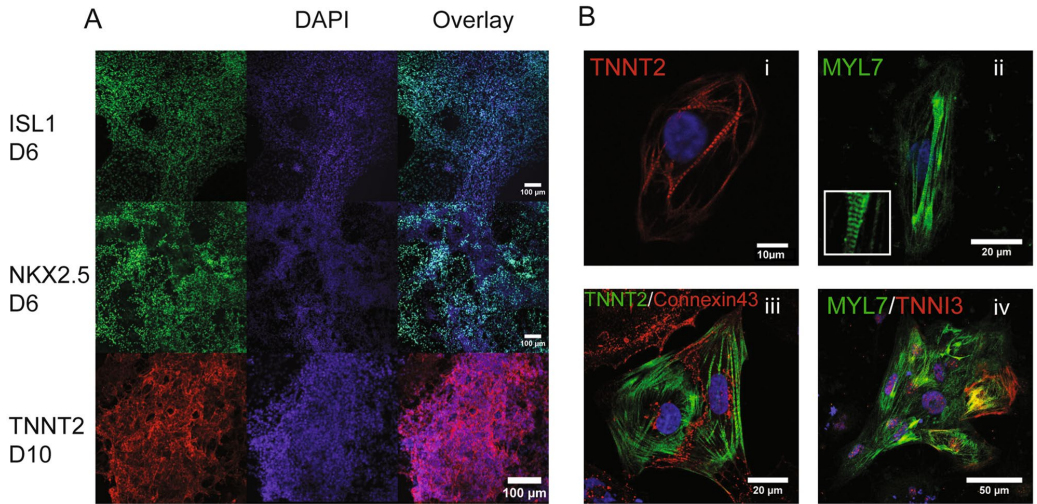


Figure 4. Cardiomyocyte characterization. Cardiomyocyte culture consists of several layers of cells, which makes it difficult to stain the cells in single well of 96 well plate. Cardiomyocyte characterization using immunocytochemistry was performed by transferring cells one well of 96 well plate into a single well of 12 well plate. (A) Detroit 551-A cells were differentiated in a 96 well format and transferred at day 5–12-well plates and cultured for a further 1–5 days. They were then stained for markers of cardiomyocyte differentiation (i.e. differentiation time points 6 and 10 days). Scale bar, 100 μm. (B) hiPSCs differentiated to CM and transferred on day 8 from 96-well plate to cover slips in a 12-well plate. (i) Detroit 551-A stained with TNNT2; (ii) AG05836B-15 stained with MYL7 showing the typical cardiac sarcomere organization; (iii) hESC-H1 co-stained for connexin43 in TNNT2 positive cells showing the formation of both organized sarcomeres and gap junctions; (iv) hESC-H9 cells are co-stained for TNNI3 and MYL7. Images collected between day 10–12 using Leica TCS SP5 confocal microscope.

Electrophysiological validation of hiPSC-derived cardiomyocyte. Cardiac function including rhythmicity and contractility depend on the expression of number of ion channels such as sodium, potassium and calcium channels. To test whether the differentiated cardiomyocytes had proper electrophysiological properties, we employed Microelectrode arrays, MEA, and challenge them with different cardiac drugs. Microelectrode arrays provide a highly sensitive, non-invasive method for studying physiological properties of electrically active cells. MEA records electrical waveform signals that are called extracellular field potentials (FPs) and which are generated and shaped by monolayers or small clusters of cardiomyocytes. FP contour represents the cardiac action potential and, reflects to some extent the electrocardiogram recording. Typically, one sees a rapid upstroke that corresponds to the Na^+ influx (R/Q peak) and membrane depolarization, a slow wave/plateau phase thought to correspond to the Ca^{2+} influx, and a repolarization phase corresponding to a predominant K^+ efflux (T peak) (Fig. 7A).

We transferred H1 and Detroit551-A line-derived cardiomyocytes into the MEA chamber on day 11–13 of differentiation and monitored the steadiness and beat consistency signatures up to 14 days (Day 12–26 of differentiation). The period of observation was selected based on the previous studies suggesting the best stage of differentiation for transferring the cardiomyocytes to MEA chamber for checking their electrophysiological activities^{5,24}.

H1-derived cardiomyocytes showed an average FP duration of 298 ± 20 ms, and a beat interval (BI) of 42 ± 2 beats/min, whereas Detroit551-A-derived cardiomyocytes showed an average FP duration of 75 ± 5 ms, and a BI of 49 ± 4 beats/min, respectively. Beating interval became more irregular after 26 days in culture as has been previously described⁵. To test functionality of the hPSC-derived cardiomyocytes, the following drugs were applied— β_1 and β_2 adrenoreceptor agonist isoproterenol (1 μM), potassium channel antagonist E4031 (1 μM), sodium channel antagonist tetrodotoxin (TTX, 5 μM), L-type calcium channel antagonist nifedipine (5 nM), and the 5-hydroxytryptamine (serotonin) receptor -HT4 agonist and HT3 antagonist Mosapride (350 nM) (Fig. 7Biv, Table 1). While a more limited number of drugs were applied to Detroit 551-A, these cells exhibited the same alterations in their electrophysiological pattern following the application of isoproterenol and E4031.

As expected, isoproterenol increased the beating frequency and led to a significant reduction of the FP duration (FPD, Fig. 7Bi, Table 1). E4031 reduced the FP amplitude (FPA, Fig. 7Bii, Table 1) as expected, but contrary to other reports, we observed an increased in the FP duration (FPD) and a minor prolongation of the beat interval^{5,24}. Application of TTX led to significant reduction of the positive peak amplitude (pPA), increased FPA, prolonged BI, but no effect on FPD (Fig. 7Biii, Table 1). Nifedipine, behaved as described by reducing the pPA and FPD with no effect on the BI (Fig. 7Biv, Table 1). Mosapride^{25,26} impacted the FPA and led to a notable

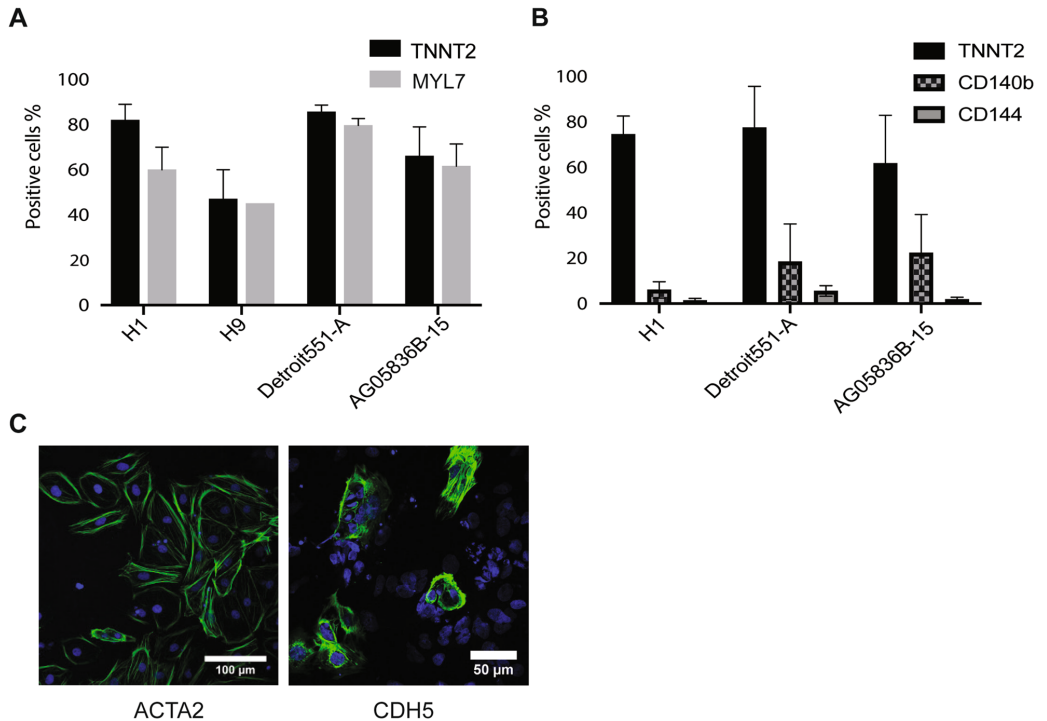


Figure 5. Verification of cardiomyocytes differentiation using flow cytometric analysis. (A) Results presented as the percentage of TNNT2 and MYL7 positive cells in different hiPSC lines (Detroit 551-A and AG05836B-15) and hESC lines (H1 and H9). Detroit 551-A (85%) and H1 (82%) showed higher level of TNNT2 positive cells compared to AG05836B-15 (66%) and H9 (47%). Bar graphs showing average and error bars represent \pm SD of at least three independent differentiation runs (except MLY7 for H9 which is represents a single differentiation run). (B) Cardiomyocytes derived from hESC-H1 and hiPSC lines (Detroit 551-A and AG05836B-15) were collected on Day 15 of differentiation and stained with either surface (CD144-FITC and CD140b-PE) or intracellular markers (TNNT2). Cells were stained first to distinguish live/dead cells and then co-stained with conjugated antibodies against surface markers including CD144-FITC and CD140b-PE or stained for the intracellular marker, TNNT2. The H1-derived cardiomyocyte culture with 74.5% TNNT2⁺ cells contained 9.5% CD140b positive and 3.7% CD144 positive cells. In the Detroit 551-A culture that 77% of the cells were positive for TNNT2, 18% and 5% of the cells were positive for CD140b and CD144 respectively. In addition, while 21% of the cell in AG05836B-15 culture expressed smooth muscle marker, only 2% of the cells expressed endothelial marker. This culture contained 67% TNNT2 positive cells. (C) Results of immunofluorescent staining showing positive staining for either the smooth muscle marker ACTA2 (scale bar, 100 μ m) or the endothelial cell marker CDH5 (Scale bars, 50 μ m). Blue is DAPI and green is Alexa-448 stained ACTA2 (smooth muscle marker) and CDH5 (endothelial cell marker). Pictures were taken using Leica TCS SP5 confocal microscope.

reduction of the FPA/FPD ratio, also called field potential amplitude upstroke speed (FPUS), an indicator of sodium and L-type calcium channel function²⁷ (Fig. 7Bv, Table 1).

Discussion

The aim of this study was to develop a scaled down platform for cardiac differentiation that was amenable for high throughput screening, efficient and reproducible without any genetic modification or additional enrichment processes, while at the same time reducing overall cost. We modified the monolayer-based, small molecule approach described by Lian and colleagues⁸ to achieve these goals. We replaced 12-well plate with 96-well plate format, mTeSR1 medium with the simpler Essential 8 formulation and substituted Matrigel with the cheaper and more defined extra cellular matrix, Geltrex at the undifferentiated hPSC expansion stage. This combination of modifications reduced the cost of differentiation while still yielding high levels of TNNT2 positive cells at later stages of differentiation.

The impact of confluency on differentiation has been addressed^{12,18} and we also showed that the yield of differentiated cardiomyocytes was highly dependent on hPSC colony density (Fig. 2, Supplementary Fig. S1). Thus, the 12-well format produced the best yield at a confluency of 85–90%^{7,28}, whereas in 96-well plates, we

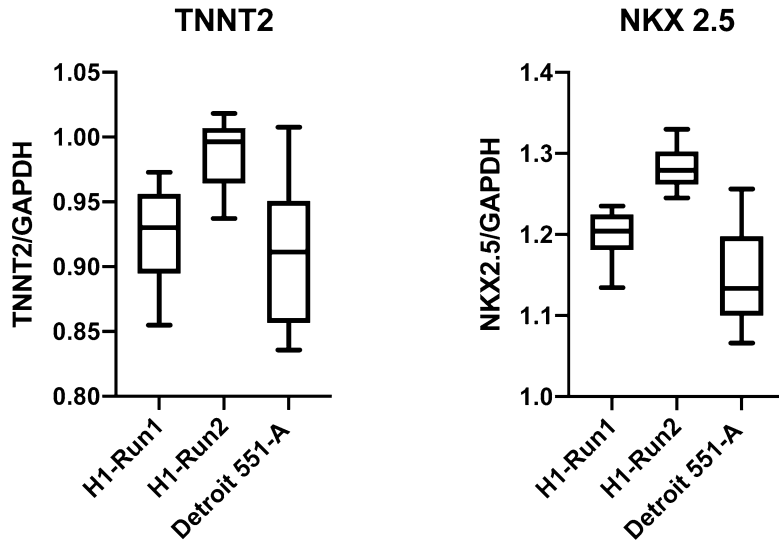


Figure 6. Investigation of inter-well heterogeneity across a 96 well plate and different runs of differentiation. The boxplot analysis shows the variation in expression of two cardiomyocyte markers, *TNNT2* and *NKX2-5* related to the house keeping gene *GAPDH* in the ES line H1 and the iPSC line Detroit 551-A. Cells in both runs were >25 days of differentiation. Run 1 comprises 12 separate well samples collected from one plate of differentiation of H1 while Run 2 comprises 12 samples taken from 3 different plates of one round of H1 differentiation. The Detroit cell samples are collected from 3 different plates of one run of differentiation.

found that a confluency of 60–70% gave excellent numbers of cardiomyocytes (H1 82%, Detroit551-A 85%). Further, we observed that CHIR99021 had to be adjusted to altered confluency^{10,29} and that the concentration was dependent on the cell type used for differentiation. Cardiomyocytes derived from the hESC lines H1 and H9 required a higher CHIR990201 concentration than those derived from hiPSCs (Detroit 551-A and AG05836B-15) to achieve an optimal differentiation yield. The yield of cardiomyocytes did vary between the two hiPSC lines (85% for Detroit 551-A and 66% for AG05836B-15). This might be due to the different reprogramming systems used (Detroit 551-A—retroviral reprogrammed, AG05836B-15 integration free Sendai virus reprogrammed), but we did not investigate this in detail.

Moreover, we assessed the expression of key genetic markers in the cultures to validate the developmental trajectory towards a cardiomyocyte fate (Fig. 3, Supplementary Fig. S2 and Fig. S3A). *ISL-1* is one of the key markers for cardiac progenitors and it has been shown that *ISL-1* expression levels gradually decline in committed cardiomyocytes after its rise at the progenitor stage (day 5)^{30,31}. Of note, H1 followed this pattern and resulted in a high level of *TNNT2* + (more than 80%), while the expression level of *ISL-1* remained high throughout the H9 differentiation resulting in 47% *TNNT2* positive cells (Supplementary Fig. S3A). Our findings, which are similar to previous reports showing the poor differentiation capacity of H9 toward cardiomyocytes, may be explained by the inability to reduce expression of *ISL-1* after the progenitor stage²³. Correct expression patterns of mature cardiomyocytes markers such as *HOPX*, *MYH6*, *MYH7* and *NKX2.5* on D30 of differentiation confirmed the maturity of the cardiomyocytes generated in this 96-well microplate format (supplementary Fig. S4)⁶.

Cardiovascular progenitors are able to develop into cardiomyocytes, endothelial cells, cardiac fibroblasts and smooth muscle cells. Using our protocol, we demonstrated that between day 10 and 15 the majority of hPSC derived cardiomyocytes stained for *TNNT2* as well as *MYL7* (Fig. 5A). We also investigated the non-cardiomyocyte populations generated using our protocol. The number of *TNNT2* positive varied between $64 \pm 8\%$ for hESC and $76 \pm 8\%$ for hiPSC. Differentiation of H1 resulted in 3–4% endothelial cells and 9–11% smooth muscle cells. The percentage of endothelial cells in hiPSC-derived cultures was higher than in ES derived cultures with 18.45% in Detroit 551-A and 21% in AG05836B-15, smooth muscle cell numbers were lower in the Detroit 551-A and AG05836B-15 hiPSC lines compared to H1 (Fig. 5B).

In order to ensure that each well of the 96 well plate provided a similar complement of cells, an important factor if we are to use this method for e.g. drug screening, we investigated the well-to-well heterogeneity in our cultures. We used both immunocytochemistry and RT-qPCR to determine the relative amount of cardiomyocytes in each well. We used microscopy to assess the homogeneity of the cardiomyocyte population and found that the cultures contained high numbers of *TNNT2* positive cells at day 10 (Fig. 4). We also studied the composition using PCR to identify the cardiac specific marker *TNNT2* and *NKX2-5* (Fig. 6). This assay suggested that there was a low heterogeneity between the wells of one run of differentiation and between two separate runs of

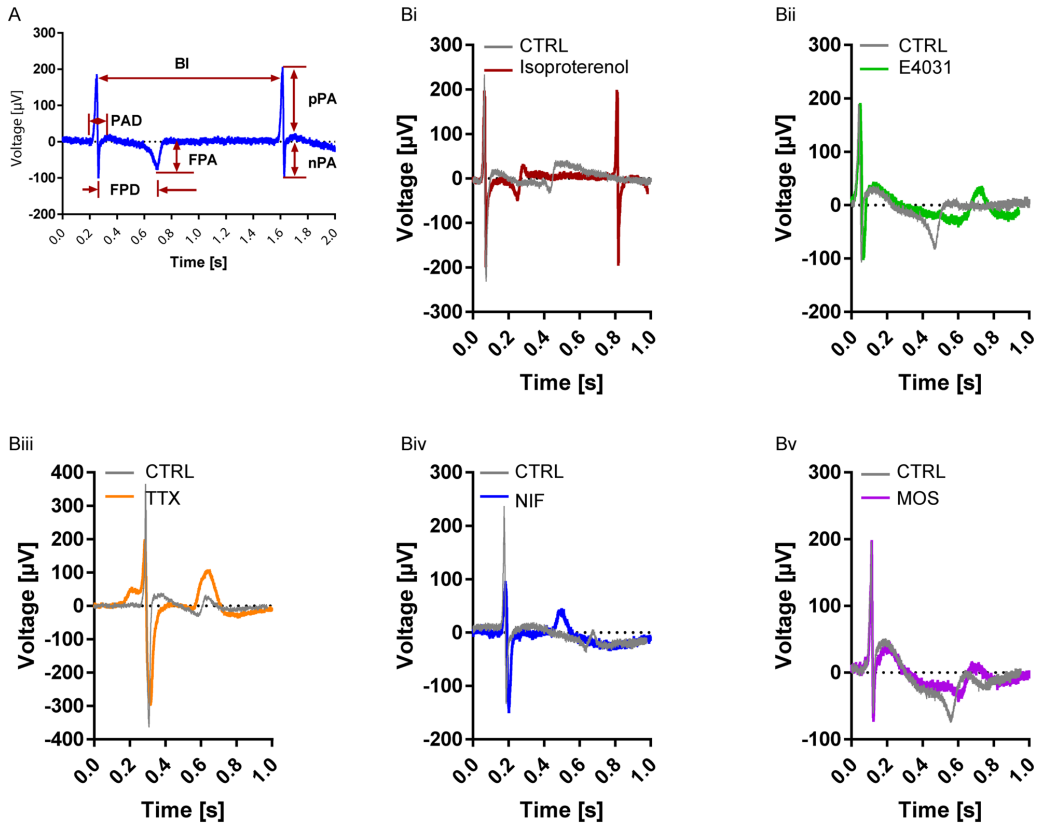


Figure 7. MEA Recording of hiPSC-derived cardiomyocytes. (A) Representative trace recorded with the MEA showing the analysis parameter to evaluate the functionality of hiPSC-derived cardiomyocytes. R/Q and T peak; field potential duration (FPD), field potential amplitude (FPA), Q/R peak differentiated into positive peak amplitude (pPA) and negative peak amplitude (nPA), beat interval (BI); (B) Representative the electrophysiological properties of H1-derived cardiomyocytes before (no-drug) and after applying (i) β_1 and β_2 adrenoreceptor agonist Isoproterenol (ISO), (ii) potassium channel antagonist E4031, (iii) sodium channel antagonist tetrodotoxin (TTX), (iv) L-type calcium channel antagonist Nifedipine (NIF) and (v) 5-Hydroxytryptamine (serotonin) receptor-HT4 agonist and HT3 antagonist Mosapride (MOS). The shaded area represents the field potential duration (FPD), also known as QT interval, measured during analysis. Electrophysiological parameters were analyzed and visualized using the analysis tools Analyzer and Spike sorter in the MC_Rack software (Version 4.6.2).

differentiation. These results demonstrate that this smaller format method produces reproducible cardiomyocyte populations both within a single plate and in different runs of differentiation.

Our electrophysiological data (Fig. 7, Table 1) are in line with previous publications and confirm that the cardiomyocytes produced by this method are physiologically functional. Beating rate increased in both, cardiomyocytes derived from H1 and Detroit 551-A following addition of the β -adrenergic agonist isoprenaline, known to have a positive chronotropic effect on hPSC-derived cardiomyocytes^{34,35}. Our cardiomyocytes also showed TTX-sensitive and TTX-resistance Na^+ channels: TTX induced a significant reduction of pPA, without complete elimination as demonstrated previously^{34,35}. Furthermore, manipulation of K^+ efflux by E4031, L-type VGCC dependent calcium influx by Nifedipine or 5-Hydroxytryptamine (serotonin) receptor—HT4/HT3 function by Mesopride showed a clear alterations of cardiomyocyte extracellular FP trace that was consistent with the previous reports⁵. These findings suggest that our established 96-well format in vitro system recapitulates the functional characteristics of cardiomyocytes.

Several approaches to enrich the cardiomyocyte population have been described including genetic-modification (by the expression of MYH6), using surface protein as a specific marker for cardiomyocytes (signal-regulatory protein alpha) or selection based on targeting highly active mitochondria using a mitochondrial membrane potential marker (TMRM)^{36–38}.

| Drugs | CM line | Exp | Groups | BI (beats/min) | FPA (μ V) | FDP (ms) | FPUS (μ V/ms) | pPA (μ V) | | | | | |
|--------------------|------------------|---------------------------|-----------------------|----------------|---------------------|------------------|---------------------|----------------|---------------------|-----------------|---------------------|------------------|---------------------|
| ISO 1 μ M | H1 | $n_C = 6;$ $n_R = 11;$ | CTRL _{ISO} | 47 \pm 3 | $P < 0.0001^{****}$ | 66.5 \pm 11.6 | $P = 0.2792$ | 315 \pm 22 | $P < 0.0001^{****}$ | 0.25 \pm 0.05 | $P = 0.0139^*$ | 245.3 \pm 27.7 | $P = 0.3884$ |
| | | | ISO | 78 \pm 3 | | 70.7 \pm 10.2 | | 183 \pm 14 | | 0.44 \pm 0.07 | | 264.1 \pm 30.2 | |
| | Detroit 551-A | $n_C = 3;$ $n_R = 4;$ | CTRL _{ISO} | 44 \pm 8 | $P < 0.0001^{****}$ | 48.5 \pm 5.8 | $P = 0.3548$ | 66 \pm 8 | $P = 0.1099$ | 0.95 \pm 0.13 | $P = 0.1514$ | 125.9 \pm 29.0 | $P = 0.1439$ |
| | | | ISO | 64 \pm 7 | | 54.3 \pm 5.9 | | 57 \pm 8 | | 1.41 \pm 0.32 | | 81.0 \pm 10.6 | |
| E4031 1 μ M | H1 | $n_C = 6;$ $n_R = 10;$ | CTRL _{E4031} | 50 \pm 2 | $P = 0.0046^{**}$ | 70.9 \pm 7.6 | $P < 0.0001^{****}$ | 302 \pm 18 | $P < 0.0001^{****}$ | 0.25 \pm 0.03 | $P < 0.0001^{****}$ | 165.9 \pm 19.8 | $P < 0.0001^{****}$ |
| | | | E4031 | 42 \pm 1 | | 36.9 \pm 4.0 | | 651 \pm 47 | | 0.07 \pm 0.01 | | 113.4 \pm 18.5 | |
| | Detroit 551-A | $n_C = 3;$ $n_R = 3;$ | CTRL _{E4031} | 77 \pm 1 | $P = 0.0078^{**}$ | 44.3 \pm 6.4 | $P = 0.1294$ | 57 \pm 6 | $P = 0.0078^{**}$ | 0.74 \pm 0.11 | $P = 0.0078^{**}$ | 292.9 \pm 33.6 | $P = 0.0078^{**}$ |
| | | | E4031 | 66 \pm 1 | | 32.4 \pm 3.7 | | 143 \pm 21 | | 0.28 \pm 0.02 | | 143.6 \pm 13.8 | |
| TTX 5 μ M | H1 | $n_C = 6;$ $n_R = 12;$ | CTRL _{TTX} | 41 \pm 2 | $P < 0.0001^{****}$ | 79.5 \pm 7.6 | $P = 0.0033^{**}$ | 353 \pm 18 | $P = 0.0622$ | 0.25 \pm 0.03 | $P = 0.4393$ | 303.1 \pm 27.0 | $P < 0.0001^{****}$ |
| | | | TTX | 25 \pm 2 | | 109.4 \pm 11.0 | | 394 \pm 23 | | 0.35 \pm 0.05 | | 147.4 \pm 20.4 | |
| | Detroit 551-A | $n_C = 3;$ $n_R = 3;$ | CTRL _{TTX} | 46 \pm 4 | $P = 0.0137^*$ | 48.5 \pm 12.1 | $P = 0.1250$ | 45 \pm 4 | $P = 0.0625$ | 0.76 \pm 0.11 | $P = 0.0122^*$ | 253.1 \pm 25.2 | $P = 0.0005^{***}$ |
| | | | TTX | 33 \pm 7 | | 67.3 \pm 13.2 | | 40 \pm 3 | | 1.35 \pm 0.32 | | 123.6 \pm 13.6 | |
| NIF 5 nM | H1 | $n_C = 6;$ $n_R = 10;$ | CTRL _{NIF} | 45 \pm 2 | $P = 0.0044^{**}$ | 59.3 \pm 8.7 | $P = 0.1796$ | 361 \pm 25 | $P < 0.0001^{****}$ | 0.19 \pm 0.04 | $P = 0.0066^{**}$ | 160.1 \pm 25.4 | $P = 0.0027^{**}$ |
| | | | NIF | 36 \pm 2 | | 69.9 \pm 12.0 | | 195 \pm 10 | | 0.36 \pm 0.06 | | 111.3 \pm 15.9 | |
| MOS 350 nM | H1 | $n_C = 6;$ $n_R = 11;$ | CTRL _{MOS} | 46 \pm 2 | $P = 0.0067^{**}$ | 39.8 \pm 3.1 | $P = 0.0110^*$ | 325 \pm 26 | $P = 0.0562$ | 0.14 \pm 0.02 | $P = 0.0039^{**}$ | 137.7 \pm 20.9 | $P = 0.0562$ |
| | | | MOS | 52 \pm 2 | | 25.4 \pm 2.1 | | 387 \pm 30 | | 0.08 \pm 0.01 | | 127.6 \pm 18.5 | |

Table 1. Electrophysiological properties of H1- and Detroit551A-derived cardiomyocytes. *ISO* Isoproterenol, *TTX* Tetrodotoxin, *NIF* nifedipine, *MOS* mosaprid, *BI* beat interval, *FPA* field potential amplitude, *FDP* field potential amplitude, *FPUS* field potential amplitude upstroke speed, *pPA* positive peak amplitude, n_C numbers of independent cultures, n_R numbers of independent recordings, statistic: mean \pm SEM, paired-nonparametric Wilcoxon signed rank test.

One of the most effective and straightforward approaches appears to be the metabolic selection using lactate instead of glucose to force the cells to use their respiratory chain instead of glycolysis and selecting cardiac cells based on their energy profile^{28,39,40}.

Since we are interested in studying disease mechanisms, one key aim of our study was to produce a high number of cardiomyocytes without over manipulation, as this may have unwanted cellular and molecular effects. We did not therefore investigate the use of these additional measures. Our protocol results in a high percentage of cardiomyocytes that express the cardiac marker *TNT2* in both hESCs and hiPSCs without the use of any purification method. In principle, however, any of these methods could be combined with our protocol to further enhance purification.

Although, well-defined differentiation conditions have greatly improved reproducibility of differentiation, inter-experimental reproducibility still remains a key challenge¹². The strength of this protocol is the 96-well format, which allows inter-experimental comparability, thus potentially reducing inter-experimental variability and increasing the precision of reported results. Further, it offers the possibility of combining differentiated cells from different wells or pooling data from individual wells of the 96-well format to balance out the inter-experimental variation and improve reproducibility. This protocol also demonstrates it is not necessary to first differentiate the cells in larger format before reseeding them in to 96 wells for experimentation such as high throughput analysis^{41,42}.

Conclusion

Here we have demonstrated the efficient differentiation of cardiomyocytes in a 96-well microplate format, that reduces both workload and cost, improving both consistency and precision. This platform provides an adaptable system for monitoring the differentiation and development of cardiac tissue from very early stages all the way to functional tissue in 96-well format and is well suited to the investigation of early disease development.

Material and methods

hiPSC generation and characterization. H1 and H9 were obtained from WiCell Research Institute (Madison, Wisconsin, WiCell) and well characterized as previously described¹. Detroit 551-A fibroblasts were obtained from ATCC (American Type Culture Collection), AG05836B-15 fibroblasts were obtained from the Coriell Cell Repositories and reprogrammed into hiPSCs and characterized as previously described in Mathipathi et al.^{19,20}.

Cardiomyocyte differentiation. Geltrex (#A1413302, Thermo Fisher Scientific) was diluted 1:100 in ice cold Advanced DMEM/F-12 (#12634010, Thermo Fisher Scientific) to coat wells in the 96-well plate (85 μ l/well). Coated plates were incubated at 37 °C for at least 30 min before use. Before plating the hiPSC cells, colonies were broken down to single cells after treating with 0.5 mM EDTA to have a homogeneous cell suspension. Human iPSCs were seeded in Geltrex coated wells at a density of 2.4×10^4 cells/cm² using Essential 8 Medium (E8) (#A1517001, Thermo Fisher Scientific) supplemented with 10 μ M Rock inhibitor (Y27632; #1254, Tocris Bioscience) for 24hrs. After 24hrs, the medium was changed with freshly prepared E8 medium without Y27632 and medium was exchanged every day. After two or three days, when the confluency of the culture reached 60–70%,

cells were treated with 6 μM (optimal concentration for hiPSC) or 8 μM (optimal concentration for hESC) of CHIR99021 (#4423, Tocris Bioscience) in RPMI 1640 (#61,870, Thermo Fisher Scientific) supplemented with B27-without insulin (#A1895601, Thermo Fisher Scientific). After 24 h the medium containing CHIR99021 was changed to RPMI-B27 without insulin alone and left for 48 h. On day 3 cells were treated with 5 μM IWP2 (#3533, Tocris Bioscience) diluted in RPMI-B27 without insulin and incubated for 48 h. On day 5 medium was changed to freshly prepared RPMI-B27 without insulin for 48 h. At day 7 medium was changed to RPMI-B27 with insulin (#17,504,044, Thermo Fisher Scientific) without any extra supplement and medium was changed every two days thereafter. Schematic representation of the protocol (Fig. 1A). Working volume in all the steps of the protocol was 200 μl per well of 96-well plate.

Gene expression via real-time PCR. RNA used for gene expression studies was isolated by MagMAX-96 Total RNA Isolation Kit (#AM1830, Thermo Fisher Scientific). Cells were lysed using lysis buffer supplemented by the kit directly inside the plate after a quick wash with PBS. Lysate was either processed immediately for RNA isolation using an automated MagMAX express 96 or stored in -80°C for later extraction. cDNA synthesis and Real-time qPCR were performed using EXPRESS One-Step Superscript qRT-PCR Kit (#11781-01 K, Thermo Fisher Scientific) and TaqMan probes (see Supplementary Table S2 online). Applied Biosystems 7500-Fast real-time PCR System (Thermo Fisher Scientific) was used to perform qPCR. All qPCR reactions were performed in triplicate and normalized to the geometric mean of *ACTB* and *GAPDH* as endogenous control genes, and assessed using the comparative $\Delta\Delta\text{Ct}$ method by normalizing differentiated cells to undifferentiated pluripotent stem cells. Results are shown as the mean of three independent differentiation runs and error bars represent standard deviation of the mean.

Fluorescent microscopy. Cells of single well of 96 well plate were seeded either on Geltrex coated glass coverslips or in Geltrex coated Millicell EZ SLIDES (#PEZGS0816, Merck Millipore). Cells were fixed with 4% paraformaldehyde (#43368, Alfa Aesar) for 10 min at room temperature and permeabilized with 0.3% Tween 20 (#822184, Merck Millipore) diluted in PBS for 1 hr at room temperature. All the primary and secondary antibodies were diluted in blocking buffer consisting of 0.3 M glycine, 5% goat serum and 1% BSA in PBS. Final concentration of 10 $\mu\text{g}/\text{ml}$ was used for all the primary antibodies and incubated overnight at 4°C . Alexa Fluor 488 and 568 (Thermo Fisher Scientific) was used as secondary antibodies and were diluted in blocking buffer (1:1000) and incubated for 1 h at room temperature. Nuclei were stained with Gold Antifade Reagent with DAPI (#P36935, Thermo Fisher Scientific). Confocal microscopy images were taken by either Zeiss LSM 510 META or Leica TCS SP5 at Molecular Imaging Center (MIC), University of Bergen, and data analysis and image editing were done with Fiji⁴³. Antibodies are listed in Supplementary Table S2 online.

Flow cytometry. *Sample preparation for detecting extracellular antigens; surface markers.* Cells were dissociated into single cells using 100 μl TrypLE Express Enzyme (Thermo Fisher Scientific) for 20 min at 37°C and after a quick wash with PBS. Cells were collected after adding 100 μl of culture medium (e.g. RPMI B27+) supplemented with 20% FBS and each eight wells of 96-well format were pooled and filtered using 40 μm pre-wet cell strainer (#431750, Sigma). Each sample counted prior to spinning down at 400 g for 5 min at RT.

Cell pellet was resuspended in Running buffer consisting of autoMACS Rinsing Solution (#130-091-222, Miltenyi Biotec) and MACS BSA Stock Solution (#130-091-376, Miltenyi Biotec)-final concentration of BSA was 0.5%. Number of cells in each sample was adjusted for 10^5 cells/100 μl . Cells were stained with Dead Cell Discriminator (1:50), provided by the Fixation and Dead Cell Discrimination Kit (#130-091-163, Miltenyi Biotec) and incubated on ice while exposing to a 60 W light bulb for 10 min. Subsequently, the optimal concentration of conjugated antibodies for flow cytometry reported by the supplier for each batch was used. Cells were incubated for 10 min at 4°C in the dark with pre-conjugated antibodies; CD144-FITC and CD140b-PE. Cells were washed by adding 1 ml of running buffer per 10^5 cells and spinning down at 300 g for 10 min at RT. Cell pellet was resuspended in 300 μl of running buffer and cells were fixed by adding 150 μl of FiX solution and 5 μl of Discriminator Stop Reagent provided by the Fixation and Dead Cell Discrimination Kit. Fluorescence minus one control was used to adjust the gate for positive cells, due to the co-staining for live/dead staining and different markers within one sample. Proper Isotype controls and compensation beads were also included for gating (Supplementary Fig. S5). At least 30,000 events were collected for each sample with a 100 μm nozzle by a Sony cell sorter SH800 (Sony Biotechnology Inc.) and data were analyzed and visualized using FlowJo V.10.5.0 (FlowJo LLC, OR, USA) software (www.FlowJo.com). Antibodies are listed in Supplementary Table S2 online.

Sample preparation for detecting the intracellular antigens. Cells were washed in DPBS (#14190250, ThermoFisher) three times and dissociated into single cells using Enzyme T diluted in Buffer X (1:10) provided by Multi Tissue Dissociation Kit 3 (#130-110-204, Miltenyi Biotec) for 10–15 min at 37°C . Equal volume of culture medium (e.g. RPMI B27+) supplemented with 20% FBS was added to each well and each eight wells of 96-well format were pooled and filtered using 40 μm pre-wet cell strainer (#431750, Sigma). Cells were counted prior to spinning down at 400 g for 5 min at RT. Cell pellet was resuspended in InsideFix solution, provided by Inside Stain Kit (#130-090-477, Miltenyi Biotec), diluted in DPBS (1:1) and incubated for 10 min at RT. Number of cells in each sample was adjusted for 10^5 cells/100 μl . Cells were washed by adding 1 ml of running buffer per 10^5 cells and spinning down at 300 g for 10 min at RT. Cell pellet was resuspended in Inside Perm solution—a component of the Inside Stain Kit— and stained with recommended dilution of pre-conjugated antibodies for 10 min in the dark at RT. Antibodies were pre-conjugated with Fluorescein isothiocyanate (FITC). Cells were washed with 1 ml Inside Perm solution per 10^5 cells for 5 min at 400 g. Cell pellet was resuspended in 300 μl of running buffer and proceed to analysis. Fluorescence minus one control was used to adjust the gate for positive

cells (Supplementary Fig. S5). At least 30,000 events were collected for each sample with a 100 μm nozzle by a Sony cell sorter SH800 (Sony Biotechnology Inc.) and data were analyzed and presented using V.10.5.0 (FlowJo LLC, OR, USA, www.FlowJo.com) software. Antibodies are listed in Supplementary Table S2 online.

NOTE: Adherent cardiomyocytes generated in 96 well plate were dissociated into single cells by using TrypLE Express enzyme for detecting extracellular antigens and using Multi Tissue Dissociation Kit 3 for detecting intracellular antigen by flow cytometry. The difference between the efficiency of these two methods was not significant (P value = 0.17) for dissociating cardiomyocytes. Dissociation of cardiomyocytes in to single cell with Multi Tissue Dissociation Kit 3 was faster specifically for dissociating more mature culture, however it caused changes in extracellular antigens structure that could not be detected by antibodies and subsequently, no detectable signal for flow cytometric analysis. Therefore, we used TrypLE Express enzyme for detection of extracellular antigens.

Microelectrode array measurements. Human Pluripotent stem cells including H1 and Detroit 551-A were differentiated towards the cardiomyocytes as describe in cardiomyocyte differentiation section. At day 11–14 of differentiation, 1×10^6 cells of cardiomyocyte culture from eight wells of a 96-well plate were pooled, and transferred into a single chamber microelectrode array (MEA) unit containing 60 integrated TiN electrodes (#60MEA200/30iR-Ti-gr; Multichannel Systems).

To dissociate the cardiomyocytes into single cells or small cell clump of 10–12 cells, cells were quickly washed with DPBS and incubated with TRYPLE Express Enzyme (Thermo Fisher Scientific) at 37 °C for 10–15 min (100 μl per well). TRYPLE Express Enzyme was neutralized with the equal volume of RPMI-B27 with insulin (#17504044, Thermo Fisher Scientific) supplemented with 20% FBS. Collected cells from each well were transferred into a falcon tube and washed with RPMI-B27 containing insulin and 20% FBS. Cells suspension was centrifuged at 400 g for 5 min at RT and cell pellet was gently resuspended in 1 ml of RPMI-B27 with insulin supplemented with 10 μM of Y27632 (#1254, Tocris Bioscience) and plated in MEA chamber that was pre-coated with Geltrex, 1:100 diluted in Advanced DMEM/F-12, for at least 30 min at 37 °C. After 12 h of incubation at 37 °C with 5% CO_2 , Cardiomyocytes were anchored over the electrode field using a 0.8 g glass coated steel ring covered with a nylon mesh (#ALA HSG-MEA-5BD; Multichannel systems). After observing spontaneous beating of the cell accumulate 48 h post transferring, field potential (FP) recordings were commenced. At a sampling rate of 20 kHz local field potentials at each electrode were collected over a period of 15 min at 35 °C using the MEA2100-HS2 \times 60 system and the MC-Rack software (Version 4.6.2; Multichannel system, Reutlingen, Germany).

FPs were recorded for 5 min under control conditions, after applying chemical compounds such as selective β -adrenergic agonist Isoprenalolol (ISO, 1 μM ; #1747; Tocris), $\text{K}_v11.1$ (hERG) channel antagonist E4031 (1 μM ; #1808; Tocris), L-type Ca_v channel antagonist Nifedipine (NIF, 5 nM; #N-120; Alomone), Na channel antagonist Tetrodotoxin (TTX, 5 μM ; #1069; Tocris) and 5-HT $_3/4$ receptor antagonist Mosapride (MOS, 350 nM; #M-225; Alomone) and post-washout.

Electrophysiological parameter analysis. Using the analysis tools Analyzer and Spike sorter in the MC_Rack software (Version 4.6.2) positive (pPA) and negative peak amplitude (nPA), field potential duration (FPD) and amplitude (FPA) as well as beat interval (BI) were evaluated (Fig. 7A). Field potential amplitude upstroke speed was calculated by dividing FPA by FPD. All data sets are represented as mean \pm SD compiling 5 randomly chosen electrodes of at least 5 independent experiments. The chemical compound data were normalized to control for each experiment.

Received: 3 January 2020; Accepted: 21 September 2020

Published online: 28 October 2020

References

- Thomson, J. A. Embryonic stem cell lines derived from human blastocysts. *Science* **282**, 1145–1147. <https://doi.org/10.1126/science.282.5391.1145> (1998).
- Takahashi, K. & Yamanaka, S. Induction of pluripotent stem cells from mouse embryonic and adult fibroblast cultures by defined factors. *Cell* **126**, 663–676. <https://doi.org/10.1016/j.cell.2006.07.024> (2006).
- Takahashi, K. *et al.* Induction of pluripotent stem cells from adult human fibroblasts by defined factors. *Cell* **131**, 861–872. <https://doi.org/10.1016/j.cell.2007.11.019> (2007).
- Zwi, L. *et al.* Cardiomyocyte differentiation of human induced pluripotent stem cells. *Circulation* **120**, 1513–1523. <https://doi.org/10.1161/circulationaha.109.868885> (2009).
- Zhu, H. *et al.* Two dimensional electrophysiological characterization of human pluripotent stem cell-derived cardiomyocyte system. *Sci. Rep.* **7**, 43210. <https://doi.org/10.1038/srep43210> (2017).
- Friedman, C. E. *et al.* Single-cell transcriptomic analysis of cardiac differentiation from human PSCs reveals HOPX-dependent cardiomyocyte maturation. *Cell Stem Cell* **23**, 586–598.e588. <https://doi.org/10.1016/j.stem.2018.09.009> (2018).
- Lian, X. *et al.* Cozzarelli prize winner: robust cardiomyocyte differentiation from human pluripotent stem cells via temporal modulation of canonical Wnt signaling. *Proc. Natl. Acad. Sci. USA* **109**, E1848–E1857. <https://doi.org/10.1073/pnas.1200250109> (2012).
- Lian, X. *et al.* Directed cardiomyocyte differentiation from human pluripotent stem cells by modulating Wnt/ β -catenin signaling under fully defined conditions. *Nat. Protoc.* **8**, 162–175. <https://doi.org/10.1038/nprot.2012.150> (2013).
- Lian, X. *et al.* Chemically defined, albumin-free human cardiomyocyte generation. *Nat. Methods* **12**, 595–596. <https://doi.org/10.1038/nmeth.3448> (2015).
- Laco, F. *et al.* Unraveling the Inconsistencies of Cardiac Differentiation Efficiency Induced by the GSK3 β Inhibitor CHIR99021 in Human Pluripotent Stem Cells. *Stem Cell Rep.* **10**, 1851–1866. <https://doi.org/10.1016/j.stemcr.2018.03.023> (2018).

11. Mummery, C. L. *et al.* Differentiation of human embryonic stem cells and induced pluripotent stem cells to cardiomyocytes. *Circ. Res.* **111**, 344–358. <https://doi.org/10.1161/circresaha.110.227512> (2012).
12. Kempf, H. *et al.* Bulk cell density and Wnt/TGF β signalling regulate mesodermal patterning of human pluripotent stem cells. *Nat. Commun.* **7**, 13602. <https://doi.org/10.1038/ncomms13602> (2016).
13. Osafune, K. *et al.* Marked differences in differentiation propensity among human embryonic stem cell lines. *Nat. Biotechnol.* **26**, 313–315. <https://doi.org/10.1038/nbt1383> (2008).
14. Yamanaka, S. Induced pluripotent stem cells: past, present, and future. *Cell Stem Cell* **10**, 678–684. <https://doi.org/10.1016/j.stem.2012.05.005> (2012).
15. Vitale, A. M. *et al.* Variability in the generation of induced pluripotent stem cells: importance for disease modeling. *Stem Cells Transl. Med.* **1**, 641–650. <https://doi.org/10.5966/sctm.2012-0043> (2012).
16. Boland, M. J., Nazor, K. L. & Loring, J. F. Epigenetic regulation of pluripotency and differentiation. *Circ. Res.* **115**, 311–324. <https://doi.org/10.1161/circresaha.115.301517> (2014).
17. Nolbrant, S., Heuer, A., Parmar, M. & Kirkeby, A. *Generation of high-purity human ventral midbrain dopaminergic progenitors for in vitro maturation and intracerebral transplantation*. Vol. 12 (2017).
18. Ghosh, S. *et al.* Cell density-dependent transcriptional activation of endocrine-related genes in human adipose tissue-derived stem cells. *Exp Cell Res.* **316**, 2087–2098. <https://doi.org/10.1016/j.yexcr.2010.04.015> (2010).
19. Siller, R., Greenhough, S., Naumovska, E. & Gareth, T. Small-molecule-driven hepatocyte differentiation of human pluripotent stem cells. *Stem Cell Rep.* **4**, 939–952. <https://doi.org/10.1016/j.stemcr.2015.04.001> (2015).
20. Siller, R. *et al.* Development of a rapid screen for the endodermal differentiation potential of human pluripotent stem cell lines. *Sci. Rep.* **6**, 37178. <https://doi.org/10.1038/srep37178> (2016).
21. Mathapati, S. *et al.* Small-molecule-directed hepatocyte-like cell differentiation of human pluripotent stem cells. *Curr. Protoc. Stem Cell Biol.* **38**, 1g.6.1–1g.6.18. <https://doi.org/10.1002/cpsc.13> (2016).
22. Sturzu, A. C. & Wu, S. M. Developmental and regenerative biology of multipotent cardiovascular progenitor cells. *Circ. Res.* **108**, 353–364. <https://doi.org/10.1161/circresaha.110.227066> (2011).
23. Sepac, A. *et al.* Comparison of cardiomyogenic potential among human ESC and iPSC lines. *Cell Transpl.* **21**, 2523–2530. <https://doi.org/10.3727/096368912X653165> (2012).
24. Himmel, H. M. Drug-induced functional cardiotoxicity screening in stem cell-derived human and mouse cardiomyocytes: effects of reference compounds. *J. Pharmacol. Toxicol. Methods* **68**, 97–111. <https://doi.org/10.1016/j.vascn.2013.05.005> (2013).
25. Wang, Q. *et al.* 5-HTR3 and 5-HTR4 located on the mitochondrial membrane and functionally regulated mitochondrial functions. *Sci. Rep.* **6**, 37336. <https://doi.org/10.1038/srep37336> (2016).
26. Ayme-Dietrich, E., Aubertin-Kirch, G., Maroteaux, L. & Monassier, L. Cardiovascular remodeling and the peripheral serotonergic system. *Arch. Cardiovasc. Dis.* **110**, 51–59. <https://doi.org/10.1016/j.acvd.2016.08.002> (2017).
27. Tertoolen, L. G. J., Braam, S. R., van Meer, B. J., Passier, R. & Mummery, C. L. Interpretation of field potentials measured on a multi electrode array in pharmacological toxicity screening on primary and human pluripotent stem cell-derived cardiomyocytes. *Biochem. Biophys. Res. Commun.* **497**, 1135–1141. <https://doi.org/10.1016/j.bbrc.2017.01.151> (2018).
28. BurrIDGE, P. W. *et al.* Chemically defined generation of human cardiomyocytes. *Nat. Methods* **11**, 855–860. <https://doi.org/10.1038/nmeth.2999> (2014).
29. Kempf, H. & Zweigert, R. in *Engineering and Application of Pluripotent Stem Cells* (eds Ulrich Martin, Robert Zweigert, & Ina Gruh) 39–69 (Springer International Publishing, 2018).
30. Quaranta, R. *et al.* Revised roles of ISL1 in a hES cell-based model of human heart chamber specification. *eLife* <https://doi.org/10.7554/eLife.31706> (2018).
31. Gao, R. *et al.* Pioneering function of Isl1 in the epigenetic control of cardiomyocyte cell fate. *Cell Res.* <https://doi.org/10.1038/s41422-019-0168-1> (2019).
32. Moretti, A. *et al.* Patient-specific induced pluripotent stem-cell models for long-QT syndrome. *Sci. Rep.* **363**, 1397–1409. <https://doi.org/10.1056/nejmoa0908679> (2010).
33. Yokoo, N. *et al.* The effects of cardioactive drugs on cardiomyocytes derived from human induced pluripotent stem cells. *Biochem. Biophys. Res. Commun.* **387**, 482–488. <https://doi.org/10.1016/j.bbrc.2009.07.052> (2009).
34. Zimmer, T. Effects of tetrodotoxin on the mammalian cardiovascular system. *Mar. Drugs* **8**, 741–762. <https://doi.org/10.3390/md8030741> (2010).
35. Maier, S. K. G. *et al.* Distinct subcellular localization of different sodium channel α and β subunits in single ventricular myocytes from mouse heart. *Circulation* **109**, 1421–1427. <https://doi.org/10.1161/01.cir.0000121421.61896.24> (2004).
36. Dubois, N. C. *et al.* SIRPA is a specific cell-surface marker for isolating cardiomyocytes derived from human pluripotent stem cells. *Nat. Biotechnol.* **29**, 1011–1018. <https://doi.org/10.1038/nbt2005> (2011).
37. Ma, J. *et al.* High purity human-induced pluripotent stem cell-derived cardiomyocytes: electrophysiological properties of action potentials and ionic currents. *Am. J. Physiol. Heart Circ. Physiol.* **301**, H2006–H2017. <https://doi.org/10.1152/ajpheart.00694.2011> (2011).
38. Hattori, F. *et al.* Nongenetic method for purifying stem cell-derived cardiomyocytes. *Nat. Methods* **7**, 61–66. <https://doi.org/10.1038/nmeth.1403> (2010).
39. Tohyama, S. *et al.* Distinct metabolic flow enables large-scale purification of mouse and human pluripotent stem cell-derived cardiomyocytes. *Cell Stem Cell* **12**, 127–137. <https://doi.org/10.1016/j.stem.2012.09.013> (2013).
40. Fuerstenau-Sharp, M. *et al.* Generation of highly purified human cardiomyocytes from peripheral blood mononuclear cell-derived induced pluripotent stem cells. *PLoS ONE* **10**, e0126596. <https://doi.org/10.1371/journal.pone.0126596> (2015).
41. Zwartsen, A. *et al.* Cardiotoxicity screening of illicit drugs and new psychoactive substances (NPS) in human iPSC-derived cardiomyocytes using microelectrode array (MEA) recordings. *J. Mol. Cell. Cardiol.* <https://doi.org/10.1016/j.yjmcc.2019.09.007> (2019).
42. McPheeters, M. T., Wang, Y. T., Werdich, A. A., Jenkins, M. W. & Laurita, K. R. An infrared optical pacing system for screening cardiac electrophysiology in human cardiomyocytes. *PLoS ONE* **12**, e0183761. <https://doi.org/10.1371/journal.pone.0183761> (2017).
43. Schindelin, J. *et al.* Fiji: an open-source platform for biological-image analysis. *Nat. Methods* **9**, 676–682. <https://doi.org/10.1038/nmeth.2019> (2012).

Acknowledgements

We thank Hege Avsnes Dale and Endy Spriet of the Molecular Imaging Center (MIC), University of Bergen for their technical guidance in confocal microscopy. This work was supported by grants from The Research Council of Norway (NFR) (LAB 229652; GS/RS 221333), Bergen Stem Cell Consortium (BSCC), Helse Vest and Rakel og Otto-Kristian Bruun's Legat. The authors wish to acknowledge the help and resources provided by the National Core Facility for Human Pluripotent Stem Cells, Norwegian Center for Stem Cell Research, Oslo University Hospital.

Authors contributions

R.S. and G.S performed reprogramming and establishment of iPSC lines. N.B., S.M. and X.L. performed the cell cultures. N.B., S.M., M.S. and performed the biological experiments and data collection. N.B. and S.M. performed assembly and analysis of data, and wrote the manuscript. L.B., G.S., S.M. and N.B. were involved in study concept and design, revision of the manuscript and all authors approved the final version of the manuscript.

Competing interests

The authors declare no competing interests.

Additional information

Supplementary information is available for this paper at <https://doi.org/10.1038/s41598-020-73656-2>.

Correspondence and requests for materials should be addressed to L.A.B.

Reprints and permissions information is available at www.nature.com/reprints.

Publisher's note Springer Nature remains neutral with regard to jurisdictional claims in published maps and institutional affiliations.



Open Access This article is licensed under a Creative Commons Attribution 4.0 International License, which permits use, sharing, adaptation, distribution and reproduction in any medium or format, as long as you give appropriate credit to the original author(s) and the source, provide a link to the Creative Commons licence, and indicate if changes were made. The images or other third party material in this article are included in the article's Creative Commons licence, unless indicated otherwise in a credit line to the material. If material is not included in the article's Creative Commons licence and your intended use is not permitted by statutory regulation or exceeds the permitted use, you will need to obtain permission directly from the copyright holder. To view a copy of this licence, visit <http://creativecommons.org/licenses/by/4.0/>.

© The Author(s) 2020

SUPPLEMENTARY FIGURE LEGENDS AND TABLES

A method for differentiating human induced pluripotent stem cells toward functional cardiomyocytes in 96-well microplates

Novin Balafkan, Sepideh Mostafavi, Manja Schubert, Richard Siller, Xiao Liang, Gareth Sullivan, Laurence A. Bindoff

Supplementary Figure S1. Seeding hPSC in 96well plate at different cell densities.

The figure shows the morphology of AG05836B-15 cells cultured at different cell density one day after (panels A) and two days (panels B) after seeding in 96 well plates. The A panels show the cells cultured for 24 hrs in E8 supplemented by Y27632, while the B panels show the cells cultured for a further 24 hrs in E8 alone. We tested the following seeding densities 1.2×10^4 (i), 2.4×10^4 (ii), 4.8×10^4 (iii) and 7.2×10^4 cells/cm² (iv). We found that the best cell density for seeding cells to achieve 60-70% confluency prior to the start of differentiation was 2.4×10^4 cells/cm² (equal to 8000 cells per one well of 96 well plate). This cell density gave cells enough time to recover from the Y27632 effects in E8 medium (Aii) and reach to the optimal confluency (Bii). Cells seeded at lower density (1.2×10^4 cells/cm²: panels (i)) required more time to reach optimal confluency while seeding cells at higher densities gave rise to very confluent cultures one day after seeding and resulted in poor differentiation efficiency (Panels (iii) and (iv) are representative of 4.8×10^4 cells/cm² and 7.2×10^4 cells/cm² respectively). The effect of confluency on differentiation efficiency is shown in Figure.2.

Supplementary Figure S2. Characterization of Detroit 551-A-derived cardiomyocytes by gene expression. Relative quantification of mRNA expression profile of 15 markers, representing different stages of differentiation from hiPSC (D0) to mesodermal layer (D3) following by cardiac progenitor state (D5) and committed cardiomyocyte on D15. Treatment of hiPSC with CHIR99021 led to expression of mesodermal markers such as *MESPI* and *MIXL1* on D3. Expression of *ISL1* on D5 following the application of the inhibitor of WNT production-2, IWP2, indicated the presence of cardiac progenitors in the culture. Substantial increase in expression of committed cardiomyocyte markers such as *TBX5*, *TNNT2*, *MYH6* and *MYL7* revealed the presence of committed cardiomyocytes on D15 of differentiation. Data are presented as the mean of three independent differentiation runs and error bars are the

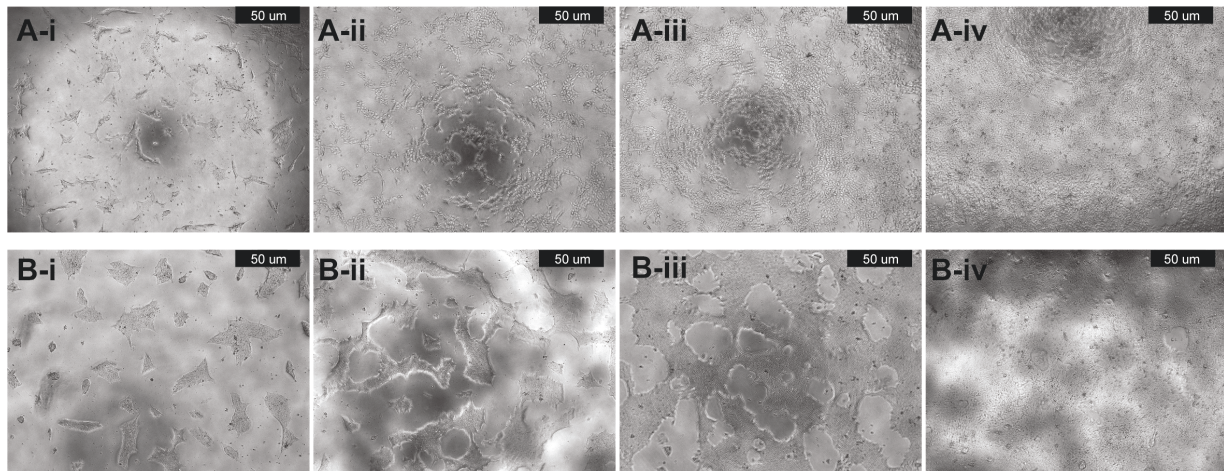
standard deviation of the mean. Changes in expression level are related to the pluripotent stage, D0.

Supplementary Figure S3. A) Gene expression study showed a drop of the pluripotency marker *POU5F1* and the appropriate increase in the level of different cardiac lineage markers. Data are collected from experiments using hESC-H9 for cardiac differentiation and presented as mean of 3 independent experiments and error bars are standard deviation of the mean. Changes in expression levels are related to hiPSC, i.e. Day 0. B) Expression of pluripotency marker (*POU5F1*) and lack of expression of cardiac specific marker (*TNNT2*) in hiPSC on D0. *TNNT2* positive cells were detectable from day 7 where expression of *POU5F1* is highly reduced. Images are taken using an epifluorescent microscope (LEITZ DMRBE, Leica). Scale bars, 50 μ m.

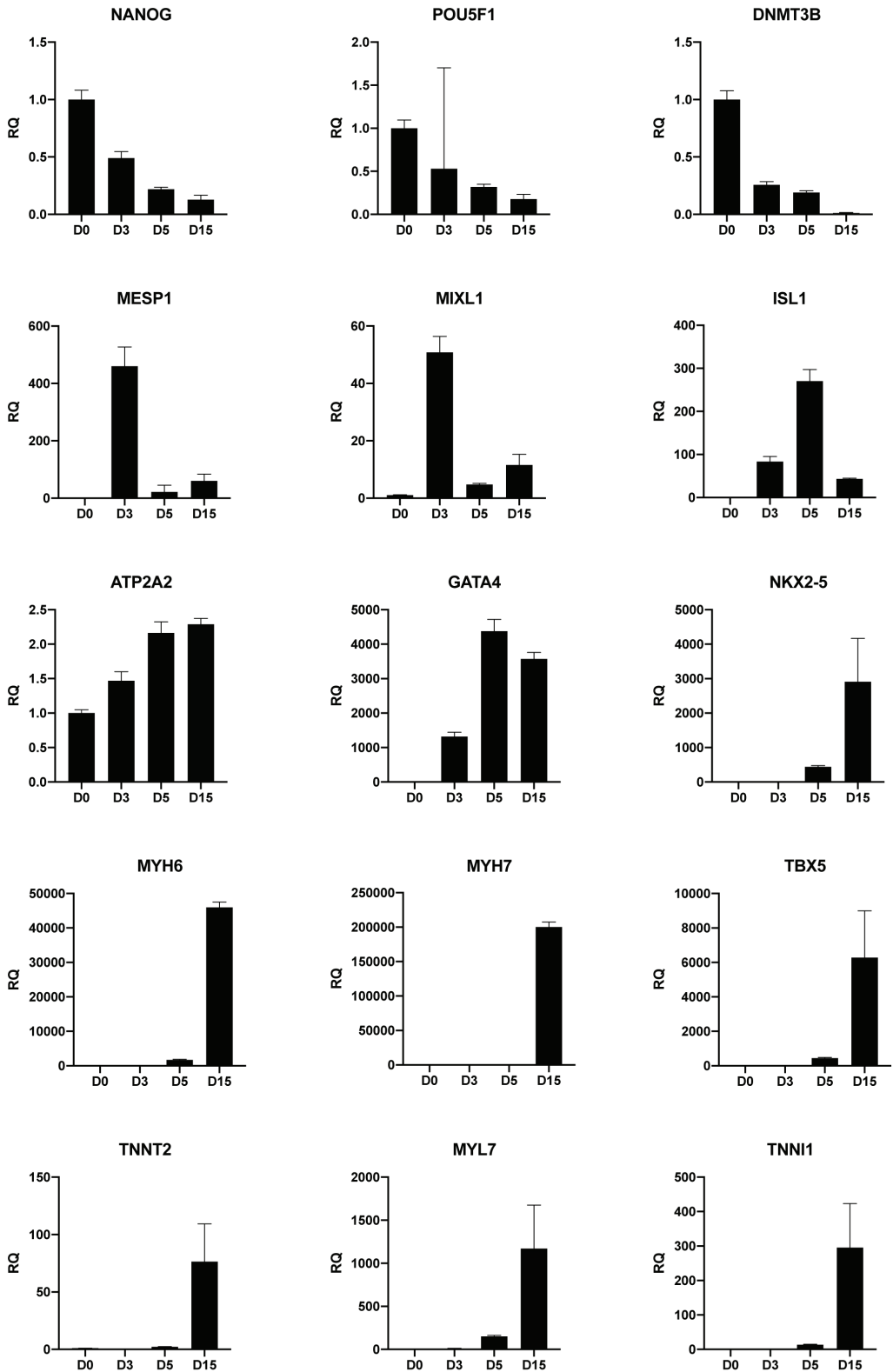
Supplementary Figure S4. RT-qPCR analysis of aged cardiomyocyte gene expression. This shows the relative quantification of mRNA expression of *HOPX*, *MYH7*, *MYH6* and *NKX2.5*. These results show that cardiomyocytes on D30 express age appropriate markers. This was performed one run of H1 differentiation.

Supplementary Figure S5. A) Representative histogram plots showing the fluorescence minus one (FMO), isotype and unstained controls of surface markers. The committed cardiomyocytes were gated for CD140b (PE) and CD144 (FITC) and gates were drawn by using FMO together with isotype control to analyze these surface markers. B) Representative histogram plot of fluorescence minus one (FMO) control of internal marker *TNNT2* (FITC). Graphs were prepared and presented using FlowJo 10.5.0 (FlowJo LLC, OR, USA) software.

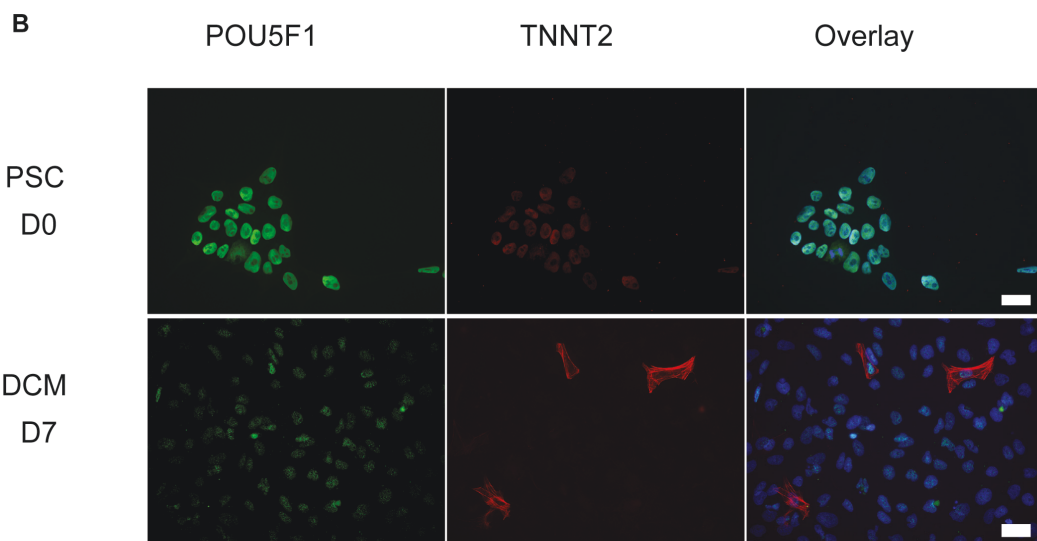
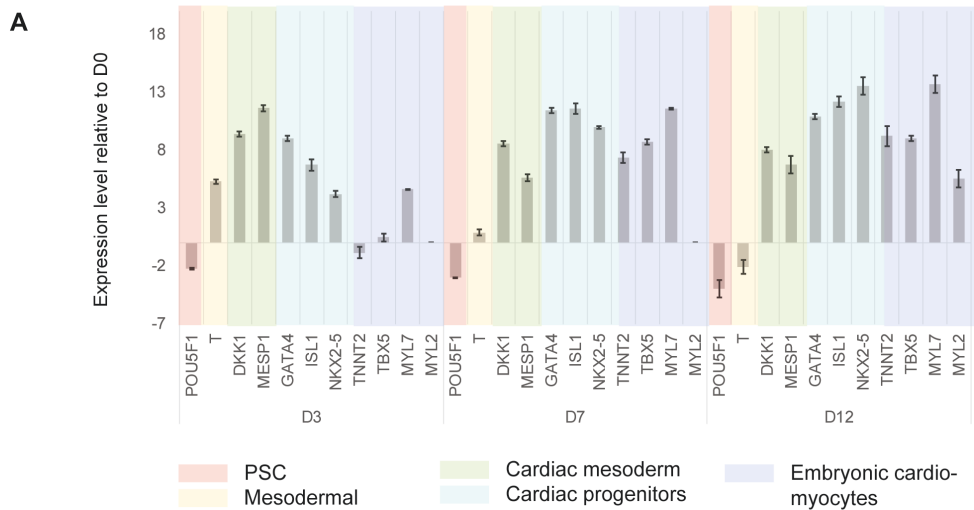
Supplementary Fig. 1



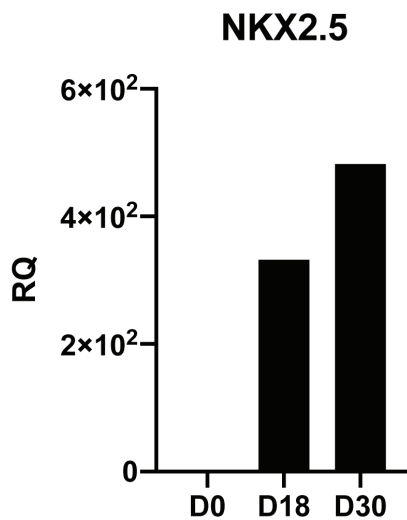
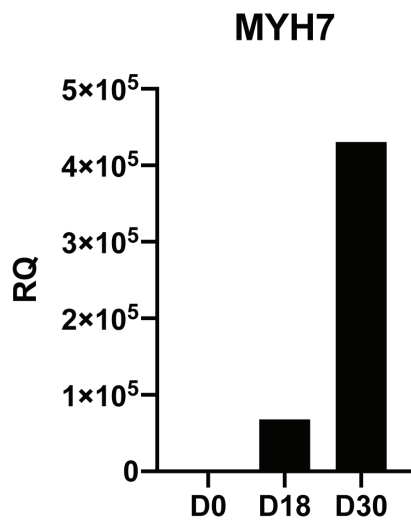
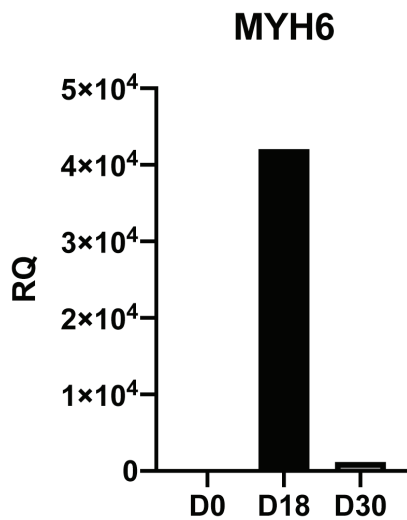
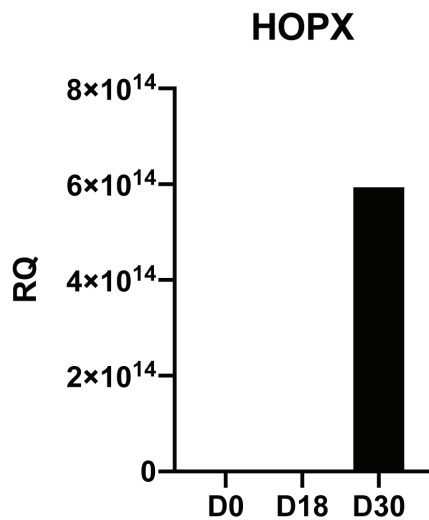
Supplementary Fig. 2



Supplementary Fig. 3

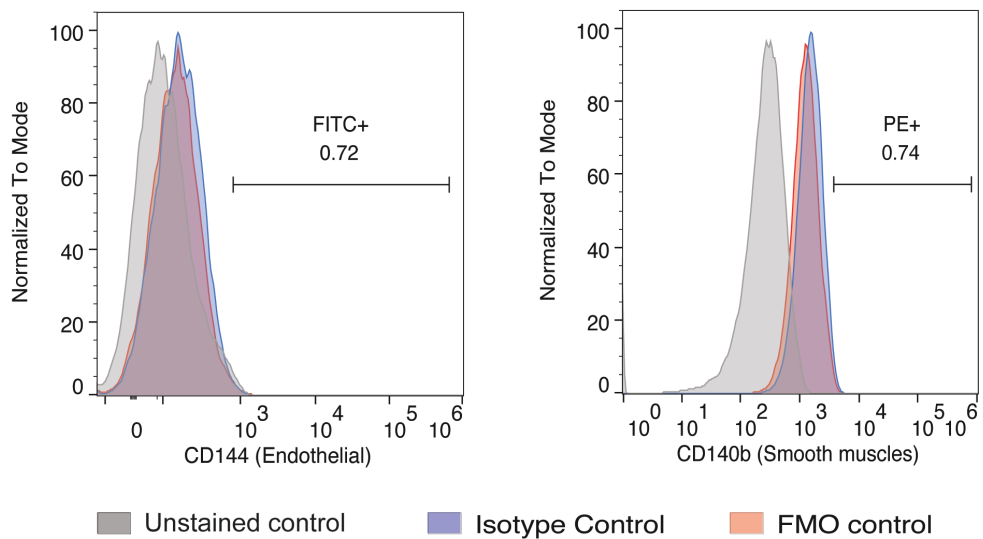


Supplementary Fig. 4

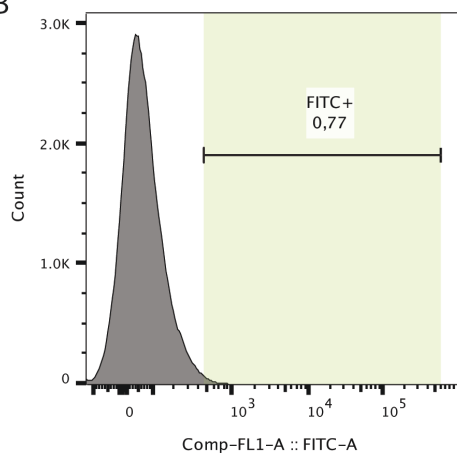


Supplementary Fig. 5

A



B



SUPPLEMENTARY TABLES

A method for differentiating human induced pluripotent stem cells toward functional cardiomyocytes in 96-well microplates

Novin Balafkan, Sepideh Mostafavi, Manja Schubert, Richard Siller, Xiao Liang, Gareth Sullivan, Laurence A. Bindoff

Supplementary Table S1. Expression of two cardiomyocyte markers, *TNNT2* and *NKX2-5* in single well of 96 well plate. The ratio of CT value of *TNNT2* and *NKX2-5* to CT value of the housekeeping gene (*GAPDH*) of the same well was calculated and used for boxplot analysis.

| | H1-Run1 | | | H1-Run2 | | | Detroit- 551-A | |
|----------------|-------------------------|--------------------------|--------------------|-------------------------|--------------------------|-------------------|-------------------------|--------------------------|
| | TNNT2/ GAPDH | NKX2-5/ GAPDH | | TNNT2/ GAPDH | NKX2-5/ GAPDH | | TNNT2/ GAPDH | NKX2-5/ GAPDH |
| Plate 1 | 0.956139536 | 1.015778015 | Plate 1 | 1.194772754 | 1.302516732 | Plate 1 | 1.00756806 | 1.25257046 |
| | 0.972867659 | 1.005521616 | | 1.206018698 | 1.308690262 | | 0.98687557 | 1.25630243 |
| | 0.866792522 | 0.937277184 | | 1.13410478 | 1.258217263 | | 0.8955656 | 1.10212642 |
| | 0.910855933 | 0.96281839 | | 1.183462783 | 1.283911434 | | 0.92707995 | 1.14802946 |
| | 0.854842318 | 0.996865388 | Plate 2 | 1.055617383 | 1.284905175 | Plate 2 | 0.92830478 | 1.16168319 |
| | 1.120783689 | 1.018326948 | | 1.438343182 | 1.329944629 | | 0.86026702 | 1.11449094 |
| | 0.894715841 | 0.968538453 | | 1.172014938 | 1.274410378 | | 0.93855131 | 1.17942924 |
| | 0.971535661 | 1.004025319 | | 1.222110169 | 1.270765593 | | | |
| | 0.93476675 | 1.007464663 | Plate 3 | 1.234872769 | 1.301884353 | Plate 3 | 0.87943181 | 1.09338735 |
| | 0.916651164 | 0.939988766 | | 1.201630107 | 1.245197324 | | 0.83583114 | 1.06603565 |
| | 0.938247181 | 0.978614518 | | 1.214696227 | 1.251713162 | | 0.8453753 | 1.11879248 |
| | 0.930002506 | 0.995752786 | | 1.231765242 | 1.27419605 | | | |
| Min | 0.854842318 | 0.937277184 | 1.055617383 | 1.245197324 | 0.83583114 | 1.06603565 | | |
| Q1 | 0.90682091 | 0.967108437 | 1.180600821 | 1.267628511 | 0.86505822 | 1.10521755 | | |
| Median | 0.932384628 | 0.996309087 | 1.203824402 | 1.279160906 | 0.91132277 | 1.13341097 | | |
| Q3 | 0.959988568 | 1.006007378 | 1.224523937 | 1.302042447 | 0.93598967 | 1.17499272 | | |
| Max | 1.120783689 | 1.018326948 | 1.438343182 | 1.329944629 | 1.00756806 | 1.25630243 | | |
| Mean | 0.93901673 | 0.985914337 | 1.207450753 | 1.28219603 | 0.91048505 | 1.14928476 | | |
| Range | 0.26594137 | 0.081049764 | 0.382725798 | 0.084747305 | 0.17173692 | 0.19026679 | | |

Supplementary table S2. Antibodies and TaqMan probes used in this study.

| Marker | Host | Company | Catalog Number | Application |
|--------------------------------------|-------------------|--------------------------|-----------------------|--------------------|
| MYL7 | recombinant human | Miltenyi Biotec | 130-106-142 | Flow Cytometry |
| TNNT2 | recombinant human | Miltenyi Biotec | 130-119-575 | Flow Cytometry |
| Nkx-2.5 | Rabbit | Santa Cruz Biotechnology | sc-14033 | Flow Cytometry |
| Nkx-2.5 | Rabbit | abcam | ab35842 | Flow Cytometry |
| Anti-MLC2v-PE, human, mouse, rat | Rabbit | Miltenyi Biotec | 130-119-680 | Flow Cytometry |
| Anti CD140b-PE, human | recombinant human | Miltenyi Biotec | 130-105-321 | Flow Cytometry |
| Anti CD144 (VE-Cadherin)-FITC, human | recombinant human | Miltenyi Biotec | 130-100-713 | Flow Cytometry |
| FcR Blocking Reagent, human | | Miltenyi Biotec | 130-059-901 | Flow Cytometry |
| | | | | |
| Marker | Host | Company | Catalog Number | Application |
| ACTA2 | Mouse | abcam | ab7817 | IF |
| CDH5 | Rabbit | abcam | ab33168 | IF |
| GJA1 | Rabbit | abcam | ab11370 | IF |
| MYL7 | Mouse | abcam | ab68086 | IF |
| TNNT2 | Mouse | abcam | ab8295 | IF |
| TNNI3 | Rabbit | abcam | ab47003 | IF |
| Nkx2-5 | Rabbit | abcam | ab35842 | IF |
| ISL1 | Rabbit | abcam | ab20670 | IF |
| | | | | |
| Marker | | Company | Catalog Number | Application |
| Human GAPD | | Thermo Fisher | Hs02786624_g1 | TaqMan Probe |
| Beta ACT (ACTB) | | Thermo Fisher | Hs01060665_g1 | TaqMan Probe |
| Nanog | | Thermo Fisher | Hs02387400_g1 | TaqMan Probe |
| POU5F1 (OCT 4) | | Thermo Fisher | Hs00999634_gH | TaqMan Probe |
| DNMT3B | | Thermo Fisher | Hs00171876_m1 | TaqMan Probe |
| MESP1 | | Thermo Fisher | Hs01001283_g1 | TaqMan Probe |
| ISL1 | | Thermo Fisher | Hs00158126_m1 | TaqMan Probe |

| | | | | |
|--------------|--|---------------|---------------|--------------|
| MIXL1 | | Thermo Fisher | Hs00430824 g1 | TaqMan Probe |
| NKX2-5 | | Thermo Fisher | Hs00231763 m1 | TaqMan Probe |
| TMEM88 | | Thermo Fisher | Hs00396750 g1 | TaqMan Probe |
| ATP2A2 | | Thermo Fisher | Hs00544877 m1 | TaqMan Probe |
| MYH6 | | Thermo Fisher | Hs01101425 m1 | TaqMan Probe |
| MYH7 | | Thermo Fisher | Hs01110632 m1 | TaqMan Probe |
| TNNI1 | | Thermo Fisher | Hs00913333 m1 | TaqMan Probe |
| TNNI3 | | Thermo Fisher | Hs00165957 m1 | TaqMan Probe |
| TNNT2 (cTnT) | | Thermo Fisher | Hs00943911 m1 | TaqMan Probe |
| MYL7-(MLC2a) | | Thermo Fisher | Hs01085598 g1 | TaqMan Probe |
| MYL2 (MLC2v) | | Thermo Fisher | Hs00166405 m1 | TaqMan Probe |
| HOPX | | Thermo Fisher | Hs05028646 s1 | TaqMan Probe |



Distinct Mitochondrial Remodeling During Mesoderm Differentiation in a Human-Based Stem Cell Model

Sepideh Mostafavi^{1†}, Novin Balafkan^{1,2,3*†}, Ina Katrine Nitschke Pettersen⁴, Gonzalo S. Nido^{1,5}, Richard Siller⁶, Charalampos Tzoulis^{1,5}, Gareth J. Sullivan^{6,7,8,9,10,11} and Laurence A. Bindoff^{1,5*}

¹ Department of Clinical Medicine, University of Bergen, Bergen, Norway, ² Division of Psychiatry, Haukeland University Hospital, Bergen, Norway, ³ Norwegian Centre for Mental Disorders Research (NORMENT)—Centre of Excellence, Haukeland University Hospital, Bergen, Norway, ⁴ Institute for Biomedicine, University of Bergen, Bergen, Norway, ⁵ Neuro-SysMed, Center of Excellence for Clinical Research in Neurological Diseases, Department of Neurology, Haukeland University Hospital, Bergen, Norway, ⁶ Stem Cell Epigenetics Laboratory, Institute of Basic Medical Sciences, University of Oslo, Oslo, Norway, ⁷ Department of Molecular Medicine, Institute of Basic Medical Sciences, University of Oslo, Oslo, Norway, ⁸ Norwegian Center for Stem Cell Research, Oslo University Hospital and the University of Oslo, Oslo, Norway, ⁹ Institute of Immunology, Oslo University Hospital, Oslo, Norway, ¹⁰ Hybrid Technology Hub—Centre of Excellence, Institute of Basic Medical Sciences, University of Oslo, Oslo, Norway, ¹¹ Department of Pediatric Research, Oslo University Hospital, Oslo, Norway

OPEN ACCESS

Edited by:

Silvia Parisi,
University of Naples Federico II, Italy

Reviewed by:

Jarmon G. Lees,
University of Melbourne, Australia
Alexandra Harvey,
The University of Melbourne, Australia

*Correspondence:

Novin Balafkan
novin.balafkan@uib.no
Laurence A. Bindoff
laurence.bindoff@nevro.uib.no

[†]These authors have contributed equally to this work and share first authorship

Specialty section:

This article was submitted to Cellular Biochemistry, a section of the journal *Frontiers in Cell and Developmental Biology*

Received: 20 July 2021

Accepted: 21 September 2021

Published: 14 October 2021

Citation:

Mostafavi S, Balafkan N, Pettersen IK, Nido GS, Siller R, Tzoulis C, Sullivan GJ and Bindoff LA (2021) Distinct Mitochondrial Remodeling During Mesoderm Differentiation in a Human-Based Stem Cell Model. *Front. Cell Dev. Biol.* 9:744777. doi: 10.3389/fcell.2021.744777

Given the considerable interest in using stem cells for modeling and treating disease, it is essential to understand what regulates self-renewal and differentiation. Remodeling of mitochondria and metabolism, with the shift from glycolysis to oxidative phosphorylation (OXPHOS), plays a fundamental role in maintaining pluripotency and stem cell fate. It has been suggested that the metabolic “switch” from glycolysis to OXPHOS is germ layer-specific as glycolysis remains active during early ectoderm commitment but is downregulated during the transition to mesoderm and endoderm lineages. How mitochondria adapt during these metabolic changes and whether mitochondria remodeling is tissue specific remain unclear. Here, we address the question of mitochondrial adaptation by examining the differentiation of human pluripotent stem cells to cardiac progenitors and further to differentiated mesodermal derivatives, including functional cardiomyocytes. In contrast to recent findings in neuronal differentiation, we found that mitochondrial content decreases continuously during mesoderm differentiation, despite increased mitochondrial activity and higher levels of ATP-linked respiration. Thus, our work highlights similarities in mitochondrial remodeling during the transition from pluripotent to multipotent state in ectodermal and mesodermal lineages, while at the same time demonstrating cell-lineage-specific adaptations upon further differentiation. Our results improve the understanding of how mitochondrial remodeling and the metabolism interact during mesoderm differentiation and show that it is erroneous to assume that increased OXPHOS activity during differentiation requires a simultaneous expansion of mitochondrial content.

Keywords: mitochondria, development, metabolism, stem cells, cardiomyocyte, OXPHOS

INTRODUCTION

Crosstalk between mitochondria, metabolism, and processes controlling stem cell fate is essential (reviewed in Wanet et al., 2015). As human pluripotent stem cells (hPSCs) exit pluripotency, they switch from a primarily glycolytic-based metabolism that provides the energy and substrates necessary for proliferation in a hypoxic niche to one more dependent on oxidative phosphorylation (OXPHOS), which is better suited for post-mitotic tissues with high energy demand (Locasale and Cantley, 2011; Varum et al., 2011; Zhang et al., 2012a). Metabolic switching during differentiation is thought to be germ layer specific, as inhibition of glycolysis inhibits neuronal differentiation but has no effect on mesodermal and endodermal differentiation (Cliff et al., 2017). In addition, the MYC transcription factor family that drives glycolysis remains activated after exit from pluripotency in nascent ectoderm, while it is silenced during mesoderm and endoderm differentiation (Cliff et al., 2017). How mitochondrial properties are adapted through metabolic switching during early stages of differentiation across different germ layers remains unclear.

It has been proposed that the switch from glycolysis to OXPHOS is the result of remodeling mitochondria from a fragmented state with lower mitochondrial DNA (mtDNA) and mass in hPSCs, to elongated mitochondria with high levels of mtDNA and mitochondrial mass in differentiated cells (Sercel et al., 2021). Experimental data for this hypothesis are, however, limited to either studies of neuronal differentiation (Zheng et al., 2016; Lees et al., 2018) or to earlier studies describing mitochondrial changes in heterogeneous cultures derived from spontaneous differentiation of embryoid bodies (St John et al., 2005; Cho et al., 2006; Belmonte and Morad, 2008; Lukyanenko et al., 2009). Notably, ectoderm differentiation showed a biphasic change in mitochondrial content: in early differentiation, mitochondrial mass, mtDNA, and superoxide production decreased, while in the later stages, there was an expansion of mitochondrial mass and mtDNA along with a higher OXPHOS activity (St John et al., 2005; Cho et al., 2006; Zheng et al., 2016; Lees et al., 2018).

Understanding the crosstalk between mitochondrial remodeling and metabolic switch is particularly crucial for improving our knowledge about the mechanisms involved in lineage-directed differentiation and tissue maturation (Wanet et al., 2015). To gain greater insight into the role of mitochondrial remodeling during metabolic switch in mesoderm differentiation, we assessed mitochondrial properties including mitochondrial abundance, ultrastructure, membrane potential, and respiratory complex activity during differentiation and maturation of cardiomyocytes derived from both human embryonic stem cells (hESCs) and human induced pluripotent stem cells (hiPSCs). Cardiomyocytes derived from hPSCs share the characteristics and functional properties of primary human heart tissue and are able to recapitulate the *in vivo* developmental process (Zwi et al., 2009; Zhu et al., 2017; Friedman et al., 2018).

In contrast to previous reports, we detected a significant reduction in mitochondrial biomass and mtDNA levels during mesoderm differentiation. Despite this marked mitochondrial

reduction, however, differentiated cells showed a higher mitochondrial coupling efficiency and appeared more dependent on OXPHOS with a higher mitochondrial membrane potential per unit mitochondria than undifferentiated hPSCs. Overall, our findings suggest a unique mitochondrial remodeling process for cardiomyocyte differentiation whereby mitochondrial biogenesis decreases during the transition from hPSCs into differentiated cardiomyocytes, while the efficiency of ATP generation through OXPHOS increases in keeping with mitochondrial maturation.

MATERIALS AND METHODS

Human Pluripotent Stem Cell Lines

Three hESC lines [H1 (male), 429 (female) and 360 (male)] and four hiPSC lines (established from two independent Detroit 551 (female) clones (clones 7 and 10) and one CRL 2097 (male) iPSC clone, CRL-8) were employed for this study. The details of reprogramming and characterization of the hiPSC lines are published elsewhere (Siller et al., 2015, 2016; Balafkan et al., 2020; Liang et al., 2020). The hPSCs were cultured using standard procedures in a 5% CO₂ incubator at 37°C. hPSCs were maintained in feeder-free conditions in Essential 8 Medium (E8) (Gibco™). The passage number of the hiPSCs was between 23 and 55 for all experiments, and there was no preference for using a specific passage number for an experiment.

Cardiomyocyte Differentiation

Cardiomyocyte differentiation was performed in 96-well microplates as previously described (Balafkan et al., 2020). Briefly, hiPSCs were seeded and propagated on Geltrex (Gibco™), under feeder-free conditions in E8. Within 3 days, when cells reached the optimum confluency (60–70%), cardiomyocyte differentiation was started by applying the GSK3 inhibitor CHIR99021 in Roswell Park Memorial Institute (RPMI) 1640 medium supplemented with B27 without insulin (RPMI-B27), in a cell-concentration-dependent manner. After 24 h, medium was changed to RPMI-B27 without CHIR99021. The differentiation process was continued by adding 5 μM of inhibitor of WNT production-2, IWP2, diluted in RPMI-B27, 72 h post-differentiation induction for 48 h. Fresh RPMI-B27 medium was provided on day 5, and from day 7, cells were fed with fresh RPMI medium supplemented with B27 with insulin without extra supplement, every 2 days. Differentiated cardiomyocytes start beating around day 10, and it becomes more synchronized after day 12 (see **Supplementary Movies 1, 2**).

Gene Expression Analysis

MagMAX™-96 Total RNA Isolation Kit was used for RNA isolation from cultured cells. EXPRESS One-Step Superscript qRT-PCR Kit (Invitrogen™) was used for cDNA synthesis and real-time PCR using TaqMan probes (**Supplementary Table 1**) on an Applied Biosystems 7,500-Fast real-time PCR System. All real-time PCR were performed in triplicate, and the average of Ct values was normalized to the geometric mean of *ACTB*

and *GAPDH* as endogenous control genes, and the result (dCt) used for further analysis. For a detailed description, see the **Supplementary Material**.

RNA Sequencing and Bioinformatics Analysis

RNA sequencing (RNA-seq) analyses were performed independently for two datasets. The first dataset (Dataset A, $N = 22$) was composed of either hESC or hiPSC lines collected from S1 (undifferentiated cells at day 0) and S4 (Isl1⁺ progenitor cells at day 7), from three independent differentiation runs of two hESC lines (429 and 360), two independent differentiation runs of Detroit-7 and CRL-8, and one of Detroit-10. The second dataset (Dataset B, $N = 12$) was composed of samples collected at four stages spanning S1–S5 (specifically days 0, 2, 5, and 15) from H1. RNA-seq sample information is provided in **Supplementary Tables 3, 4**. Differential gene expression analyses were performed using the DESeq2 R package version 1.26 (Love et al., 2014) with default parameters, using cell line as a covariate in the model for the first dataset. A corrected p -value of 0.05 and \log_2 (fold change) of 1 were set as the threshold for significantly differential gene expression. Genes then were tested for enrichment using the gene score resampling method implemented in the ermineR package version 1.0.1, an R wrapper package for ermineJ (Gillis et al., 2010) with the complete Gene Ontology (GO) database annotation (Ashburner et al., 2000), and the Kyoto Encyclopedia of Genes and Genomes (KEGG) database (Kanehisa and Goto, 2000) to obtain lists of upregulated and downregulated pathways for each cohort. The source code for the RNA-seq analyses is available in the GitLab repository¹ under GPL public license v3.0. For a detailed description of the methods, refer to the **Supplementary Material**.

Flow Cytometry

Cells were dissociated into single-cell suspension using TrypLE™ Express Enzyme (Gibco™) and stained with Zombie Red™ Fixable Viability Kit (BioLegend, San Diego, CA, United States) according to the manufacturer's instructions. Single cells were fixed, blocked, and stained accordingly (for a detailed description, see the **Supplementary Material**). Antibodies are listed in **Supplementary Table 1**. At least 30,000 events were collected for the target marker using a Sony cell sorter SH800 (Sony Biotechnology Inc., San Jose, CA, United States), and collected data were analyzed and presented by FlowJo V.10.5.0 (FlowJo LLC, Ashland, OR, United States). To conduct inter- and intra-sample analyses from different runs and minimize the batch-to-batch variation, the flow cytometer was calibrated prior to quantitative fluorescence intensity measurements using Quantum™ Alexa Fluor® 488 MESF (molecules of equivalent soluble fluorophore; Bangs Laboratories, Fishers, IN, United States), and collected median fluorescence intensity (MFI) was normalized to MESF as an external control. All gates were adjusted according to fluorescence minus one control (FMO).

¹<https://git.app.uib.no/gni042/cardiomyocytes-rna-seq>

Immunocytochemistry and Fluorescence Microscopy

Cells were seeded either on Geltrex-coated cover slips or in Millicell® EZ SLIDES (Merck Millipore, Billerica, MA, United States), fixed, and stained accordingly (for a detailed description, see the **Supplementary Material**). A final concentration of 10 $\mu\text{g/ml}$ was used for all primary antibodies, and they were incubated overnight at 4°C. Confocal microscopy images were taken on either a Zeiss LSM 510 META (Carl Zeiss, Oberkochen, Germany) or a Leica TCS SP5 (Leica Microsystems GmbH, Wetzlar, Germany) at the Molecular Imaging Center (MIC), University of Bergen; and data analysis and image editing were done with Fiji (Schindelin et al., 2012). Antibodies are listed in **Supplementary Table 1**.

Transmission Electron Microscopy

Samples were prepared by the MIC, Department of Biomedicine, University of Bergen; and grids were imaged using a Jeol JEM-1230 transmission electron microscope (TEM) at 80 kV. For a detailed description, see the **Supplementary Material**.

Mitochondrial DNA Analysis

MtDNA quantification and deletion assessment were performed on DNA isolated from cultured cells using MagMAX™-96 DNA Multi-Sample Kit (Invitrogen™) and real-time PCR, as well as long-range PCR, as previously described (Tzoulis et al., 2013). A commonly deleted region (MT-ND4) in the major arc of mtDNA and a rarely deleted region (MT-ND1) were utilized to quantify deletion, and MT-ND1 was compared with amplification of a single-copy nuclear gene (APP) to assess the number of mtDNA copies. For a detailed description (see **Supplementary Material**).

Measurement of Oxygen Consumption Rate and Extracellular Acidification Rate Using Seahorse XF^e96 Analyzer

Respiration and acidification rates were measured on a monolayer culture of undifferentiated hPSCs and cells at S5 using a Seahorse XF^e96 extracellular flux analyzer (Agilent, Santa Clara, CA, United States). For a detailed description (see **Supplementary Material**). To correct the final results for differences in cell size and number between the undifferentiated hPSCs and differentiated cells at S5, we measured the total protein concentration for each well using absorbance at 280 nm. All results were reported as pmol O₂ per min after normalization to total protein concentration. The XF reader software (Wave Desktop 2.4) was used to analyze the data.

Measurement of Mitochondrial Membrane Potential

We used a previously described protocol (Rowe and Boletta, 2013) to analyze the mitochondrial membrane potential (ψ_m) independent of cell volume using tetramethylrhodamine methyl ester (TMRM). We quantified the MFI of TMRM before and after applying the uncoupler carbonyl cyanide

4-(trifluoromethoxy)phenylhydrazine (FCCP) to dissipate the mitochondrial membrane potential. The difference between geometric means for TMRM- and TMRM-FCCP-treated cells provided the membrane potential normalized to cell size. In addition, to normalization for mitochondrial mass differences, we calculated the ratio of median MFI of TMRM to MFI of TOM20, so that we could express the level of mitochondrial membrane potential per unit of mitochondrial membrane area measured. For a detailed description (see **Supplementary Material**).

Statistical Tests

Prior to assessing statistical significance, and in order to identify the appropriate statistical test, we tested the normal distribution of the sample population using the Shapiro–Wilk and Kolmogorov–Smirnov tests. Parametric tests were only used for datasets that passed both tests. Of note, all flow cytometry data were treated as non-normally distributed populations. **Supplementary Table 2** demonstrates the statistical tests used for each assay to assess statistical significance. N represents the number of biological replicates. Each hPSC line is one biological replicate, and each round of differentiation from a given hPSC line represents one technical replicate. Data were analyzed and plotted using GraphPad-Prism (Prism 7.0, GraphPad Software, La Jolla, CA, United States).

RESULTS

Cardiomyocyte Differentiation and Characterization

Two hESC lines (429 and 360) and three hiPSC lines (established from two independent Detroit 551 clones (clones 7 and 10), and one CRL 2097 iPSC clone, CRL-8) were selected for mesoderm differentiation in a 96-well plate format (Balafkan et al., 2020). The differentiation process is shown schematically in **Figure 1A**. For comparative purposes, we divided the differentiation process into phases based on the expression of cell-type-specific markers (**Figure 1A**): pluripotent state (S1, day 0), mesendoderm cells (S2, day 2), cardiac mesoderm (S3, day 3), *Isl1*⁺ progenitor cells (S4, days 5–7), and cardiomyocyte and non-cardiac cells (S5, days 12–15). The specific markers for the mesoderm cell lineage were assigned based on previous studies (Sturzu and Wu, 2011; Vliet et al., 2012). Initial transcriptomic profiling of *Isl1*⁺ progenitor cells (dataset A) derived from different hPSCs was performed with samples collected from four hiPSCs and two of the hESC lines (429 and 360) at pluripotent state (S1) and *Isl1*⁺ progenitor cells (S4). Sample clustering based on the RNA-seq gene expression evidenced a marked transcriptional difference between S1 and S4, singling out the differentiation process as the main driver of transcriptional change (**Supplementary Figure 1A**). This was corroborated by the strong association between the first principal component of gene expression (explaining 36% of the variance) and the differentiation stage (linear regression model $p = 71 \times 10^{-3}$). Cell lines were only weakly associated with subsequent principal components (**Supplementary Figure 1B**). To validate our gene expression

analysis and further profile transcriptomes from critical stages of mesoderm differentiation, including S5, an independent RNA-seq experiment was performed using an hESC line (H1), which was solely used for transcriptomic analysis (dataset B) and not included in other sets of experiments. RNA samples from three independent differentiations of H1 were collected at the following stages: pluripotent state (S1), mesendoderm state (S2), cardiac progenitor (S4), and differentiated cells in S5. Both datasets revealed downregulation of pluripotent stem cell markers, while upregulated genes were enriched in pathways associated with cardiomyocyte differentiation including regulation of cardiac muscle, ventricular cardiac muscle tissue morphogenesis, sarcomere, and regulation of heart contraction (**Figure 1B** and **Supplementary Figures 1C–E**). The correct mesoderm differentiation route was confirmed using qPCR (**Supplementary Figure 2A**) and immunocytochemistry (**Figures 1C,D**). These data indicate that our model is a reliable model in which to assess mesoderm differentiation toward cardiomyocytes. Previously, we have shown that differentiating cells in a 96-well plate format results in a population of both cardiomyocytes and non-cardiomyocytes (Skelton et al., 2017; Balafkan et al., 2020). Thus, cells in S1 represent a pure population of PSCs ($\sim 100\% \pm 0.6$ SSEA4⁺), and those in S4 represent a relatively pure population of cardiac progenitors ($\sim 92\% \pm 1$ ISL1⁺) (Moretti et al., 2006), while S5 comprises two different cell populations, cardiomyocytes ($20\% \pm 13$ TNNT2⁺) and non-cardiomyocyte (TNNT2⁻) cell populations (**Figure 1E**).

Mitochondrial Content Decreases Progressively During Mesoderm Differentiation

Thirteen polypeptides that are essential respiratory chain components are encoded by mtDNA. Unlike nuclear DNA, mtDNA is present in multiple copies, and its copy number can impact the levels of mitochondrial RNA transcripts available for generating respiratory chain subunits (Anderson et al., 1981). We assessed the mtDNA copy number at different stages of mesoderm differentiation using real-time PCR quantification relative to the nuclear gene *APP* (Tzoulis et al., 2013). This revealed a clear and progressive reduction of mtDNA copy number ($\leq 85\%$) during differentiation of both hiPSCs and hESCs to the mesodermal lineage (**Figure 2A** and **Supplementary Figure 3A**). For comparative purposes, we quantified mtDNA in postmortem human heart using the same method and confirmed that the level of mtDNA in the mature tissue is at least 11–44-fold higher than in hPSCs and differentiated cells at S5 (**Figure 2B**).

Assessed by bulk RNA-seq, we found that the majority of genes involved in mtDNA homeostasis decreased during mesoderm differentiation, including mtDNA maintenance exonuclease 1 (*MGME1*), single-stranded DNA binding protein (*SSBP*), mitochondrial transcription factor A (*TFAM*), and mtDNA helicase (*TWNK*) (**Figure 2C**). We validated RNA-seq findings by using real-time PCR to quantify the expression of *SSBP* and *POLG*, which both have critical roles in mtDNA replication, and were able to show a progressive decline of *SSBP* with no

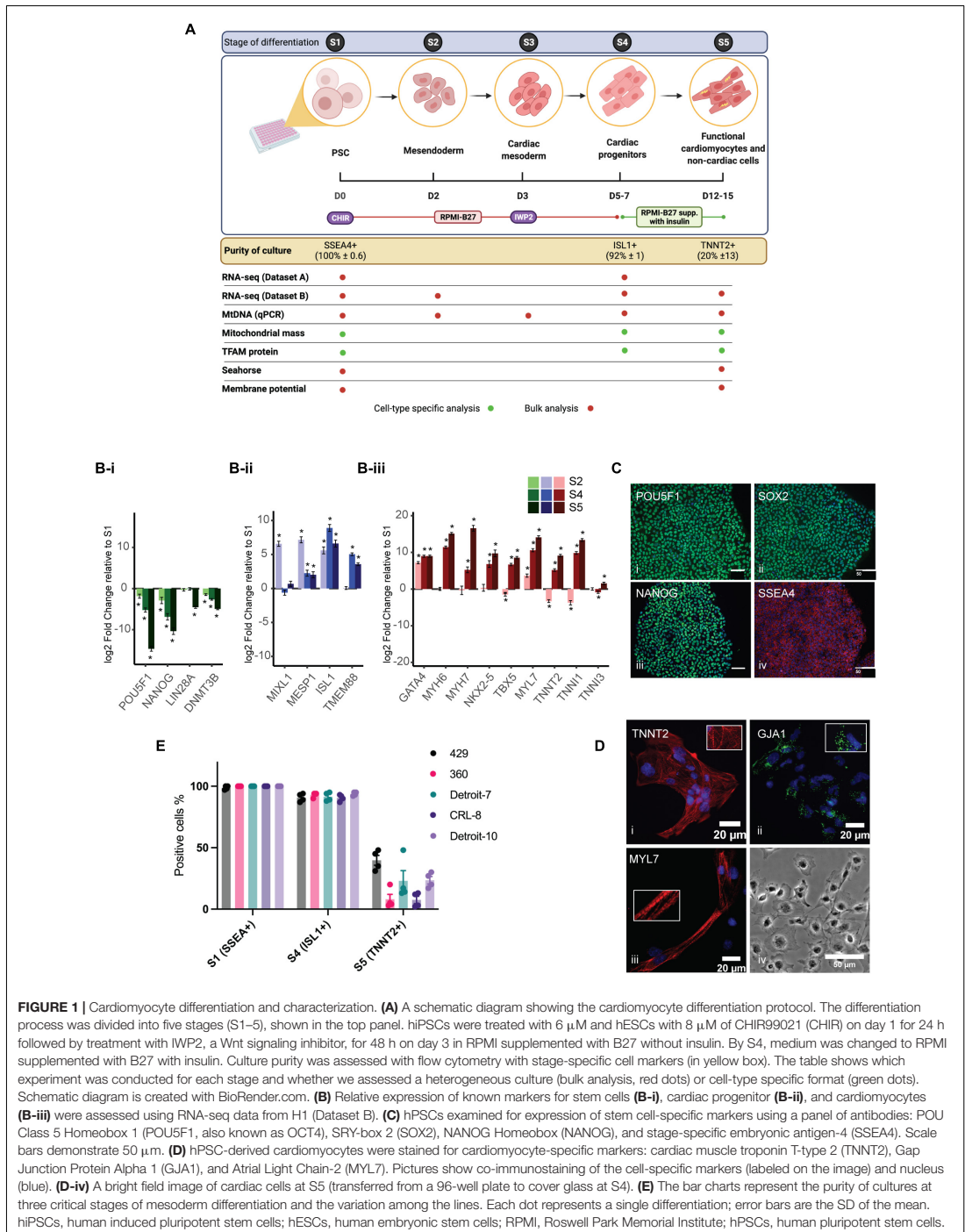
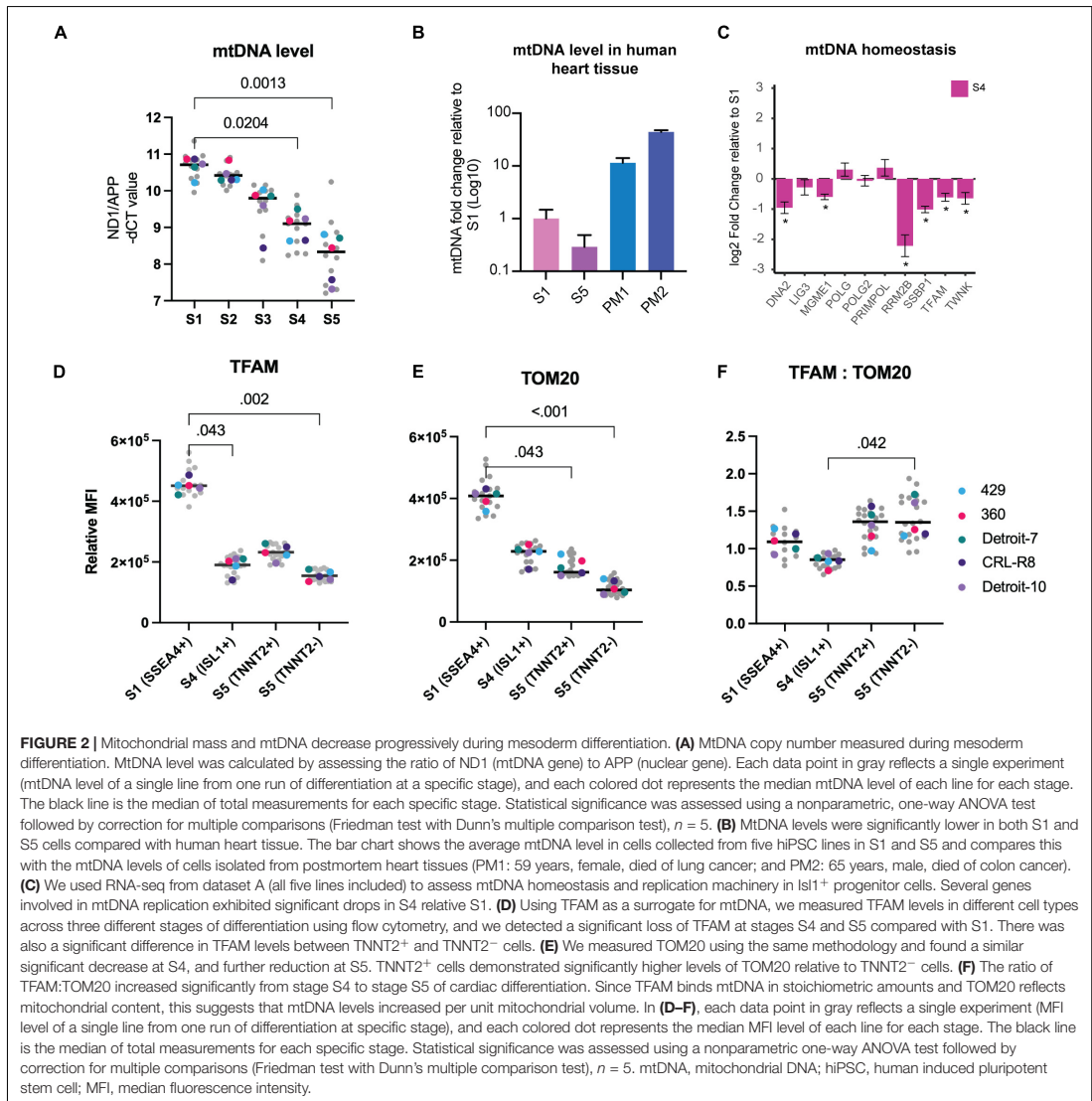


FIGURE 1 | Cardiomyocyte differentiation and characterization. **(A)** A schematic diagram showing the cardiomyocyte differentiation protocol. The differentiation process was divided into five stages (S1–5), shown in the top panel. hiPSCs were treated with 6 μ M and hESCs with 8 μ M of CHIR99021 (CHIR) on day 1 for 24 h followed by treatment with IWP2, a Wnt signaling inhibitor, for 48 h on day 3 in RPMI supplemented with B27 without insulin. By S4, medium was changed to RPMI supplemented with B27 with insulin. Culture purity was assessed with flow cytometry with stage-specific cell markers (in yellow box). The table shows which experiment was conducted for each stage and whether we assessed a heterogeneous culture (bulk analysis, red dots) or cell-type specific format (green dots). Schematic diagram is created with BioRender.com. **(B)** Relative expression of known markers for stem cells **(B-i)**, cardiac progenitor **(B-ii)**, and cardiomyocytes **(B-iii)** were assessed using RNA-seq data from H1 (Dataset B). **(C)** hPSCs examined for expression of stem cell-specific markers using a panel of antibodies: POU Class 5 Homeobox 1 (POU5F1, also known as OCT4), SRY-box 2 (SOX2), NANOG Homeobox (NANOG), and stage-specific embryonic antigen-4 (SSEA4). Scale bars demonstrate 50 μ m. **(D)** hPSC-derived cardiomyocytes were stained for cardiomyocyte-specific markers: cardiac muscle troponin T-type 2 (TNNT2), Gap Junction Protein Alpha 1 (GJA1), and Atrial Light Chain-2 (MYL7). Pictures show co-immunostaining of the cell-specific markers (labeled on the image) and nucleus (blue). **(D-iv)** A bright field image of cardiac cells at S5 (transferred from a 96-well plate to cover glass at S4). **(E)** The bar charts represent the purity of cultures at three critical stages of mesoderm differentiation and the variation among the lines. Each dot represents a single differentiation; error bars are the SD of the mean. hiPSCs, human induced pluripotent stem cells; hESCs, human embryonic stem cells; RPMI, Roswell Park Memorial Institute; hPSCs, human pluripotent stem cells.



significant change in *POLG* expression level (**Supplementary Figures 3B–D**). No evidence of qualitative damage such as mtDNA deletion was found at any stage of differentiation, which further confirms that reduction of mtDNA is not an artifact of damaged mtDNA replication machinery that can be caused, for example, by the continued culture of hPSCs (**Supplementary Figures 3E,F**).

The link between the TFAM protein and mtDNA has been investigated in depth (Larsson et al., 1994, 1998), and studies show that it binds mtDNA in molar quantities

(Ekstrand et al., 2004; Kaufman et al., 2007; Kukut and Larsson, 2013). Using flow cytometry, we assessed TFAM both as a direct measure of a mitochondrial matrix protein and as an indirect measure of mtDNA level within each cell population co-stained with antibodies against stage-specific markers, to validate our findings from real-time PCR. We found a 58% reduction of TFAM in *Isl1*⁺ progenitor cells (S4) relative to the pluripotent stage (S1) (**Figure 2D**). The TFAM level decreased further in the *TNNT2*⁻ population but showed an increase in the *TNNT2*⁺ cells (**Figure 2D**).

Next, we examined changes in mitochondrial mass during mesoderm differentiation at the single-cell level. We used flow cytometry and co-staining with antibodies against stage-specific markers and Translocase of Outer Mitochondrial Membrane 20 (TOMM20), a well-established marker of mitochondrial mass. The TOMM20 level showed a significant fall (43%) from S1 to S4 and reached its lowest level at S5 (60%) (Figure 2E). As expected, the level of TOM20 was lower (~40%) in non-cardiomyocytes than cardiomyocytes (TNNT2⁺), potentially indicating a lower level of mitochondria in non-cardiac cells. The fall in mitochondrial mass could also be followed by looking at VDAC expression. VDAC encodes a vital outer membrane protein that is routinely used as a mitochondrial mass marker; its expression started decreasing from S3 (Supplementary Figure 3D). Given the link between cell size and mitochondrial mass (Zheng et al., 2016), the finding of a lower mitochondrial mass was surprising; differentiated cells at S5 are much larger than PSCs (Figure 1D-iv). Interestingly, when we measured changes in mtDNA level relative to mitochondrial content, by plotting the level of TFAM (an indirect marker of mtDNA) against TOM20 (a direct marker for mitochondrial content), we found that this ratio varied during the course of mesoderm differentiation. The ratio of TFAM to TOM20 was significantly higher in differentiated cells in S5 relative to Isl1⁺ progenitor cells (S4) (Figure 2F), suggesting that the lowest level of mtDNA per unit mitochondrial mass occurred in Isl1⁺ progenitor cells and then rose in the more differentiated stage. Together, these findings suggest a progressive fall of mitochondrial content during mesoderm differentiation.

Despite Lower Mitochondrial Content, Differentiated Cells Generate More Energy Through Tricarboxylic Acid Than Glycolysis

Despite analyzing a heterogeneous population (TNNT2⁺ and TNNT2⁻ cells), we were able to verify a significant increased expression of mtDNA genes in S5 relative to other stages of differentiation via bulk RNA-seq (Figure 3A). Demonstrating a significant increase in the expression of mtDNA genes in the differentiated cells in S5 suggests that differentiated cells rely more on mitochondrial respiration, regardless of the cell type they are committed to, and despite having much lower mitochondrial mass. Thus, we assessed mitochondrial oxidative activity by measuring OCR in undifferentiated stem cells (Figure 3C) and differentiated cells at S5, which contain beating cardiomyocytes (see Supplementary Movies 3, 4 and Figure 3D), using a Seahorse XF⁹⁶ extracellular flux analyzer. Interestingly, despite a major drop in mitochondrial mass, no major change in basal respiration—the amount of oxygen consumed by mitochondria under basal conditions—was detected: differentiated cells at S5 137 pmol/min, undifferentiated hPSCs at S1 148 pmol/min (Figure 3E and Supplementary Figure 4A). This suggests that the remaining mitochondria have higher levels of oxygen consumption that compensates for the lower mitochondrial mass in differentiated

cells. Maximal OCR and spare capacity (also known as reserve capacity) showed a slight increase in S5 compared with S1 cells (Supplementary Figures 4B,C), while the coupling efficiency—the proportion of mitochondrial respiratory chain activity used to drive ATP synthesis (Divakaruni and Brand, 2011)—was significantly higher (Figure 3F). The ratio of OCR to extracellular acidification rate (ECAR), an indicator of how much lactate is produced through glycolysis, also rose in S5 cells relative to S1, suggesting a shift to mitochondrial respiration (Figure 3G). The finding of a negative value for spare capacity in hPSC lines (360 and CRL-8) raised the possibility that uncoupling by CCCP had collapsed the membrane potential in these lines (see blue bars in Supplementary Figure 4A-iv) and that, with a respiratory chain already working maximally, there was no further reserve capacity to be used with the extra stress (Varum et al., 2011; Zhang et al., 2012b).

We also investigated mitochondrial membrane potential as a marker for mitochondrial activity. Membrane potential is generated by proton movement driven by the electron transport chain; and although mitochondrial membrane potential is an excellent marker for assessing mitochondrial function, it also reflects mitochondrial volume (Perry et al., 2011). We therefore employed a lipophilic cationic fluorescent probe, TMRM, to evaluate mitochondrial membrane potential at the single-cell level by flow cytometry; and we normalized our data to the MFI of TOM20 from the same differentiation batch to further adjust membrane potential to mitochondrial content within a single cell (see Supplementary Methods 1.10). We did not use cell stage-specific markers for this assessment, as this was done in live cells; and the result therefore reflects the membrane potential of total live cells in S1 and S5. The absolute median MFI of TMRM was significantly lower at S5 relative to S1 (Figure 3H and Supplementary Figure 4E); however, when we adjusted the MFI of TMRM for mitochondrial mass, using the ratio of MFI-TMRM to MFI-TOM20, we found a more than twofold increase in mitochondrial membrane potential at S5 compared with undifferentiated hPSCs at S1 (Figure 3I and Supplementary Figure 4F). The significantly higher mitochondrial membrane potential per unit of mitochondrial mass in differentiated cells at S5 relative to undifferentiated hPSCs further suggested that the mitochondria in differentiated cells are more efficient in generating ATP.

Crista Remodeling in Differentiated Cells

We examined cells collected on S1, S4, and S5 by TEM to assess the mitochondrial morphology and crista structure. The mitochondria in S1 appear to have wide cristae with a dense matrix, while in S4 and S5, cristae appear more compact with a clearer matrix (Figure 3J). We also identified a significant increase in the expression of genes associated with mitochondrial biogenesis and respiration activities (e.g., *PPARA*, *PPARG*, *PGC-1A*, and *ESSRA*; see Figure 3B and Supplementary Figure 5). Since no increase in mitochondrial mass was demonstrated relative to Isl1⁺ progenitor cells (Figure 2E), together, these data suggested remodeling of mitochondrial membrane and cristae as a potential explanation for the increase in mitochondrial respiration.

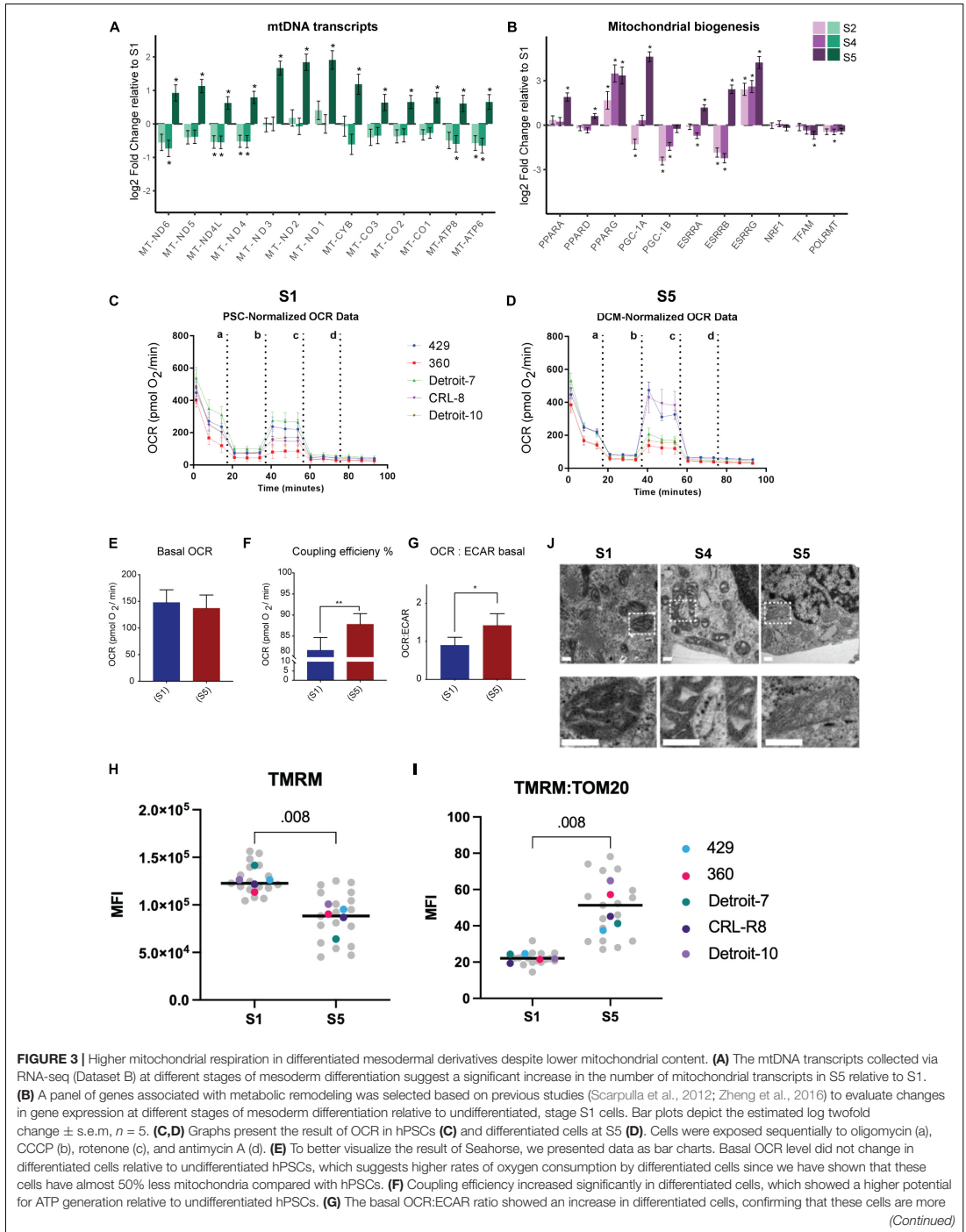


FIGURE 3 | (Continued)

reliant on OXPHOS compared with undifferentiated hPSCs. Each bar in **(E–G)** shows mean \pm SD, $n = 5$; and two-tailed unpaired *t*-tests with Welch's correction were chosen to assess the statistical significance of the difference between undifferentiated hPSCs and S5. In all bar charts, * $p < 0.05$ and ** $p < 0.01$. **(H)** We assessed mitochondrial membrane potential by treating live cells with TMRM and subsequently with FCCP and plotting the difference in delta MFI (TMRM-MFI - FCCP-MFI) for each stage. We found an apparent higher TMRM concentration in hPSCs relative to S5 cells. **(I)** Next, we used the TOM20-MFI collected from a previous step **(Figure 2E)** and computed TOM20-MFI for all live cells in S1 and S5 (both TNNT2⁺ and TNNT2⁻ included) as an indicator of mitochondrial mass. We then adjusted the TMRM level to the mitochondrial content of cells in each stage (TMRM-MFI:TOM20-MFI). The ratio of TMRM and TOM20 suggested a higher level of mitochondrial membrane potential per unit of mitochondrial mass for differentiated cells compared with undifferentiated hPSCs. In H and I plots, each data point in gray reflects a single experiment (MFI level of a single line from one run of differentiation at specific stage), and each colored dot represents the median MFI level of each line for each stage. The black line is the median of total measurements for each specific stage. Statistical significance was assessed using a two-tailed unpaired nonparametric *t*-test (Mann–Whitney test), $n = 5$. **(J)** Representative TEM pictures of mitochondria during cardiomyocyte differentiation of an hiPSC line (Detroit-7) at S1, S4, and S5. Mitochondria appear smaller with wider, more immature cristae at stages S1 and S4; while at S5, more mitochondria show an expanded matrix with typical narrow, mature cristae. The bottom panel is the magnification of the indicated areas in the top panel. Scale bar: 200 nm. mtDNA, mitochondrial DNA; OCR, oxygen consumption rate; hPSC, human pluripotent stem cell; OXPHOS, oxidative phosphorylation; MFI, median fluorescence intensity; TEM, transmission electron microscope; hiPSC, human induced pluripotent stem cell.

DISCUSSION

The control of mitochondrial biogenesis and ATP generation is a dynamic and complex process that is involved in governing pluripotency and pathways of differentiation (Friedman and Nunnari, 2014; Wanet et al., 2015). Previous studies have shown that following the inactivation of mtDNA replication during preimplantation, mtDNA levels fall as copies segregate into the newly divided daughter cells, reaching their lowest level at the embryoblast stage before starting to increase at some point during differentiation (Pikó and Taylor, 1987; Cao et al., 2007). Although the first part of this process is well established (Taylor and Pikó, 1995; Floros et al., 2018), the timing of the second part of the process remains uncertain. Earlier studies suffer from low sample number and the tendency to focus only on the comparison between differentiated and undifferentiated cells without considering transitional states during differentiation or the heterogeneous nature of the cultures resulting from spontaneous differentiation (St John et al., 2005; Cho et al., 2006). Importantly, recent findings suggest that metabolic switching during differentiation is germ layer-specific and is regulated differently in the ectoderm compared with mesoderm and endoderm (Cliff et al., 2017).

Our findings corroborate previous studies showing a change in energy profile between hPSCs and terminally differentiated cells with a shift from glycolysis to OXPHOS (Folmes et al., 2012). However, contrary to what was previously thought, we show that mitochondrial content drops progressively at the start of differentiation in mesoderm, a trend that continues despite increased mitochondrial activity and higher levels of ATP-linked respiration. A reduction of both mtDNA and mitochondrial mass was detected in the very early stages of ectoderm differentiation, but both markers started to increase again from the neuroprogenitor cell stage onward (Birket et al., 2011; Zheng et al., 2016; Lees et al., 2018). A decline in mtDNA content has also been reported during hematopoietic differentiation, as well as during differentiation of hESCs toward primordial germ cells (de Almeida et al., 2017; Floros et al., 2018). Thus, our findings in a mesodermal lineage suggest that the reduction of mtDNA and mitochondrial content from pluripotent to multipotent stem cells may be a more general phenomenon than previously thought and not limited to one specific cell lineage. At the same time, our results showing that this loss continues up to and including

differentiated cells at S5 suggest that there are cell-lineage-specific metabolic pathways following commitment to a specific cell type. This contrasts with earlier studies that suggested a simultaneous expansion of mitochondrial content and increase in OXPHOS activity during all lineage differentiation.

Our findings showing that the lowest level of mtDNA per unit mitochondrial mass was observed in cardiac progenitor cells are very similar to those reported in neural progenitor cells during ectoderm differentiation (Lees et al., 2018). A possible explanation for the reduction in mitochondrial content during very early stages of differentiation is that this occurs in order to generate a mitochondrial bottleneck to select mtDNA with specific variants and specialized mitochondria for development of specific germ layers (Gong et al., 2015; Floros et al., 2018; Rossmann et al., 2021). MtDNA bottlenecks were originally thought to be limited to the germline; however, evidence increasingly suggests the presence of cell-specific mtDNA bottlenecks during development (Zhang et al., 2018). This phenomenon may, in part, explain the observed differences between mtDNA levels in differentiated cells in S5 and postmortem human heart tissue. Another important factor in our protocol, which gave rise to low numbers of cardiomyocytes, is that the resulting functionally differentiated cardiomyocytes poorly reflect characteristics of mature cardiomyocytes *in vivo*. For example, it is known that hiPSC-derived cardiomyocytes are transcriptionally, structurally, and functionally immature and resemble fetal cardiomyocytes (for review, see Karbassi et al., 2020). Other factors include differences in cell-type composition (e.g., absence of interaction between cardiac progenitors and surrounding tissue; Miquerol and Kelly, 2012), maturity level, and microenvironment (e.g., presence of fatty acids as a source of energy), which are not mutually exclusive. Epigenetic modifications add another layer of complexity to stage-specific mtDNA regulation, as was shown by in-depth profiling of human heart tissue during development (Gilsbach et al., 2018).

In this study, we assessed cells starting 48 h after WNT activation, when expression of mesendoderm markers (e.g., MESP1) was stabilized, while other studies demonstrated a metabolic shift starting as early as 24 h after CHIR99021 treatment (Cliff et al., 2017). One of the limitations of our study is that we have not investigated this initial timepoint, which is particularly important in mesoderm differentiation, as a very recent study suggested that assessing metabolic switch during the

first 24-h time window can be used as an indicator for efficiency of cardiomyocyte differentiation (Qian et al., 2021). More importantly, our findings demonstrating variation in the mtDNA level relative to mitochondrial mass highlight that mtDNA levels may not act as a proxy for mitochondrial level, particularly during differentiation, and that it is therefore important to use a complementary method to assess mitochondrial levels directly. Our findings also emphasize the importance of differentiating between active loss of mtDNA and failure to expand mtDNA copy number when studying tissues derived from mesodermal lineages in infants with mitochondrial disease.

Collectively, high levels of oxygen consumption, lactate reduction, and significantly higher level of mitochondrial membrane potential at S5 relative to undifferentiated cells demonstrate the metabolic shift from glycolysis to OXPHOS, despite lower mitochondrial content. Together, our findings suggest that the mitochondria in terminally differentiated cells are indeed more mature and more efficient at generating ATP. These findings offer experimental validation for the previously proposed mathematical model that suggests mammalian cells can modulate their mitochondrial membrane potential, rather than their mtDNA level, to quickly adapt to changes in energy demands (Miettinen and Björklund, 2016; Aryaman et al., 2017). Previous findings have revealed that mitochondrial inner membrane morphology modulates OXPHOS function by modifying the kinetics of chemical reactions and regulating the arrangement of protein complexes (Cogliati et al., 2016). It is also known that modulating crista structure affects mitochondrial respiratory efficiency independently of changes to mitochondrial protein synthesis (Cogliati et al., 2013). Our findings align with previous studies that reported the formation of cristae and mitochondrial permeability transition pore (mPTP) closure in differentiated cardiomyocytes, which are known characteristics of the developmental maturation of mitochondria (Hom et al., 2011; Teixeira et al., 2015; Dai et al., 2017).

Whether our findings are physiologically relevant or reflect changes in signaling pathways during the early stages of differentiation under the normoxic culture conditions remains an unanswered question. Nevertheless, our findings emphasize the importance of investigating changes in mitochondrial properties across different cell lineages, and highlight a narrow time window during differentiation that is crucial in the relationship between mitochondrial remodeling and cell fate that can be a target for future investigations. These findings may have significant implications in developing strategies for lineage-directed differentiation. Better understanding of the molecular basis of mitochondrial remodeling during differentiation can potentially help us to better understand the key regulatory mechanism underlying the pathophysiology of mitochondrial and degenerative diseases and will further assist us in identification of novel therapeutic agents targeting metabolic

pathways. We suggest that future studies use more advanced iPSC-based models [e.g., cardiac spheroids (Giacomelli et al., 2017) and gastruloids (Rossi et al., 2021)] that more closely mimic early human cardiogenesis in combination with single-cell transcriptomic analysis to gain even deeper understanding of the underlying molecular mechanisms.

DATA AVAILABILITY STATEMENT

The original contributions presented in the study are publicly available. This data can be found here: <https://www.ebi.ac.uk/ena/browser/view/PRJEB47044?show=reads>.

AUTHOR CONTRIBUTIONS

LB and NB: conceptualization and supervision. NB, SM, and GS: methodology. GN: software. NB, SM, and GN: validation and formal analysis, and visualization. SM, NB, IP, and RS: investigation. LB, GS, and CT: resources. GN and NB: data curation. NB: writing—original draft preparation. LB, NB, and SM: writing—review and editing. LB: project administration and funding acquisition.

FUNDING

This work was supported by grants from The Research Council of Norway (NFR, Project No. 229652), Bergen Stem Cell Consortium (BSCC), Haukeland University Hospital, University of Bergen, and the Rakel og Otto-Kristian Bruun's Legat. This work was also supported by the Research Council of Norway through its Centre of 248 Excellence Scheme (Project No. 262613).

ACKNOWLEDGMENTS

We wish to acknowledge the help and resources provided by the Flow Cytometry Core Facility, University of Bergen, and the Molecular Imaging Center (MIC), Department of Biomedicine, University of Bergen. We would like to thank Tilo W. Eichler and Christian Dölle for helpful discussions.

SUPPLEMENTARY MATERIAL

The Supplementary Material for this article can be found online at: <https://www.frontiersin.org/articles/10.3389/fcell.2021.744777/full#supplementary-material>

REFERENCES

Anderson, S., Bankier, A. T., Barrell, B. G., de Bruijn, M. H. L., Coulson, A. R., Drouin, J., et al. (1981). Sequence and organization of the human mitochondrial genome. *Nature* 290, 457–465. doi: 10.1038/290457a0

Aryaman, J., Hoitzing, H., Burgstaller, J. P., Johnston, I. G., and Jones, N. S. (2017). Mitochondrial heterogeneity, metabolic scaling and cell death. *Bioessays* 39:1700001. doi: 10.1002/bies.201700001

Ashburner, M., Ball, C. A., Blake, J. A., Botstein, D., Butler, H., Cherry, J. M., et al. (2000). Gene ontology: tool for the unification of biology.

- The gene ontology consortium. *Nat. Genet.* 25, 25–29. doi: 10.1038/75556
- Balafkan, N., Mostafavi, S., Schubert, M., Siller, R., Liang, K. X., Sullivan, G., et al. (2020). A method for differentiating human induced pluripotent stem cells toward functional cardiomyocytes in 96-well microplates. *Sci. Rep.* 10:18498. doi: 10.1038/s41598-020-73656-2
- Belmonte, S., and Morad, M. (2008). Shear fluid-induced Ca²⁺ release and the role of mitochondria in rat cardiac myocytes. *Ann. N. Y. Acad. Sci.* 1123, 58–63. doi: 10.1196/annals.1420.007
- Birket, M. J., Orr, A. L., Gerencser, A. A., Madden, D. T., Vitelli, C., Swistowski, A., et al. (2011). A reduction in ATP demand and mitochondrial activity with neural differentiation of human embryonic stem cells. *J. Cell Sci.* 124, 348–358. doi: 10.1242/jcs.072272
- Cao, L., Shitara, H., Horii, T., Nagao, Y., Imai, H., Abe, K., et al. (2007). The mitochondrial bottleneck occurs without reduction of mtDNA content in female mouse germ cells. *Nat. Genet.* 39, 386–390. doi: 10.1038/ng1970
- Cho, Y. M., Kwon, S., Pak, Y. K., Seol, H. W., Choi, Y. M., Park, D. J., et al. (2006). Dynamic changes in mitochondrial biogenesis and antioxidant enzymes during the spontaneous differentiation of human embryonic stem cells. *Biochem. Biophys. Res. Commun.* 348, 1472–1478. doi: 10.1016/j.bbrc.2006.08.020
- Cliff, T. S., Wu, T., Boward, B. R., Yin, A., Yin, H., Glushka, J. N., et al. (2017). MYC controls human pluripotent stem cell fate decisions through regulation of metabolic flux. *Cell Stem Cell* 21, 502–516.e9. doi: 10.1016/j.stem.2017.08.018
- Cogliati, S., Enriquez, J. A., and Scorrano, L. (2016). Mitochondrial cristae: where beauty meets functionality. *Trends Biochem. Sci.* 41, 261–273. doi: 10.1016/j.tibs.2016.01.001
- Cogliati, S., Frezza, C., Soriano, M. E., Varanita, T., Quintana-Cabrera, R., Corrado, M., et al. (2013). Mitochondrial cristae shape determines respiratory chain supercomplexes assembly and respiratory efficiency. *Cell* 155, 160–171. doi: 10.1016/j.cell.2013.08.032
- Dai, D. F., Danoviz, M. E., Wiczor, B., Laflamme, M. A., and Tian, R. (2017). Mitochondrial maturation in human pluripotent stem cell derived cardiomyocytes. *Stem Cells Int.* 2017:5153625. doi: 10.1155/2017/5153625
- de Almeida, M. J., Luchsinger, L. L., Corrigan, D. J., Williams, L. J., and Snoeck, H.-W. (2017). Dye-independent methods reveal elevated mitochondrial mass in hematopoietic stem cells. *Cell Stem Cell* 21, 725–729.e4. doi: 10.1016/j.stem.2017.11.002
- Divakaruni, A. S., and Brand, M. D. (2011). The regulation and physiology of mitochondrial proton leak. *Physiology* 26, 192–205. doi: 10.1152/physiol.00046.2010
- Ekstrand, M. I., Falkenberg, M., Rantanen, A., Park, C. B., Gaspari, M., Hulthenby, K., et al. (2004). Mitochondrial transcription factor A regulates mtDNA copy number in mammals. *Hum. Mol. Genet.* 13, 935–944. doi: 10.1093/hmg/ddh109
- Floros, V. I., Pyle, A., Dietmann, S., Wei, W., Tang, W. C. W., Irie, N., et al. (2018). Segregation of mitochondrial DNA heteroplasmy through a developmental genetic bottleneck in human embryos. *Nat. Cell Biol.* 20, 144–151. doi: 10.1038/s41556-017-0017-8
- Folmes, C. D., Dzeja, P. P., Nelson, T. J., and Terzic, A. (2012). Metabolic plasticity in stem cell homeostasis and differentiation. *Cell Stem Cell* 11, 596–606. doi: 10.1016/j.stem.2012.10.002
- Friedman, C. E., Nguyen, Q., Lukowski, S. W., Helfer, A., Chiu, H. S., Miklas, J., et al. (2018). Single-cell transcriptomic analysis of cardiac differentiation from human PSCs Reveals HOPX-dependent cardiomyocyte maturation. *Cell Stem Cell* 23, 586–598.e8. doi: 10.1016/j.stem.2018.09.009
- Friedman, J. R., and Nunnari, J. (2014). Mitochondrial form and function. *Nature* 505, 335–343. doi: 10.1038/nature12985
- Giacomelli, E., Bellin, M., Sala, L., van Meer, B. J., Tertoolen, L. G. J., Orlova, V. V., et al. (2017). Three-dimensional cardiac microtissues composed of cardiomyocytes and endothelial cells co-differentiated from human pluripotent stem cells. *Development* 144, 1008–1017. doi: 10.1242/dev.143438
- Gillis, J., Mistry, M., and Pavlidis, P. (2010). Gene function analysis in complex data sets using ErmineJ. *Nat. Protoc.* 5, 1148–1159. doi: 10.1038/nprot.2010.78
- Gilsbach, R., Schwaderer, M., Preissl, S., Grüning, B. A., Kranzhöfer, D., Schneider, P., et al. (2018). Distinct epigenetic programs regulate cardiac myocyte development and disease in the human heart in vivo. *Nat. Commun.* 9:391. doi: 10.1038/s41467-017-02762-z
- Gong, G., Song, M., Csordas, G., Kelly, D. P., Matkovich, S. J., and Dorn, G. W. (2015). Parkin-mediated mitophagy directs perinatal cardiac metabolic maturation in mice. *Science* 350:aad2459. doi: 10.1126/science.aad2459
- Hom, J. R., Quintanilla, R. A., Hoffman, D. L., Bentley, K. L., de, M., Molkentin, J. D., et al. (2011). The permeability transition pore controls cardiac mitochondrial maturation and myocyte differentiation. *Dev. Cell* 21, 469–478. doi: 10.1016/j.devcel.2011.08.008
- Kanehisa, M., and Goto, S. (2000). KEGG: kyoto encyclopedia of genes and genomes. *Nucleic Acids Res.* 28, 27–30. doi: 10.1093/nar/28.1.27
- Karbassi, E., Fenix, A., Marchiano, S., Muraoka, N., Nakamura, K., Yang, X., et al. (2020). Cardiomyocyte maturation: advances in knowledge and implications for regenerative medicine. *Nat. Rev. Cardiol.* 17, 341–359. doi: 10.1038/s41569-019-0331-x
- Kaufman, B. A., Durisic, N., Mativetsky, J. M., Costantino, S., Hancock, M. A., Grutter, P., et al. (2007). The mitochondrial transcription factor TFAM coordinates the assembly of multiple DNA molecules into nucleoid-like structures. *Mol. Biol. Cell* 18, 3225–3236. doi: 10.1091/mbc.e07-05-0404
- Kukat, C., and Larsson, N. G. (2013). mtDNA makes a U-turn for the mitochondrial nucleoid. *Trends Cell Biol.* 23, 457–463. doi: 10.1016/j.tcb.2013.04.009
- Larsson, N. G., Oldfors, A., Holme, E., and Clayton, D. A. (1994). Low levels of mitochondrial transcription factor A in mitochondrial DNA depletion. *Biochem. Biophys. Res. Commun.* 200, 1374–1381. doi: 10.1006/bbrc.1994.1603
- Larsson, N. G., Wang, J. M., Wilhelmsson, H., Oldfors, A., Rustin, P., Lewandowski, M., et al. (1998). Mitochondrial transcription factor A is necessary for mtDNA maintenance and embryogenesis in mice. *Nat. Genet.* 18, 231–236. doi: 10.1038/ng0398-231
- Lees, J. G., Gardner, D. K., and Harvey, A. J. (2018). Mitochondrial and glycolytic remodeling during nascent neural differentiation of human pluripotent stem cells. *Development* 145:dev168997. doi: 10.1242/dev.168997
- Liang, K. X., Kristiansen, C. K., Mostafavi, S., Vatne, G. H., Zantingh, G. A., Kianian, A., et al. (2020). Disease-specific phenotypes in iPSC-derived neural stem cells with PDLG mutations. *EMBO Mol. Med.* 12:e12146. doi: 10.15252/emmm.202012146
- Locasale, J. W., and Cantley, L. C. (2011). Metabolic flux and the regulation of mammalian cell growth. *Cell Metab.* 14, 443–451. doi: 10.1016/j.cmet.2011.07.014
- Love, M. I., Huber, W., and Anders, S. (2014). Moderated estimation of fold change and dispersion for RNA-seq data with DESeq2. *Genome Biol.* 15:550. doi: 10.1186/s13059-014-0550-8
- Lukyanenko, V., Chikando, A., and Lederer, W. J. (2009). Mitochondria in cardiomyocyte Ca²⁺ signaling. *Int. J. Biochem. Cell Biol.* 41, 1957–1971. doi: 10.1016/j.biocel.2009.03.011
- Miettinen, T. P., and Björklund, M. (2016). Cellular allometry of mitochondrial functionality establishes the optimal cell size. *Dev. Cell* 39, 370–382. doi: 10.1016/j.devcel.2016.09.004
- Miquero, L., and Kelly, R. G. (2012). Organogenesis of the vertebrate heart. *Wiley Interdiscip. Rev. Dev. Biol.* 2, 17–29. doi: 10.1002/wdev.68
- Moretti, A., Caron, L., Nakano, A., Lam, J. T., Bernshausen, A., Chen, Y., et al. (2006). Multipotent embryonic isl1+ progenitor cells lead to cardiac, smooth muscle, and endothelial cell diversification. *Cell* 127, 1151–1165.
- Perry, S. W., Norman, J. P., Barbieri, J., Brown, E. B., and Gelbard, H. A. (2011). Mitochondrial membrane potential probes and the proton gradient: a practical usage guide. *Biotechniques* 50, 98–115. doi: 10.2144/000113610
- Pikó, L., and Taylor, K. D. (1987). Amounts of mitochondrial DNA and abundance of some mitochondrial gene transcripts in early mouse embryos. *Dev. Biol.* 123, 364–374. doi: 10.1016/0012-1606(87)90395-2
- Qian, T., Heaster, T. M., Houghtaling, A. R., Sun, K., Samimi, K., and Skala, M. C. (2021). Label-free imaging for quality control of cardiomyocyte differentiation. *Nat. Commun.* 12:4580.
- Rossi, G., Brogiere, N., Miyamoto, M., Boni, A., Guiet, R., Girgin, M., et al. (2021). Capturing cardiogenesis in gastruloids. *Cell Stem Cell* 28, 230–240.e6. doi: 10.1016/j.stem.2020.10.013
- Rossmann, M. P., Dubois, S. M., Agarwal, S., and Zon, L. I. (2021). Mitochondrial function in development and disease. *Dis. Model. Mech.* 14:dmm048912. doi: 10.1242/dmm.048912
- Rowe, I., and Boletta, A. (2013). Mitochondrial transmembrane potential (ψ_m) assay using TMRM. *Bio Protoc.* 3:e987. doi: 10.12769/bioprotoc.987

- Scarpulla, R. C., Vega, R. B., and Kelly, D. P. (2012). Extramural review. *Trends Endocrinol. Metab.* 23, 459–466. doi: 10.1016/j.tem.2012.06.006
- Schindelin, J., Arganda-Carreras, I., Frise, E., Kaynig, V., Longair, M., Pietzsch, T., et al. (2012). Fiji: an open-source platform for biological-image analysis. *Nat. Methods* 9, 676–682. doi: 10.1038/nmeth.2019
- Sercel, A. J., Carlson, N. M., Patananan, A. N., and Teitell, M. A. (2021). Mitochondrial DNA dynamics in reprogramming to pluripotency. *Trends Cell Biol.* 31, 311–323. doi: 10.1016/j.tcb.2020.12.009
- Siller, R., Greenhough, S., Naumovska, E., and Sullivan, G. J. (2015). Small-molecule-driven hepatocyte differentiation of human pluripotent stem cells. *Stem Cell Rep.* 4, 939–952. doi: 10.1016/j.stemcr.2015.04.001
- Siller, R., Naumovska, E., Mathapati, S., Lycke, M., Greenhough, S., and Sullivan, G. J. (2016). Development of a rapid screen for the endodermal differentiation potential of human pluripotent stem cell lines. *Sci. Rep.* 6:37178. doi: 10.1038/srep37178
- Skelton, R. J. P., Kamp, T. J., Elliott, D. A., and Ardehali, R. (2017). Biomarkers of human pluripotent stem cell-derived cardiac lineages. *Trends Mol. Med.* 23, 651–668. doi: 10.1016/j.molmed.2017.05.001
- St John, J. C. S., Ramalho-Santos, J., Gray, H. L., Petrosko, P., Rawe, V. Y., Navara, C. S., et al. (2005). The expression of mitochondrial DNA transcription factors during early cardiomyocyte in vitro differentiation from human embryonic stem cells. *Cloning Stem Cells* 7, 141–153. doi: 10.1089/clo.2005.7.141
- Sturzu, A. C., and Wu, S. M. (2011). Developmental and regenerative biology of multipotent cardiovascular progenitor cells. *Circ. Res.* 108, 353–364. doi: 10.1161/circresaha.110.227066
- Taylor, K. D., and Pikó, L. (1995). Mitochondrial biogenesis in early mouse embryos: expression of the mRNAs for subunits IV, Vb, and VIIc of cytochrome c oxidase and subunit 9 (P1) of H⁺-ATP synthase. *Mol. Reprod. Dev.* 40, 29–35. doi: 10.1002/mrd.1080400105
- Teixeira, F. K., Sanchez, C. G., Hurd, T. R., Seifert, J. R., Czech, B., Preall, J. B., et al. (2015). ATP synthase promotes germ cell differentiation independent of oxidative phosphorylation. *Nat. Cell Biol.* 17, 689–696. doi: 10.1038/ncb3165
- Tzoulis, C., Tran, G. T., Schwarzmuller, T., Specht, K., Haugarvoll, K., Balafkan, N., et al. (2013). Severe nigrostriatal degeneration without clinical parkinsonism in patients with polymerase gamma mutations. *Brain* 136, 2393–2404. doi: 10.1093/brain/awt103
- Varum, S., Rodrigues, A. S., Moura, M. B., Momcilovic, O., Easley, C. A., Ramalho-Santos, J., et al. (2011). Energy metabolism in human pluripotent stem cells and their differentiated counterparts. *PLoS One* 6:e20914. doi: 10.1371/journal.pone.0020914
- Vliet, P. V., Wu, S. M., Zaffran, S., and Puceat, M. (2012). Early cardiac development: a view from stem cells to embryos. *Cardiovasc. Res.* 96, 352–362. doi: 10.1093/cvr/cvs270
- Wanet, A., Arnould, T., Najimi, M., and Renard, P. (2015). Connecting mitochondria, metabolism, and stem cell fate. *Stem Cells Dev.* 24, 1957–1971. doi: 10.1089/scd.2015.0117
- Zhang, H., Burr, S. P., and Chinnery, P. F. (2018). The mitochondrial DNA genetic bottleneck: inheritance and beyond. *Essays Biochem.* 62, 225–234. doi: 10.1042/ebc20170096
- Zhang, J., Nuebel, E., Daley, G. Q., Koehler, C. M., and Teitell, M. A. (2012a). Metabolic regulation in pluripotent stem cells during reprogramming and self-renewal. *Cell Stem Cell* 11, 589–595. doi: 10.1016/j.stem.2012.10.005
- Zhang, J., Nuebel, E., Wisidagama, D. R., Setoguchi, K., Hong, J. S., Horn, C. M. V., et al. (2012b). Measuring energy metabolism in cultured cells, including human pluripotent stem cells and differentiated cells. *Nat. Protoc.* 7, 1068–1085. doi: 10.1038/nprot.2012.048
- Zheng, X., Boyer, L., Jin, M., Mertens, J., Kim, Y., Ma, L., et al. (2016). Metabolic reprogramming during neuronal differentiation from aerobic glycolysis to neuronal oxidative phosphorylation. *Elife* 5:e13374. doi: 10.7554/elife.13374
- Zhu, H., Scharnhorst, K. S., Stieg, A. Z., Gimzewski, J. K., Minami, I., Nakatsuji, N., et al. (2017). Two dimensional electrophysiological characterization of human pluripotent stem cell-derived cardiomyocyte system. *Sci. Rep.* 7:43210. doi: 10.1038/srep43210
- Zwi, L., Caspi, O., Arbel, G., Huber, I., Gepstein, A., Park, I. H., et al. (2009). Cardiomyocyte differentiation of human induced pluripotent stem cells. *Circulation* 120, 1513–1523. doi: 10.1161/circulationaha.109.868885

Conflict of Interest: The authors declare that the research was conducted in the absence of any commercial or financial relationships that could be construed as a potential conflict of interest.

Publisher's Note: All claims expressed in this article are solely those of the authors and do not necessarily represent those of their affiliated organizations, or those of the publisher, the editors and the reviewers. Any product that may be evaluated in this article, or claim that may be made by its manufacturer, is not guaranteed or endorsed by the publisher.

Copyright © 2021 Mostafavi, Balafkan, Pettersen, Nido, Siller, Tzoulis, Sullivan and Bindoff. This is an open-access article distributed under the terms of the Creative Commons Attribution License (CC BY). The use, distribution or reproduction in other forums is permitted, provided the original author(s) and the copyright owner(s) are credited and that the original publication in this journal is cited, in accordance with accepted academic practice. No use, distribution or reproduction is permitted which does not comply with these terms.

Supplementary Material

1 Supplementary Methods

1.1 Cardiomyocyte differentiation

Cardiomyocyte differentiation was performed in 96-well microplate as previously described (Balafkan et al., 2020). HiPSCs were seeded at 2.4×10^4 cells/cm and propagated on Geltrex (#A1413302, Thermo Fisher Scientific) and diluted (1:100) in Advanced DMEM/F-12 (#12634010, Thermo Fisher Scientific) under feeder-free conditions in Essential 8 Medium (E8) (#A1517001, Thermo Fisher Scientific). Within three days, when cells reached the optimum confluency, 60% to 70%, cardiomyocyte differentiation was started by applying the GSK3 inhibitor CHIR99021 (#4423, Tocris Bioscience) in RPMI 1640 (#61870, Thermo Fisher Scientific) medium supplemented with B27-without insulin (RPMI-B27) (#A1895601, Thermo Fisher Scientific) in a concentration-cell-dependent manner. After 24 hours, the medium was changed to RPMI-B27 without CHIR99021. The differentiation process was continued by adding 5 μ M inhibitor of WNT production-2, IWP2 (#3533, Tocris Bioscience), diluted in RPMI-B27, 72 h post-differentiation induction for 48 h. Fresh RPMI-B27 medium was provided on day five, and from day seven cells were fed with fresh RPMI medium supplemented with B27 with insulin (#17504044, Thermo Fisher Scientific) without extra supplement) every two days.

1.2 Gene expression analysis

MagMAX™-96 Total RNA Isolation Kit (#AM1830, Thermo Fisher Scientific) was used for RNA isolation from cultured cells. Cells were rinsed with DPBS (#14190250, ThermoFisher) and lysis buffer, provided in the kit, was added directly to the cells. Lysates were immediately used for RNA isolation using automated MagMAX express 96 or stored at -80°C . EXPRESS One-Step Superscript qRT-PCR Kit (#11781-01K, Thermo Fisher Scientific) was used for cDNA synthesis from 70ng of RNA ($> 30\text{ng}/\mu\text{l}$), and real-time PCR using TaqMan probes (Table S1) on an Applied Biosystems 7500-Fast real-time PCR System (Thermo Fisher Scientific). All real-time PCR reactions were performed in triplicate and the average Ct values were normalized to the geometric mean of *ACTB* and *GAPDH* as endogenous control genes. The result (dCt) was used for further analysis. A stable expression of housekeeping genes (i.e., *ACTB* and *GAPDH*) was confirmed prior to use in Realtime PCR. In our hands, expression of *RPLPO*—another well-known housekeeping gene—was not constant during mesoderm differentiation.

1.3 RNA sequencing

RNA sequencing was carried out on two different data sets, that were analyzed independently and separately. Dataset A contained RNA sequences from hESCs and hiPSC lines collected from S1 (Undifferentiated cells, day 0) and S4 (cardiac progenitors, day 7) of cardiomyocyte differentiation. Dataset A was composed of samples collected from three independent differentiations of two hESC lines (429 and 360), two independent differentiations of Detroit-7 and CRL-8, and one differentiation of Detroit-10. Dataset B corresponded to RNA sequences collected from four stages ranging from S1 to S5 (days 0, 2, 5 and 15) of three independent differentiation runs of the H1 line (hESC). The total RNA samples were isolated using MagMAX™-96 Total RNA Isolation Kit. Sample information is shown in Supplementary Tables 3 and 4.

RNA sequencing for the dataset A was carried out at the Finnish Microarray and Sequencing Centre's analysis service and Biocenter Finland. The quality of the total RNA samples ($> 30 \text{ ng}/\mu\text{l}$) and libraries was ensured with Advanced Analytical Fragment Analyzer. Sample

concentration was measured with Qubit® Fluorometric Quantitation, Life Technologies. RNA quality, as measured by RNA integrity number (RIN), was well above seven for all samples (median RIN = 9,25)—with the exception of a single sample, with RIN = 5.5. The samples were sequenced with an Illumina HiSeq 3000 instrument. We performed single-read sequencing with 1 x 50bp read length, followed by a dual index 8bp run. The base calling was performed using Illumina's standard bcl2fastq2 software, automatic adapter trimming was used. RNA sequencing for dataset B was carried out at the HudsonAlpha Genome Sequencing Center, USA, at 100bp paired-end reads. RNA quality as measured by RIN was well above seven for all samples (median RIN = 8,8). Raw fastq files were deposited in the European Nucleotide Archive (ENA) with accession number PRJEB47044. RNA sequencing analyses were performed independently for each of the datasets. Raw FASTQ files were assessed using fastQC version 0.11.8 (Andrews, 2010), and reads were mapped using Salmon version 1.3.0 (Patro et al., 2017) with the fragment-level GC bias correction option (-gcBias) against the GENCODE Release 32 (GRCh38.p13) reference transcriptome and the GRCh38 reference genome, including the whole genome as decoy sequences. Transcript quantification was collapsed to the gene-level using the R package tximport version 1.14.2 (Soneson et al., 2015) with default parameters and the GENCODE Release 32 (GRCh38.p13) annotation. Low-expressed genes (i.e., genes with less than ten reads in more than 75% of the samples of the corresponding dataset) were filtered out, resulting in 19,273 genes in dataset A—of which, 80% annotated as protein-coding—and 22,480 in dataset B (73% annotated as protein-coding).

1.4 Differential gene expression and functional enrichment analyses

Differential gene expression analyses were performed using the DESeq2 R package version 1.26 (Love et al., 2014) with default parameters. Samples from dataset A originated from different cell lines, and this was accounted for explicitly in the model by incorporating it as a covariate into the statistical model. Multiple hypothesis testing was performed with the default automatic filtering of DESeq2 followed by false discovery rate (FDR) calculation by the Benjamini-Hochberg procedure. Analyses were carried out independently for the two datasets. Genes were scored according to their significance by transforming the p-values to account for direction of change. In summary, for each gene, the up-regulated score (S_{up}) was calculated as $S_{up} = 1 - p/2$ if $LFC < 0$, and $p/2$ if $LFC \geq 0$. The down-regulated score (S_{down}) as $S_{down} = 1 - S_{up}$, where LFC corresponds to the log fold change and p to the nominal p-value of the gene. Genes were then tested for enrichment using alternatively $\log(S_{up})$ and $\log(S_{down})$ scores employing the gene score resampling method implemented in the ermineR package version 1.0.1, an R wrapper package for ermineJ (Gillis et al., 2010) with the complete Gene Ontology (GO) database annotation (Ashburner et al., 2000), the KEGG database (Kanehisa and Goto, 2000) and a curated version of mitocarta (Calvo et al., 2016; Gaare et al., 2018) to obtain lists of up- and down-regulated pathways for each cohort. The source code for the RNA sequencing analyses is available in the GitLab repository (<https://git.app.uib.no/gni042/cardiomyocytes-rna-seq>) under the GPL public license v3.0.

1.5 Flow cytometry

Cells were washed in DPBS (#14190250, ThermoFisher) three times and dissociated into single cell suspension using TrypLE™ Express Enzyme (#12604013, Thermo Fisher Scientific) for 10–20 minutes at 37°C, and were collected in the micro centrifuge tube. After a quick wash with DPBS cells were stained with Zombie Red™ Fixable Viability Kit (#423110, BioLegend) according to the manufacturer's instructions. Single cells were fixed with 4% (vol/vol) paraformaldehyde for ten minutes at room temperature (RT) and permeabilized for ten minutes at -20°C with 90% ice-cold methanol diluted in PBS. Cells were blocked in blocking buffer consisting of 0.3M glycine, 5% goat serum, and 1% BSA in PBS for 20 minutes at RT. We used the optimal concentration of conjugated antibodies for flow cytometry reported by the supplier for

each batch. Antibodies are listed in Supplementary Table (Table S1). All the primary and secondary antibodies, as well as conjugated antibodies, were diluted in blocking buffer and stained for 30 minutes at RT. Cells were washed after staining and collected in 300µl of 1% FBS in PBS. Samples were analyzed quickly after staining. At least 30,000 events were collected for the target marker using a Sony cell sorter SH800 (Sony Biotechnology Inc.), and data was analyzed and presented by FlowJo V.10.5.0 (FlowJo LLC, OR, USA, www.FlowJo.com). 8-Peaks Rainbow Calibration Particles (Biolegend #422903) was used for routine alignment and performance verification of the flow cytometry. The flow cytometer was calibrated prior to quantitative fluorescence intensity measurements using Quantum™ Alexa Fluor® 488 MESF (molecules of equivalent soluble fluorophore) (Bangs Laboratories, Inc. #488). In order to test the integrity of the results over time, collected median fluorescence intensity (MFI) was normalized to MESF as an external control and the resulting values reported as *relative MFI*. All gates were adjusted according to fluorescence minus one control (FMO). To analyze the flow cytometry data the median values of relative MFI were used to compare the samples.

1.6 Immunocytochemistry and fluorescence microscopy

Cells were seeded on Geltrex coated cover slips or in Millicell® EZ SLIDES (#PEZGS0816, Merck Millipore). Cells were fixed with 4% (vol/vol) paraformaldehyde for ten minutes at RT and permeabilized with 0.3% Tween 20 (#822184, Merck Millipore). All the primary and secondary antibodies were diluted in blocking buffer consisting of 0.3M glycine, 5% goat serum, and 1% BSA in PBS. A final concentration of 10µg/ml was used for all primary antibodies and they were incubated overnight at 4°C. Alexa Fluor 488 or 594-conjugated (Thermo Fisher Scientific) secondary antibodies were diluted in blocking buffer 1:1000 and incubated for 30 minutes to 1 hour at RT. Nuclei were stained with Gold Antifade Reagent with DAPI (#P36935, Thermo Fisher Scientific). Confocal microscopy images were taken on a Zeiss LSM 510 META or a Leica TCS SP5 at the Molecular Imaging Center (MIC), University of Bergen, and data analysis and image editing were done with Fiji (Schindelin et al., 2012). Antibodies are listed in Supplementary Table (Table S1).

1.7 Transmission electron microscopy

Cells were washed in DPBS and dissociated into single cell suspension using TrypLE™ Express Enzyme for 10–20 minutes at 37°C, and were collected in the micro centrifuge tube and centrifuged at 300g for ten minutes at RT. Cells were fixed in 2,5% glutaraldehyde (diluted in a 0,1M sodium cacodylate buffer) for 24 hours at 4°C and delivered to MIC facility at the University of Bergen. Post-fixation was performed for 1 hour (on ice) in 1% osmium tetroxide (EMS # 19134) diluted in 0,1M sodium cacodylate buffer, followed by two washing steps. The samples were then dehydrated using a graded ethanol series (30%, 50%, 70%, 96% and 100%) before being transferred to a 1:1 solution of 100% ethanol:propylene oxide (15 minutes). Samples were then transferred to 100% propylene oxide (15 minutes) before gradually introducing agar 100 resin (AgarScientific R1031) drop-by-drop over the next hours. Samples were then transferred to a small drop of 100% resin, and excess propylenoxid was allowed to evaporate (1hour). Samples were then transferred to 100% resin and placed in molds and left at RT overnight. The molds were placed at 60°C for 48 hours to polymerize. Ultrasections of approximately 60nm were placed on 100 mesh formvar coated (EMD # 15820) copper grids (EMS #G100H-Cu) and stained with 2% uranyl acetate (EMS # 22400) and lead citrate (VWR #1.07398). Grids were imaged using a Jeol JEM-1230 transmission electron microscope at 80kV.

1.8 MtDNA analysis

MtDNA quantification and deletion assessment was performed in DNA isolated from cultured cells using MagMAX™-96 DNA Multi-Sample Kit (#4413021, Thermo Fisher Scientific) and

real-time PCR, as well as long range PCR, as previously described (Tzoulis et al., 2013). A commonly deleted region (MT-ND4) in the major arc of mitochondrial DNA, and a rarely deleted region (MT-ND1), were utilized to quantify deletion. MT-ND1 was compared with amplification of a single-copy nuclear gene (APP) to assess the number of mtDNA copies. A triplex reaction of ND1, ND4 and APP was performed simultaneously within the same well using a 7500 fast sequence detection system (Thermo Fisher Scientific). Efficiency of the triplex reaction was measured prior sample analysis.

1.9 Measurement of OCR and ECAR using Seahorse XF-96 analyzer

Respiration and acidification rates were measured on monolayer culture of undifferentiated hPSCs and cells at S5 using a Seahorse XFe96 extracellular flux analyzer (Agilent, Santa Clara, CA, US). Geltrex coated XFe96 assay plates were utilized for seeding of 3×10^3 undifferentiated hPSCs and 2×10^5 hPSC-derived cardiac cells in each well. Cells were cultured in cell specific normal growth medium supplemented with $10 \mu\text{M}$ of Y-27632 for 24 hours at 37°C and 5% CO_2 . The next day, the supplemented growth medium was replaced with normal growth medium without supplement and kept until they reached almost 90% confluency prior to analysis. In order to find the optimal concentration of Carbonyl cyanide m-chlorophenyl hydrazone (CCCP) and oligomycin for each cell type, they were titrated prior to the cell analysis. The assay was performed in assay medium (pH 7.4, unbuffered) that was supplemented with 2mM L-glutamine, 2mM sodium pyruvate and 10mM glucose. Cells were washed twice and pre-incubated in the assay medium and kept in a CO_2 -free incubator (XF Prep Station, Seahorse Biosciences) at 37°C for 1 hour before measurement, in order to remove CO_2 from the medium. For mitochondrial respiration analysis, the final concentrations of $3 \mu\text{M}$ oligomycin, 0.5- $1 \mu\text{M}$ CCCP, $1 \mu\text{M}$ rotenone, and $1 \mu\text{M}$ antimycin A were diluted in assay medium. In order to correct the final results for differences in cell size and number between the undifferentiated hPSCs and differentiated cells at S5, we measured the total protein concentration for each well using absorbance at 280nm. All the results were reported as pmol O_2 per min after normalized to their total protein concentration. Each parameter was calculated accordingly; basal OCR = (OCR in non-treated cell - OCR after adding Antimycin A), Coupling Efficiency = (ATP Production Rate / Basal Respiration Rate \times 100), spare respiration capacity = (maximal respiration / basal respiration). The XF reader software (Wave Desktop 2.4) was used to analyses the data.

1.10 Measurement of mitochondrial membrane potential

We used a previously described protocol (Rowe and Boletta, 2013) to analyze the mitochondrial membrane potential (ψm) independent of cell volume using TMRM. We quantified the fluorescent intensity of TMRM (FI) before and after applying Carbonyl cyanide 4-(trifluoromethoxy)phenylhydrazone (FCCP) as an uncoupler for OXPHOS which eliminates the mitochondrial membrane potential. The distribution of TMRM relies on the Nernstian equilibrium (Dykens and Stout, 2001). Accumulation of TMRM in the cytosol is very small compared with mitochondria due to the low negative charge of cytosol relative to mitochondrial matrix. Thus, fluorescence readouts mirror the mitochondrial matrix:cell volume ratio. FCCP treatment of the cell releases the TMRM from mitochondrial matrix into cytosol and causes a re-equilibrium of TMRM in the cytosol. Therefore, fluorescence readout after FCCP treatment represents cell volume. The difference between median for TMRM and TMRM-FCCP treated cells provided us the membrane potential level normalized to the cell size. We analyzed mitochondrial membrane potential by flow cytometry starting with 1×10^6 cells per sample. Each sample was divided in two; one sample was treated with 25nM TMRM and another with a mixture of 25nM TMRM and $100 \mu\text{M}$ FCCP. Samples were incubated for 20 minutes at 37°C and 5% CO_2 , washed three times with HBSS, and analyzed within 1 hour. In order to adjust the measured membrane potential to the mitochondrial content of cells at single cell level, we used median of TMO20-MFI for live cells at S1 and S5 as an indicator of mitochondria mass. Using

the ratio of TMRM-MFI in live cells (only viable cells can take up TMRM) at S1 and S5 to TOM20-MFI of the total live cells (TNNT2+ and – are included for S5) from the same batch of differentiation we calculate the mitochondrial membrane potential per unit of mitochondrial mass (for more details see (Perry et al., 2011)).

1.11 References

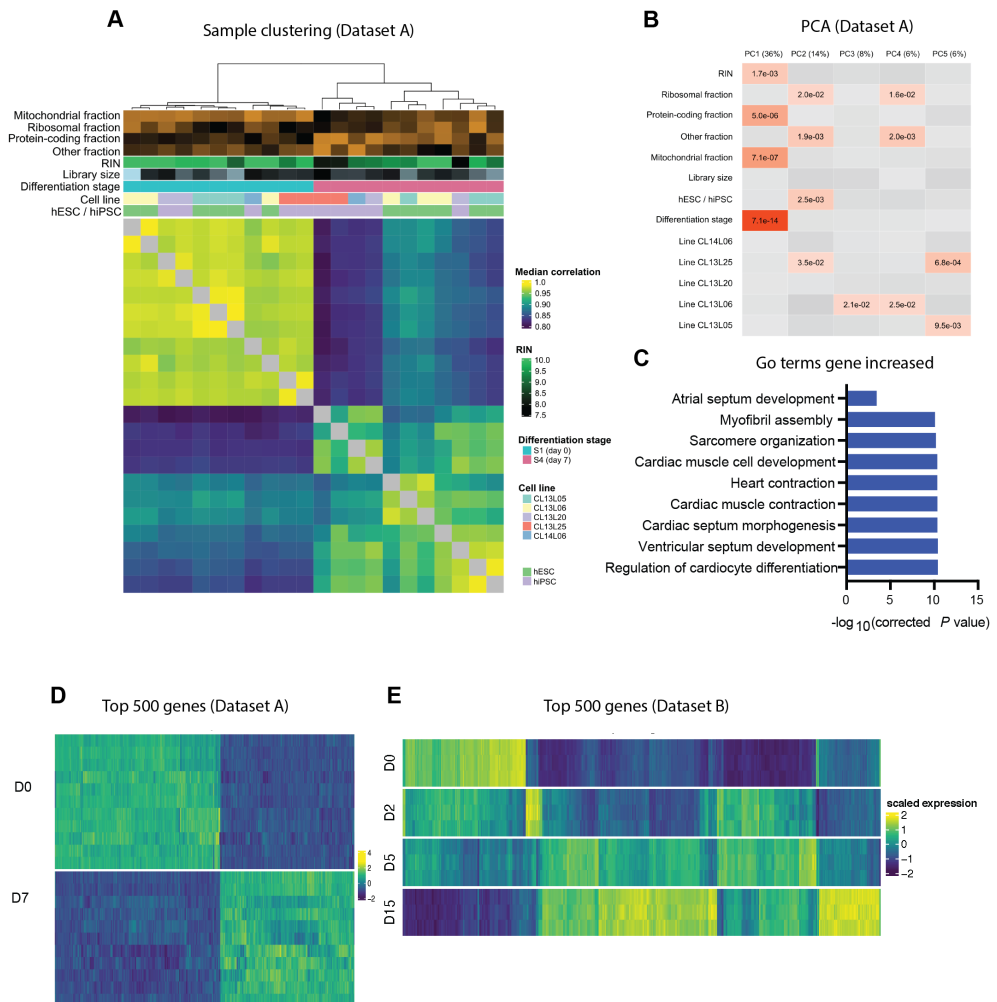
- Andrews, S. (2010). FastQC: a quality control tool for high throughput sequence data. Available at: https://www.bioinformatics.babraham.ac.uk/projects/fastqc/RNA-Seq_fastqc.html.
- Ashburner, M., Ball, C. A., Blake, J. A., Botstein, D., Butler, H., Cherry, J. M., et al. (2000). Gene ontology: tool for the unification of biology. The Gene Ontology Consortium. *Nat Genet* 25, 25–9. doi:10.1038/75556.
- Balafkan, N., Mostafavi, S., Schubert, M., Siller, R., Liang, K. X., Sullivan, G., et al. (2020). A method for differentiating human induced pluripotent stem cells toward functional cardiomyocytes in 96-well microplates. *Sci Rep-uk* 10, 18498. doi:10.1038/s41598-020-73656-2.
- Calvo, S. E., Clauser, K. R., and Mootha, V. K. (2016). MitoCarta2.0: an updated inventory of mammalian mitochondrial proteins. *Nucleic Acids Res* 44, D1251-7. doi:10.1093/nar/gkv1003.
- Dykens, J. A., and Stout, A. K. (2001). Assessment of mitochondrial membrane potential in situ using single potentiometric dyes and a novel fluorescence resonance energy transfer technique. 65, 285–309. doi:10.1016/S0091-679x(01)65018-0.
- Gaare, J. J., Nido, G. S., Sztromwasser, P., Knappskog, P. M., Dahl, O., Lund-Johansen, M., et al. (2018). Rare genetic variation in mitochondrial pathways influences the risk for Parkinson’s disease. *Movement Disord* 33, 1591–1600. doi:10.1002/mds.64.
- Gillis, J., Mistry, M., and Pavlidis, P. (2010). Gene function analysis in complex data sets using ErmineJ. *Nat Protoc* 5, 1148–59. doi:10.1038/nprot.2010.78.
- Kanehisa, M., and Goto, S. (2000). KEGG: kyoto encyclopedia of genes and genomes. *Nucleic Acids Res* 28, 27–30. doi:10.1093/nar/28.1.27.
- Love, M. I., Huber, W., and Anders, S. (2014). Moderated estimation of fold change and dispersion for RNA-seq data with DESeq2. *Genome Biol* 15, 550. doi:10.1186/s13059-014-0550-8.
- Patro, R., Duggal, G., Love, M. I., Irizarry, R. A., and Kingsford, C. (2017). Salmon provides fast and bias-aware quantification of transcript expression. *Nat Methods* 14, 417–419. doi:10.1038/nmeth.4197.
- Perry, S. W., Norman, J. P., Barbieri, J., Brown, E. B., and Gelbard, H. A. (2011). Mitochondrial membrane potential probes and the proton gradient: a practical usage guide. *Biotechniques* 50, 98–115. doi:10.2144/000113610.

Rowe, I., and Boletta, A. (2013). Mitochondrial Transmembrane Potential (ψ_m) Assay Using TMRM. *Bio-protocol* 3. doi:10.21769/bioprotoc.987.

Schindelin, J., Arganda-Carreras, I., Frise, E., Kaynig, V., Longair, M., Pietzsch, T., et al. (2012). Fiji: an open-source platform for biological-image analysis. *Nat Methods* 9, 676–82. doi:10.1038/nmeth.2019.

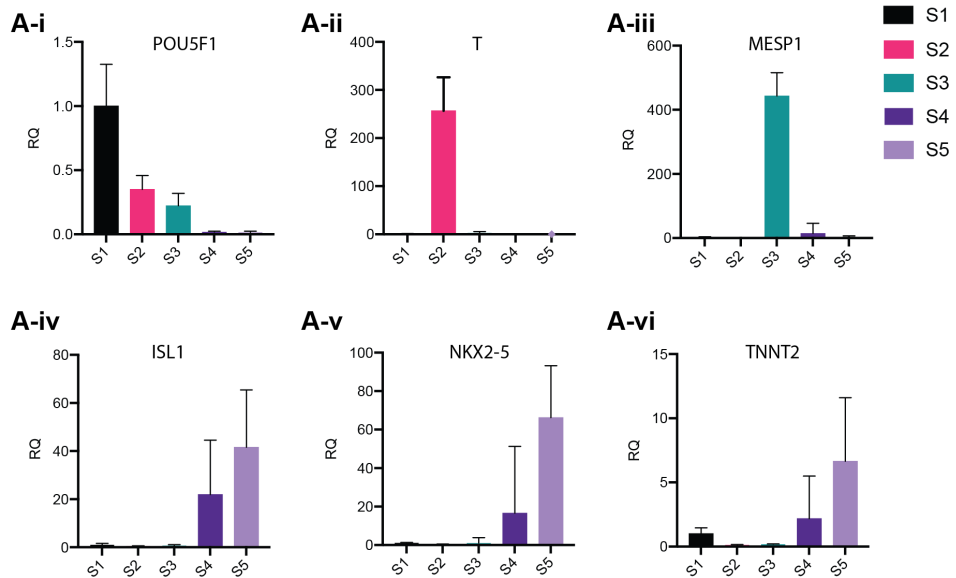
Soneson, C., Love, M. I., and Robinson, M. D. (2015). Differential analyses for RNA-seq: transcript-level estimates improve gene-level inferences. *F1000research* 4, 1521. doi:10.12688/f1000research.7563.2.

Supplementary Figure 1



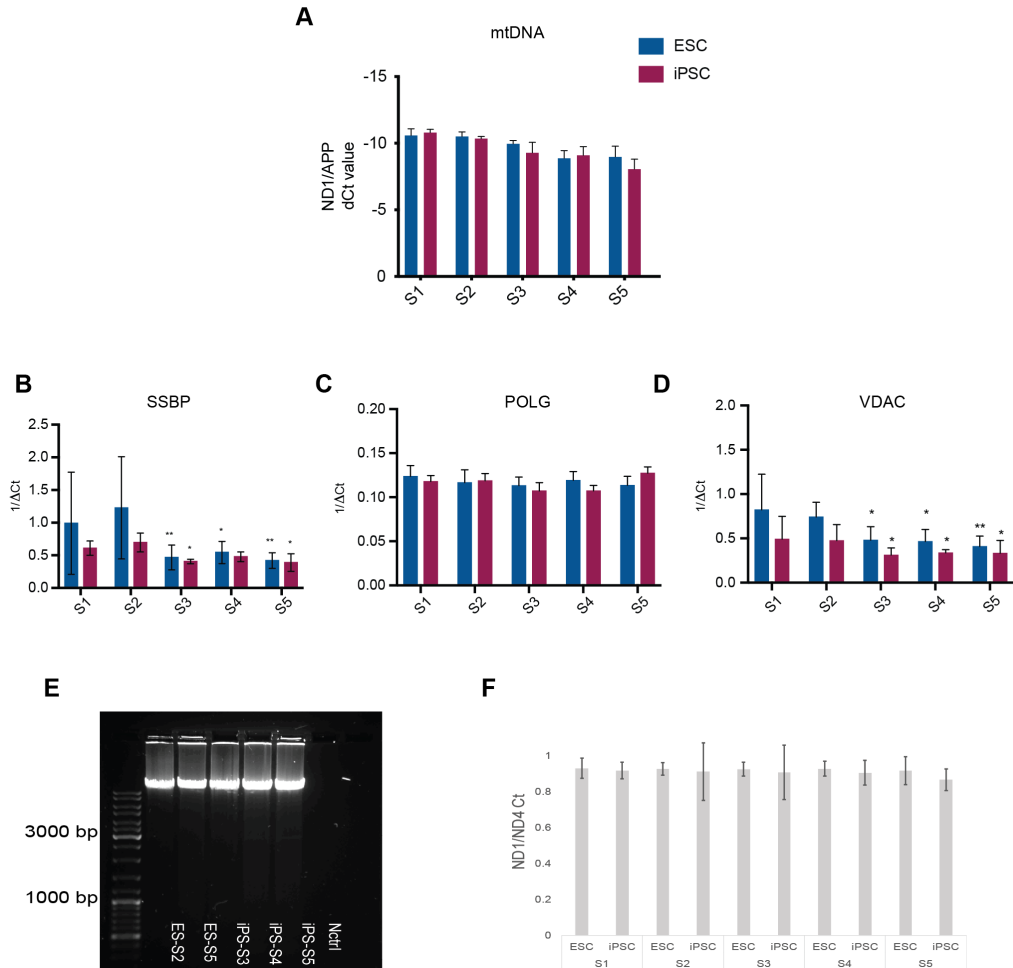
Supplementary Figure 1. (A) Sample clustering from Dataset A (stages S1 and S4) based on normalized RNA-seq counts. The heatmap depicts median sample correlation in expression, with column annotation based on experimental variables. (B) Association between main lines of variation in gene expression (first five principal components) and experimental variates for Dataset A (stages S1 and S4). P values below 0.05 are annotated in the cells (linear regression model). (C) GO term enrichment analysis shows up-regulated cellular pathways during cardiomyocyte differentiation (Dataset B). Barplot representing $-\log_{10}$ corrected p-values for gene set enrichment analysis of representative pathways involved in cardio-myocyte differentiation, all up-regulated. (D) Heatmap representing scaled gene expression for the top 500 differentially expressed genes (columns) between day 0 and day 7 for all samples in dataset A (rows). (D-E) Heatmaps representing scaled gene expression for the top 500 differentially expressed genes (columns) across time for all samples in each dataset (rows).

Supplementary Figure 2



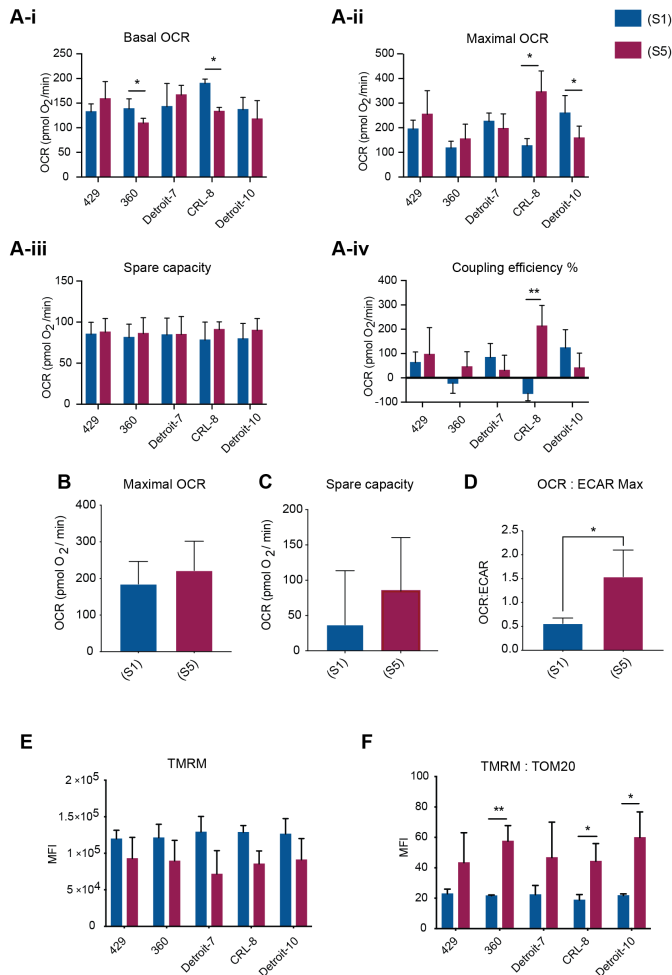
Supplementary Figure 2. Transcriptomic profiling of cells during cardiomyocyte differentiation. (A i-vi) Gene expression of selected markers is individually examined using real-time PCR for different stages of cardiomyocyte differentiation. Markers include: POU Class 5 Homeobox 1 (POU5F1), T-Box Transcription Factor T (T), Mesoderm Posterior BHLH Transcription Factor 1 (MESP1), ISL LIM Homeobox 1 (ISL1), NK2 Homeobox 5 (NKX2-5), and Cardiac Muscle Troponin T (TNNT2). HESC (360) was used for gene expression analysis and the expression of each gene normalized to geometric mean of GAPDH and ACTB (relative quantification, RQ). Each bar represents the expression level of specific genes relative to expression of housekeeping genes. An average of four independent experiments and error bars represent the 95% confidence interval (CI) of the mean.

Supplementary Figure 3

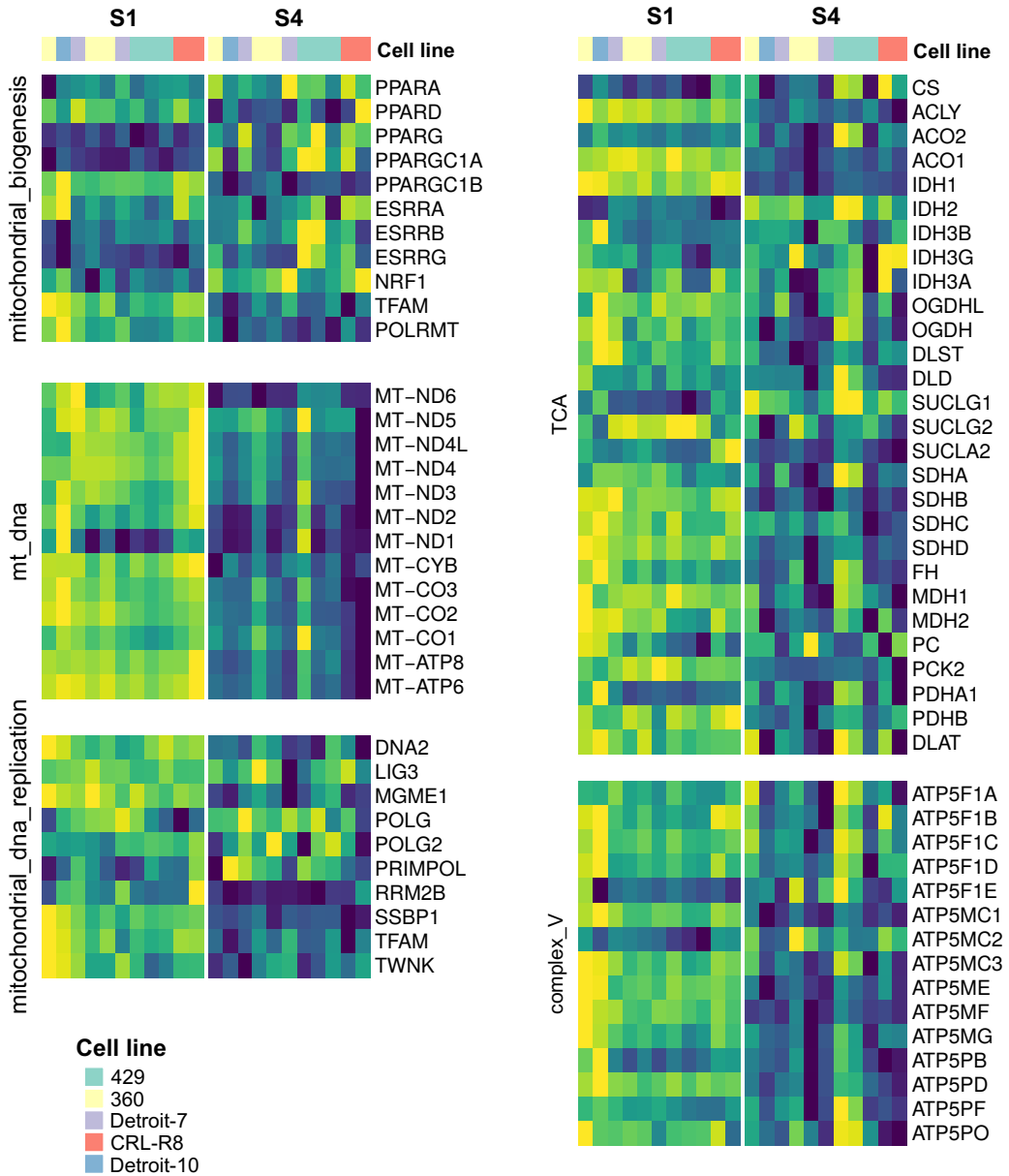


Supplementary Figure 3. Assessing mtDNA replication machinery and integrity during cardiomyocyte differentiation. **(A)** Cycle threshold (Ct) of real-time PCR demonstrated no significant difference in mtDNA level between the two different types of hPSCs (i.e., hiPSC and hESC). **(B, C, and D)** Real-time PCR gene expression analysis for selected markers of the different stages of cardiomyocyte differentiation. HESC (360) was used for gene expression analysis and the expression of each gene normalized to geometric mean of two internal controls (*GAPDH* and *ACTB*). Each bar represents the average of 3–4 independent experiments and error bars represent the 95% confidence interval (CI) of the mean. **(E and F)** We examined the mtDNA integrity of hESCs and hiPSCs in different stages of cardiac differentiation utilizing long-range PCR and real-time PCR, and we could not find any mtDNA deletion.

Supplementary Figure 4



Supplementary Figure 4. Assessing the oxygen consumption rate (OCR) and extracellular acidification rate (ECAR) using a Seahorse XF-96 extracellular flux analyser. **(A)** Bar charts presenting different status of OCR in each individual hPSC line before and after differentiation (S1 vs. S5). **(B and C)** Maximal OCR and spare capacity were showed a slight increase in differentiated cells relative to undifferentiated hPSCs. **(D)** Maximal OCR: ECAR significantly increased, which suggests an increase in mitochondrial respiration activity relative to glycolysis in S5. All of the data collected from the Seahorse experiment normalized to the total protein concentration measured for each well at OD of 280nm. T-tests with Holm-Sidak multiple testing correction was used to assess statistical significance of the difference between S1 and S5 in individual lines. **(E and F)** MFI of TMRM was measured for undifferentiated hPSCs and differentiated cells at S5. We could not detect any significant difference between hESC and hiPSC before or after differentiation. We found significant increase in TMRM level after correction for mitochondrial content. P value= * <0.05 , ** <0.01 , *** <0.001 calculated by Mann Whitney test.



Supplementary Figure 5. Heat map of differentially express genes (S1 versus S4) involved mtDNA homeostasis, mitochondria abiogenesis and ATP-linked activity of mitochondria. 1 is yellow/bright, 0 is blue/dark.

3. Supplementary Movies

Movie 1) Beating cardiomyocytes at S5 generated from hESC (429).

Movie 2) Beating cardiomyocytes at S5 generated from hiPSC (Detroit-7).

Movie 3) Functional cardiomyocytes in the seahorse plate generated from hESC (429).

Movie 4) Functional cardiomyocytes in the seahorse plate generated from hiPSC (Detroit-7).

4. Supplementary Table

Table S1. Reagents

| Flow cytometry antibodies | | | | |
|----------------------------------|-------------------|--------------------------|-----------------------|--------------------|
| Marker | Host | Company | Catalog Number | Application |
| TNNT2 | recombinant human | Miltenyi Biotec | 130-106-688 | Flow Cytometry |
| SSEA4 | Mouse | Thermo Fisher | MA1-021-PE | Flow Cytometry |
| ISL1 | Mouse | dbiosciences | 562547 | Flow Cytometry |
| TOM20 | Mouse | Santa Cruz Biotechnology | sc-17764 | Flow Cytometry |
| TFAM | Mouse | abcam | ab198308 | Flow Cytometry |
| Microscopy antibodies | | | | |
| Marker | Host | Company | Catalog Number | Application |
| POUF5A | Rabbit | abcam | ab19857 | IF |
| SOX2 | Rabbit | abcam | ab97959 | IF |
| NANOG | Rabbit | abcam | ab21624 | IF |
| SSEA4 | Mouse | abcam | ab16287 | IF |
| ACTA2 | Mouse | abcam | ab7817 | IF |
| CDH5 | Rabbit | abcam | ab33168 | IF |
| GJA1 | Rabbit | abcam | ab11370 | IF |
| MYL7 | Mouse | abcam | ab68086 | IF |
| TNNT2 | Mouse | abcam | ab8295 | IF |
| TaqMan probes | | | | |
| Marker | Company | Catalog Number | Application | |
| Human GAPD | Thermo Fisher | 4333764F | TaqMan Probe | |
| Beta ACT (ACTB) | Thermo Fisher | Hs01060665_g1 | TaqMan Probe | |
| POU5F1 (OCT 4) | Thermo Fisher | Hs00999634_gH | TaqMan Probe | |
| T (BRACHYURY) | Thermo Fisher | Hs00610080_m1 | TaqMan Probe | |
| MESP1 | Thermo Fisher | Hs01001283_g1 | TaqMan Probe | |
| ISL1 (ISLET1) | Thermo Fisher | Hs00158126_m1 | TaqMan Probe | |
| NKX2-5 | Thermo Fisher | Hs00231763_m1 | TaqMan Probe | |
| TNNT2 (cTnT) | Thermo Fisher | Hs00943911_m1 | TaqMan Probe | |
| VDAC1 | Thermo Fisher | Hs01631624_gH | TaqMan Probe | |
| SSBP1 | Thermo Fisher | Hs00995376_g1 | TaqMan Probe | |
| TFAM | Thermo Fisher | Hs00273372_s1 | TaqMan Probe | |
| POLG | Thermo Fisher | Hs00160298_m1 | TaqMan Probe | |

Table S2. Statistical tests description

| Experiments | Conditions (stages) | test | N |
|---------------------------|------------------------|--|---|
| MtDNA qPCR | S1, S2, S3, S4, and S5 | Friedman test with Dunn's multiple comparison test | 5 |
| Mitochondria mass | S1, S4, and S5 | Friedman test with Dunn's multiple comparison test | 5 |
| Tfam | S1, S4, and S6 | Friedman test with Dunn's multiple comparison test | 5 |
| Membrane potential | S1 and S5 | Two-tailed unpaired nonparametric t-test (Mann-Whitney test) | 5 |
| Seahorse | S1 and S5 | Two-tailed unpaired t-test with Welch's correction | 5 |

Table S3. RNA-seq Dataset A

| Sample ID | Day | Cell line | Type | RIN |
|----------------|-----|-----------|-------|-----|
| 1_15S784_S1 | D0 | CL13L05 | hESC | 9.8 |
| 2_15S872_S6 | D0 | CL13L05 | hESC | 10 |
| 3_15S952_S11 | D0 | CL13L05 | hESC | 8.9 |
| 4_15S977_S16 | D7 | CL13L05 | hESC | 9.7 |
| 5_15S1104_S21 | D7 | CL13L05 | hESC | 9.1 |
| 6_15S1160_S26 | D7 | CL13L05 | hESC | 9.3 |
| 7_15S792_S31 | D0 | CL13L06 | hESC | 10 |
| 8_15S865_S36 | D0 | CL13L06 | hESC | 10 |
| 9_15S945_S2 | D0 | CL13L06 | hESC | 10 |
| 10_15S984_S7 | D7 | CL13L06 | hESC | 10 |
| 11_15S1096_S12 | D7 | CL13L06 | hESC | 10 |
| 12_15S1152_S17 | D7 | CL13L06 | hESC | 9.4 |
| 13_15S1416_S22 | D0 | CL13L25 | hiPSC | 9.2 |
| 14_15S1468_S27 | D0 | CL13L25 | hiPSC | 9.8 |
| 15_15S1564_S32 | D7 | CL13L25 | hiPSC | 8 |
| 16_15S1612_S37 | D7 | CL13L25 | hiPSC | 8.1 |
| 17_15S554_S3 | D0 | CL14L06 | hiPSC | 10 |
| 18_15S586_S8 | D7 | CL14L06 | hiPSC | 9.1 |
| 19_15S1425_S13 | D0 | CL13L20 | hiPSC | 10 |
| 20_15S1477_S18 | D0 | CL13L20 | hiPSC | 9.8 |
| 21_15S1573_S23 | D7 | CL13L20 | hiPSC | 9.2 |
| 22_15S1622_S28 | D7 | CL13L20 | hiPSC | 7.8 |

Table S4. RNA-seq Dataset B

| Sample ID | Day | RIN |
|------------------|------------|------------|
| S1_SL403714 | D0 | 9.6 |
| S2_SL403715 | D2 | 8.1 |
| S3_SL403716 | D5 | 7.1 |
| S4_SL403717 | D15 | 8 |
| S5_SL403718 | D0 | 10 |
| S6_SL403719 | D2 | 9.8 |
| S7_SL403720 | D5 | 9.8 |
| S8_SL403721 | D15 | 10 |
| S9_SL403722 | D0 | 9.4 |
| S10_SL403723 | D2 | 7.7 |
| S11_SL403724 | D5 | 8.2 |
| S12_SL403725 | D15 | 7.3 |

Table S5. List of differentially expressed genes between S1 and S4.

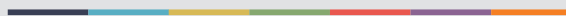
Table S6. List of enriched pathways (GO analyzes) between S1 and S4.

Table S7. List of differentially expressed genes between hiPSC and hESC.

Table S8. List of enriched pathways (GO analyzes) between hiPSC and hESC.



Graphic design: Communication Division, UIB / Print: Skjipes Kommunikasjon AS



uib.no

ISBN: 9788230869499 (print)
9788230853658 (PDF)